MICRO FLUIDIC CYTOMETRY
FOR ANALYSIS OF MARINE MICROORGANISMS

by

Giuseppe Benazzi

A thesis submitted for the degree of Doctor of Philosophy

School of Electronics and Computer Science,
University of Southampton,
United Kingdom.

January 2010

UNIVERSITY OF SOUTHAMPTON

ABSTRACT

FACULTY OF ENGINEERING

SCHOOL OF ELECTRONICS AND COMPUTER SCIENCE

Doctor of Philosophy

MICRO FLUIDIC CYTOMETRY FOR ANALYSIS OF MARINE MICROORGANISMS

by Giuseppe Benazzi

Knowledge of the distribution and concentration of phytoplankton (microscopic algae that live in the oceans) is important, as this reflects and may modify environmentally important events such as pollution, climate change and carbon dioxide sequestration. Optical based flow cytometry has proved to be strategically important for the study of marine environments in general and of phytoplankton in particular because it enables rapid, simultaneous quantitative analysis of multiple optical properties of particles. Unfortunately, cost, complexity and size limit the widespread use of this technique for the study and monitoring of phytoplankton.

The objective of this research was to solve some of the above mentioned problems by developing a small device for deployment on remote underwater vehicles (RUV) for *in situ* flow cytometric analysis of marine organisms. The core of the system was a lab-on-a-chip (LOC) device with a microfluidic channel with integrated optics and electrodes for the detection of the optical and electrical characteristics of phytoplankton.

The work describes the design, fabrication, characterisation and testing of various LOC devices, together with data and analysis of results. The devices were able to clearly distinguish different populations of phytoplankton and other micro-particles on the basis of their optical and electrical properties. The systems had performance comparable with commercial instruments.

Research also included bio-physical measurements (electro rotation and dielectrophoresis) of marine organisms to allow further modelling of the information obtained from the LOC cytometer.

Dedicata a mia mamma

Contents

List of Figures

List of Tables

Acknowledgements

I would like to thank Professor Hywel Morgan for giving me the opportunity to work in such an interesting field. His guidance, encouragement and enthusiasm made this experience extremely rewarding and helped me to become independent. I would also like to thanks my advisor Dr Matt Mowlem, for his support and many stimulating suggestions.

I would also like to acknowledge funding from the University of Southampton Life Sciences Institute (LSI) and Dr. Debora Iglesias Rodriguez and Dr John Gittins from the National Oceanographic Centre of Southampton (NOCS) for sample culturing.

A special acknowledgement goes to Dr David Holmes who I owe my deepest gratitude for teaching me the basics of the field, for his technical support and for his sincere friendship; his support really was an essential parts of my experience. I am also grateful to many people who have taught and assisted me doing the laboratory work: Dr Nicola Green for patient explanation on the principles of AC electrokinetics, my colleagues Ferran, Catia Bernabini, Diego Morganti, David Barat, Barbara Cortese, Shady Gawad, Raph Tornay, Mairi Sandison, Michele Zagnoni, Daniele Malleo, Florian L'Hostis, Sun Tao, Andrew Witton and Katie Chamberlain. Many thank also to all the other members of the Bioelectronics group that I met along the way and made my experience extremely enjoyable.

During these years I met many friends that made this experience unique and deeply enjoyable. I am deeply grateful to all this people, and in particular I would like to thank Mario, Marty, Tobias, Ferran, Carla, Shady, Raph, Armando, Andy, Michele, David (B and H), Catia, Kt, Bianca, Barbara, Davide, Nino, Cecio, and Elena for the special relationship I build with them and for being close to me and offer me friendship and support whenever I needed it. Additional mention goes to Mario for the lovely years spent living in the same house, Catia for the "mental distress" in the lab and Marty, Andy, Mairi, David, Barbara, Rupert, Kt and Veronica for patiently satisfying my endless need of document proof reading!

I would also like to thank all friends at Nano Group and Ms. Glenys C. Howe, Ms. Lucia Hewett, and Ms. Azra Jaffry, librarians and IT Unit in the School of Electronics and Computer Science of Southampton University, for assisting me in many different ways.

Un ringraziamento va anche a tutte le persone che mi hanno sostenuto dall'Italia e che mi hanno sempre fatto sentire a casa ad ogni mio ritorno. Sopra tutti c'è ovviamente mia mamma che mi ha sempre sostenuto e incoraggiato nonostante il sacrificio di sapermi lontano. Ringrazio anche Gianni per tutti i viaggi Cento-Bologna (e oltre) che si e' dovuto sciroppare. Un ringraziamento particolare va poi a Oscar, Giovanni (a 'sto giro ti ho lasciato ...) ed Elma per il loro supporto morale a distanza e l'impegno e il tempo che mi hanno dedicato ogni volta che tornavo in Italia.

Definitions and Abbreviations

a	Particle radius
a_N	Radius of the Nth-shell
A	Total area under a curve
C_{smem}	Specific membrane capacitance
CHA	Chlorophyll A
CHB	Chlorophyll B
CSW	Central Steam Width
CV	Coefficient of Variation
$\mathrm{D_h}$	Hydraulic diameter
dt	Transit time
f_0	Cross-over frequency
f_c	Lift coefficient
f_{CM}	Clausius-Mossotti factor
FACS	Fluorescence Activated Cell Sorter
FCM	Flow Cytometry
FGO	Green-Orange Fluorescence
FGR	Green-Red Fluorescence
FGFR	Green-Far Red Fluorescence
FR	Flow Rate
FRR	Red-Red Fluorescence
FSC	Forward Scatter light
FWHM	Full-width at half maximum
G_{smem}	Specific membrane conductance
I_0	Incident radiation
I_1	Radiation at the tip of the optical fibre
IS	Impedance Spectroscopy
l_{ch}	Channel length
LIF	Light Induced Fluorescence
LOC	Lab-on-a-Chip
MEMS	micro-electromechanical systems

OD600	Optical Density at 600nm
p	Pressure
P_{LASER}	Emission power at 532 nm measured at the laser
P_{Rhod}	Output fluorescence emission power of Rhodamine 6G at 550 nm
PBS	Phosphate Buffer Saline
PDMS	Poly-dimetil-syloxane
PE	Phycoerythrin
PHY	Phycocyanin
PP	Primary Production (photosynthesis)
PS-DVB	Polystyrene divinylbenzene
r	Characteristic size of the channel
rpm	Rounds per minute
R_c	Channel Reynold's number
R_e	Reynold's number
R_p	Particle Reynold's number
R^2	Coefficient of determination
RFD	Red Food Dye
RUV	Remote Underwater Vehicle
SAG	Self Alignment Groove
SSC	Side Scatter light
STD	Standard Deviation
t_0	Time immediately before a particle enters the detection region
t_1	Time immediately after a particle exits the detection region
t_x	Time for the period of a particle passing in the detection region
TEM	Transmission Electron Microscopy
TOF	Time of Flight
$\|v\|$	Average particle flow velocity
v	Flow velocity
v_p	Migration velocity of the particle from the centre of the channel
v_{max}	Maximum channel velocity
w_{ch}	Channel width
x_c	Horizontal coordinate of the peak of the Gaussian curve
y_0	Baseline off-sett of the Gaussian curve
$\|Z\|_{xxx}$	Magnitude of the impedance signal measured with an input

ε	Permittivity
ε^*	Complex permittivity
ε_m	Permittivity of the medium
ε^*_{mix}	Complex permittivity from Maxwell's mixture formula
ε_p	Permittivity of the particle
ε^*_p	Complex permittivity of the particle
ε^*_{Neff}	Effective complex permittivity of the N-shelled sphere model
φ	Volume fraction
η	Dynamic viscosity
ν	Kinematic viscosity
μTAS	micro Total Analytical Systems
ρ	Fluid density
σ	Conductivity
σ^*	Complex conductivity
ω	Angular frequency

Declaration of Authorship

Preface

In this work the design and testing of microfluidic devices for the study of the marine environment are reported. The literature of the field is presented in the first chapters (1-2) whilst the experimental part is described in chapters 4-7.

Chapter 1 presents a literature review that describes how flow cytometry has been applied to the study and monitoring of phytoplankton.

Chapter 2 reviews the literature on micro-system technology. The chapter briefly introduces the history and fabrication of the field than focus on micro-systems for flow cytometry applications and integration of optics.

Chapter 3 presents two micro-fluidic systems able to perform simultaneous measurement of impedance and optical properties of particles. The two chips presented will be used in the following chapters for flow cytometric measurements.

Chapter 4 describes the preparation methods for the various samples and solutions, and details the apparatus used for these experiments.

Chapter 5 presents measurements for the characterisation of the optical system of the microfluidic device developed in this work.

Chapter 6 presents the results obtained by performing cytometric measurements with the sensors presented in chapter 3.

Chapter 7 presents the measurement of the electrical properties of the marine algae *I. galbana* using AC electrokinetics experiments.

Chapter 8 Conclusions and future work.

Declaration

This report describes research undertaken by the author whilst working within a collaborative research environment. This report documents the original work of the author except in the following sections: 3.6, 4.5, 7.3.

Chapter 1

Phytoplankton monitoring by flow cytometry

1.1 Introduction

Phytoplankton are plant-like autotrophic micro-organisms that live in the oceans and are at the base of the marine food chain. Phytoplankton are taxonomically and functionally diverse, exist in a wide range of sizes (0.2 µm to 200 µm)[1] and have biogeochemical characteristics that depend on taxonomy. Measurement and analysis of phytoplankton taxa in the oceans is important for a number of reasons, including pollution monitoring [1], climate change [2] and climate modelling [3]. A recent review by Legendre *et* al. [4] describes the analysis of phytoplankton in biological oceanography. These authors describe the contribution made by flow cytometric analysis to the understanding of the four major environmental crises; contamination of near-shore water, collapse of marine resources, loss of biodiversity and global climate change.

Phytoplankton contain photopigments including chlorophylls, phycoerythrin and allophycocyanine. The organisms perform photosynthesis, fix carbon and generate carbohydrates. This Primary Production (PP) results in the sequestration and fixation of carbon dioxide, a greenhouse gas which is linked to climate change. Phytoplankton

---

[1] Phytoplankton can be differentiated into three size classes: picoplankton (0.2-2µm), nanoplankton (2-20 µm) and microplankton (20-200 µm).

are responsible for 90-96% of oceanic PP and therefore accurate models of phytoplankton activity are vital for understanding and prediction of climate change. Phytoplankton may be responsible for uptake and fixation of excess carbon dioxide produced by human activities [4] and global warming may change the biological pump which transfers carbon to deep oceans [5]. Phytoplankton may also have an important role to play in the global sulphur cycle [6].

Analysis of phytoplankton density and species can be used to evaluate the release of contaminants into marine waters. Contaminants can lead to poisoning of the phytoplankton population or conversely to the formation of algal blooms that can create large amounts of toxins or rapidly sequester dissolved oxygen, causing problems to other marine life. Toxins from algal blooms are responsible for the death of the marine fauna and can cause diseases in humans [1].

Phytoplankton studies at the single cell level were traditionally performed using optical microscopy but as this technique is laborious and time consuming, scientists have begun to use flow cytometry (FCM) for such analysis. FCM is an automatic technique initially developed for biomedical applications that enables precise, rapid, and quantitative measurement of multiple optical properties of individual particles. For these reasons a number of studies have been presented for the improvement of flow cytometric techniques on phytoplankton study and monitoring; a literature review of these studies that includes history, detection parameters and data processing is presented in this chapter.

1.2 Flow cytometry (FCM) principle

Figure 1.1 shows the general working principle of FCM. A sample is ejected through a nozzle and is focussed by sheath flow that places the sample in a narrow stream and arranges particles in single file (hydrodynamic focussing). As single particles pass through the detection region (detail on the right in Figure 1.1) they are hit by a focussed optical beam; the emission light (fluorescence or scattered) is collected by a system of optics and delivered to a photodetector which measures the optical intensity. This data is acquired by a PC where data can be stored, processed and analysed.

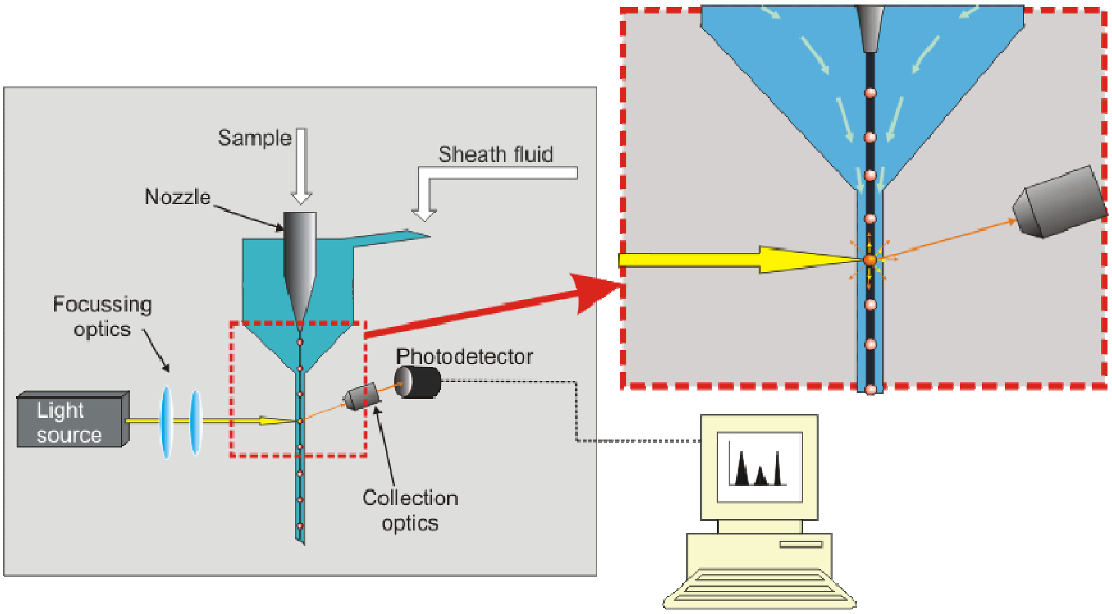

Figure 1.1 - Schematic representation of the working principle of flow cytometry. Hydrodynamic focussing is formed with a nozzle for the sample and a funnel for the sheath flow. The detection system is formed by a light source, free space optics and photodetectors. A personal computer is used for flow control and data acquisition.

1.3 Flow cytometry and the study of phytoplankton

FCM has been used to analyse mixed population of phytoplankton since the early 1980s [7; 8; 9; 10]. It has also been used to discriminate differences between very small plankton [11] (picoplankton with diameter < 2μm). Flow cytometry was central to the discovery of a new class of phytoplankton [12; 13] which was difficult to detect with traditional microscopy.

After the first studies in this field, in the 1990s flow cytometry became more widely used for phytoplankton monitoring and at the present stage of research flow cytometry is very useful for determining biomass and dominant phytoplankton species [14; 15]. The technique is often used with more traditional techniques for phytoplankton monitoring [15; 16] and sometimes is the only instruments used for the analysis [8; 17].

Despite flow cytometry being able to identify dominant species, it is not able to provide detailed information about species composition [14; 15; 17; 18], this is because phytoplankton cells are similar in size and pigmentation and this makes it difficult to distinguish cells only according to optical characteristics. Furthermore, FCM in phytoplankton monitoring is also affected by other problems such as smaller size range of commercial instruments (typically between 1µm and 50µm) compared to that found in phytoplankton, data processing and the high cost of flow cytometers. Problems also arise when comparing data from different instruments [19] because different brands have different settings (e.g. laser used and angle of detection for scattered light).

Scientists tried to solve some of these problems by modifying commercial instruments [20], building flow cytometers with features more suited to phytoplankton analysis [21; 22], integrating flow cytometry with other techniques [15] or using automated recognition techniques [19]. But progresses to date have not been sufficient to solve the above mentioned problems.

1.3.1 CytoBuoy for in situ monitoring of phytoplankton

In addition to identification problems, phytoplankton monitoring is also affected by the difficulty of performing *in situ* automated analysis that would enable continuous monitoring and better understanding of seasonal and spatial dynamics of ecosystems. For these reasons Dubelaar *et al.* [21; 23; 24] presented an instrument able to perform autonomous *in situ* flow cytometry. The device was mounted on a buoy in water and used traditional FCM techniques such as conventional optics and hydrodynamic focussing and was designed on the basis of a flow cytometer specifically developed for phytoplankton analysis [22]. Furthermore, the device implemented features such as low power consumption, reduced size, wireless transmission of the data and a mechanical arrangement to make it resistant to shocks and wave motion.

Parameters measured by the CytoBuoy are forward and side scatter light, time of flight, pulse shape, and fluorescence in the orange and red region (see section 1.4). The power provided by the internal batteries enabled the registration of 3000-4000 samples (according to the organisms concentration) at a flow rate of 0.3 ml min^{-1}; every sample contained a maximum of 4000 events for battery saving reasons. The size of particles that could be analysed ranged between 1 and 800 µm with a standard deviation measured to be 10% CV (coefficient of variation)[2] on the forward scatter signal of 4 µm calibration beads. Tests performed *in situ* showed that CytoBuoy had a lower

---

[2] Coefficient of variation is given by:

$$\mathrm{CV} = \frac{\mathrm{STD}}{\mathrm{Mean}} \times 100$$

where STD is the standard deviation and Mean is the average value of the set of data.

characterisation power compared to a conventional flow cytometer, probably because of the different laser excitation source, the lower accuracy and maybe the modification of optical properties of cells fixed for analysis with a conventional flow cytometer.

In conclusion, the first work published on CytoBuoy demonstrated that autonomous flow cytometry is feasible. Despite the judicious assembly of the instruments and encouraging results of the first tests, the instrument still needs improvements in terms of battery power and analytical resolution. Furthermore, the instrument is mounted on a buoy and collects only samples from the upper layer of the ocean while real underwater analysis requires the development of a pressure proof housing that separates the cytometer fluidics from the water pressure at high depth. A device with limited pressure tolerance has been deployed on the AUV Autosub [25], but the depth rating, size of the instrument, sample rate, and deployment duration currently limit more widespread acceptance.

1.4 Flow cytometric identification of phytoplankton

The main parameters detected in FCM are fluorescence and light scattering. Some instruments can be modified in order to measure other characteristics such as the time of flight (TOF) [19; 22] or signal shape [21; 23]; the following paragraphs present an overview of how these optical parameters are investigated in the analysis of phytoplankton.

1.4.1 Fluorescence

Traditionally, light induced fluorescence (LIF) in FCM is performed on cells stained with fluorescent antibodies; however, this is not generally done with phytoplanktonic organisms as they contain photosynthetic pigments (e.g. chlorophyll) and phycobiliproteins that have a characteristic autofluorescence. Furthermore, different algae contain different amounts of these pigments and sometimes the same type of phycobiliprotein within different organisms will return a different fluorescence emission spectra. It is then possible to identify different taxa (groups) of phytoplankton looking at their fluorescence emission [14; 15; 16; 18; 19; 26; 27].

Pigment	**Excitation (nm)**	**Emission (nm)**	**Fluorescence Type**
Chlorophyll – a	<540	>660	**FGR** Green-Red Fluorescence
Chlorophyll - b	630	>660	**FRR** Red-Red fluorescence
Phycoerythrin	<540	550-620	**FGO** Green-Orange Fluorescence
Phycocyanin	<540	650	**PC** Phycocyanin fluorescence

Table 1.1- Typical auto-fluorescence investigated in flow cytometry, sources [14; 15; 16; 18; 19; 26].

Table 1.1 presents a summary of the main pigments involved in algae fluorescence together with characteristic excitation and emission wavelengths. The main pigments responsible for fluorescence in phytoplankton are chlorophyll A (CHA, present in every cell), chlorophyll B (CHB), phycoerythrin (PE) and phycocyanin (PHY). Other pigments are also present in phytoplankton (e.g. carotenoids and chlorophyll *c*) but they are not fluorescent.

Since fluorescent pigments are excited by light sources in the blue green region, the main excitation wavelengths used are 488nm and 532nm. However, light sources in the violet (407nm) and red (633nm) are sometimes used.

As the intrinsic fluorescence of phytoplankton is not enough for characterisation of single taxa in complex populations, attempts have been made to label phytoplankton with fluorescent pigments. Vrieling *at al.* [28] employed immunochemical labelling techniques and were able to accurately characterise selected species using FCM. Fluorescent in situ hybridization (FISH) and immunofluorescence detection by epifluorescence, already used in phycology [29], were used together with flow cytometry in order to characterise some phytoplanktonic species [30].

1.4.2 Light scattering

Light scattering is a useful technique that enables the label-free characterisation of particles by measuring the amount of light deflected by particles. As shown in Figure 1.2, in commercial flow cytometers light scattering is usually collected at two points: one at a small angle (Forward Scattered or FSC) between 0.5° and 5° to the normal pathway; the other a large angle (Side Scatter or SSC) between 15° and 150° to the

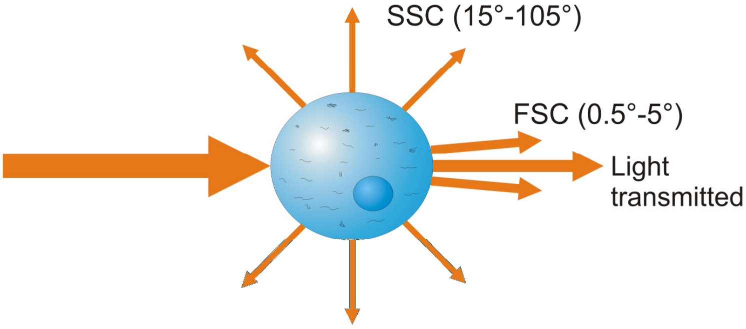

Figure 1.2 – Schematic representation light scattering events detected by conventional FCM. Copied from [27].

normal pathway.

FSC is usually considered proportional to cell size and SSC to structural characteristics of cells such as granularity and cell shape [23]. However, Shapiro [27] warns that light scattering is a complex phenomena and simplifications are not always correct, especially when correlating FSC to cell size. Furthermore, SSC can be used to obtain information about cell size when small particles (< 2μm) are analysed. In phytoplankton monitoring, several studies used scatter light in order to obtain information about cells size and shape [21; 31; 32].

1.4.3 Time of Flight

In addition to fluorescence and light scattering, time of flight (TOF) has been used in a number of works [15; 19; 22] to obtain information about cell length. As shown in Figure 1.3, TOF is the time needed for a particle to pass through a detection region (light spot). This information is very useful in phytoplankton monitoring because some species are formed by elongate cells or multi-cellular filaments and therefore give an higher TOF than unicellular organisms.

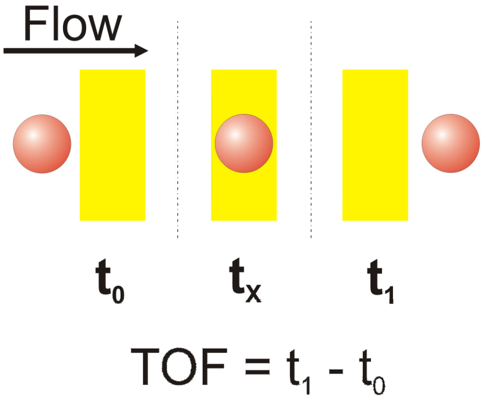

Figure 1.3 - Schematic representation of the principle of TOF. t_0 is the time immediately before the cell enters the light spot, t_x is the time during the particles pass through the light spot and t_1 is the time immediately after the cell exit the light spot. TOF is given by the difference between t_0 and t_1.

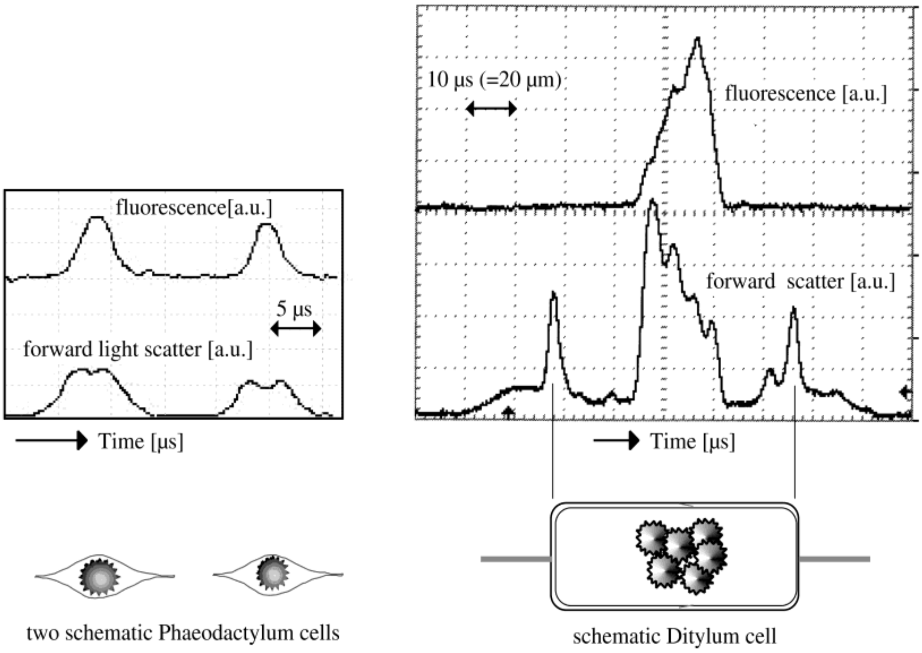

Figure 1.4 – Shape of signals generated by FSC and autofluorescence of two *Phaeodactylum* cells (left) and a *Ditylum* cell (right). Copied from [21].

1.4.4 Signal profile

The profile of a signal depends on the intensity profile of the laser beam as traversed by the particles and the shape of the particles along their long axis [23]. Since the profile of the signal is highly dependent on the particles shape (Figure 1.4), the peak height or area values of the signal were used to increase the characterisation power of flow cytometers [21; 23].

1.5 Automatic data elaboration

The use of flow cytometry allows the detection of a large number of properties simultaneously; this huge amount of data has to be processed in order to identify the different groups and get information such as size, structure, numbers and percentages of the different populations. Usually, an operator manually processes histograms and two dimensional scatter plots (Figure 1.5) but this kind of analysis can be laborious, time consuming and affected by human mistakes; that is why attempts have been made to develop automated classification techniques [18; 33], defined as *discriminant functions,* for the characterisation of marine organisms using multiple parameters obtained by flow cytometry. Discriminant functions are essentially functions of several

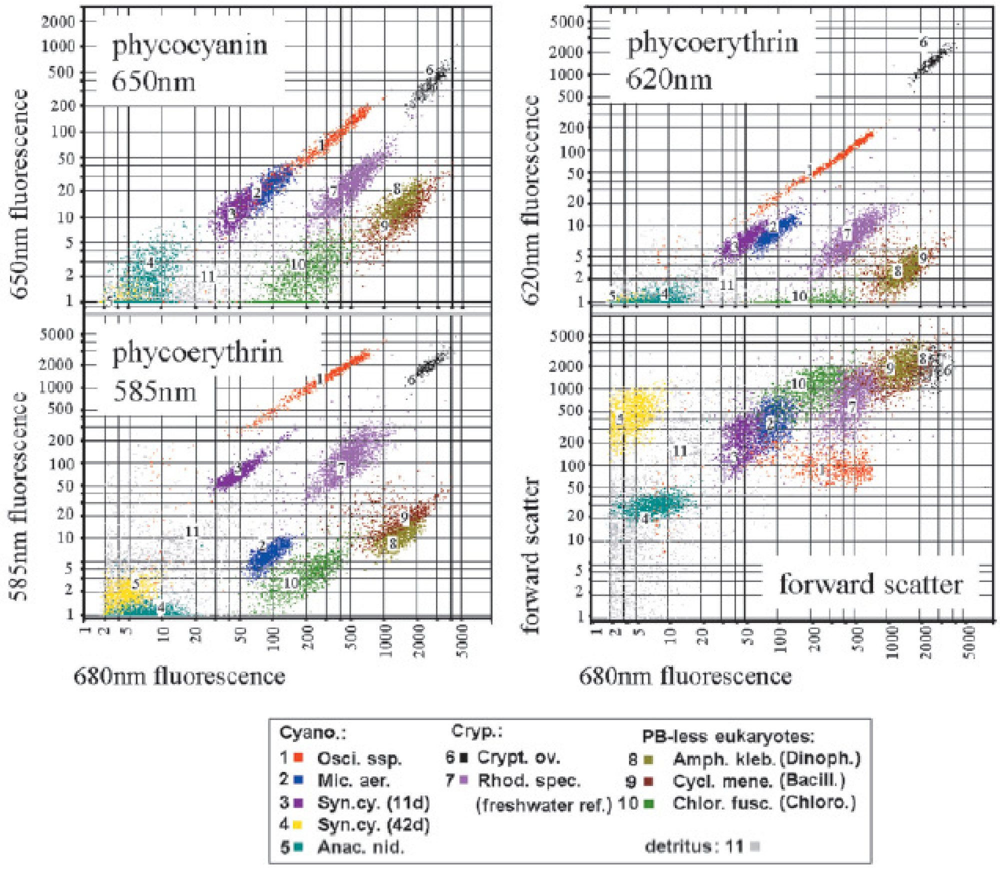

Figure 1.5 – Scatter plots obtained from flow cytometric analysis. The populations are identified according to the different intensity in light scattered and fluorescence emission at specific wavelength. Copied from [16].

parameters (e.g. FGR, FGO, SSC, etc) that for different cell types assume different ranges of values. The functions are fitted by a computer program and the value of the different parameters are initially set with data from reference cells (typically from lab cultures).

Despite the good results obtained, discriminant functions have been proven able to identify only mixture of algae grown in laboratory and using the same cultures as reference. As environmental conditions in seawater can be different from lab conditions in terms of temperature, illumination and nutrients concentration, natural samples can significantly differ from the references used. Therefore, discriminant techniques may not be able to recognise organisms grown in the natural environment.

1.6 Summary

This chapter presents a review of flow cytometry and its use in the study and monitoring of phytoplankton where it enables rapid and quantitative analysis of single cells. Since FCM was originally developed for biomedical applications, modified bespoke cytometers have been proposed and developed.

The main parameters used by flow cytometry are fluorescence and light scatter. Marine organisms already contain fluorescent pigments that make them especially suited to fluorescence analysis. However, intrinsic fluorescence and light scatter are not enough for the complete characterisation of the single taxa; to solve this problem, different techniques have been applied such as hybridisation with fluorescent antibodies, modification of commercial instruments, use of new parameters (e.g. time of flight, and signal shape) and development of automated analysis techniques.

REFERENCES

[1]L.E. Graham, and L.W. Wilcox, Algae, Prentice-Hall, Upper Saddle River, NJ 07458, 2000.

[2]S. Nehring, Establishment of thermophilic phytoplankton species in the North Sea: biological indicators of climatic changes? Ices Journal of Marine Science 55 (1998) 818-823.

[3]J.L. Sarmiento, and C. LeQuere, Oceanic carbon dioxide uptake in a model of century-scale global warming. Science 274 (1996) 1346-1350.

[4]L. Legendre, C. Courties, and M. Troussellier, Flow cytometry in oceanography 1989-1999: Environmental challenges and research trends. Cytometry 44 (2001) 164-172.

[5]K.R. Arrigo, D.H. Robinson, D.L. Worthen, R.B. Dunbar, G.R. DiTullio, M. VanWoert, and M.P. Lizotte, Phytoplankton community structure and the drawdown of nutrients and CO2 in the Southern Ocean. Science 283 (1999) 365-367.

[6]G. Malin, S.M. Turner, P.S. Liss, and Aiken, Sulfur - the Plankton Climate Connection. Journal of Phycology 28 (1992) 590-597.

[7]C.M. Yentsch, P.K. Horan, K. Muirhead, Q. Dortch, E. Haugen, L. Legendre, L.S. Murphy, M.J. Perry, D.A. Phinney, S.A. Pomponi, R.W. Spinrad, M. Wood, C.S. Yentsch, and B.J. Zahuranec, Flow-Cytometry and Cell Sorting - a Technique for Analysis and Sorting of Aquatic Particles. Limnology and Oceanography 28 (1983) 1275-1280.

[8]G. Gregori, A. Colosimo, and M. Denis, Phytoplankton group dynamics in the Bay of Marseilles during a 2-year survey based on analytical flow cytometry. Cytometry 44 (2001) 247-256.

[9]W.K.W. Li, Annual average abundance of heterotrophic bacteria and Synechococcus in surface ocean waters. Limnology and Oceanography 43 (1998) 1746-1753.

[10]L.A. Pan, J. Zhang, Q. Chen, and B. Deng, Picoplankton community structure at a coastal front region in the northern part of the South China Sea. Journal of Plankton Research 28 (2006) 337-343.

[11]L. Campbell, H.A. Nolla, and D. Vaulot, The Importance of Prochlorococcus to Community Structure in the Central North Pacific-Ocean. Limnology and Oceanography 39 (1994) 954-961.

[12]C. Courties, A. Vaquer, M. Troussellier, J. Lautier, M.J. Chretiennotdinet, J. Neveux, C. Machado, and H. Claustre, Smallest Eukaryotic Organism. Nature 370 (1994) 255-255.

[13]S.W. Chisholm, R.J. Olson, E.R. Zettler, R. Goericke, J.B. Waterbury, and N.A. Welschmeyer, A Novel Free-Living Prochlorophyte Abundant in the Oceanic Euphotic Zone. Nature 334 (1988) 340-343.

[14]J.W. Hofstraat, W.J.M. Vanzeijl, M.E.J. Devreeze, J.C.H. Peeters, L. Peperzak, F. Colijn, and T.W.M. Rademaker, Phytoplankton Monitoring by Flow-Cytometry. Journal of Plankton Research 16 (1994) 1197-1224.

[15]T.P.A. Rutten, B. Sandee, and A.R.T. Hofman, Phytoplankton monitoring by high performance flow cytometry: A successful approach? Cytometry Part A 64A (2005) 16-26.

[16]A. Becker, A. Meister, and C. Wilhelm, Flow cytometric discrimination of various phycobilin-containing phytoplankton groups in a hypertrophic reservoir. Cytometry 48 (2002) 45-57.

[17]M. Thyssen, D. Mathieu, N. Garcia, and M. Denis, Short-term variation of phytoplankton assemblages in Mediterranean coastal waters recorded with an automated submerged flow cytometer. Journal of Plankton Research 30 (2008) 1027-1040.

[18]M.R. Carr, G.A. Tarran, and P.H. Burkill, Discrimination of marine phytoplankton species through the statistical analysis of their flow cytometric signatures. Journal of Plankton Research 18 (1996) 1225-1238.

[19]H.W. Balfoort, T. Berman, S.Y. Maestrini, A. Wenzel, and T. Zohary, Flow-Cytometry - Instrumentation and Application in Phytoplankton Research. Hydrobiologia 238 (1992) 89-97.

[20]K.K. Cavender-Bares, S.L. Frankel, and S.W. Chisholm, A dual sheath flow cytometer for shipboard analyses of phytoplankton communities from the oligotrophic oceans. Limnology and Oceanography 43 (1998) 1383-1388.

[21]G.B.J. Dubelaar, P.L. Gerritzen, A.E.R. Beeker, R.R. Jonker, and K. Tangen, Design and first results of CytoBuoy: A wireless flow cytometer for in situ analysis of marine and fresh waters. Cytometry 37 (1999) 247-254.

[22]G.B.J. Dubelaar, A.C. Groenewegen, W. Stokdijk, G.J. Vandenengh, and J.W.M. Visser, Optical Plankton Analyzer - a Flow Cytometer for Plankton Analysis .2. Specifications. Cytometry 10 (1989) 529-539.

[23]G.B.J. Dubelaar, and P.L. Gerritzen, CytoBuoy: a step forward towards using flow cytometry in operational oceanography. Scientia Marina 64 (2000) 255-265.

[24]http://www.cytobuoy.com/.

[25]A. Cunningham, D. McKee, S. Craig, G. Tarran, and C. Widdicombe, Fine-scale variability in phytoplankton community structure and inherent optical properties measured from an autonomous underwater vehicle. Journal of Marine Systems 43 (2003) 51-59.

[26]R.J. Olson, E.R. Zettler, and O.K. Anderson, Discrimination of Eukaryotic Phytoplankton Cell-Types from Light Scatter and Autofluorescence Properties Measured by Flow-Cytometry. Cytometry 10 (1989) 636-643.

[27]M.S. Howard, (Ed.), Practical Flow Cytometry, John Wiley & Sons, 2003.

[28]E.G. Vrieling, A. Draaijer, W.J.M. Vanzeijl, L. Peperzak, W.W.C. Gieskes, and M. Veenhuis, The Effect of Labeling Intensity, Estimated by Real-Time Confocal Laser Scanning Microscopy, on Flow Cytometric Appearance and Identification of Immunochemically Labeled Marine Dinoflagellates. Journal of Phycology 29 (1993) 180-188.

[29]A.S. Paau, J.R. Cowles, J. Oro, A. Bartel, and E. Hungerford, Separation of Algal Mixtures and Bacterial Mixtures with Flow-Microfluorometer Using Chlorophyll and Ethidium-Bromide Fluorescence. Archives of Microbiology 120 (1979) 271-273.

[30]N. Simon, R.G. Barlow, D. Marie, F. Partensky, and D. Vaulot, Characterization of Oceanic Photosynthetic Picoeukaryotes by Flow-Cytometry. Journal of Phycology 30 (1994) 922-935.

[31]A. Cunningham, and G.A. Buonnacorsi, Narrow-Angle Forward Light-Scattering from Individual Algal Cells - Implications for Size and Shape-Discrimination in Flow-Cytometry. Journal of Plankton Research 14 (1992) 223-234.

[32]M. Kerker, Elastic and Inelastic Light-Scattering in Flow-Cytometry. Cytometry 4 (1983) 1-10.

[33]H.W. Balfoort, J. Snoek, J.R.M. Smits, L.W. Breedveld, J.W. Hofstraat, and J. Ringelberg, Automatic Identification of Algae - Neural Network Analysis of Flow Cytometric Data. Journal of Plankton Research 14 (1992) 575-589.

Chapter 2

Micro-Total Analytical Systems (µTAS) for single cells analysis

2.1 Introduction

As explained in the previous section, flow cytometry is a very useful technique for the analysis and monitoring of microscopic algae [1; 2]. However, the widespread use of flow cytometry for the study of phytoplankton is limited by the high cost of the instrumentation and the inability to provide detailed information on species composition, making it very difficult and sometimes impossible to characterise the different populations. Furthermore, the high cost of flow cytometers inhibits their widespread use for monitoring phytoplankton, slowing down the process of improvement of the various flow cytometry techniques that would allow characterisation of algae with flow cytometry alone.

One solution to the high cost of flow cytometer instruments is the development of a lab-on-a-chip (LOC) micro-fabricated fluidic device, which is a miniaturised biochemical analysis system based on micro-electromechanical systems (MEMS) technology. The motivation behind creating such miniaturized devices is to perform analyses with small, inexpensive tools rather than the bulky and expensive instruments typically used, such as a FACS machine, Flow-Injection Analysis systems (FIA), High Performance Liquid Chromatography (HPLC), etc. Furthermore, the use of LOC enables the possibility to work with much smaller volumes of samples (nanolitres) than conventional techniques. The reduced size allows diminution in reagents and the development of highly sensitive devices, capable of isolating and analysing minute quantities of samples.

As the development of micro-electronics enabled a revolution in computing, moving it from slow, expensive and bulky calculators to inexpensive (any family can afford one), fast and small personal computers, in the same way the development of a microfabricated device will lead to a reduction of size (hence, of volume of sample required), weight and power requirements, allowing the creation of cheaper and smaller instruments. Furthermore, the size and the cost of the devices offer the possibility of performing all the chemical steps (from the starting sample to the final analysis) in the same instrument, allowing unskilled personnel to perform complex analysis.

It is therefore possible that the development of LOC devices could improve the process of phytoplankton monitoring using flow cytometry by reducing the cost of instrumentation and allowing widespread use of the technique. A small microfluidic system could be used to perform *in-situ* flow cytometric analysis of algae. This kind of analysis is very important because once removed from its environment, the internal characteristics of the algae may change (e.g. pH, temperature). The analytical system could be deployed using a remote-controlled submarine, perform *in-situ* analysis at various depths and position in the sea.

2.2 Micro-TAS: History and Development

The first attempts to build a miniaturised device were at the beginning of 1980s [3] but a serious study of microfabricated analysis systems started only in the late 1980s, driven by the need to build sensors with better selectivity and lifetime than the ones available at that time. As the study of microfabricated devices increased, a new idea was introduced: integrate all the necessary chemical processing steps to perform chemical or bio-chemical analysis in the same device. Microfabricated systems able to perform this kind of work were defined “Micro Total Analytical Systems” (µTAS), or “Lab-on-a-Chip devices” (LOC). The first work at this level was presented by Manz *et al.* in 1990 [4] with a silicon chip analyzer that incorporated sample pre-treatment, separation and detection.

Since this early work [4], several basic fluidic components have been developed for sample preparation, detection and treatment (dispose, sort or recoup) using micropumps [5; 6], interconnections and flow control systems [7; 8; 9], separation systems [10; 11], mixers [12; 13], reactors [14; 15], detectors [16; 17; 18] and other types of components [14; 19]; meanwhile devices able to perform single cell analysis [18; 20; 21; 22; 23] or chemical and bio-chemical analysis [24; 25; 26] were fabricated and successfully tested.

2.3 Microfabrication

Initially, existing techniques developed for micro-electronics fabrication (e.g. photolithography) were used to manufacture devices. Now, polymeric materials and new fabrication techniques have solved some of the problems associated with classical photolithography.

A detailed description of the basic techniques used for fabricating microfluidic devices is beyond the objective of this thesis. However, comprehensive information on this topic can be found in a number of reviews and books [27; 28; 29; 30]. In this section, a brief description of the most widely used techniques (photolithography, polymer photolithography and soft lithography) is reported.

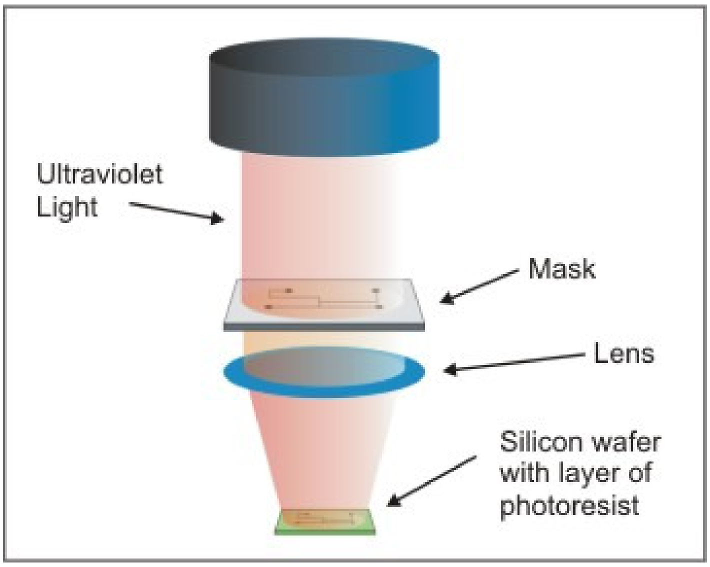

Figure 2.1 – Schematic representation of a typical photolithographic fabrication process: The image of the mask is projected and reduced at the same time onto a thin film of photoresist (previously spin-coated on a wafer) through a high numerical aperture lens system. Wet etching is then be used to define the structure on the substrate (not shown).

2.3.1 Photolithography

Photolithography is a technique that uses a mask or a master which is a negative of the final structure. The image of the mask is projected and reduced at the same time onto a thin film of photoresist (previously spin-coated on a wafer) through a high numerical aperture lens system (Figure 2.1). Fabrication of the mask can be very expensive and complicated, depending on the precision required, but it can be used several times. Wet etching is then used to define the structure on the substrate; this process is able to remove material in the non-protected area and form microchannels on a planar substrate.

Materials used as substrate are usually silicon, glass and quartz, but these materials have many drawbacks: e.g. multiple steps to fabricate the chip; the use of harmful wet chemistry (e.g., HF) which increases the cost of the reagents needed for the fabrication; limitations in geometrical design (the process allows only shallow, semicircular cross section channels); interaction between the silicon surfaces and biomulecules (e.g. oligonucleotides, DNA, proteins) that tend to create a bond to silicon surface groups.

2.3.2 Polymers for microfabrication

The use of polymers for microfabrication has grown rapidly due to their low cost and a wide range of materials with various characteristics to chose from (mechanical, optical, temperature stability, resistance against chemicals such as acids, alkaline or organic solutions). Furthermore, polymers are applicable to a large range of fabrication methods that are more suitable for mass production and academic applications compared to traditional photolithographic techniques on silicon or glass [28; 29]. However, in comparison with glass, polymers have less resistance to chemicals, time (aging) and UV stability; they also have different mechanical behaviour and higher fluorescence at shorter wavelengths.

Polymers that can be used in microfluidic fabrication are divided in two main categories: general polymers and photoresist. In *general polymers*, since the mass of the molecules is not fixed, there is a temperature interval in which the viscosity changes strongly and the material turns into a highly viscous mass (*Glass Transition Temperature,* T_g): below this temperature the polymer is hard and brittle (glassy), above this temperature the polymer is viscous and can be moulded.

A further classification within general polymers can be made according to the moulding behaviour, due to the strength of the cross-linking forces within the molecules:

- *Thermoplastic polymers:* when heated above T_g they become plastic and can be moulded into specific shapes. They retain the shape after cooling below T_g.
- *Elastomeric polymers:* if a force is applied, the molecular chains can be stretched but they return to their original state once the force is removed.
- *Duroplastic polymers:* harder and more brittle, a change in shape is not possible because of their strong molecular cross-linking.

In photoresist polymers, the chemical properties of the material change if it is irradiated with electromagnetic rays (X-rays, UV or visible light). Two categories of photoresist can be distinguished according to the photochemical reaction produced (Figure 2.2):

- *negative tone resists*: the solubility of the irradiated area decreases.
- *positive tone resists*: the solubility of the irradiated area increases.

2.3.3 Polymer photolithography

A schematic diagram of polymer phtolithography is showed in Figure 2.2: first, a layer of photoactive polymers is patterned on a solid substrate (usually glass or polymer) and selected regions are irradiated. The polymer is then developed using solvents in order to remove the regions that are not cross-linked, revealing the microfluidic structures. In addition to simple two-dimensional structure, this technique can be also used for the fabrication of complex three dimensional channel geometries [31; 32].

Polymer photolithography uses many technologies and clean room facilities (e.g. resist spinners, mask aligners and solvent development tanks) used for silicon based fabrication. The most commonly used materials are epoxy based polymers such as polyimides [33] and SU-8 [18; 34]. Various fabrication techniques based on polymer photolithography appeared on the literature and have been comprehensively described in a number of reviews and books [27; 28; 29].

Figure 2.2 – Schematic representation of polymer photolithography with positive and negative resist. In negative resist, the solubility of irradiated area decrease and only the non irradiated part is removed during the development process. In positive resist the solubility of irradiated area increases and is removed during the development process.

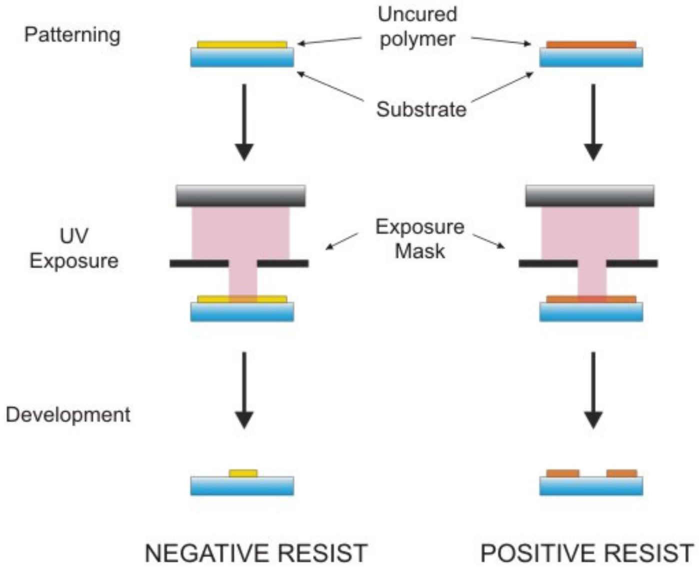

2.3.4 *Soft lithography*

The term *soft lithography* defines a set of polymer fabrication techniques that uses soft material (elastomeric polymers and gels) for the fabrication of structures. Soft lithography is based on two main techniques: moulding and embossing.

2.3.4.1 *Moulding*

A general moulding process in showed in Figure 2.3. Typically, a mould (master tool) is fabricated by using hard micromachining (e.g. sawing, cutting or milling), photolithography or etching (wet or dry). Uncured polymer is then poured (casted) on top of the master tool and cured. As silicon-base elastomeric polymers are used, the chip can simply be peeled off the mould at the end of the process. The channel obtained can then be sealed with a substrate such as a glass slide.

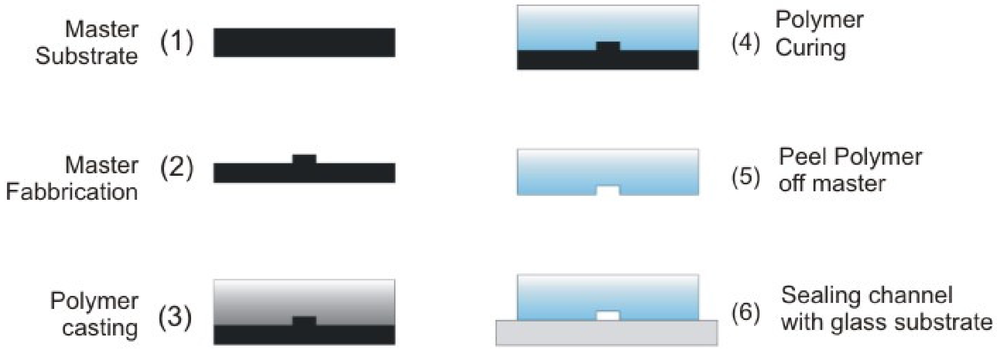

Figure 2.3 – Schematic representation of a general moulding process. Hard micromachining is used to fabricate a master tool (1, 2). Uncured polymer is then poured on top of the master tool and cured (3, 4). The cured polymer can then be peeled off the master (5) and sealed with glass (6).

Figure 2.4 – Schematic representation of a general hot embossing process. Polymer and master tool are heated just above the glass transition temperature (1) and put in contact (2). After cooling the master tool is removed from the Polymer.

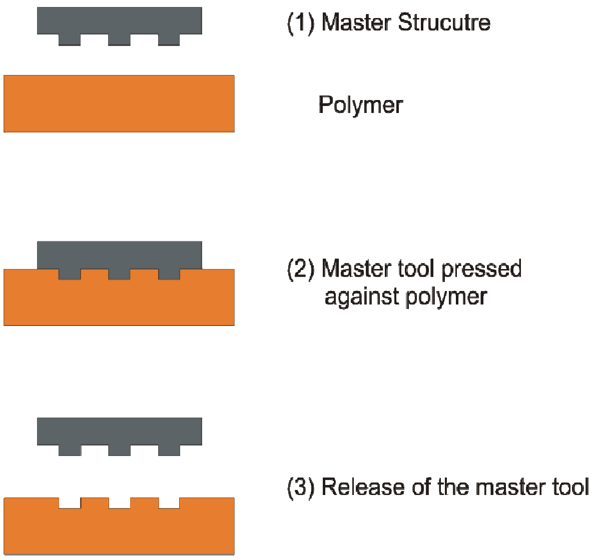

The most widely used polymer for this application is poly(dimethylsiloxane), or PDMS, an elastomeric polymer that has a number of advantages such as good transparency, biocompatibility and little autofluorescence above 230 nm [28; 30; 35; 36]. Furthermore, PDMS has excellent sealing properties both to glass and itself, allowing the creation of complex 3D structures [35; 36]. The use of PDMS revolutionised the field of microfluidics, allowing the creation of devices with a limited budget and without the need of complex machinery (clean room facilities).

2.3.4.2 Hot embossing

A schematic representation of a general embossing process is presented in Figure 2.4; the polymer and the master tool (created as described in section 2.3.4.1) are heated just above the glass transition temperature and put into contact. When the shape of the mould has been embossed in the polymer, the substrate is cooled and removed from the mould. The heating and the embossing processes are performed in a vacuum chamber to avoid the formation of air bubbles due to trapping of air in small cavities. The level of accuracy that can be obtained is such that the technique has also been used to fabricate optical components such as micro lenses and waveguides [37]. Polycarbonate and PMMA are the most widely used polymers for embossing [27; 38; 39].

2.3.5 Fabrication considerations

Overall, fabrication methods based on polymers allow cheaper and easier fabrication of microfluidic structures than glass-based methods. Furthermore, the use of polymers allows the fabrication of complex constructions such as 3D structures [28] or glass/polymer structures that benefit from the different properties of the two materials. Glass, for example, can be used for electrodes patterning while polymers allow easier fabrication of microfluidic structures [40].

Polymers in general and PDMS and SU-8 in particular are the preferred choice for the integration of optical structures within the new microfluidic devices presented in this thesis (see section 2.4.4). PDMS and SU-8 are usually chosen because of their optical transparency and ease of fabrication. SU-8 can be used directly for fabrication of microfluidic structures or as a mould for PDMS. The latest solution is often adopted for three reasons; because the SU-8 mould can be used for several devices, because PDMS feature an easier and cheaper fabrication (see section 2.3.4.1) and because channels made in SU-8 are difficult to seal [34]. However, structures made in SU-8 are usually chosen for structures that are difficult to obtain with PDMS (e.g. planar waveguides).

2.4 Flow cytometry on chip

There is a growing interest in developing microfluidic devices for flow cytometry (microfabricated cytometers) [41; 42]. In particular, there is high interest in creating a more compact, robust and less expensive system when compared to conventional flow cytometers. Furthermore the design flexibility offered by microfabrication techniques allows the insertion of additional functionalities within a single cytometer (e.g. sample preparation, culturing of selected cells and multiple detection system [43; 44]).

Over the last ten years, a number of flow cytometric devices featuring different flow generation, focussing and detection systems have been presented. The first devices consisted of microfluidic channels coupled with simple particles focusing systems, conventional optics for the detection of fluorescence and side scatter light [45; 46; 47; 48]; occasionally microfluidic cytometers where coupled with additional functionalities such as sample purification and sorting [21; 23], Wolff *et al.* also presented a device with on-chip cell culture capabilities [43]. These devices demonstrated the feasibility and design flexibility of microfluidic-cytometry. However, the use of conventional optics hindered the development of low-cost, portable devices. Therefore a number of devices were published afterwards that implemented micron-sized optical elements or electrodes directly integrated in the microfluidic chip [18; 21; 33; 40; 43; 44; 49; 50; 51]. In particular, the first example in which integrated optics were used for particle detection was presented by Cui *et al.* [51] but this device was limited by the absence of a focusing system that limited the precision of the system. A solution where a micron-sized avalange photodiode (μAPD) was directly integrated into the chip was presented by Kruger *et al.* [21] but only limited experimental data was reported for this device. The solutions proposed by Wang *et al.* [18] and Tung *et al.* [52], are instead more interesting: the first presented devices with integrated optical fibres, planar waveguides and microlenses for the detection of scatter light, while the second presented a chip with integrated fibres for the detection of multiple colour fluorescence. At the present stage, a number of devices that integrate optics able of fluorescence, scatter light or impedance detection have been presented. However, microfabricated cytometers are still in a development stage as fully integrated systems have not been presented: most of the devices that were capable of multi parameters detection used conventional optics [45; 46; 47; 48]; devices that used integrated optics or electrodes could detect only a limited number of parameters [18; 21; 33; 40; 43; 49; 50; 51; 53], or the integrated detection system was coupled with conventional optics to increase the characterisation power [18; 54].

In addition to the integrated detection systems, another critical component in the development of microfabricated cytometers is a focussing system able to make particles flow exactly in the middle of the detection region. The first microfluidic cytometers used only mono-dimensional hydrodynamic focussing (i.e. able to position particles only along the width of the channel); these systems were implemented because of their easy fabrication and operation and gave flow cytometric results with CVs between 15 and 35% at particles flow speed between 0.1 and 20 mm sec^{-1} [17; 18; 45; 46; 48]. In contrast, the latest development feature devices able to focus particles along width and height of the channel (bi-dimensional or 2D focussing) [32; 43; 53; 54; 55]; these devices were able to obtain results with CV ranging from 2.5% to 15% at particles flow speeds up to 3 m sec^{-1}, demonstrating that the implementation of a 2D focussing system can drastically improve the performance of a microfabricated cytometer. Devices not implementing a focussing system but with channel size similar to the sample were also presented [56; 57; 58]; these devices demonstrated a precision comparable to commercial instruments and throughputs one order of magnitude lower than the commercial instruments (no CVs were reported for these devices). However devices not implementing a focussing system are suitable only for specific application where the size of the sample is known and relatively constant because samples with high size variability increase the risk of channel clogging and reduce the precision of the results.

To sum up, a number of microfabricated cytometers have been presented in the literature and the latest development in particle focussing allowed the obtainment of precise results, comparable to commercial instruments. A lot of work was also done on the integration of the detection system into a microfluidic device but a powerful fully integrated device has not been developed yet. Therefore, the state of the art devices indicate that the main challenges in the development of powerful and efficient microfabricated cytometers is the implementation of integrated detection and focussing system that are easy to fabricate and control. In the following paragraphs the basics principles of these components are presented together with their development and latest advances.

2.4.1 Flow in a microfluidic channel

The most common way to generate a flow into a microfluidic channel is called volumetric displacement and is obtained by placing the sample or buffer into a syringe and compressing it with a syringe pump (Figure 2.5(a)) [59]. This method is widely applied because it is easy to implement and allows a direct setting of the flow rate. The flow throughput obtainable depends also from the size of the channel, however flow speed of about 10 m sec^{-1} can be easily obtained for channel cross-section of about 10^3 μm^2 [52].

If high precision and fast modulation of the fluid flow is required, differential pressure is preferred to volumetric displacement [60]. In differential pressure, fluid flow is obtained by applying a constant pressure in the reservoir containing the sample

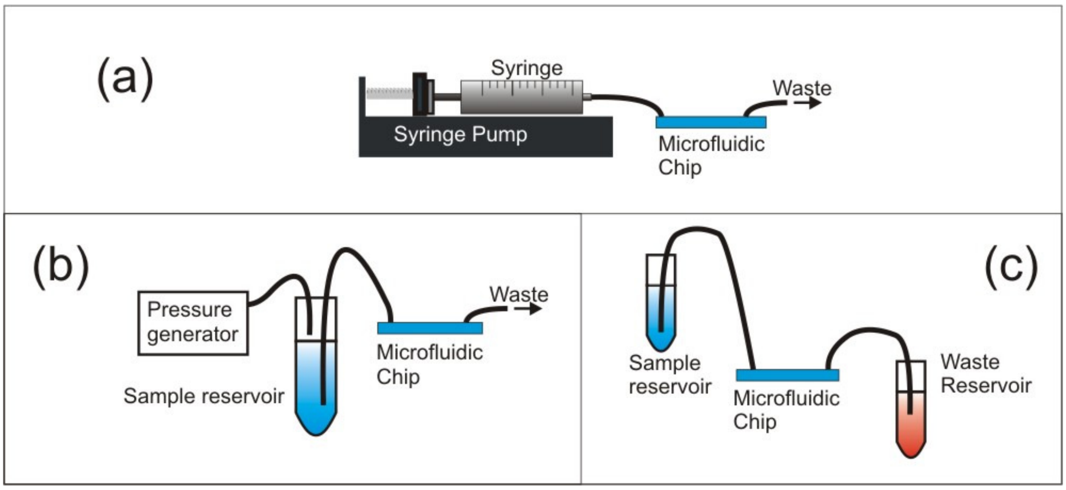

Figure 2.5 – Mechanical flow generator systems: (a) volumetric displacement; (b) differential pressure using a pump or a gas cylinder; (c) differential pressure using gravity.

or a buffer solution; the sample is then pushed into a pipe immersed in the medium and connected to the microfluidic channel. The pressure is usually applied by a pneumatic set up (conventional pump or gas cylinder filled with nitrogen), as shown in Figure 2.5(b), or by gravity; in the latter, the pressure is obtained placing the inlet and outlet reservoir at different heights, as shown in Figure 2.5(c). Flow velocities in the order of 10^{-2} m sec^{-1} can be easily obtained using this method.

Since the stability of the flow generated by volumetric displacement and differential pressure is affected by vibrations of the pipes that connect the reservoir to the chip, Braschler *et al.* [61] proposed a holder with integrated reservoirs connected to a pneumatic set up Figure 2.6. The solution is interesting because in addition to reduce irregularity in the flow due to environmental conditions, it simplifies the overall set up; however, the system appears applicable only where small amounts of sample are required.

In alternative to pressure driven, flow in a microfluidic channel can be generated by electroosmotic pumping. The principle of the technique is based on the building up of charges at the interface between channel wall and suspending medium. If an electric potential is applied across the length of the channel, the charges at the interface move, dragging the fluid. Electroosmotic pumping has been extensively applied because of its easy implementation, requiring only the dipping of electrodes into reservoirs at the ends of the micro-channel. However, the technique suffers a series of drawbacks such as slow throughput (e.g. 10^{-3} mm sec^{-1} with 10^{4} V m^{-1} [20]), evaporation, buffer incompatibilities, cell viability, requirement of frequent voltage adjustment due to ion

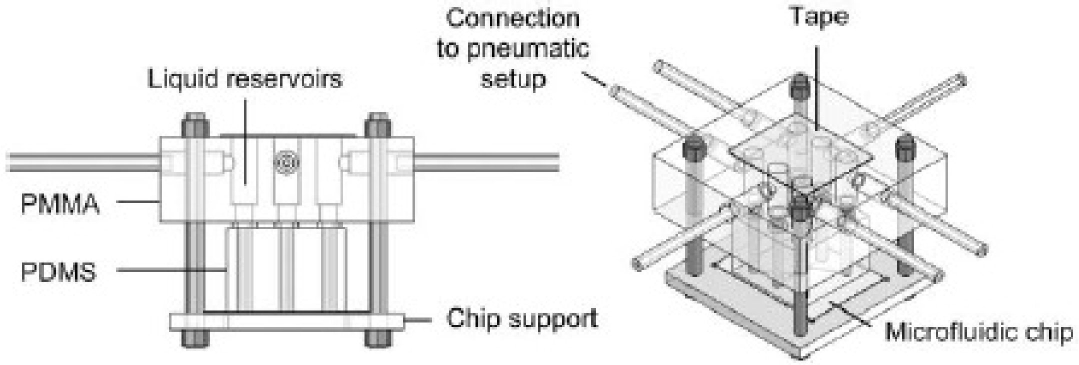

Figure 2.6 - Layout of the chip holder proposed by Braschler *et al.* [61]. The microfluidic chip is placed on top of a plastic support and blocked by fluidic interface (chip holder). A PDMS layer is used as gasket between the microfluidic chip and the chip holder. The latter contains reservoirs for the various medium and is connected to a pneumatic set up. The different fluids are pipetted into the reservoirs and sealed with tape in order to enable pressure build up. Copied from [61].

depletions, flow speed and direction highly dependent on the surface properties of the channel and the sample composition. Because of these drawbacks, volumetric displacement is preferred for microfluidic applications.

Fluid motion in micron-sized channels is usually analysed with Newtonian mechanics [62]. In Newtonian fluids the velocity profile of the fluid inside the channel is given by a factor called *Reynold's number* (Re) [63]:

$$\mathrm{Re} = \frac{\rho v r}{\eta} \qquad \text{2-1}$$

where v is the velocity, ρ is the fluid density, η is the viscosity of the fluid and r is the characteristic size of the channel in which the fluid is flowing.

Low values of Reynold's number (Re<<1) indicate that the flow is dominated by the viscous term, while high values (Re>>1) indicate that the inertia term dominates. Since most of the microfabricated flow channels (included the ones used in this work) has at least one characteristic dimension in the micrometer range with low fluid velocity, the fluid flow is in the low Reynold's number regime and the viscous effects dominate. This type of flow is termed laminar, meaning that it flows following streamlines and is free of turbulence.

When the flow in a microchannel is generated by applying a hydrostatic pressure the effect obtained is a particular type of laminar flow called Pouiselle type flow. This is characterised by a parabolic flow profile of velocities across the channel, with the maximum flow velocity at the channel centre and zero flow velocity at the channel walls (Figure 2.7(a)) [64]. On the other side, electroosmotic pumping generates a flat profile of velocities (plug-like, Figure 2.7(b)) [63]. The plug-like flow profile is preferable for flow cytometry measurements because particles are all dragged at the same speed, ultimately reducing the variation of the signals intensities obtained by the instruments.

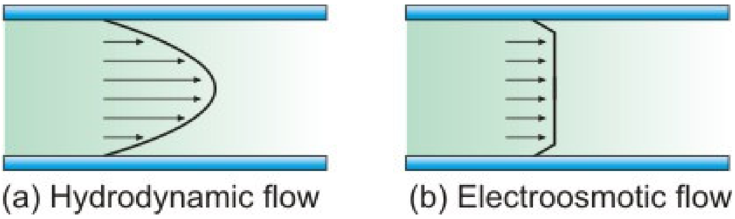

Figure 2.7 – Fluid velocity profiles resulting from different flow generation systems (a) Velocity profile for a Pouiselle type flow generated by hydrostatic pressure. (b) plug-like profile from electroosmotic driven fluid flow.

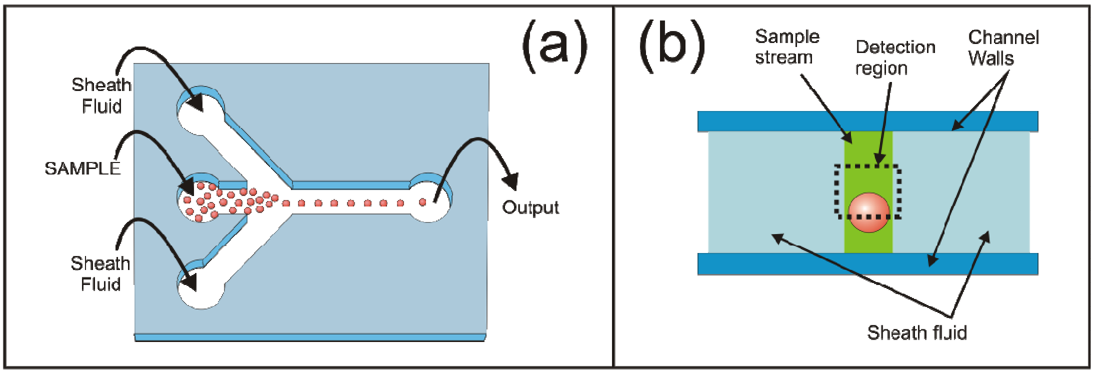

Figure 2.8 – Schematic diagram showing the principle of mono-dimensional Hydrodynamic Focussing. (a) Top view; (b) cross section.

2.4.2 Sample focussing

The reliability and reproducibility of flow cytometric analysis strongly depends on the confinement of a sample stream into an accurately controlled detection/measurement region because of the high dependence of the signal to the position of the particle in respect to the excitation source [65]. For this reason, different focusing systems have been proposed in the literature.

The most widely used confinement technique is mono-dimensional (1D) hydrodynamic focusing whose popularity is due to its simple implementation. In 1D hydrodynamic focusing two side streams confine the sample stream (containing the particles) in one dimension (Figure 2.8(a)). Despite its simplicity, mono-dimensional confinement can lead to great variation in the signal detected because the particles are not confined in the vertical direction and can still flow far from the detection region (Figure 2.8(b)). The limited performance of 1D focussing systems is demonstrated by lower coefficients of variations (CV) obtained from instruments implementing bi-dimensional (2D) focussing systems [32; 43; 53; 54; 55] compared to CV obtained from systems implementing mono-dimensional focussing systems [17; 18; 45; 46; 48; 66].

Due to the limited performances of 1D focussing, many attempts have been made to implement 2D hydrodynamic focussing in microfluidic devices. In the early attempts, complex structures obtainable only with complicate fabrication procedures were proposed. For example, Yang *et al.* [31] presented a device with slope surfaces that required high precision, a non-conventional lithography method and the modification of the machinery. Solutions have been proposed that progressively reduced the complexity of the fabrication system: Wolf *et al.* [43] proposed a chimney-like structure positioned in the middle of the sheath fluid channel (see Figure 2.9(a)). Once the flow was activated, the sheath fluid surrounded the sample, carrying it downstream from the inlet. Simonnet and Groisman [32] presented a device featuring an array of input channels. The sample was inserted from the middle channel, surrounded by the streams arising from the other channels and focussed in the middle of the analysis channel (see Figure 2.9(b)). In terms of fabrication the device in [32] was interesting because, despite the master tool required a multistep photolithographic process, it could be used several times and the final device could be easily made of a single cast of PDMS. However, the high number of channels in [32] increases the complexity and sensitivity to shocks of the device. Interesting is also the work by Golden *et al.* [67] that illustrated an hydrodynamic effect based on chevron-like grooves rising from top and bottom of the microfluidic channel. The authors claim that, when combined with classical 1D hydrodynamic focussing, the grooves are able to confine the sample stream in the middle of the channel (see Figure 2.9(b)). However, the authors report simulations but no experimental data to prove the vertical displacement of the sample stream.

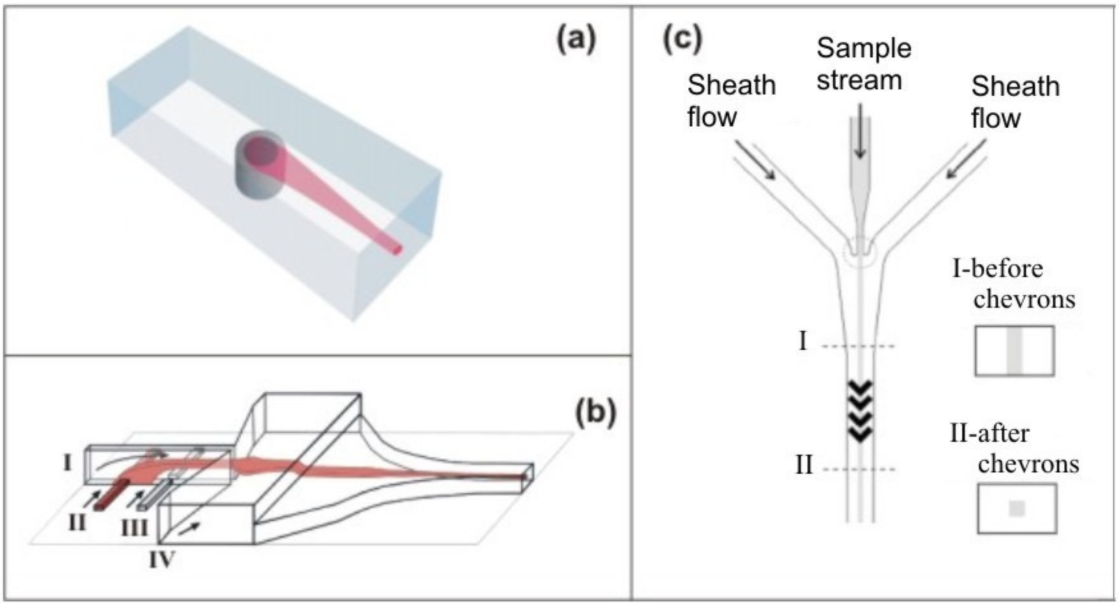

Figure 2.9 – Schematics representing various structures for bi-dimensional hydrodynamic focussing. (a) Chimney-like structure positioned in the middle of the sheath fluid channel and used for sample stream injection. Picture copied from [43]. (b) Multiple channels device where sample streams are inserted from II and the sheath fluid are inserted from I, III and IV. Picture copied from [32]. (c) Conventional 1D hydrodynamic focussing coupled with chevron-shaped grooves. I and II are cross section of the channel and show the expected focussing of the central stream before and after the chevrons. Picture copied from [67].

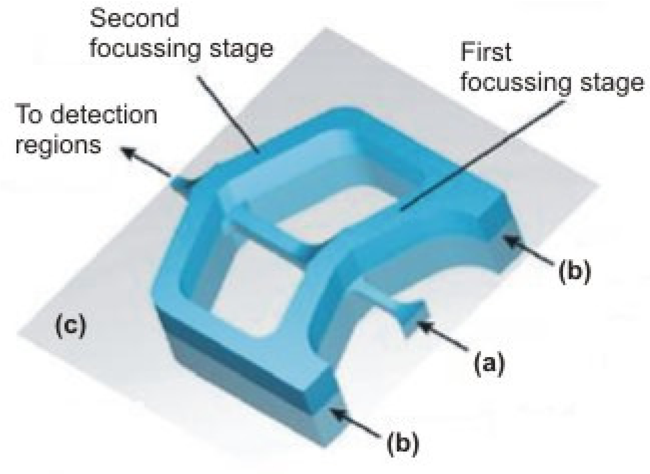

Figure 2.10 – Schematic representation of the layout used for 2D hydrodynamic focusing in Kummrow *et al.* [54]. (a) and (b) represents the sample and sheath flow channel respectively. The grey plane (c) indicate the junction plane between two different structures bonded together. Copied from [54].

One of the most interesting structures for 2D hydrodynamic focusing was proposed by Kummrow *et al.* [54] that used micromachining techniques to easily fabricate 3D master structures for hot embossing. The layout of the final focussing system is presented in Figure 2.10 and is composed of one inlet (a) for the sample stream and two inlets (b) for the sheath flow. As in 1D focussing, the sample is inserted in the sample channel in the middle and is focussed by the sheath channels on the side. Sheath channels are deeper than the sample channel so that 2D hydrodynamic focussing can be generated. Note that the structure proposed by Kummrow *et al.* [54] implements 2 stages of focussing, the first step reduce the size of the central stream from a 125x125 μm cross-section to a 30 μm diameter while the second step reduces the diameter of the central stream to 5 μm.

Recent works also showed the possibility to obtain two-dimensional focusing by accurate study of flow dynamics and channels geometry. Di Carlo *et al.* [68] obtained 2D focussing of particles with different densities, sizes and shapes using a curving channel at medium Reynold's number regimes ($1<Re<100$) as shown in Figure 2.11. A more complicated design was presented by Mao *et al.* [55] that produced two-dimensional focusing with an array of curved channel and hydrodynamic focusing (Figure 2.12). Di Carlo and Mao's works are very interesting because of their simple to fabricate structures, in fact both devices require only a single soft lithographic step as no three dimensional structures are involved. Furthermore, the device presented by Di Carlo *et al.* features a single inlet, reducing the complexity of flow control.

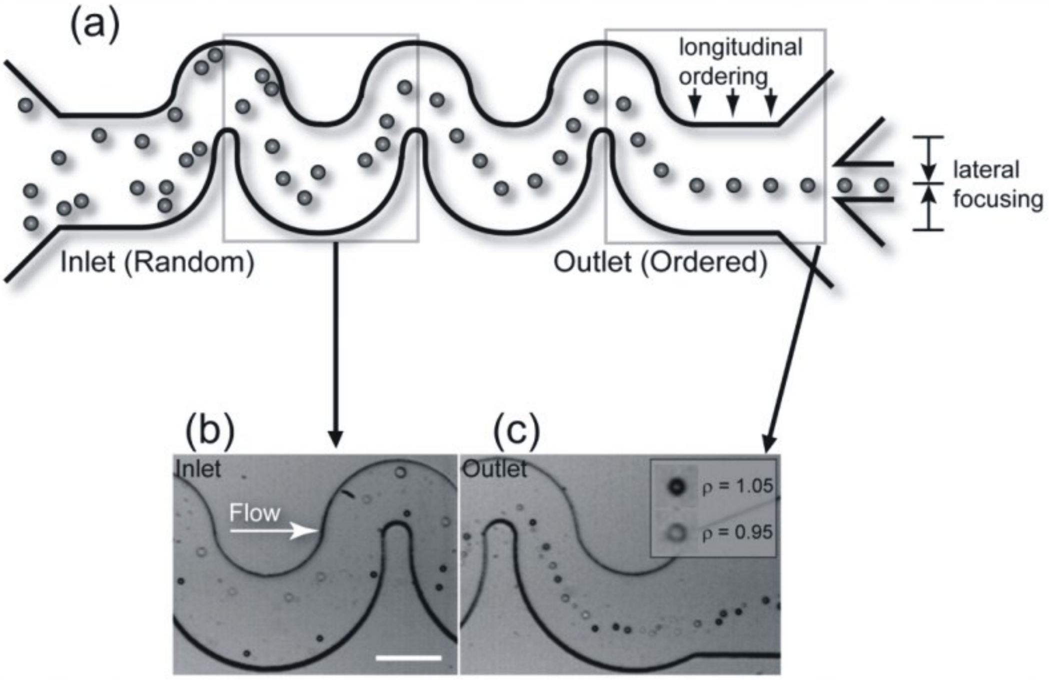

Figure 2.11 –Structure of the device presented by Di Carlo *et al.* [68]. (a) Schematic of the curving channel able to focus the particles. (b) Microscope picture of the inlet of the channel with particle randomly distributed. (c) Microscope picture of the outlet of the channel with particles focussed. Copied from [68].

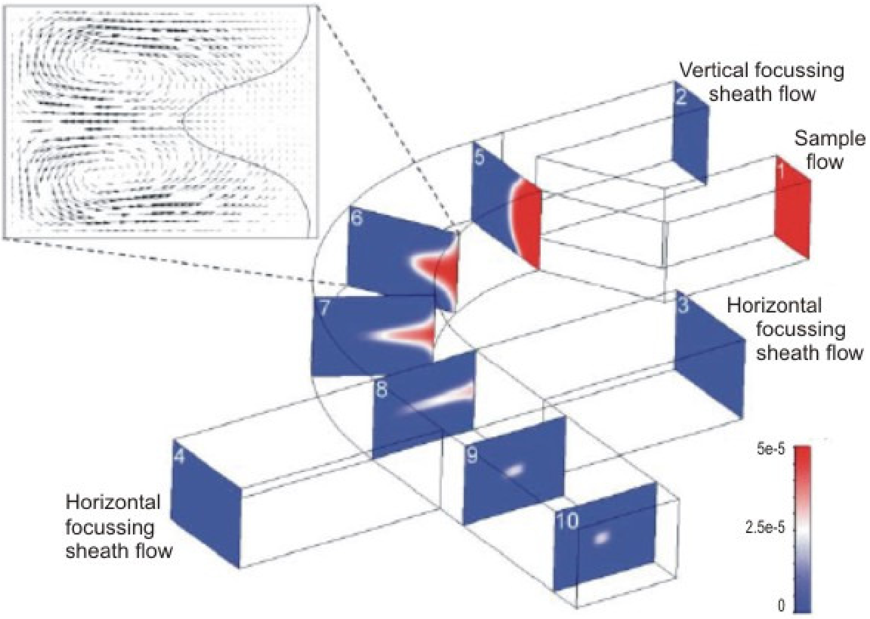

Figure 2.12 – Schematic representation of the device presented by Mao *et al.* [55]. Vertical focussing is obtained by a single sheath flow channel and a curved channel. Vortex formed in the curve (see simulation in the top left picture) focus the stream in the vertical direction wile horizontal focusing is obtained with two sheath flow channel placed at the end of the curved channel. Copied from [55].

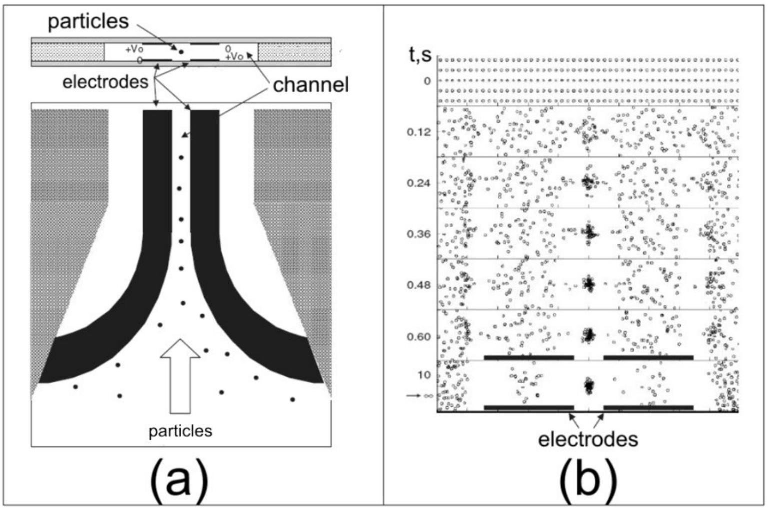

Figure 2.13 – (a) Schematic representation of top view and cross section of a device that implements DEP focusing. (b) Simulation of particles behaviour in the microfluidic layout showed in (a). The pictures represent the cross section of the channel and the numbers on the left indicate the time the particles have been subjected to the electric field. The simulations were performed considering an applied voltage of 10 V_{pp}. Copied from [69].

An alternative to hydrodynamic is Dielectrophoresis (DEP) which can be used for two-dimensional confinement of samples into a microfluidic channel. DEP is a physical phenomenon generated by AC electric fields that can move particles towards or away from the electrodes generating the electric field (see section 7.2.1). In DEP focusing, electrodes patterned on top and bottom of the microfluidic channel generate a negative-DEP effect that pushes particles in the middle of the channel (see Figure 2.13).

DEP focusing is not as easy to implement as mono-dimensional hydrodynamic focusing but it allows a relatively simple way to obtain two-dimensional focusing. Furthermore, DEP focusing works without creating structures inside the microfluidic channel, reducing the risk of channel blocking. It is also a versatile technique because using DEP it is possible to align, trap and sort cells into a microfluidic channel [70]. On the other hand, DEP focusing is not suitable for high flow rates because its efficiency decreases as the flow rate increases [69]. In the literature, DEP have been used to improve the sensitivity and resolution of a microfluidic cytometer as demonstrated by Gawad *et al.* [56] or by Holmes *et al.* [53].

Another non-hydrodynamic focussing technique uses acoustic waves that generate pressure gradients in liquid, ultimately focusing particles in the middle of the measurement channel. Traditionally, the technique could be applied only to glass-based chips because soft polymers such as PDMS have poor acoustic reflection properties. However, Shi *et al.* [71] recently presented a PDMS device able to focus particles using acoustic waves. Experimental evidence showed that the device was able to focus particles along channel width. No data were reported to evaluate the confinement along channel height probably because of limitations in the optical set-up used.

To sum up, mono-dimensional hydrodynamic focussing is still the most used technique for particle positioning in microfluidic devices because it is easy to fabricate and control. However, in recent years a number of publications appeared proposing techniques relatively simple to fabricate and easy to control [54; 67; 71]. In particular, in the optics of creating a portable system, the most appealing is the one proposed by Di Carlo *et al.* This is because it features a simple single fabrication step and a simple control due to the fact that it implements a single channel without the need of a focusing buffer or additional electronics that increase energy consumption.

2.4.3 Detection systems

Light induced fluorescence (LIF) is the most widely used detection system in microfluidic devices because of it is high sensitivity and easy implementation in microfluidic device [17; 21; 22; 34; 72; 73; 74]. Devices able to detect scattered light were also published [18; 45; 46; 50; 54] but not commonly implemented because, except for back-scatter light, they required the fabrication of integrated structures (see section 2.5) or complicate arrangements of free space optics.

An alternative to LIF is impedance spectroscopy (IS), which can be used as a detection system for microfluidic devices. IS has been studied since the first half of the twentieth century [75; 76; 77] and measures the dielectric properties of a system by applying a frequency-dependent excitation signal and measuring the response. For spherical particles, the response of the system can be linked to the dielectric properties of the particles using Maxwell's mixture formula [78]:

$$\varepsilon^*_{mix} = \varepsilon_m \frac{1 + 2\varphi f_{CM}}{1 - \varphi\, f_{CM}} \qquad \text{2-2}$$

where ε_m is the permittivity of the medium, φ is the volume fraction of the particles, f_{CM} is the Clausius-Mossotti factor, given by [79]:

$$f_{CM} = \left(\frac{\varepsilon^*_p - \varepsilon^*_m}{\varepsilon^*_p + 2\varepsilon^*_m} \right) \qquad \text{2-3}$$

where ε^*_p and ε^*_m are the complex permittivities of the particle and medium. In general the complex permittivity of a material is given by

$$\varepsilon^* = \varepsilon - i\frac{\sigma}{\omega} \qquad 2\text{-}4$$

where ε is the permittivity, σ the conductivity, ω is the angular frequency and $i = \sqrt{-1}$.

IS is interesting because it is non-invasive, but is traditionally performed on large numbers of cells in suspension, giving average value of all the particles. The first cytometer capable of measuring the electrical properties of single cells was developed by Coulter [80] in 1956. The device measured the DC resistance between two electrically isolated fluid-filled chambers as cells passed through a small connecting orifice. For a fixed sized orifice, the change in electrical current can be used to count and size the cells. Recently, a number of microfluidic devices able to perform impedance spectroscopy on single cells have been presented; the devices measure the current variation between pairs of micron-sized electrodes integrated into the microfluidic channel [25; 33; 40; 81; 82] (see example in Figure 2.14(a)) or the change

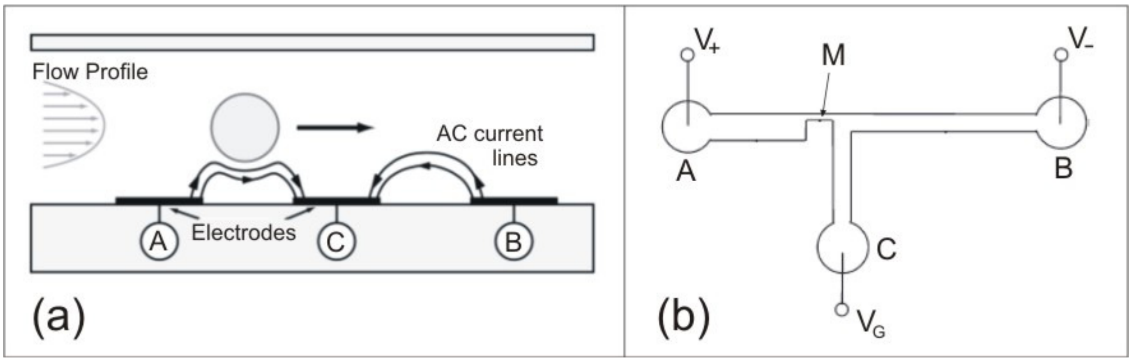

Figure 2.14 – Schematics depicting possible solutions for on-chip measurement of single cell impedance. (a) Measure of current change using electrodes integrated in the microfluidic channel. Three electrodes (A, B, C) are implemented in this example. Current flows between A and C and between B and C electrodes. When no cells flow in the microfluidic channel the two currents are exactly the same. When a cell flow between A and C, the current between the pair of electrodes changes and an external electronic amplifier measure the difference in current flow between the two pairs of electrodes. The second pair of electrodes (B and C) act as reference so that the change in current measured is not affected by changes in temperature and conductivity in the microfluidic channel. Copied from [33]. (b) Measure of the current change in a microfluidic channel using external electrodes. Particles flow from A to B that are connected with electrodes (V_+ and V_-) for electroosmotic flow generation. C is connected to an electrode (V_G) for impedance measurements. Electrical properties of particles are measured as they flow through region M. Since channels dimensions of M are comparable to particles size, when particles pass through M they reduce the current flowing between A and C. The change in current is measured by a MOFSET connected to electrodes V_+ and V_G. Copied from [66].

of current in a narrow microfluidic channel [54; 66] (see example in Figure 2.14(b)). The latter approach is interesting because it is an easier implementation. Integration of micro-electrodes in the microfluidic channel allows the insertion of an additional detection region in the microfluidic channel that works as reference (see Figure 2.14(a)).

IS and LIF were simultaneously measured on a microfluidic chip by Morgan *et al.* [44] and by Kummrow *et al.* [54]. However, in the latter work optical and impedance detection measurements where performed in different point of the measuring channel and therefore generated un-correlated signals.

Particularly interesting is the work presented by Cheung *et al.* [40] that used a microfabricated cytometer to study how the IS response changed on the basis of particles internal properties at the single cell level. The device used by Cheung *et al.* only measured two frequencies at the time; additional frequencies could have been measured simultaneously but that would have involved the use of additional expensive instrumentation. To solve this problem, Sun *et al.* [83] presented a technique (Maximum Length Sequences, or MLS) that enabled simultaneous measurement of the impedance at 512 discrete frequencies and reduced the complexity of the system because it works without the instrumentation used by Cheung *et al*.

2.4.4 Integration of optics

Microfluidic devices for high throughput cell detection and characterisation could create robust, compact and low-cost systems. In the case of fluorescence detection, most of the papers presented so far used conventional optics for delivery and collection of light within the microfluidic chip (Figure 2.15(a)). However, conventional optics are not the ideal solution for LOC cytometry application because they are bulky (Figure 2.15(b)), difficult to miniaturise, sensitive to shocks and require precise alignment. It follows that the integration of the optical structure into micro-fluidic systems is an essential step for the creation of a low-cost, portable device.

Various solutions for the integration of optical system have been proposed. The first optical elements integrated into a microfluidic chip were mirror planes [84], used to increase the sensitivity of the detection system. Processes to fabricate micro lenses [85] and insert them into microfluidic chips [86; 87] have been published, but this kind of approach still requires a precise alignment of the different components with the chip. The latest strategies involve the direct integration of the optical elements in the

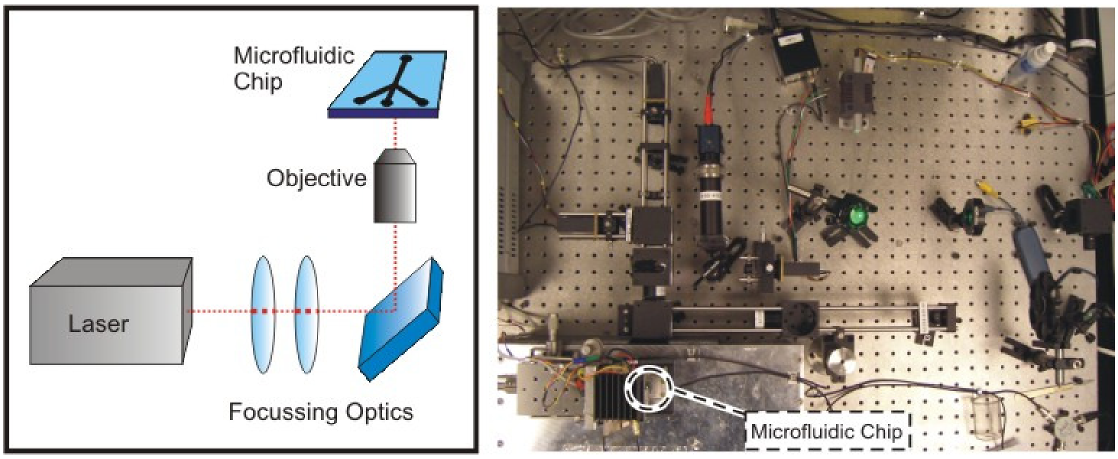

Figure 2.15 - (a) Schematic layout for a system of conventional optics coupled with a microfluidic chip; (b) photograph of a flow cytometry system that uses conventional optics. The position of the microfluidic chip is highlighted to give an idea of the size proportions.

photolithographic step. Since this solution avoids the need precise alignment procedures and the use of conventional optics, it appears to be ideal for the construction of low-cost and portable LOC cytometers.

2.4.4.1 Integration of optical fibres

The simplest solution to eliminate conventional optics for carrying light between the microfluidic chip and detector/excitation source is the integration of an optical fibre within the microfluidic chip. The fibre is then coupled with the emission source or a photodetector. This idea was first proposed by Liang *et al.* [88] in order to increase the sensitivity of a micro-fluidic device designed for capillarity electrophoresis. A schematic representation of the analytical chamber in [88] is presented in Figure 2.16. Grooves for optical fibres were etched in glass on the same

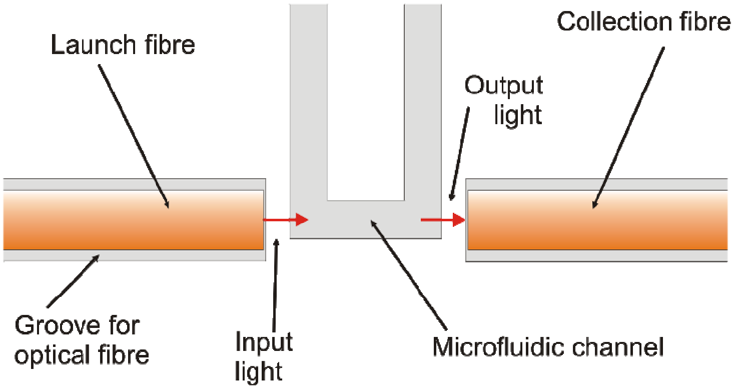

Figure 2.16 – Schematic representation of the detection region in the device presented by Liang *et al.* [88]. Fibres are pushed into grooves up to the edge of the channel wall. One fibre is used to deliver light into the channel (launch fibre) and one fibre is used to collect the light transmitted (collection fibre) from the detection region. The channel has a u-shape to increase the excitation volume. Picture copied from [88].

plane as the microfluidic structure and fibres were pushed into the grooves up to the point that their tips reached the edge of a 50 μm thick channel wall. This paper contained two innovative and very interesting solutions: the insertion of optical fibres within the chip, immediately beside the microfluidic channel, and the integration of alignment elements within the fabrication step. The latter solution allowed an easy fabrication and alignment procedure while the integration of optical fibres avoided using conventional optics.

Since the publication of the paper from Liang *et al.*, a number of chips with integrated optical fibres were proposed: Chabinyc *et al.* [89] presented a device that simplified the fabrication process by using polymers instead of silicon. Integration of the optical fibre within the structure was obtained by placing it on top of the master, PDMS was then cast on the mould/fibre complex; after curing the PDMS structure was peeled off the master and bonded on top of a glass slide. This procedure was used to glue the fibre to the structure and to avoid the use of matching index liquids but had the drawback of difficult alignment because no grooves were designed for the optical fibre. An improved solution was suggested by Xiang *et al.* [50] that used fresh PDMS to fill grooves with fibres already inserted. The polymer was allowed to solidify at room temperature. This additional PDMS glued the fibre to the channel, replaced the etched cladding layer of the fibre and acted as a matching index material.

The first example in which monolithically integrated grooves and embedded fibres were used for particle detection was presented by Cui *et al.* [51] in an easy-to-fabricate chip where grooves and channels were defined within a SU-8 structure. The

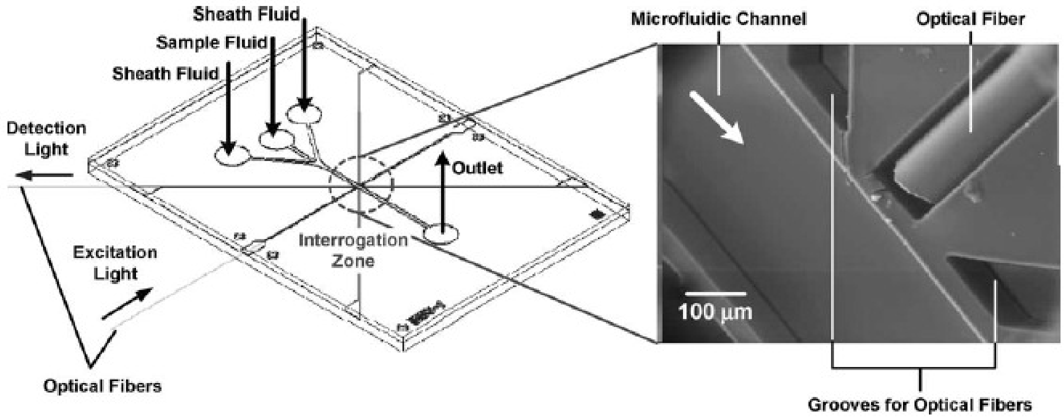

Figure 2.17 – Schematic representation of the device presented by Tung *et al.* [52]. The device incorporate several grooves at different angles for the simultaneous multi-colour excitation/detection using a single interrogation zone. Hydrodynamic focusing is used to focus particles in the channel. Picture copied from [52].

device incorporated the interesting solution to insert two optical fibres within the same groove and use them for excitation/detection of scattered and fluorescence light from fluorescently labelled microspheres. The main drawback of the system was the absence of a focusing system that made the device produce signals with high variation in intensity.

An improved design for a microfluidic flow cytometer with embedded fibres was introduced by Tung *et al.* [52], which was a device with several grooves at different angles for simultaneous multi-colour excitation/detection using a single interrogation zone (Figure 2.17). Hydrodynamic focussing was used to position particles in the middle of the microfluidic channel. The optical fibres were coupled to PIN photodiodes and lock-in amplification was used to increase the signal to noise ration (S/N). Two-colour fluorescent detection of particles at a count rate of 500 particles s^{-1} was demonstrated and different S/N ratios were obtained ranging from 2 to 9. This device is one of the best solution presented so far for the integrations of optics on chip because it is easy to fabricate, it has a flexible design and uses apparently low cost instrumentation. However, the device still needs improvement in terms of sensitivity and focusing power.

To sum up, the papers presented proved that integration of optical fibre is effective for a number of application such as chemical or cytometric analysis. At the present state of the art, the integration of optical fibres is the best solution for the integration of optics within a microfluidic chip. In addition it is an easy implementation because of simple fabrication and alignment, the integration of optical fibres allows robust and flexible designs. Furthermore, using standard connectors, fibres can be connected to different sources or detectors, increasing the flexibility of the system.

2.4.4.2 Monolithic integration of planar waveguides

Another technique to deliver/collect light at the edge of a microfluidic channel is the integration of planar waveguides. The first example of this kind was presented by Mogesten *et al.* [90] that coupled the light coming from an optical fibre to planar waveguides fabricated within the chip. Since this device required a difficult and time-consuming fabrication, an improved device was presented [34] with optical waveguides monolithically integrated into a structure fabricated using SU-8, a negative photoresist. A schematic representation of the structure of the waveguide is presented in Figure 2.18. Because of its high refractive index ($n_{SU\text{-}8} = 1.59$ at 633 nm), SU-8 was used as core while the cladding layers were glass and air that have a lower refractive index than

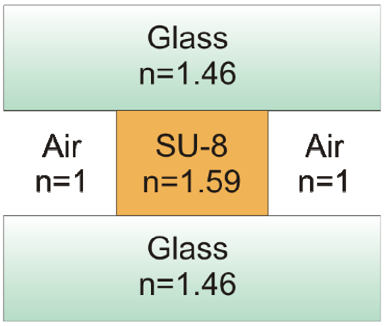

Figure 2.18 – Cross-section of the waveguide structure. The core of the waveguide is given by the high refractive index SU-8 wile the cladding are given by air at the side and glass on top and bottom. Copied from [34].

SU-8 ($n_{AIR} = 1$; $n_{glass} = 1.46$ at 633 nm). In this way the light passes into the waveguides by total internal reflection [91]. The great advantage of this solution was an easy and fast fabrication process; once the resist had been patterned on the glass substrate, only one exposure step was necessary to define channel, waveguides and grooves to guide the coupling of optical fibres to the waveguides. The waveguide loss was measured to be 6 dB cm^{-1} at 633 nm. The authors claim that the high loss was due to a thin layer (5 µm) of SU-8 between the structure and the glass top lid. The layer was inserted in order to obtain good bonding but it probably caused bad confinement of the light, increasing losses. The assumption was confirmed by the fact that a lower loss (1.4 dB cm^{-1}) was obtained by sealing the top of the channel with a PDMS lid directly connected to the structure.

Ever since the work of Mogesten *et al.* [34] polymer waveguides have been widely investigated and a number of publications appeared, because of easy fabrication, the high flexibility of the structures and the possibility to use an elevate number of materials and fabrication procedures. Bilinger *et al.* [92] sealed the top of the SU-8 structure with another polymer with lower refractive index increasing the performance of the waveguide up to 11 times compare to a SU-8 sealed structure. Lee *et al.* [93] presented a device with grooves obtained by etching soda-lime glass. The grooves were coated with SOG polymer and filled with SU-8 (Figure 2.19). The SU-8 worked as core and the SOG worked as cladding for the waveguide. Characterisation of the waveguide

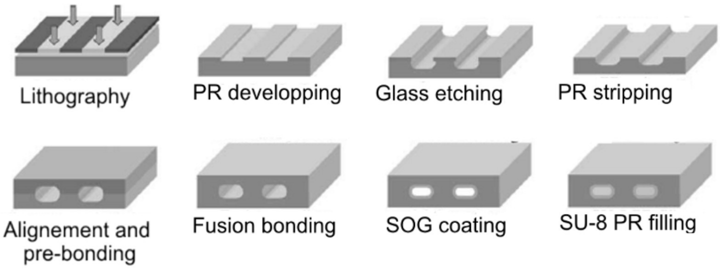

Figure 2.19 - Fabrication process for grooves coated with SOG polymer and filled with SU-8. The SU-8 worked as core and the SOG worked as cladding for the waveguide. Copied from [93].

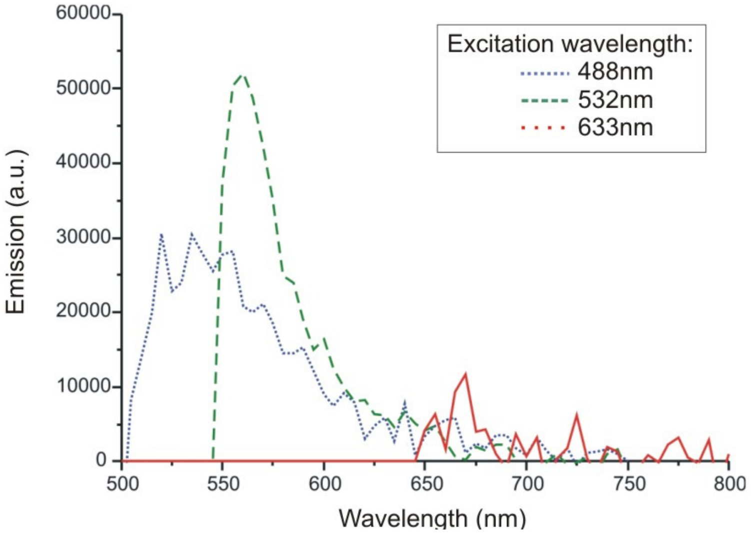

Figure 2.20 – Fluorescence emission spectra generated by cured SU-8 when excited with different wavelengths. Unpublished data collected by Dr D. Holmes (University of Southampton).

returned a loss of 4 dB cm^{-1}. Polymer waveguides with tailored refractive index were also proposed. The modification in the refractive index was obtained by dissolving chemicals in the uncured material (doped polymers). Devices in PMMA, SU-8 and PDMS were obtained using doped polymers with losses ranging from 1.27 to 3 dB cm^{-1} [94; 95; 96]. However, the improvement of performance of tailored waveguides is obtained increasing the fabrication complexity because more fabrication steps are required. Furthermore, it is possible that the high losses in polymer waveguides are due to the resolution of the fabrication process rather than their structure [97].

In addition to the quality of the fabrication process, losses in polymer planar waveguides are affected by the autofluorescence generated by the polymers used (Figure 2.20). A solution to solve these problems could be the use of glass waveguides fabricated by using laser or ion exchange techniques to modify the refractive index of a glass substrate in a specific region [98; 99; 100]. Glass waveguides have losses between 0.3 and 0.8 dB cm^{-1}, confirming that removing auto-fluorescence and improving the quality of the fabrication process can actually reduce power losses.

2.4.4.3 Monolithical integration of planar microlenses

Another class of optical element that can be easily integrated into a microfluidic structure is planar microlenses that can increase the sensitivity of an optical integrated systems. For example, Camou *et al.* [101] presented a device with grooves for the self-alignment of optical fibres and a 2D micro lens obtained by ending one of the grooves with a curved interface (Figure 2.21). As in [34], all the structures were fabricated in

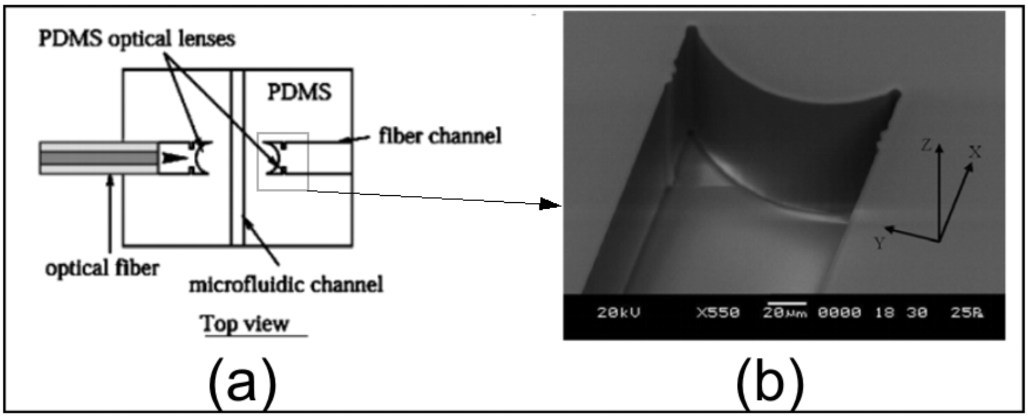

Figure 2.21 – (a) Layout of the device presented by Camou *et al.* [101]. (b) Microscope picture of integrated planar microlens obtained at the end of the groove. Copied from [101].

the same step, avoiding alignment problems and complicated fabrication. Tests showed how the insertion of the optical lens increased the excitation of a fluorescent dye by a factor of 4 and lowered the detection limit threshold by a factor of 3. However, the device suffered from a not ideal positioning of the lens that could block the use of a matching index for the reduction of scattering losses.

More complex designs can also be used, as was demonstrated by Seo *et al.* [102] (Figure 2.22) where an array of integrated microlenses was used to focus light coming from an external source. It was demonstrated that the use of the lenses increased the light in the channel 7 times compared to the system without lenses.

Interesting is the device proposed by Wang *et al.* [18] that integrated most of the functionalities described so far. The layout of the detection region is shown in Figure 2.23(a, b). Optical fibres were coupled to the planar waveguides using self-alignment grooves. Excitation light coming from an optical fibre passed through a tapered waveguide (that gave a higher degree of collimated light) and ended in an elliptical lens. The final result is shown in Figure 2.23(c). For the detection, 5° forward scatter

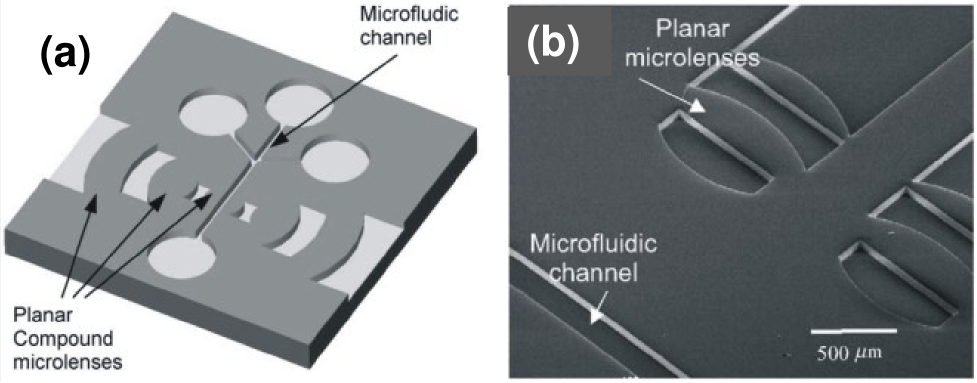

Figure 2.22 – (a) Layout of the device presented by Seo *et al.* [102]. (b) Microscope picture of the lens array. Copied from [102].

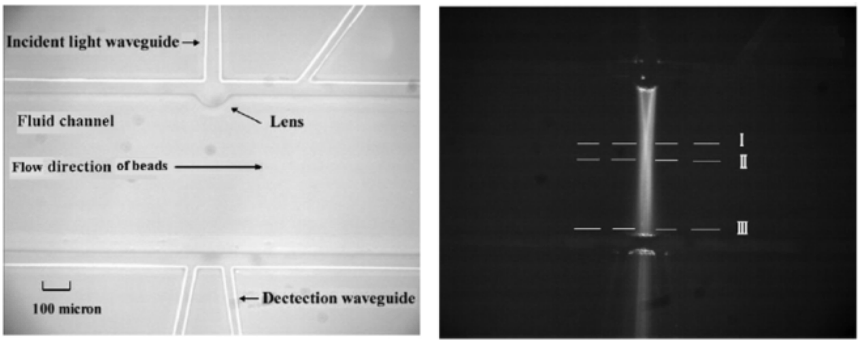

Figure 2.23 – Details of the device presented by Wang *et al.* (a) Microscope picture of the detection region in bright field. (b) Microscope picture of the detection region in dark field. Copied from [18].

light was collected by a waveguide coupled with another optical fibre. The device was tested measuring the forward scatter signal of polystyrene beads as they flow through the channel at a throughputs up to 25 beads s^{-1}.

To sum up, monolithical integration of planar microlenses was demonstrated to be a suitable and reliable technique for the integration of optics. Planar microlenses can be easily coupled with optical fibres and they have been proven to increase the sensitivity of the optical detection system. Furthermore, all the devices presented in this section are fabricated with a single step resulting in a simple fabrication process that returns optics and microfluidic already aligned. The only drawbacks of this technique are the need to use fabrication procedures with optical quality resolution and the geometry is limited only to cylindrical microlenses.

2.4.4.4 Optofluidics structures

As an alternative to the monolithical integration of optical components, liquid can be used as material for light manipulation (optofluidics) [103]. This solution allows the creation of flexible structures whose properties can be modified to suit the requirements of the specific application.

Simple examples of optofluidics are liquid-filled structures defined within the wall of the microfluidic chip. The elements posses moderate flexibility because their ability to handle light can be modified by changing the liquid [97; 104]. More complicated structures are based on fluidic effects generated between two or more flowing streams [105; 106; 107; 108; 109; 110]. These works exploit fluidic effects to generate lens or other structures and laminar flow to generate interfaces with optical resolution. For example, Tang *et al.* [108] created a planar microlens with three streams that expand in a rectangular channel to form a lens as showed in Figure 2.24. The liquid used as a cladding has a lower refractive index from the liquid in the central stream so

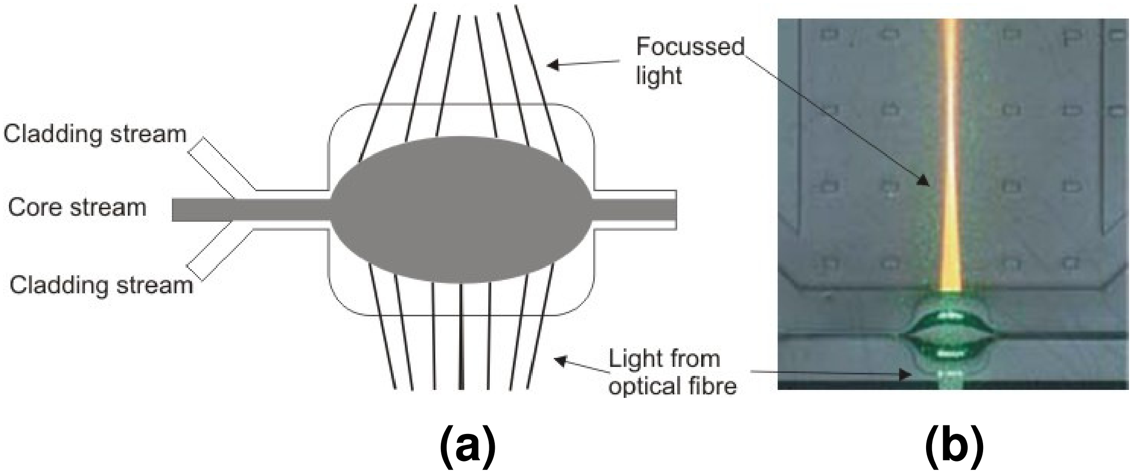

Figure 2.24 – (a) Schematic depicting the liquid-core liquid cladding lens presented by Tang *et al.* [108]. Three streams of fluid remain separate due to laminar flow. The index of refraction of the core stream is higher than the index of the cladding streams. As the stream enter the rectangular expanding chamber they expand laterally, forming a bi-convex planar microlens. (b) picture of optofluidics microlens focussing light coming from an optical fibre. Copied from [108].

that the lens formed is bi-convex. Another interesting example demonstrating the high tunability and flexibility of flow controlled optofluidics structures was presented by Mao *et al.* [110] that used diffusion phenomena between two adjacent flowing medium with different concentration of a salt to create a Gradient Index (L-GRIN) lens.

In alternative to flow controlled structures, liquid microlenses can be formed at the interface of two immiscible fluids (e.g. water and oil). In this case, the curvature of the lens can be modified by thermally or pH induced volumetric changes or by current-induced change in the wettability (electrowetting) of the chamber containing the two fluids [111; 112].

A more complicated type of optofluidics waveguides, Antiresonant reflecting optical waveguides (ARROWs), has also been proposed. These waveguides are based on the principle of the Fabry-Perot interferometer [91]. In ARROW waveguides the low-index core is surrounded by high-index cladding layers with thicknesses chosen to carry only a specific wavelength (Figure 2.25(a)). The advantage of these waveguides is the use of microfluidic channels as waveguide for excitation and detection of particle fluorescence [49; 113; 114].

Generally speaking optofluidics structures are interesting solutions because of their tunability. In particular, structures whose shape is defined within the chip and the refractive index is defined by the liquid filler [97; 104] represents an interesting solution for portable devices because they are robust and offer moderate adaptation to

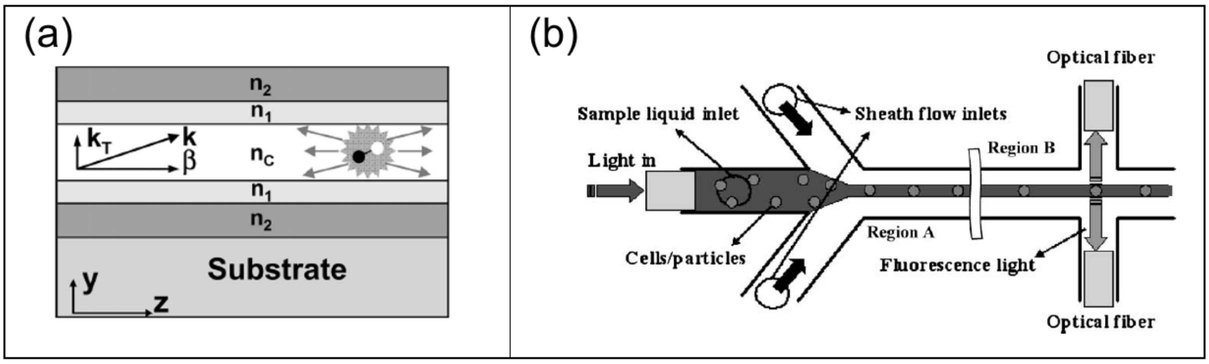

Figure 2.25 – (a) Schematic view of hollow-core ARROW waveguide. Light propagates in the liquid core because of cladding layers of higher refractive indexes ($n_c < n_1$, n_2). The design include also an emitting molecule inserted into the ARROW waveguide. Copied from [114]. (b) Example of how ARROW waveguides can be used: the sample channel is also a waveguide, used for delivery of excitation light; fluorescence is collected at 90° from the excitation source, reducing the background noise due to excitation light. Copied from [49].

the specific application. On the other hand, structures that use fluid flow to shape optical elements [105; 110] are more useful for powerful, high characterisation bench-top instruments because the need to a continuous fluid flow make them delicate, complex to control and increases their energy consumption therefore reducing their suitability for portable applications. As for ARROW waveguides, although they are robust and simple to operate, they require a complicated multi-step fabrication process that would increase complexity and ultimately, the cost of the device.

2.4.4.5 Integration of excitation sources and detection sensors

Fully integrated systems have been proposed by inserting excitation sources or detection sensors within the microfluidic chip. For example, Figure 2.26(a) show the device presented by Chabinic *et al.* [89] that integrated a micro-avalanche photodiode (µAPD) into a PDMS lid. Excitation light was delivered on the detection region by an optical fibre embedded into the PDMS structure. Light coming from the fibre irradiated the sample flowing through a curved microfluidic channel (Figure 2.26(b)). The light emitted by fluorescent samples is collected by a µAPD integrated underneath the detection region (Figure 2.26(c)). Spectral resolution was obtained by integrating a coloured filter on top of the photodiode. The device was able to detect fluorescein at a concentration as low as 25 nM, showing a sensitivity ~1000 times higher than a commercial instrument.

Kruger *et al.* [21] proposed a device where an avalanche photodiode (APD) was integrated on the lid sealing the top of the channel. The device used a leaky waveguide to excite red fluorescent beads (excitation 635 nm / emission 645-680 nm) from the

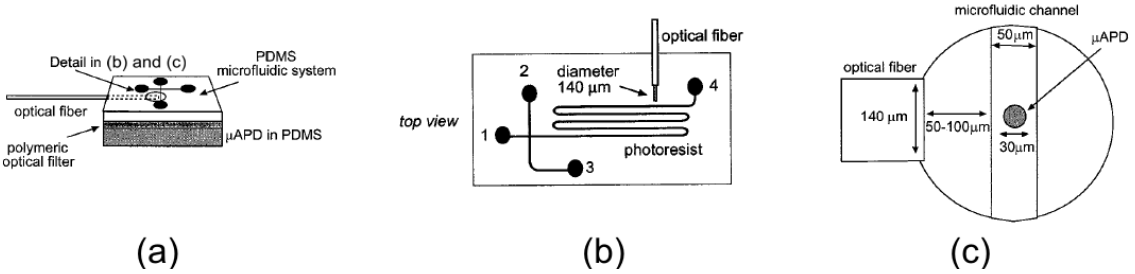

Figure 2.26 – (a) Layout of the device presented by Chabinic *et al.* [89]. (b) Details of the microfluidic array and of the detection region with curved channel. (c) Detail of the detector integrated within the microfluidic chip. Copied from [89].

bottom of the channel. Fluorescent light from beads was detected by the APD placed on top of the channel, demonstrating the feasibility of the principle.

An excitation source was integrated by Edel *et al.* [115]. An LED was inserted at the bottom of a device designed for capillary electrophoresis (CE). The device was successfully tested by separating a solution 5 mM of fluorescein and 5mM of 5-carboxy-fluorescein. An interesting layout for the insertion of the excitation source was presented in [116] where a photodiode fabricated on top of a substrate was coupled with an SU-8 waveguide for the delivery of the light into a microfluidic channel.

Several examples of integrated excitation sources and active detection elements have been recently reviewed in [117]. General structures and principles are similar to the ones presented above: excitation and emission elements are placed on top and/or on the bottom of the microfluidic channel and an integrated filtering system provide spectral filtering. In general, the complete integration of detection and excitation is an interesting solution to create a fully integrated detection system. However, realisation of such devices increase fabrication complexity and reduces the flexibility of the microfluidic device.

2.5 Summary

In this chapter, the fabrication of a microfabricated cytometer was indicated as a solution for the problems affecting the application of flow cytometry to the study of phytoplankton presented in chapter 1. Different solutions for microfluidic devices have therefore been presented in terms of fabrication, flow generation and detection systems in the optics of creating a powerful, low cost and portable microfabricated cytometer

In terms of sample focussing, recent publications showed that a 2D focussing system can drastically in increase the precision of a microfabricated cytometer and therefore several techniques have been proposed. Recent publications presented interesting solutions that appear easy to fabricate and simple in terms of hydrodynamic control. However, at the present stage mono-dimensional hydrodynamic focussing represents the easier technique to implement and control in a microfluidic system.

In terms of sample detection, the most widely used technique appears to be LIF. The technique is usually chosen for its high sensitivity and selectivity, but most of the time conventional optics are used for the detection system, restricting the development of compact and solid devices. For this reason, particular attention has been given to reviewing integrated optical elements; the different solutions have been divided into integration of optical fibres, planar waveguides, planar microlenses, optofluidics elements and excitation/detection apparatus. In the optics of creating a powerful, low cost and portable device the best solution appears to be the integration of optical fibres because they can be easily inserted and aligned into the chip using self-alignment insertion grooves. The optical performance can be improved with monolithically integrated planar microlenses. Basic optofluidic structures that are not formed by hydrodynamic effects can also be implemented to increase characterisation power and flexibility of the instrument. Planar waveguides can also be inserted for specific applications but the losses of the waveguides presented so far appear too high for flow cytometric applications. Finally, complex optofluidics structures using flow and ARROW waveguides and integration of excitation/detection apparatus do not appear to be a suitable solution because the devices are complicated to fabricate and are sensitive to shocks in the case of flow generated optofluidics structures.

REFERENCES

[1]J.L. Collier, Flow cytometry and the single cell in phycology. Journal of Phycology 36 (2000) 628-644.

[2]M. Reckermann, and F. Colijn, Aquatic flow cytometry: Achievements and prospects - Foreword. Scientia Marina 64 (2000) 119-120.

[3]S.C. Terry, J.H. Jerman, and J.B. Angell, Gas-Chromatographic Air Analyzer Fabricated on a Silicon-Wafer. Ieee Transactions on Electron Devices 26 (1979) 1880-1886.

[4]A. Manz, Y. Miyahara, J. Miura, Y. Watanabe, H. Miyagi, and K. Sato, Design of an Open-Tubular Column Liquid Chromatograph Using Silicon Chip Technology. Sensors and Actuators B-Chemical 1 (1990) 249-255.

[5]M.W.J. Prins, W.J.J. Welters, and J.W. Weekamp, Fluid control in multichannel structures by electrocapillary pressure. Science 291 (2001) 277-280.

[6]T. Suzuki, S. Kawano, I. Kanno, H. Shintaku, S. Yakushiji, and H. Kotera, High-efficient micropump with geometry optimisation of microchannel using computational fluid dynamics, Proceedings of Micro TAS, Malmo, Sweden, 2004, pp. 234-236.

[7]D. Baechi, R. Buser, and J. Dual, A high density microchannel network with integrated valves and photodiodes. Sensors and Actuators a-Physical 95 (2002) 77-83.

[8]M. Tatsuoka, T. Shimomae, Y. Shirasaki, J. Tanaka, S. Watabe, J. Mizuno, T. Edura, K. Tsutsui, Y. Wada, S. Shoji, and T. Funatsu, 2D free space flow control system using termoreversible gelation of polymer by IR-laser, Proceedings of Micro TAS, Malmo, Sweden, 2004, pp. 252-254.

[9]Q. Yu, J.M. Bauer, J.S. Moore, and D.J. Beebe, Responsive biomimetic hydrogel valve for microfluidics. Applied Physics Letters 78 (2001) 2589-2591.

[10]D. Holmes, M. Thomas, and H. Morgan, Dielectrophoretic separation/isolation of rare particles/cell types form a heterogeneous suspension within a microfluidic system. in: A. VandenBerg, P. Bergveld, and W. Olthuis, (Eds.), Micro Total Analysis Systems 2000, Proceedings, 2000, pp. 115-118.

[11]S.C. Jacobson, C.T. Culbertson, J.E. Daler, and J.M. Ramsey, Microchip structures for submillisecond electrophoresis. Analytical Chemistry 70 (1998) 3476-3480.

[12]S.C. Jacobson, T.E. McKnight, and J.M. Ramsey, Microfluidic devices for electrokinetically driven parallel and serial mixing. Analytical Chemistry 71 (1999) 4455-4459.

[13]H. Martin, and A. Manz, Contimuous-flow micromixing for fast DNA hybridisation assys, Proceedings of Micro TAS, Malmo, Sweden, 2004.

[14]A. Renaudin, V. Znag, P. Tabourier, J.C. Camart, and C. Druon, Droplet manipulation using saw actuation for integrated microfluidics, Proceedings of Micro TAS, Malmo, Sweden, 2004, pp. 551-553.

[15]C. Wiles, P. Watts, and S.J. Haswell, The use of solid-supported reagents within EOF-based micro reactors, Proceedings of Micro TAS, Malmo, Sweden, 2004, pp. 105-107.

[16]B.J. Cheek, A.B. Steel, M.P. Torres, Y.Y. Yu, and H.J. Yang, Chemiluminescence detection for hybridization assays on the flow-thru chip, a three-dimensional microchannel biochip. Analytical Chemistry 73 (2001) 5777-5783.

[17]M.A. McClain, C.T. Culbertson, S.C. Jacobson, and J.M. Ramsey, Flow cytometry of Escherichia coli on nucrifluidic devices. Analytical Chemistry 73 (2001) 5334-5338.

[18]Z. Wang, J. El-Ali, M. Engelund, T. Gotsaed, I.R. Perch-Nielsen, K.B. Mogensen, D. Snakenborg, J.P. Kutter, and A. Wolff, Measurements of scattered light on a microchip flow cytometer with integrated polymer based optical elements. Lab on a Chip 4 (2004) 372-377.

[19]T. Ito, T. Toru, and T. Higuchi, Manipulation and preparation of bubbles for gas analysis systems, Proceedings of MicroTAS, Malmo, Sweden, 2004, pp. 282-284.

[20]A.Y. Fu, C. Spence, A. Scherer, F.H. Arnold, and S.R. Quake, A microfabricated fluorescence-activated cell sorter. Nature Biotechnology 17 (1999) 1109-1111.

[21]J. Kruger, K. Singh, A. O'Neill, C. Jackson, A. Morrison, and P. O'Brien, Development of a microfluidic device for fluorescence activated cell sorting. Journal of Micromechanics and Microengineering 12 (2002) 486-494.

[22]V. Studer, R. Jameson, E. Pellereau, A. Pepin, and Y. Chen, A microfluidic mammalian cell sorter based on fluorescence detection. Microelectronic Engineering 73-74 (2004) 852-857.

[23]Z. Wang, O. Hansen, P.K. Petersen, A. Rogeberg, J.P. Kutter, D.D. Bang, and A. Wolff, Dielectrophoresis microsystem with integrated flow cytometers for on-line monitoring of sorting efficiency. Electrophoresis 27 (2006) 5081-5092.

[24]D. Fries, K.H. Bradbent, Janowiak, A.M. Cardenas-Valencia, S. Ivanov, R. Benson, and G. Steimle, Printed circuit board based oceanographic microfluidic system, 7th Internation Conference on Miniaturised Chemical and Biochemical Analysis Systems, Squaw Valley, California USA, 2003.

[25]L.L. Sohn, O.A. Saleh, G.R. Facer, A.J. Beavis, R.S. Allan, and D.A. Notterman, Capacitance cytometry: Measuring biological cells one-by-one. Biophysical Journal 80 (2001) 144A-144A.

[26]S. Usui, and T. Fujii, Development of *in situ* flow-through analyser of Mn^{2+} in seawater with a PDMS microfluidic device, 7th International Conference on Miniaturised Chemical and Biochemical Analysis Systems, Squaw Valley, California USA, 2003.

[27]M. Madou, Fundamentals of microfabrication, CRC press, Boca Raton, 1997.

[28]H. Becker, and C. Gartner, Polymer microfabrication methods for microfluidic analytical applications. Electrophoresis 21 (2000) 12-26.

[29]H. Becker, and L.E. Locascio, Polymer microfluidic devices. Talanta 56 (2002) 267-287.

[30]Y. Xia, and G.M. Whitesides, Soft lithography, 1998, pp. 153-184.

[31]R. Yang, D.L. Feeback, and W. Wang, Microfabrication and test of a three-dimensional polymer hydro-focusing unit for flow cytometry applications. Sensors and Actuators A: Physical 118 (2005) 259-267.

[32]C. Simonnet, and A. Groisman, High-throughput and high-resolution flow cytometry in molded microfluidic devices. Analytical Chemistry 78 (2006) 5653-5663.

[33]S. Gawad, L. Schild, and P. Renaud, Micromachined impedance spectroscopy flow cytometer for cell analysis and particle sizing. Lab on a Chip 1 (2001) 76-82.

[34]K.B. Mogensen, J. El-Ali, A. Wolff, and J.P. Kutter, Integration of polymer waveguides for optical detection in microfabricated chemical analysis systems. Applied Optics 42 (2003) 4072-4079.

[35]B.-H. Jo, L.M.V. Lerberghe, K.M. Motsegood, and D.J. Beebe, Three-Dimensional Micro-Channel Fabrication in Polydimethylsiloxane (PDMS) Elastomer. Journal of Micromechanical Systems 9 (2000) 76-81.

[36]H. Wu, T.W. Odom, D.T. Chiu, and G.M. Whitesides, Fabrication of Complex Three-Dimensional Microchannel Systems in PDMS, 2003, pp. 554-559.

[37]M. Heckele, W. Bacher, and K.D. Müller, Hot embossing - The molding technique for plastic microstructures. Microsystem Technologies 4 (1998) 122-124.

[38]J. Wang, M. Pumera, M.P. Chatrathi, A. Escarpa, R. Konrad, A. Griebel, W. Dörner, and H. Löwe, Towards disposable lab-on-a-chip: Poly(methylmethacrylate) microchip electrophoresis device with electrochemical detection, 2002, pp. 596-601.

[39]T.J. Johnson, D. Ross, and L.E. Locascio, Rapid Microfluidic Mixing, 2002, pp. 45-51.

[40]K. Cheung, S. Gawad, and P. Renaud, Impedance spectroscopy flow cytometry: On-chip label-free cell differentiation. Cytometry Part A 65A (2005) 124-132.

[41]C. Gruden, S. Skerlos, and P. Adriaens, Flow cytometry for microbial sensing in environmental sustainability applications: current status and future prospects. Fems Microbiology Ecology 49 (2004) 37-49.

[42]D. Erickson, and D.Q. Li, Integrated microfluidic devices. Analytica Chimica Acta 507 (2004) 11-26.

[43]A. Wolff, I.R. Perch-Nielsen, U.D. Larsen, P. Friis, G. Goranovic, C.R. Poulsen, J.P. Kutter, and P. Telleman, Integrating advanced functionality in a microfabricated high-throughput fluorescent-activated cell sorter. Lab on a Chip 3 (2003) 22-27.

[44]H. Morgan, D. Holmes, and N.G. Green, High speed simultaneous single particle impedance and fluorescence analysis on a chip. Current Applied Physics 6 (2006) 367-370.

[45]N. Pamme, R. Koyama, and A. Manz, Counting and sizing of particles and particle agglomerates in a microfluidic device using laser light scattering: application to a particle-enhanced immunoassay. Lab on a Chip 3 (2003) 187-192.

[46]D.P. Schrum, C.T. Culbertson, S.C. Jacobson, and J.M. Ramsey, Microchip flow cytometry using electrokinetic focusing. Analytical Chemistry 71 (1999) 4173-4177.

[47]A.Y. Fu, H.P. Chou, C. Spence, F.H. Arnold, and S.R. Quake, An Integrated Microfabricated Cell Sorter, 2002, pp. 2451-2457.

[48]L.-M. Fu, R.-J. Yang, C.-H. Lin, Y.-J. Pan, and G.-B. Lee, Electrokinetically driven micro flow cytometers with integrated fiber optics for on-line cell/particle detection. Analytica Chimica Acta 507 (2004) 163-169.

[49]R. Bernini, E. De Nuccio, F. Brescia, A. Minardo, L. Zeni, P.M. Sarro, R. Palumbo, and M.R. Scarfi, Development and characterization of an integrated silicon micro flow cytometer (vol 386, pg 2257, 2006). Analytical and Bioanalytical Chemistry 386 (2006) 2257-2257.

[50]Q. Xiang, X.C. Xuan, B. Xu, and D.Q. Li, Multi-functional particle detection with embedded optical fibers in a poly(dimethylsiloxane) chip. Instrumentation Science & Technology 33 (2005) 597-607.

[51]L. Cui, T. Zhang, and H. Morgan, Optical particle detection integrated in a dielectrophoretic lab-on-a-chip. Journal of Micromechanics and Microengineering 12 (2002) 7-12.

[52]Y.C. Tung, M. Zhang, C.T. Lin, K. Kurabayashi, and S.J. Skerlos, PDMS-based opto-fluidic micro flow cytometer with two-color, multi-angle fluorescence detection capability using PIN photodiodes. Sensors and Actuators B-Chemical 98 (2004) 356-367.

[53]D. Holmes, H. Morgan, and N.G. Green, High throughput particle analysis: Combining dielectrophoretic particle focussing with confocal optical detection. Biosensors & Bioelectronics 21 (2006) 1621-1630.

[54]A. Kummrow, J. Theisen, M. Frankowski, A. Tuchscheerer, H. Yildirim, K. Brattke, M. Schmidt, and J. Neukammer, Microfluidic structures for flow cytometric analysis of hydrodynamically focussed blood cells fabricated by ultraprecision micromachining. Lab on a Chip 9 (2009) 972–981.

[55]X. Mao, J.R. Waldeisen, and T.J. Huang, "Mircrofluidic drifting" - implememnting three-dimensionla hydrodynamic focusing with a single-layer planar microfluidic device. Lab on a Chip 7 (2007) 1260-1262.

[56]S. Gawad, P. Batard, U. Seger, S. Metz, and P. Renaud, Leukocytes discrimination by impedance spectroscopy flow cytometry. in: S.S.a.A.v.d.B. Y. Baba, Kluwer, Nara, Japan, (Ed.), Micro Total Analysis Systems, Kluwer Academic Publisher, Printed in the Netherlands, 2002.

[57]D. Holmes, B. Neal, N. Green, and H. Morgan, Microfabricated Device for Rapid Impedance Measurements on Single Biological Cells, Proceedings of 15th MicroMechanics Europe Workshop, Leuven Belgium, 2004, pp. pp. 195-198.

[58]D. Holmes, J.K. She, P.L. Roach, and H. Morgan, Bead-based immunoassays using a micro-chip flow cytometer. Lab on a Chip 7 (2007) 1048-1056.

[59]D.A. Ateya, J.S. Erickson, P.B. Howell-Jr, L.R. Hilliard, J.P. Golden, and F.S. Ligler, The good, the bad, and the tiny: a review of microflow cytometry. Analytical and Bioanalytical Chemistry 391 (2008) 1485–1498.

[60]U. Seger, S. Gawad, R. Johann, A. Bertsch, and P. Renaud, Cell immersion and cell dipping in microfluidic devices. Lab on a Chip 4 (2004) 148-151.

[61]T. Braschler, L. Metref, R. Zvitov-Marabi, H. van Lintel, N. Demierre, J. Theytaz, and P. Renaud, A simple pneumatic setup for driving microfluidics. Lab on a Chip 7 (2007) 420-422.

[62]G. Karniadakis, A. Beskok, and N. Aluru, Microflows and nanoflows : fundamentals and simulation, Springer, New York, 2005.

[63]B. Massey, and B. Stanford, (Eds.), Mechanics of Fluids, Taylor & Francis Group, London and New York, 2006.

[64]Pretoriu.V, B.J. Hopkins, and J.D. Schieke, Elctro-Osmosis - New Concept for High-Speed Liquid-Chromatography. Journal of Chromatography 99 (1974) 23-30.

[65]M.S. Howard, (Ed.), Practical Flow Cytometry, John Wiley & Sons, 2003.

[66]Y.-N. Wang, Y. Kang, D. Xu, C.H. Chon, L. Barnett, S.A. Kalams, D. Li, and D. Li, On-chip counting the number and the percentage of CD4+ T lymphocytes. Lab on a Chip 8 (2008) 309-315.

[67]J.P. Golden, J.S. Kim, J.S. Erickson, L.R. Hilliard, P.B. Howell, G.P. Anderson, M. Nasir, and F.S. Ligler, Multi-wavelength microflow cytometer using groove-generated sheath flow. Lab on a Chip 9 (2009) 1942-1950.

[68]D. Di Carlo, I. Daniel, R.G. Tompkins, and M. Toner, Continuous Inertial Focusing, Ordering, and Separation of Particles in Microchannels. Applied Physical Sciences (2007).

[69]H. Morgan, D. Holmes, and N. Green, AC electrokinetic focussing in microchannels: micro- and nanoparticles. Electrostatics (2004) 119-124.

[70]S. Fiedler, S.G. Shirley, T. Schnelle, and G. Fuhr, Dielectrophoretic sorting of particles and cells in a microsystem. Analytical Chemistry 70 (1998) 1909-1915.

[71]J. Shi, X. Mao, D. Ahmed, A. Colletti, and T.J. Huang, Focusing microparticles in a microfluidic channel with standing surface acoustic waves (SSAW). Lab on a Chip 8 (2007) 221-223.

[72]H.W. Bang, C.N. Chung, J.K. Kim, S.H. Kim, S. Chung, J. Park, W.G. Lee, H. Yun, J. Lee, K.C. Cho, D.C. Han, and J.K. Chang, Microfabricated fluorescence-activated cell sorter through hydrodynamic flow manipulation. Microsystem Technologies-Micro-and Nanosystems-Information Storage and Processing Systems 12 (2006) 746-753.

[73]M.A. McClain, C.T. Culbertson, S.C. Jacobson, N.L. Allbritton, C.E. Sims, and J.M. Ramsey, Microfluidic Devices for the High-Throughput Chemical Analysis of Cells, 2003, pp. 5646-5655.

[74]C.-H. Wang, and G.-B. Lee, Automatic bio-sampling chips integrated with micro-pumps and micro-valves for disease detection. Biosensors and Bioelectronics 21 (2005) 419-425.

[75]K.S. Cole, and R.H. Cole, Dispersion and absorption in dielectric I. alternating current characteristics. J. Chem. Phys. 9 (1941) 341.

[76]H. Fricke, A mathematical Tratment of the Electric conductivity and capacity of disperse system I. the electric conductivity of a suspesion of homogenoeus spheroids. J. Gen. Physiol. 9 (1925) 137.

[77]H. Pauly, and H.P. Schwan, Impedance of a suspension of ball-shaped particles with a shell; a model for the dielectric behavior of cell suspensions and protein solutions. Z. Naturforsch 14 (1959) 125-131.

[78]T.B. Jones, (Ed.), Electromechanics of Particles, Cambridge University Press, Cambridge, 1995.

[79]H. Morgan, and N.G. Green, AC Electrokinetics: colloids and nanoparticles, Research Studies Press, Ltd, Baldock, Hertfordshire, England, 2003.

[80]W.H. Coulter, High speed automatic blood cell counter and cell analyser. Proc. Natl. Electron. Conf. 12 (1956) 1034-1040.

[81]S. Gawad, K. Cheung, U. Seger, A. Bertsch, and P. Renaud, Dielectric spectroscopy in a micromachined flow cytometer: theoretical and practical considerations. Lab on a Chip 4 (2004) 241-251.

[82]R. Rodriguez-Trujillo, C.A. Mills, J. Samitier, and G. Gomila, Low cost micro-Coulter counter with hydrodynamic focusing. Microfluidics and Nanofluidics 3 (2007) 171-176.

[83]T. Sun, S. Gawad, C. Bernabini, N.G. Green, and H. Morgan, Broadband single cell impedance spectroscopy using maximum length sequences: theoretical analysis and practical considerations, 2007, pp. 2859.

[84]E. Verpoorte, A. Manz, H. Ludi, A.E. Bruno, F. Maystre, B. Krattiger, H.M. Widmer, B.H. Vanderschoot, and N.F. Derooij, A Silicon Flow Cell for Optical-Detection in Miniaturized Total Chemical-Analysis Systems. Sensors and Actuators B-Chemical 6 (1992) 66-70.

[85]P. Nussbaum, R. Volke, H.P. Herzig, M. Eisner, and S. Haselbeck, Design, fabrication and testing of microlens arrays for sensors and microsystems. Pure and Applied Optics 6 (1997) 617-636.

[86]K.S. Hong, J. Wang, A. Sharonov, D. Chandra, J. Aizenberg, and S. Yang, Tunable microfluidic optical devices with an integrated microlens array. Journal of Micromechanics and Microengineering 16 (2006) 1660-1666.

[87]J.C. Roulet, R. Volkel, H.P. Herzig, E. Verpoorte, N.F. de Rooij, and R. Dandliker, Performance of an Integrated Microoptical System for Fluorescence Detection in Microfluidic Systems. Anal. Chem. 74 (2002) 3400-3407.

[88]Z.H. Liang, N. Chiem, G. Ocvirk, T. Tang, K. Fluri, and D.J. Harrison, Microfabrication of a planar absorbance and fluorescence cell for integrated capillary electrophoresis devices. Analytical Chemistry 68 (1996) 1040-1046.

[89]M.L. Chabinyc, D.T. Chiu, J.C. McDonald, A.D. Stroock, J.F. Christian, A.M. Karger, and G.M. Whitesides, An integrated fluorescence detection system in poly(dimethylsiloxane) for microfluidic applications. Analytical Chemistry 73 (2001) 4491-4498.

[90]K.B. Mogensen, N.J. Petersen, J. Hubner, and J.P. Kutter, Monolithic integration of optical waveguides for absorbance detection in microfabricated electrophoresis devices. Electrophoresis 22 (2001) 3930-3938.

[91]E. Hecht, Optics, Addison Wesley Longman, Inc., 1998.

[92]B. Bilenberg, T. Nielsen, B. Clausen, and A. Kristensen, PMMA to SU-8 bonding for polymer based lab-on-a-chip systems with integrated optics. Journal of Micromechanics and Microengineering 14 (2004) 814-818.

[93]G.B. Lee, C.H. Lin, and G.L. Chang, Micro flow cytometers with buried SU-8/SOG optical waveguides. Sensors and Actuators a-Physical 103 (2003) 165-170.

[94]J.M. Ruano-Lopez, M. Aguirregabiria, M. Tijero, M.T. Arroyo, J. Elizalde, J. Berganzo, I. Aranburu, F.J. Blanco, and K. Mayora, A new SU-8 process to integrate buried waveguides and sealed microchannels for a Lab-on-a-Chip. Sensors and Actuators B: Chemical 114 (2006) 542-551.

[95]M. Fleger, and A. Neyer, PDMS microfluidic chip with integrated waveguides for optical detection. Microelectronic Engineering 83 (2006) 1291-1293.

[96]D. Snakenborg, G. Perozziello, H. Klank, O. Geschke, and J.P. Kutter, Direct milling and casting of polymer-based optical waveguides for improved transparency in the visible range. Journal of Micromechanics and Microengineering 16 (2006) 375-381.

[97]C. Bliss, J. McMullin, and B. CJ, Rapid fabrication of a microfluidic device with integrated opitcal waveguides for DNA fragment analysis. Lab on a Chip 7 (2007) 1280-1287.

[98]R. Mazurczyk, J. Vieillard, A. Bouchard, B. Hannes, and S. Krawczyk, A novel concept of the integrated fluorescence detection system and its application in a lab-on-a-chip microdevice. Sensors and Actuators B: Chemical 118 (2006) 11-19.

[99]S.M. Eaton, H.B. Zhang, and P.R. Herman, Heat accumulation effects in femtosecond laser-written waveguides with variable repetition rate. Optics Express 13 (2005) 4708-4716.

[100]M. Kim, D.J. Hwang, H. Jeon, K. Hiromatsu, and C.P. Grigoropoulos, Single cell detection using a glass-based optofluidic device fabricated by femtosecond laser pulses. Lab on a Chip 9 (2009) 311-318.

[101]S. Camou, H. Fujita, and T. Fujii, PDMS 2D optical lens integrated with microfluidic channels: principle and characterization. Lab on a Chip 3 (2003) 40-45.

[102]J. Seo, and L.P. Lee, Disposable integrated microfluidics with self-aligned planar microlenses. Sensors and Actuators B-Chemical 99 (2004) 615-622.

[103]V.R. Horowitz, D.D. Awschalom, and S. Pennathur, Optofluidics: field or technique? Lab on a Chip 8 (2008) 1856-1863.

[104]J. Godin, V. Lien, and Y.H. Lo, Demonstration of two-dimensional fluidic lens for integration into microfluidic flow cytometers. Applied Physics Letters 89 (2006).

[105]X. Mao, J.R. Waldeisen, B.K. Juluri, and T.J. Huang, Hydrodynamically tunable optofluidic cylindrical microlens. Lab on a Chip 7 (2007) 1303-1308.

[106]M. Rosenauer, and M.J. Vellekoop, 3D fluidic lens shaping—A multiconvex hydrodynamically adjustable optofluidic microlens. Lab on a Chip 9 (2009) 1040-1042.

[107]C. Song, N.T. Nguyen, S.H. Tan, and A.K. Asundi, Modelling and optimization of micro optofluidic lenses. Lab on a Chip 9 (2009) 1178-1184.

[108]S.K.Y. Tang, C.A. Stan, and G.M. Whitesides, Dynamically reconfigurable liquid-core liquid-cladding lens in a microfluidic channel. Lab on a Chip 8 (2008) 395-401.

[109]J.M. Lim, S.H. Kim, J.H. Choi, and S.M. Yang, Fluorescent liquid-core/air-cladding waveguides towards integrated optofluidic light sources. Lab on a Chip 8 (2008) 1580-1585.

[110]X.L. Mao, S.C.S. Lin, M.I. Lapsley, J.J. Shi, B.K. Juluri, and T.J. Huang, Tunable Liquid Gradient Refractive Index (L-GRIN) lens with two degrees of freedom. Lab on a Chip 9 (2009) 2050-2058.

[111]L. Dong, A.K. Agarwal, D.J. Beebe, and H.R. Jiang, Adaptive liquid microlenses activated by stimuli-responsive hydrogels. Nature 442 (2006) 551-554.

[112]B. Berge, and J. Peseux, Variable focal lens controlled by an external voltage: An applicaiton of electrowetting. The European Physical journal E 3 (2000) 159-163.

[113]D. Yin, E.J. Lunt, M.I. Rudenko, D.W. Deamer, A.R. Hawkins, and H. Schmidt, Planar optofluidic chip for single particle detection, manipulation, and analysis. Lab on a Chip 7 (2007) 1171.

[114]D. Yin, D.W. Deamer, H. Schmidt, J.P. Barber, and A.R. Hawkins, Single-molecule detection sensitivity using planar integrated optics on a chip Optics Letters 31 (2006) 2136-2138.

[115]J.B. Edel, N.P. Beard, O. Hofmann, J.C. DeMello, D.D.C. Bradley, and A.J. deMello, Thin-film polymer light emitting diodes as integrated excitation sources for microscale capillary electrophoresis. Lab on a Chip 4 (2004) 136-140.

[116]P. de la Fuente, J.A. Etxeberria, J. Berganzo, J.M. Ruano-Lopez, M.T. Arroyo, E. Castano, and F.J. Gracia, End-fire coupling of a SU-8 waveguide to a silicon mesa photodiode: Integrability in an optical analysis microsystem. Sensors and Actuators a-Physical 123-24 (2005) 313-318.

[117]M. Dandin, P. Abshire, and E. Smela, Optical filtering technologies for integrated fluorescence sensor. Lab on a Chip 7 (2007) 955-977.

Chapter 3

Design & considerations

3.1 Introduction

Two designs of microfluidic chip are presented in this chapter. The first (chip A) is a simple device with a single microfluidic channel cast in PDMS, with integrated electrodes for impedance spectroscopy (IS) and is used in conjunction with free space optics (confocal microscope) for laser induced fluorescence (LIF). The second (chip B) is a complex microfluidic device fabricated from glass and SU-8. Chip B features integrated optics (fibre optics, waveguides and lenses), integrated electrodes and hydrodynamic focussing. Chip A was designed and fabricated by others [1] for bio-medical applications and was used to test the efficiency of a microfluidic device for the detection and characterisation of marine micro-organisms (section 6.2). Chip B was designed as first step toward the creation of a low cost, totally integrated and robust sensor for *in-situ* marine applications.

Chip B is the first to incorporate integrated electrodes for IS and integrated micro-optical elements for LIF and light scattering. Chip B was designed, fabricated and tested in this work (fabrication was performed by CMI-EPFL (Lausanne, CH) and IKERLAN Technology research centre (Bilbao, ES)). Most of this chapter is devoted to discussion of the design of this device.

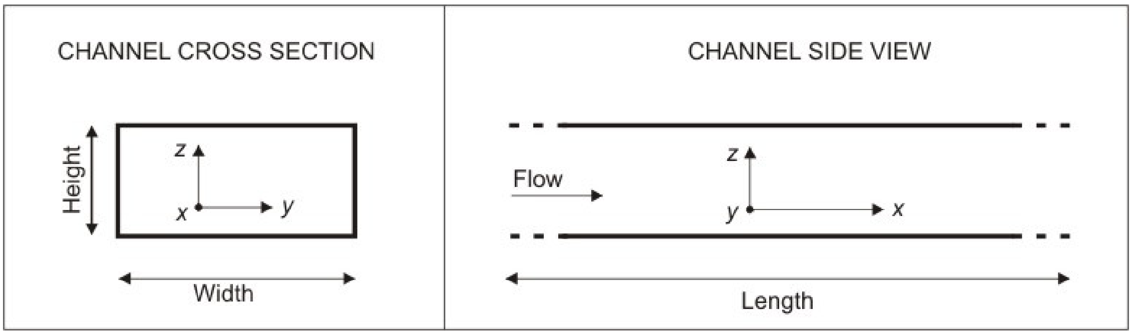

Figure 3-1 – Coordinates used in this thesis to define microfluidic channels.

3.2 Coordinates

In this thesis, reference will be made to specific features of the microfluidic device. For practical reasons, the coordinates used in this work to define the channels are (see Figure 3-1): length = x, width = y, height = z.

3.3 Chip A (PDMS chip)

As already mentioned in section 3.1, chip A was developed by others and was mainly used in this work to evaluate the potential of a microfluidic device in characterising mixtures of algae. Since the device was not developed in this work, only a simplified explanation of design and fabrication is presented.

Chip A is formed from a channel made in PDMS (polydimethylsiloxane) (Sylgard 184, VWR) sealed at the bottom to a glass substrate (Figure 3-2). Planar microelectrodes were patterned on the surface of the glass substrate to measure the electrical properties of particles. Optical detection and analysis was performed using light collected at the bottom of the chip using a microscope objective.

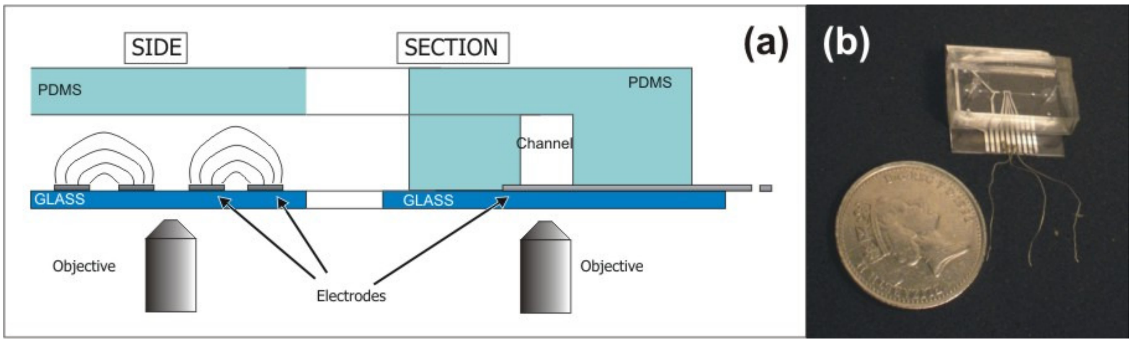

Figure 3-2 – (a) Schematic layout of the PDMS micro-fluidic chip together with electrodes for IS and an objective for fluorescence detection. (b) Picture of PDMS chip sealed to the glass substrate. Wires were soldered to electrodes for electric connections.

The general design of Chip A included a range of channels and electrodes of different dimension. The size of the channels ranged from 20x20 μm (width x height) to 10x5 μm. The size of the electrodes ranged from 20x20 μm (width x gap) to 10x10 μm. (width x gap) to 10x10 μm. Channel and electrode dimensions were chosen before each experiment on the basis of the dimensions of the organisms analysed. In particular, channel and electrodes sizes were chosen to be similar to the size of the organisms analysed because the sensitivity of the impedance detection system was directly related to the volume fraction of the particle in the detection region [1; 2; 3]. Furthermore, the use of a channel with dimension similar to the particle analysed circumvented the need of a particle focussing system. For example, for the experiments in section 6.2 a channel 10 μm wide and 20 μm high was used for particles with diameters up to 7 μm. The channel high was chosen bigger than the width because glass and PDMS were clamped together causing a reduction in the channel height.

3.3.1 Calculation of impedance output of chip A

The amplitude of the impedance spectroscopy signal generated in a microfluidic device can be estimated using an equivalent circuit model that considers the electrical properties of electrodes, suspending medium and particles in the detection region [2]. The equivalent model for chip A can be represented as in Figure 3-3, where R_m and C_m are the resistance and capacitance of the medium respectively, C_{smem} is the specific capacitance (capacitance per unit area) of the cell membrane, R_{cyt} the resistance of the cell cytoplasm and C_{DL} the capacitance of the electrical double layer (DL)[3]. The values of the individual electrical components are determined by the dielectric properties of the suspending medium, the geometry of the chip (width and height of the channel and the width of the electrode) and the dielectric properties of an individual cell. For further details see ref [2]. The values for the electrical properties of algae cells and medium were taken from the literature [4; 5]: $\varepsilon_m = 72\ \varepsilon_o$; $\sigma_m = 6.2$ S m^{-1}; $\varepsilon_i = 60\ \varepsilon_o$; $\sigma_i = 2$ S m^{-1}; $C_{smem} = 8$ mF m^{-2}. ε_m and σ_m are the permittivity and conductivity of the medium, and ε_i and σ_i are the permittivity and conductivity of the cell cytoplasm.

---

[3] The electrical double layer is a capacitance generated by charges accumulating at the interface between the electrodes and the suspending medium [REF Hywel's book]

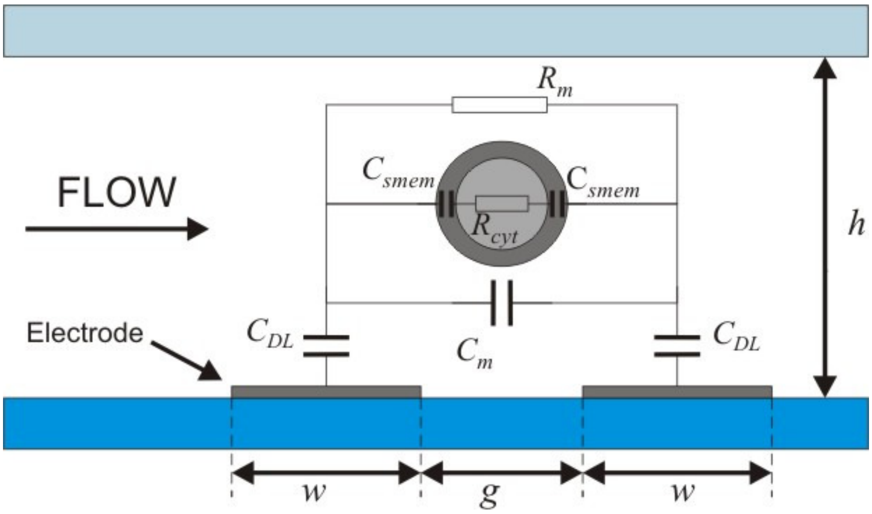

Figure 3-3 – Equivalent circuit model for chip A.

The impedance signal measured by the bridge depends on the differential voltage between the two ports (see Figure 3-3). From the equivalent circuit model, this differential voltage, V_{diff}, is given by:

$$V_{diff} = \left(\frac{\tilde{Z}_{mix}}{\tilde{Z}_{mix} + R_b} - \frac{\tilde{Z}_{med}}{\tilde{Z}_{med} + R_b} \right) V \qquad \textbf{3.1}$$

where $\tilde{Z}_{mix}$ and $\tilde{Z}_{med}$ are the complex impedance of the mixture containing the cell and the pure medium and are given by , respectively, R_b is the balance resistor (10kΩ) and V is the applied voltage. For further details on the calculations of the complex impedance, see ref [2].

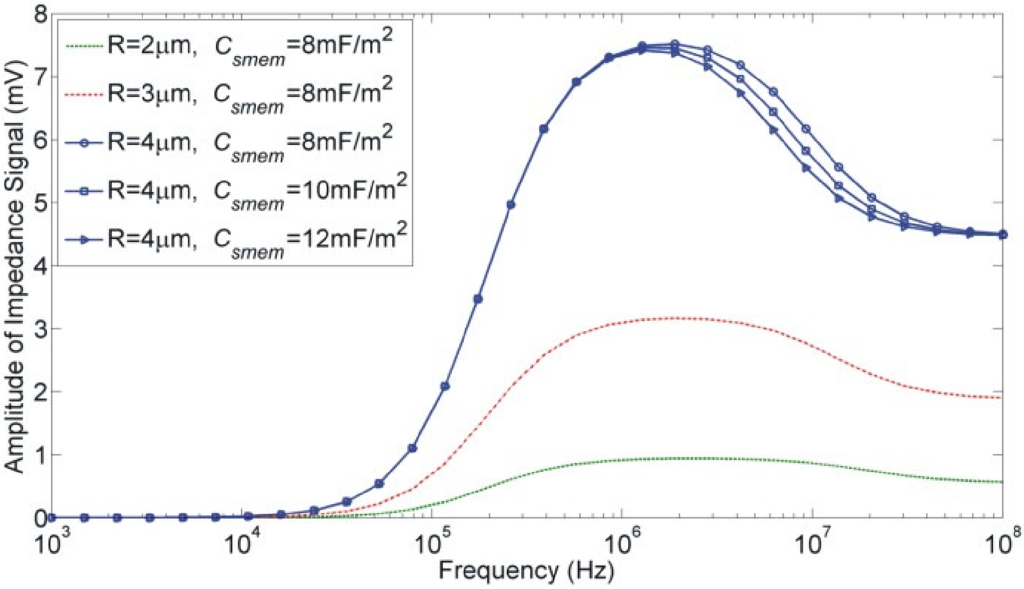

Figure 3-4 – Amplitude of the impedance signal obtained with calculations based on the equivalent circuit showed in Figure 3-1. In the legends, R indicates the radius of the particle and C_{smem} the specific membrane capacitance.

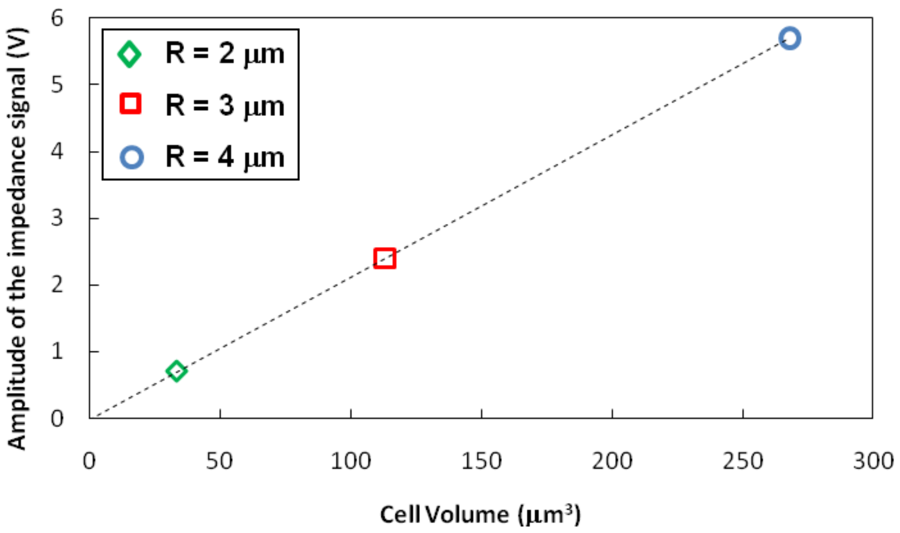

Figure 3-5 - Amplitude of the signal at a frequency of 327 kHz plotted against particles volume. In the legends, R indicates the radius of the particle.

Calculations of the impedance signal were performed in MatLab^{TM} (Mathworks, Inc. USA) and the results, at different frequencies, are shown in Figure 3-4 [6]. Note that calculations with different values of C_{smem} were also carried out for 4 µm radius particles. Since different signal amplitudes are obtained in the frequency range 10^6-10^8 Hz, the calculations show that an accurate choice of the frequency of the input signal is critical in collecting data proportional to the electrical properties of the particles analysed.

The amplitude calculated at a frequency of 327 kHz (used for the experiments presented in section 6) for three different sizes of particle with identical electrical properties were also plotted in Figure 3-5. Since the limit of detection is 2 times the standard deviation of the signal fluctuation (noise) [7] the calculations indicate that a spherical particle with a radius of 2 µm can be detected if the standard deviation of the noise is ≤ 0.35 V.

3.4 Chip B (SU-8 chip)

As it will be showed in chapter 6, Chip A was demonstrated to be extremely efficient in characterising a mixture of Algae but suffered two major drawbacks which limit its use in the study of micro-algae: (1) the size of the channel restricts the size range of particles that could be analysed (size range of micro-algae = 0.2÷200 µm) and increased the risk of debris and particles blocking the channel; (2) the optical system for LIF was made using free space optics that are bulky, sensitive to shocks and therefore not suitable for *in-situ* analysis. Therefore, a new device (chip B) was designed and fabricated in this work to overcome the limitations presented by chip A.

Chip B was designed to create a microfluidic system capable of *in-situ* flow cytometric analysis and therefore implemented used optical elements (e.g. optical fibres and microlenses), micron-sized electrodes and a hydrodynamic focussing system for particles focussing. Free space optics requires air filled vessels; this is minimised by the use of optical fibres. Air filled chambers are only required at the distal ends of these fibres which house the laser source, and the detectors. Hydrodynamic focusing is used with a large sample channel (200 μm). The use of hydrodynamic focussing reduces the risk of channel blockage and allows analysis of a wider size range of particles. Different versions of chip B were manufactured to test different combinations of integrated optics, and microfluidic design. Various versions of chip B were manufactured in two stages (first and second generation devices). The first generation included two inlets for hydrodynamic focusing, self-alignment grooves (SAG) for optical fibres insertion (section 2.8.1) and planar waveguides. Preliminary tests were run on the first generation of chips and the results were used to develop a second generation which included a single inlet for hydrodynamic focussing, tapered waveguides and planar microlenses.

3.4.1 General structure

The structure of the microfluidic chip is shown in Figure 3-6. It consists of an SU-8 layer, sandwiched between two Pyrex glass slides. SU-8 is advantageous in this application because it has high transparency and can be used to fabricate devices with integrated optics [8; 9; 10]. Microfluidic structures were formed in SU-8 using lithographic techniques (see section 2.3.3) whilst electrodes were patterned on the surface of the two glass slides that formed the top and bottom of the channel using a lift off process. This particular configurations was chosen so that electrodes could be patterned on top and bottom and bottom of the channel as it has been calculated that this configurations has higher sensitivity compared to the configuration with coplanar electrodes [11].

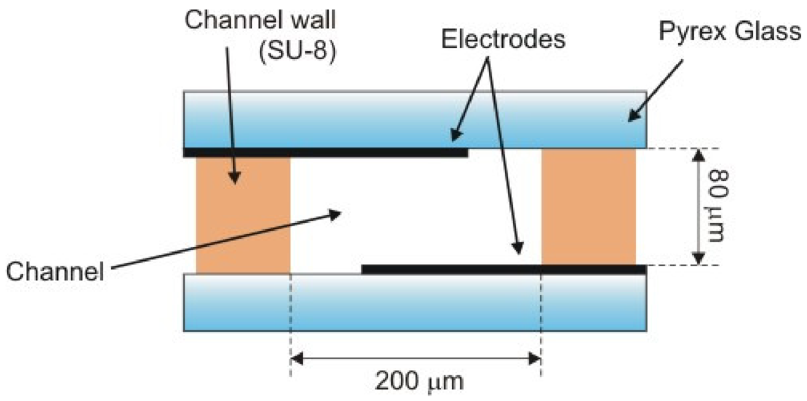

Figure 3-6 - Cross section of the structure of the microfluidic chip. SU-8, glass and electrodes are indicated along with channel sizes.

3.4.2 Channel layout and hydrodynamic focussing

As already discussed in section 2.4 and 2.4.3, a particle focussing system is an essential component in a microfabricated cytometer because it affects the precision, increase the size range of the particles analysed and reduces the risk of channel clogging. Since chip B was the first step in the development a micro-flow cytometer for the *in-situ* detection and characterisation of marine micro-algae, and because the project already involved the integration of a number of complex detection systems, it was decided implement a mono-dimensional system that was proven easy to implement and to control (see section 2.4.2). Furthermore, it was not advisable to adopt complicate structures also because chip B was fabricated by others in a different country (IKERLAN Technology research centre - Bilbao, ES) and relatively simple 2D focusing solution have been proposed only when chips were already fabricated and in the testing stage [12; 13; 14; 15; 16].

The schematic layout of the first generation microfluidic device is shown in Figure 3-7(a). A middle channel (sample channel) is merged with two side channels. Sample is injected at the left of the sample channel while sheath fluid is injected in the two channels placed at the sides of the sample channel. As the sample flows into the junction, sheath fluid coming from the side channels focuses the sample stream into the middle of the detection channel (hydrodynamic focussing). Particles present in the sample fluid are focused in single file and are analysed one by one when they pass through the detection area.

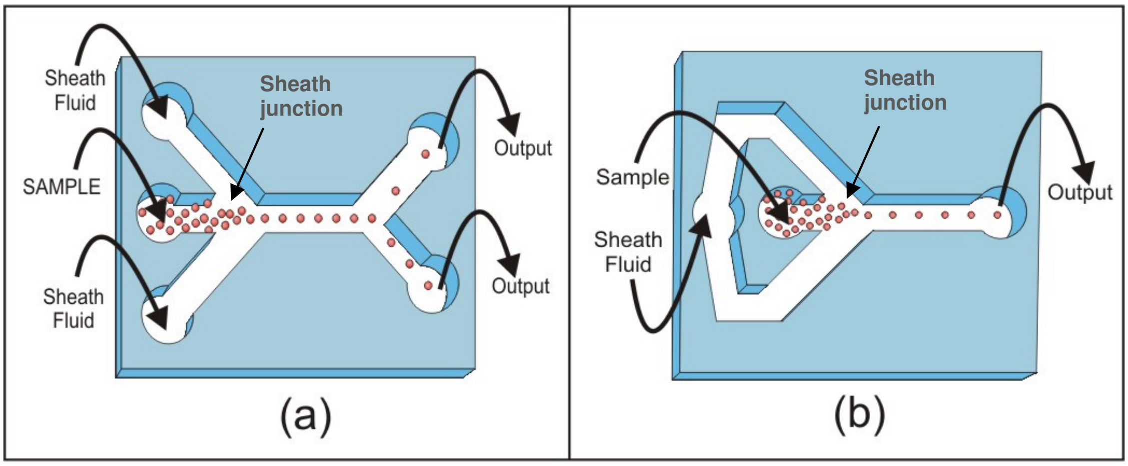

Figure 3-7 - Schematic layout of the microfluidic channels. The flow direction is from left to right and the sample consists of particles in a suspending medium. (a) First generation of chips. The sample is injected in the middle channel on the left hand side, the sheath flow from the side channels on the left hand side and the waste flows out through the two channels on the right hand side. (b) Second generation of chips. The sheath fluid is fed to the first reservoir on the left for both the sheath channels. The sample is fed into the reservoir surrounded by the sheath channels. Only one output channel is present.

In the first generation of devices it was decided to implement a standard solution with two inputs for the sheath flow; the input reservoirs where placed close to the sample input and in a straight line so that a single custom made gasket with three holes was used for all input fluidic connections. Since it was demonstrated that the relative orientation of sheath and sample channels was not affecting hydrodynamic focussing [17] it was decided to connect the inlet reservoirs and the sheath junction with straight channels. The first generation of devices also featured two output channels that were inserted in the optics of perform sorting experiments. However, preliminary tests showed that two outputs made the hydrodynamic system more difficult to control.

In the second generation of devices it was decided to reduce the complexity of the system by implementing a single output and a common inlet for the sheath flow (Figure 3-7(b)). The reduction of fluidic connection made the system easier to assemble and reduced the risk of leakages while the implementation of a single input for hydrodynamic focussing and a single output simplified the control of the hydrodynamic control.

Channel width and depth was the same for both generations. The width of the microfluidic channels was 200 µm. This width was chosen in order to accommodate a wide size range of phytoplankton organisms and reduce the risk of channel blockage. The height of the channel was chosen to be 80µm for three reasons: the chip had to accommodate a 65±2 µm optical fibre (FVP050055065, Polymicro Technologies, AZ, USA); the process was optimised for thicknesses in multiples of 20 or 35µm because the fabrication was performed by IKERLAN Technology research centre (Spain) that previously developed the process for different applications; the tolerance of the fabrication process was ± 5 µm.

3.4.3 Integrated optical system

The general solution adopted for the integration of optical components was the use of self-alignment grooves (SAGs) for the insertion of optical fibres. Various optical elements including microlenses, planar and tapered waveguides were also coupled with SAGs in different combinations. The different designs are presented in this section.

3.4.3.1 SAGs orientation

The general structure of the positioning and orientation of the SAGs around the microfluidic channel is presented in Figure 3-8. The integrated optical system was designed to detect fluorescence and scattered light. Fluorescence in conventional flow cytometers is normally detected at 90° to the axis of the excitation light, to minimise coupling from the excitation source. Adopting this principle, SAGs input for light and detection were positioned at 45° to the channel in the detection region and 90° to each other (see Figure 3-8). Scattered light detection was performed using a SAG

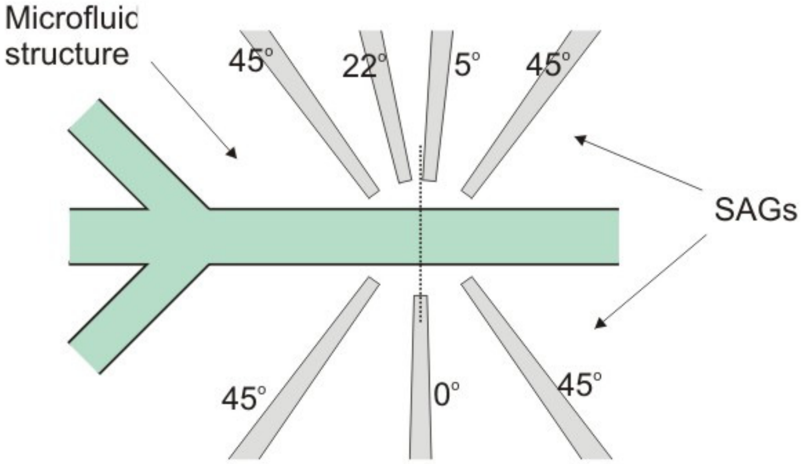

Figure 3-8 – General layout for SAGs positioning and orientation in chip B. The angle indicated on each SAG is referred to the dashed line normal to the sample channel. Four SAGs are arranged at 45° for excitation/collection of fluorescence; one SAG is perpendicular to the sample channel (0°) and two are positioned at angles able to detect scatter light (5°, 22°).

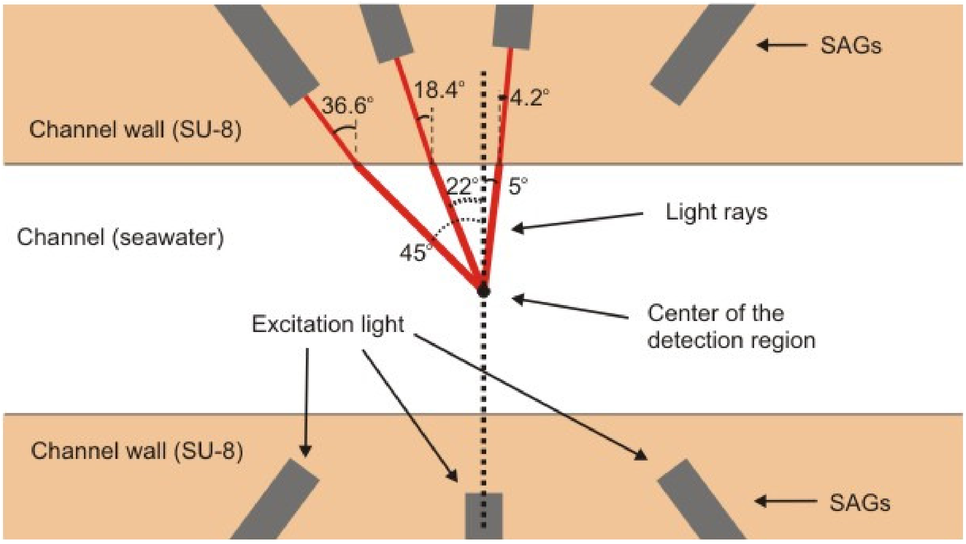

Figure 3-9 – Schematic depicting rays propagating from the centre of a microfluidic channel filled with seawater to SAGs in the SU-8 structure. The angles were calculated using Snell's law and are referred to the normal to the channel wall (dashed line).

perpendicular to the channel (normal SAG) to launch light and two SAGs on the other side of the channel to collect light at angles of 5° and 22° normal to the channel axis.

As explained in section 1.3.2, light collected at angles between 0.5° and 5° (forward scatter light or FSC) to the incident beam is proportional to cell size and scatter light collected at angles between 15° and 150° (side scatter light or SSC) is proportional to the intrinsic properties of the particles (e.g. surface roughness, and internal granularity) [18; 19]. 5° was chosen as the FSC collection angle to minimize the amount of excitation light (coming from the normal SAG). Since the design of a SAG with an orientation angle higher than 45° would have been difficult for the limited space available between the 45° oriented SAG and the channel wall, a 22° oriented SAG was arbitrary chosen for SSC collection.

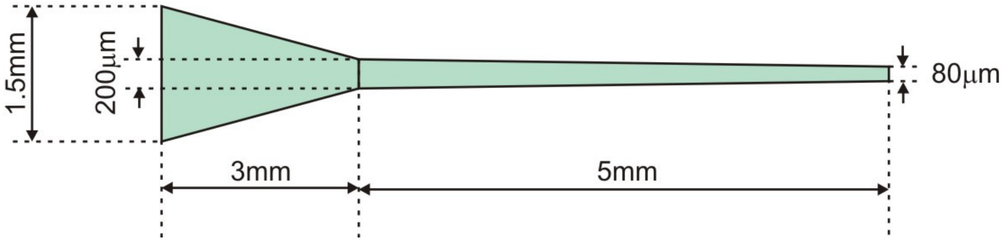

Figure 3-10 - Design of tapered SAGs for the insertion of optical fibres. Dimensions are given for a normal SAG ending 200µm from the microfluidic channel edge.

Light launched from the optical fibres passes through a series of materials with different refractive indices (glass, SU-8 and seawater). Since the direction of the beam is modified at each interface, Snell's Law[4] [20] was used to calculate the refraction angles and the correct orientation of SAGs for detection of fluorescence and scattered light. Calculations were performed using a refractive index of 1.59 for SU-8 [8] and 1.34 for seawater at 5° C with a salinity of 35[5] [21]. The angles were calculated with reference to the normal to the channel wall (dashed line in Figure 3-9). Results from calculations are presented in Figure 3-9 and show that that SAGs placed at 36.6°, 18.4° and 4.2° collect rays coming from the centre of the detection region with angles of 45°, 22° and 5° respectively.

3.4.3.2 SAGs structure

A schematic layout of a typical SAG is shown in Figure 3-10. The grooves start with a width of 1.5 mm in order to facilitate the insertion of the optical fibre. This is then tapered to 200 μm after which a gentler taper is employed to allow for precise positioning of the fibres. The width at the end of the grooves is 80 μm in order to accommodate the 65±2 μm outer diameter optical fibre. The large width of the taper (compared to the optical fibre) was chosen because in [22] it is shown that tight SAGs were scratched by fibres, creating debris that remained trapped between the tip of the fibre and the SAG end. This debris increased light scattering at the fibre/wall interface.

3.4.3.3 Planar waveguides

As discussed in section 2.8.2, polymer waveguides have been monolithically integrated into microfluidic chips for light delivery/collection inside the channel [9; 22; 23; 24; 25; 26]. The waveguides are based on the principle of total internal reflection [20] and use a high refractive index polymer as core material and glass and air as cladding. Despite the high losses reported for these waveguides (>1 dB/cm), it was decided to test planar waveguides due to their simple fabrication and the flexibility offered by their structure. Two designs were investigated based on the design of

---

[4] **Snell's law**: $n_1 \sin \theta_1 = n_2 \sin \theta_2$

n_1, n_2 = refractive index of the two mediums.

θ_1, θ_2 = incident and refracted angle.

[5] The amount of salt dissolved in a given volume of seawater is different from one part of the ocean to another. The term salinity is conventionally used to indicate the amount of salt dissolved in seawater. **Salinity is defined as the amount of salt (in grams) dissolved in 1000g of seawater.** Salinity is expressed in part per thousand (i.e. seawater with salinity of 25 contains 25g of salt in 1000g of water) [8].

Mogesten *et al.* design [9]: (1) Long, bent waveguides to test if it was possible to insert optical fibres from different positions on the chip whilst maintaining an acceptable sensitivity; (2) straight and short waveguides with reduced losses compared to bent waveguides.

Figure 3-11(a) outlines the general structure of a planar straight waveguide formed from a 30 µm wide layer of SU-8 with two 25 µm wide air gaps at both sides of the waveguide. The air gaps terminate 30 µm away from the microfluidic channel (preventing leakage of the sheath fluid into the waveguide) and the length of the waveguides is 850 µm. The design of a bent waveguide is presented in Figure 3-11(b).

3.4.3.4 Integrated tapered waveguide and microlenses

The second generation of devices implemented a solution with a tapered waveguide coupled with a planar microlens (referred to as design WL), shown in Figure 3-12(a), or a compound microlens coupled with a SAG (referred to as design L), shown in Figure 3-12(b)). In both designs, no optical elements were inserted at the end of 45°, 22° and 5° SAGs (see Figure 3-1(a, b)). In design WL the tapered waveguide was chosen because the literature shows that, for light coming from optical fibres, it produces a higher degree of collimation [8; 27]. However, polymer waveguides generate high power losses (from 1 to 6 dB cm^{-1}) [9; 22; 23; 24; 25; 26] therefore a solution incorporating only a microlens was also designed.

Tapered waveguides and integrated microlenses were modelled with TracePro® ray tracing software (Lambda Research corp.) using the following conditions:

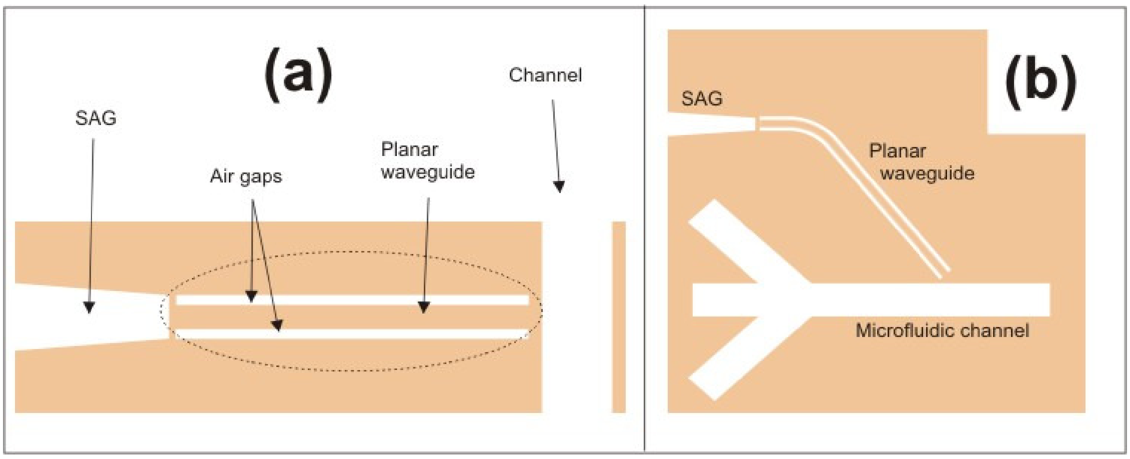

Figure 3-11 – Schematics diagrams of planar waveguides where orange represents SU-8 and white represents air. (a) Straight, 850 µm long waveguide. (b) Bent waveguide, 7 mm long, the structure of the waveguide is the same as in (a).

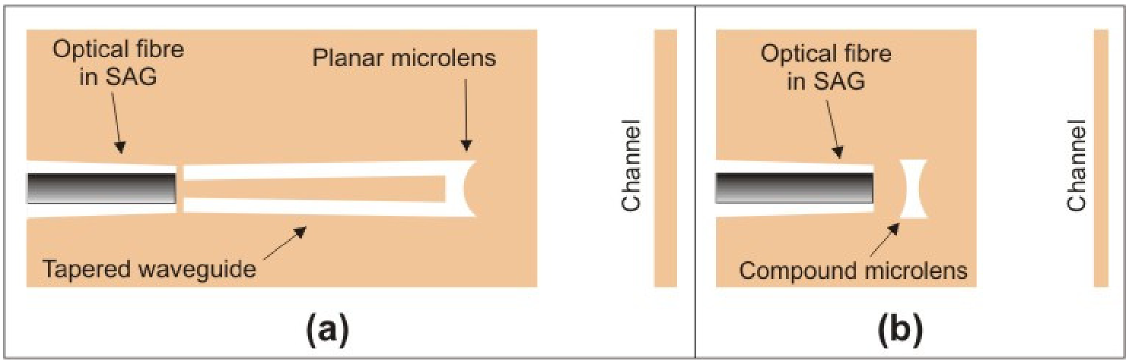

Figure 3-12 – Schematics depicting tapered planar waveguides and planar microlenses where orange represents SU-8 and white represents air. (a) Design WL: tapered waveguide coupled with a plano-convex microlens; (b) design L: planar compound microlenses

- The light source was a circular shaped grid pattern with a diameter of 25 μm and Gaussian spatial profile. The light source emitted rays with constant power, a Gaussian distribution on the grid and an angular distribution of 12.7° in air (n=1).
- The source wavelength was set at 546 nm to match the data for seawater [21].
- 30,000 rays where traced in each calculation.
- As for section 3.4.3.1, the refractive indexes were 1.59 for SU-8 [8] and 1.34 for seawater [21].
- Since the data on absorption of SU-8 were not available, the absolute emission power obtained from simulations was considered unreliable.
- The optical path of the various rays was assumed constant, therefore the relative intensity of the rays was considered reliable.

The quality of the focussing of the designs modelled with TracePro® was evaluated by extrapolating the incident radiance on *xz* planes at $y = 0, 30, 70, 100, 130, 170, 200$ μm (Figure 3-13(a)) with $y = 0$ being the channel wall on the lens side and $y = 100$ μm the middle of the channel. Figure 3-13(b) shows an example of irradiation plot along the *xz* plane. The intensity profiles along the dashed lines inserted in Figure 3-13(b) were extrapolated for comparison of the various optical profiles. The intensity profiles along *x* (Figure 3-15(a) and Figure 3-16(b)) were also fitted to Gaussian curves using Origin® software and the spot width was measured at the $1/e^2$ (0.135) point of the Gaussian curve[6].

---

[6] The $1/e^2$ point on a Gaussian curve is where the beam intensity is $1/e^2$ (or 0.135) times the value of the maximum intensity. As a convention, the radius of a Gaussian beam is given by the distance from the beam centre (where the intensity is at the maximum) to the $1/e^2$ point [5; 16].

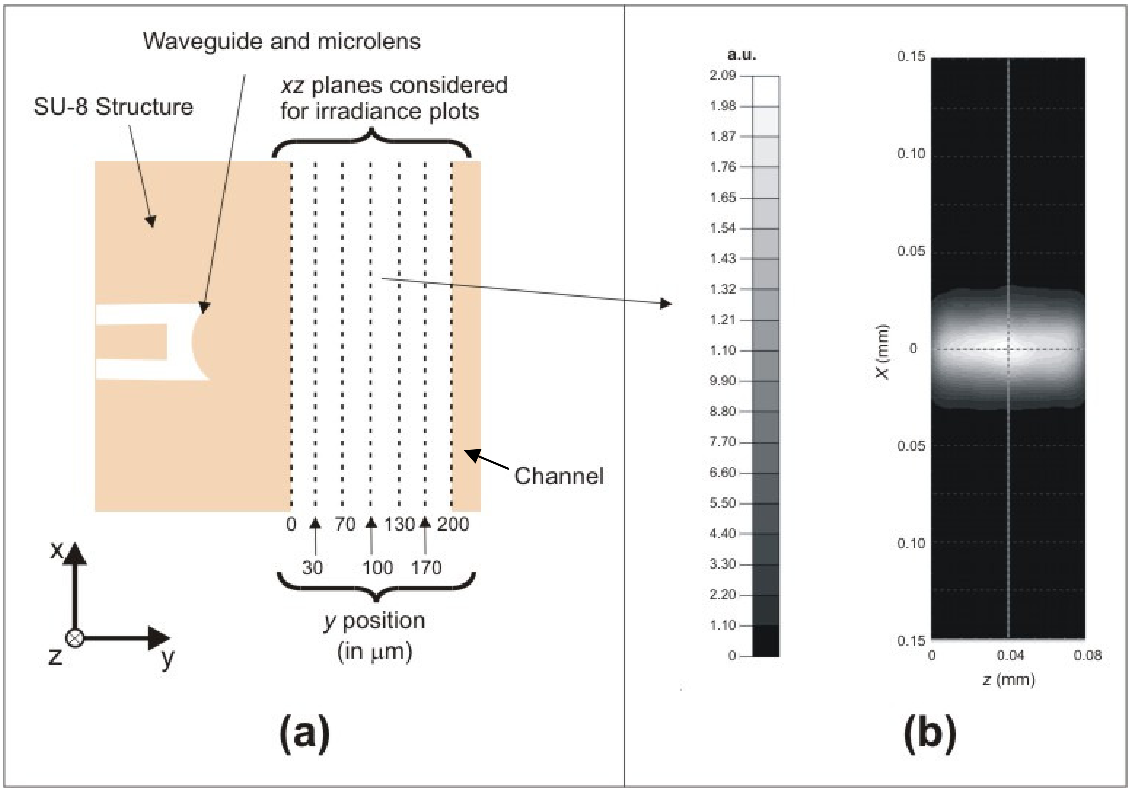

Figure 3-13 – (a) Schematic layout showing positions of xz planes considered for evaluating the focussing power. (b) Example of irradiance intensity plot of the xz plane at y = 100 µm. Intensity profiles from Figure 3-14 to Figure 3-16 are extrapolated from the two dashed line in (b).

Optimised designs for WL and L were obtained after modelling with TracePro®. These designs were then implemented in the second generation, chips B. The optimised design for WL consisted of a tapered waveguide 400 µm long, with an input aperture of 30 µm and an exit aperture of 44 µm; the tapered waveguide was coupled with a plano-convex planar microlens with a radius of 120 µm. The optimised version L consisted of a compound microlens formed by two plano-convex micro-lenses with diameters 83 and 102 µm.

When focussing the light inside a microfluidic channel, it is important to obtain a uniform intensity distribution along *y* and *z* axes in order to reduce the dependence of the signal on the position of the particle with respect to the excitation source. In order to evaluate this property for the optimised designs, the width of the beams generated by WL and L are presented in Figure 3-14 while the intensity profiles generated along *x* and *z* are presented in Figure 3-15 and Figure 3-16.

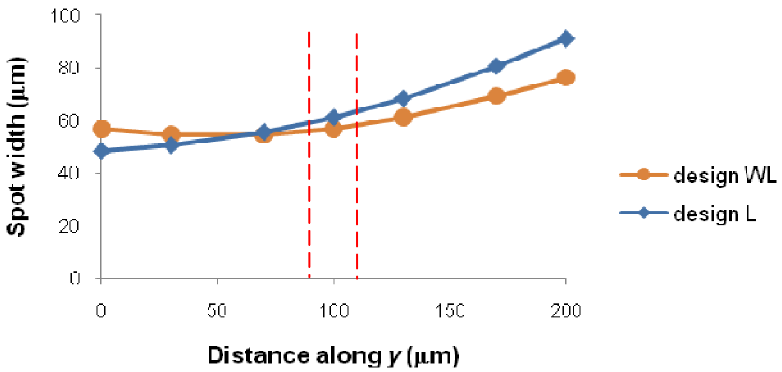

Figure 3-14 – Graph showing the spot size at the 1/e^2 point for design WL and L. The width of the spot is calculated by fitting the profiles along *z* obtained by TracePro® ray tracing and by calculating the distance between the two 1/e^2 point of the Gaussians. The vertical red dashed lines represent the limit of the central stream used for the experiments in chapter 6. Note that the intensity generated by design WL is approximatelly constant while the intensity generated by profile L has high variability.

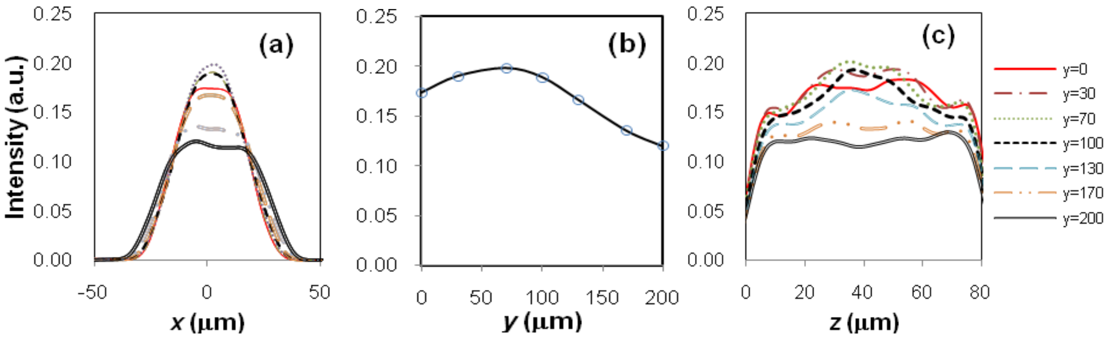

Figure 3-15 – Intensity profiles along *x* (a), *y* (b) and *z* (c) axes obtained from TracePro® modelling for the WL optimised design. The profiles along x and z were obtained from irradiation plot along *xz* planes for values of *x* = 0, *z* = 40 µm and *y* ranging from 0 to 200 µm with *y* = 0 being the channel wall on the microlens side (see Figure 3-13(a)). The profile along *y* was obtained extracting the intensity value for *x* = 0 from the various profiles at different *y* in graph (a).

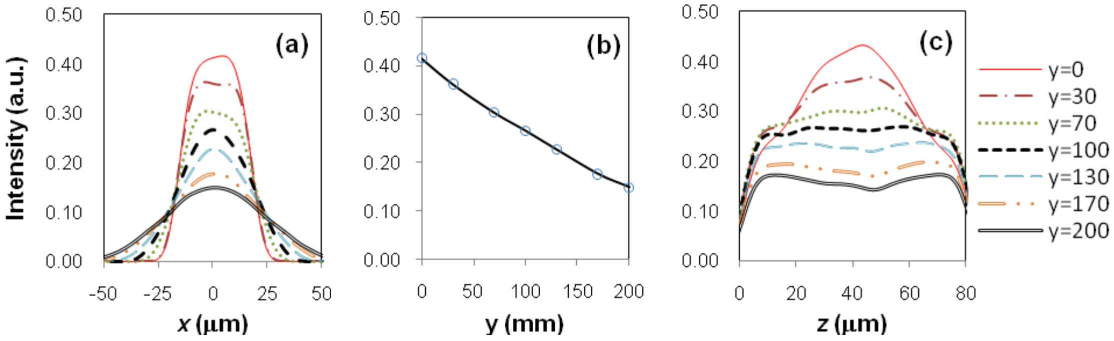

Figure 3-16 – Intensity profiles along *x* (a), *y* (b) and *z* (c) axes obtained from TracePro® modelling for the L optimised design. The profiles along x and z were obtained from irradiation plot along *xz* planes for values of *x* = 0, *z* = 40 µm and *y* ranging from 0 to 200 µm with *y* = 0 being the channel wall on the microlens side (see Figure 3-13(a)). The profile along *y* was obtained extracting the intensity value for *x* = 0 from the various profiles at different *y* in graph (a).

Figure 3-14 and Figure 3-15 (b) show that the intensity distribution generated by design WL has little variation between $0 < y < 130$ μm (CV = 7%) and start diverging for $y > 130$ μm. The variation for $y > 130$ μm is not critical because the microfluidic set up has been designed with a hydrodynamic focussing system (section 0) that is supposed to confine the particles between $y = 70$ and 130 μm. On the other hand, Figure 3-15(c) shows uneven profiles generated by WL along *z* for various value of *y*. However, the CV calculated for $y = 100$ μm is 16%, which is still acceptable.

Figure 3-14 and Figure 3-16(b) show that the intensity distribution generated by design L along *y* is strongly divergent. However, the CV of 14% for $70 < y < 130$ μm is still acceptable considering that particles will be focussed using hydrodynamic focussing (section 0). On the other hand, the high divergence of the profile implies a high level of incident light falling into the SAG for the collection of scatter light; the incident light will probably increase the noise level at the scatter light collection and reduce the sensitivity of the signals. On the other hand, Figure 3-16(b) shows even profiles generated by L along *z* especially for $70 < y < 130$ μm.

In conclusion design WL is preferable to design L because, despite a higher variability of the intensity along *z*, it generates a better profile along the *xy* plane with a reduced amount of incident light entering scatter light detection.

3.4.4 IS detection electrodes

Impedance detection was performed with facing electrodes because, as already mentioned in section 3.4.1, this configuration is more sensitive than the configuration with coplanar electrodes [11]. The details of the electrodes are shown in Figure 3-17 and consists of two pairs of electrodes patterned on the top and bottom of the glass substrate. The electrodes are 20 μm wide with a 40 μm gap from edge to edge. The electrodes do not overlap along the entire width of the channel but only for 40 μm to reduce the dimensions of the detection region. As the intensity of the impedance signal is proportional to the size of the detection region [2; 3], the small detection region size increases the sensitivity of the system without altering the dimensions of the microfluidic channel.

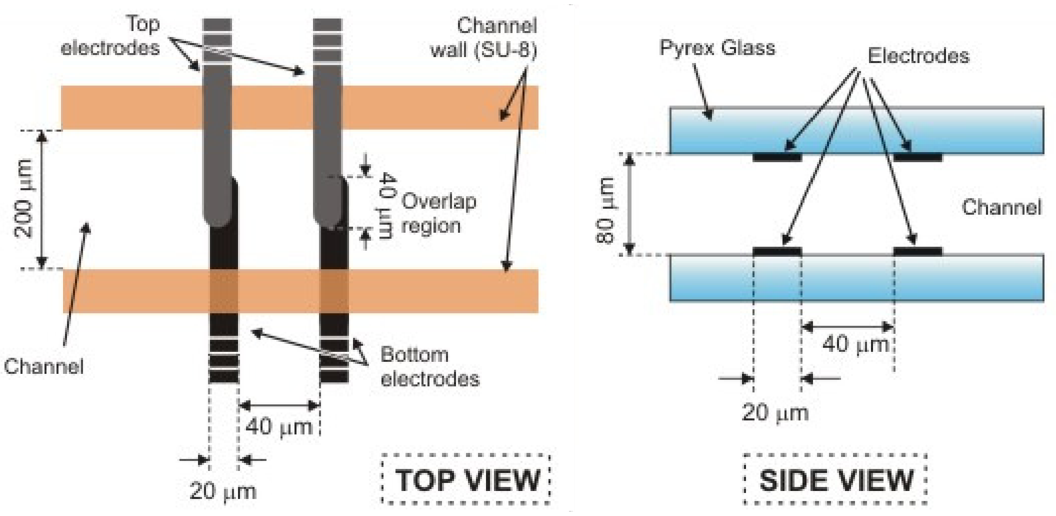

Figure 3-17 – Schematic layout of the electrodes used for impedance spectroscopy. SU-8, Pyrex glass and electrodes are indicated along with dimensions of channel and electrodes.

3.5 Chip B - Final designs

A picture of chip B is presented in Figure 3-18 and examples of the microfluidic structures are presented in Figure 3-19. Figure 3-19(a-c) shows designs from the first generation with two inlets for the sheath flow, two outlets, integrated self alignment SAGs for optical fibres (SAG) and planar waveguides. Figure 3-19(d) is a general design for the second generation with one inlet for the sheath flow, one outlet, a SAG coupled with optical elements and the other SAGs terminating close to the microfluidic channel.

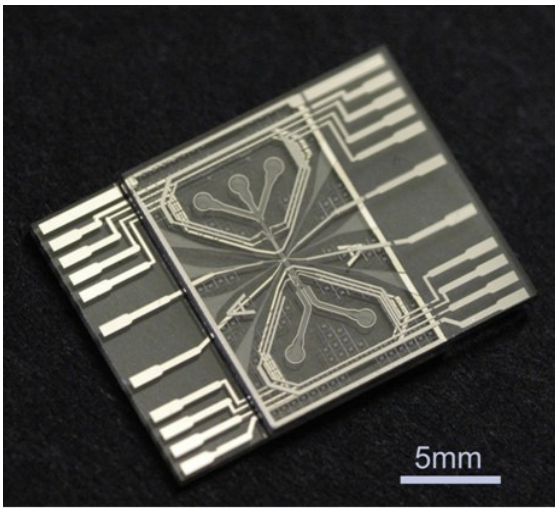

Figure 3-18 – Picture of a microfluidic chip type B.

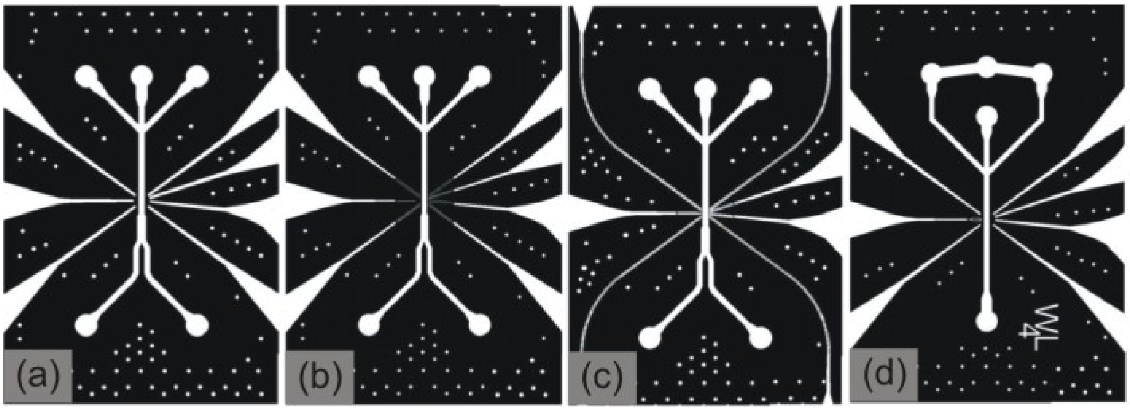

Figure 3-19 – Chip layouts (shown as the inverse of the photolithographic mask, black is SU-8 and white air). (a) chip with SAGs terminating adjacent to the main microfluidic channel; (b) chip with SAGs for butt-coupling of fibres with short, straight waveguides; (c) chip with bent waveguides; (d) chip with only the normal SAG coupled with integrated optical elements, one inlet for sheath flow and one outlet.

Microscope pictures of the detection regions are shown in Figure 3-20. The following names have been assigned to the different designs for future references:

- Design **G**: All SAGs terminate close to the channel (Figure 3-20(a)).
- Design **W**: All SAGs coupled with planar waveguides (Figure 3-20(b)).
- Design **L**: Normal SAG coupled with a compound microlens at the end. The rest of the SAGs terminating close to the channel (Figure 3-20(c)).
- Design **WL**: Normal SAG coupled with a tapered waveguide and planar microlens. The rest of the SAGs terminating close to the channel (Figure 3-20(d)).

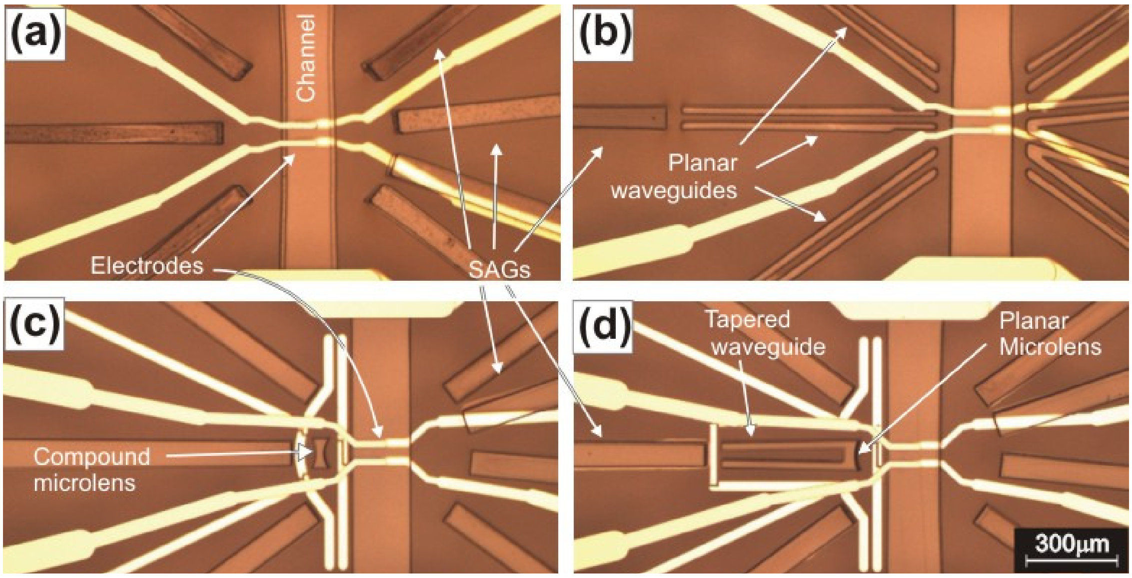

Figure 3-20 – Microscopic pictures of chip B measuring regions. The pictures show the four design of detection region fabricated for chip B: (a) Design G; (b) design W; (c) design L; (d) design WL. All the integrated detection elements are clearly indicated.

Design G and W (Figure 3-20(a, b) were implemented in the first generation of chip B while design L and WL (Figure 3-20(c, d)) were included in the second generation. Note that in Figure 3-20 (c) and (d) some metal structures have been inserted around the optical elements. This thin layer of metal is fabricated together with the electrodes. The metal structures were inserted to increase the bonding efficiency around the optical elements.

3.6 Fabrication

Fabrication of chip A was completed by Becky Neal in collaboration with Dr David Holmes (University of Southampton, UK). Chip B was fabricated in collaboration with CMI-EPFL (Lausanne, CH) and IKERLAN Technology research centre (Bilbao, ES). The fabrication was not performed by the author, therefore simplified description of the processes are reported. Details can be found in [1; 28; 29].

3.6.1 Chip A

A simplified fabrication process for the microfluidic structure is shown in Figure 3-21. A master was made with photolithography and dry etching of a silicon substrate. A microfluidic channel was made by casting PDMS on top of the master and pealing the cured PDMS off. The channel was sealed to a 500µm thick Pyrex substrate with micro-electrodes patterned on the surface of the substrate.

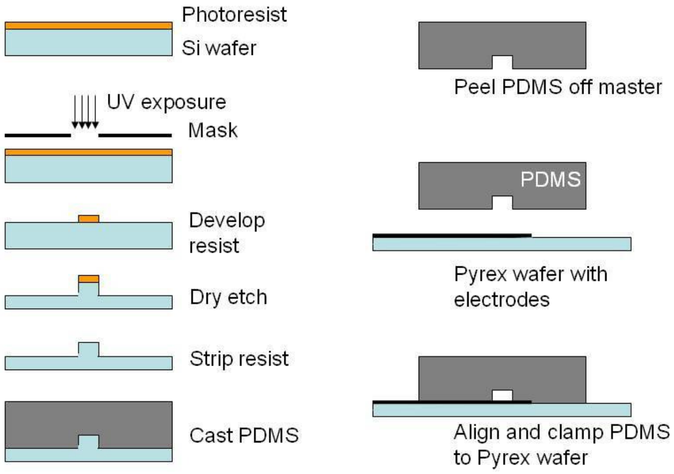

Figure 3-21 – Fabrication process of micro-channel and micro-electrodes. Copied from [1; 28].

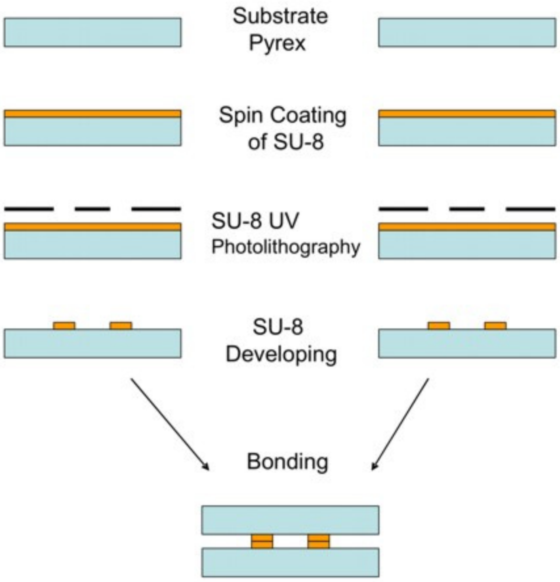

Figure 3-22 – Outline of the SU-8 fabrication process for forming the microfluidic structures and waveguides.

The microelectrodes were made of three successive metal layers: Ti - Au - Ti (30 nm – 100 nm – 30 nm), and patterned using standard photolithography and wet etching. The wafer was diced to release individual chips (dimensions = 2 cm x 2 cm).

3.6.2 Chip B

The microelectrodes were made of a thin metal bi-layer: Ti - Pt (20 nm - 200 nm) and patterned using standard photolithography and lift off. The SU-8 fabrication process is outlined in Figure 3-22. A spin coater was used to deposit an SU-8 layer onto the surface of two Pyrex wafers over the patterned electrodes. The coated wafers were soft baked, exposed to UV light through a photolithographic mask, baked again and developed. The two wafers were then thermally bonded to form sealed microfluidic structures. Finally, the wafer was diced to release the individual chips.

The total thickness of the SU-8 structure was always 80 μm. In the first generation, the structures were obtained by bonding two 40 μm thick layers while in the second generation the structures were obtained by bonding a 60 μm and a 20 μm layer.

3.7 Summary

In this chapter the design of two microchips (chip A and B) for the detection and characterisation of microscopic marine organisms have been presented. Chip A was designed and developed in previous work [1] but is discussed briefly (see section 3.3). Chip A has a simple microfluidic design and uses conventional optics for LIF. The design of chip B was completed during this work using ray tracing software and lessons learnt from previous results. Different designs of chip B were fabricated. The various designs differed in terms of microfluidics, impedance electrodes design and integrated optical elements.

REFERENCES

[1]D. Holmes, B. Neal, N. Green, and H. Morgan, Microfabricated Device for Rapid Impedance Measurements on Single Biological Cells, Proceedings of 15th MicroMechanics Europe Workshop, Leuven Belgium, 2004, pp. pp. 195-198.

[2]H. Morgan, T. Sun, D. Holmes, S. Gawad, and N.G. Green, Single cell dielectric spectroscopy. J. Phys. D: Appl. Phys. 40 (2007) 61-70.

[3]H. Morgan, and N.G. Green, AC Electrokinetics: colloids and nanoparticles, Research Studies Press, Ltd, Baldock, Hertfordshire, England, 2003.

[4]R. Somaraju, and J. Trumpf, Frequency, temperature and salinity variation of the permittivity of seawater. Ieee Transactions on Antennas and Propagation 54 (2006) 3441-3448.

[5]J. Wang, V.L. Sukhorukov, C.S. Djuzenova, U. Zimmermann, T. Muller, and G. Fuhr, Electrorotational spectra of protoplasts generated from the giant marine alga Valonia utricularis. Protoplasma 196 (1997) 123-134.

[6]G. Benazzi, D. Holmes, T. Sun, M.C. Mowlem, and H. Morgan, Discrimination and analysis of phytoplankton using a microfluidic cytometer. Iet Nanobiotechnology 1 (2007) 94-101.

[7]D.A. Skoog, and J.J. Leary, Principles of Instrumental Analysis Saunders Cllege Publishing, Orlando, 1992.

[8]Z. Wang, J. El-Ali, M. Engelund, T. Gotsaed, I.R. Perch-Nielsen, K.B. Mogensen, D. Snakenborg, J.P. Kutter, and A. Wolff, Measurements of scattered light on a microchip flow cytometer with integrated polymer based optical elements. Lab on a Chip 4 (2004) 372-377.

[9]K.B. Mogensen, J. El-Ali, A. Wolff, and J.P. Kutter, Integration of polymer waveguides for optical detection in microfabricated chemical analysis systems. Applied Optics 42 (2003) 4072-4079.

[10]A.R. Leeds, E.R. Van Keuren, M.E. Durst, T.W. Schneider, J.F. Currie, and M. Paranjape, Integration of microfluidic and microoptical elements using a single-mask photolithographic step. Sensors and Actuators A: Physical 115 (2004) 571-580.

[11]S. Gawad, K. Cheung, U. Seger, A. Bertsch, and P. Renaud, Dielectric spectroscopy in a micromachined flow cytometer: theoretical and practical considerations. Lab on a Chip 4 (2004) 241-251.

[12]X. Mao, J.R. Waldeisen, and T.J. Huang, "Mircrofluidic drifting" - implememnting three-dimensionla hydrodynamic focusing with a single-layer planar microfluidic device. Lab on a Chip 7 (2007) 1260-1262.

[13]D. Di Carlo, D. Irimia, R.G. Tompkins, and M. Toner, Continuous inertial focusing, ordering, and separation of particles in microchannels. Proceedings of the National Academy of Sciences of the United States of America 104 (2007) 18892-18897.

[14]C. Simonnet, and A. Groisman, High-throughput and high-resolution flow cytometry in molded microfluidic devices. Analytical Chemistry 78 (2006) 5653-5663.

[15]A. Kummrow, J. Theisen, M. Frankowski, A. Tuchscheerer, H. Yildirim, K. Brattke, M. Schmidt, and J. Neukammer, Microfluidic structures for flow cytometric analysis of hydrodynamically focussed blood cells fabricated by ultraprecision micromachining. Lab on a Chip 9 (2009) 972–981.

[16]J.P. Golden, J.S. Kim, J.S. Erickson, L.R. Hilliard, P.B. Howell, G.P. Anderson, M. Nasir, and F.S. Ligler, Multi-wavelength microflow cytometer using groove-generated sheath flow. Lab on a Chip 9 (2009) 1942-1950.

[17]J. Kruger, K. Singh, A. O'Neill, C. Jackson, A. Morrison, and P. O'Brien, Development of a microfluidic device for fluorescence activated cell sorting. Journal of Micromechanics and Microengineering 12 (2002) 486-494.

[18]M.S. Howard, (Ed.), Practical Flow Cytometry, John Wiley & Sons, 2003.

[19]J.L. Collier, Flow cytometry and the single cell in phycology. Journal of Phycology 36 (2000) 628-644.

[20]E. Hecht, Optics, Addison Wesley Longman, Inc., 1998.

[21]X.H. Quan, and E.S. Fry, Empirical-Equation for the Index of Refraction of Seawater. Applied Optics 34 (1995) 3477-3480.

[22]J.M. Ruano-Lopez, M. Aguirregabiria, M. Tijero, M.T. Arroyo, J. Elizalde, J. Berganzo, I. Aranburu, F.J. Blanco, and K. Mayora, A new SU-8 process to integrate buried waveguides and sealed microchannels for a Lab-on-a-Chip. Sensors and Actuators B: Chemical 114 (2006) 542-551.

[23]B. Bilenberg, T. Nielsen, B. Clausen, and A. Kristensen, PMMA to SU-8 bonding for polymer based lab-on-a-chip systems with integrated optics. Journal of Micromechanics and Microengineering 14 (2004) 814-818.

[24]M. Fleger, and A. Neyer, PDMS microfluidic chip with integrated waveguides for optical detection. Microelectronic Engineering 83 (2006) 1291-1293.

[25]D. Snakenborg, G. Perozziello, H. Klank, O. Geschke, and J.P. Kutter, Direct milling and casting of polymer-based optical waveguides for improved transparency in the visible range. Journal of Micromechanics and Microengineering 16 (2006) 375-381.

[26]C. Bliss, J. McMullin, and B. CJ, Rapid fabrication of a microfluidic device with integrated opitcal waveguides for DNA fragment analysis. Lab on a Chip 7 (2007) 1280-1287.

[27]D. Snakenborg, K.B. Mogensen, and J.P. Kutter, Optimization of signal-to-noise ratio in absorbance detection by integration of microoptical components, 7th lnternational Conference on Miniaturized Chemical and Blochemlcal Analysts Systems (µTAS), Squaw Valley, Callfornla USA, 2003.

[28]D. Holmes, Advanced Dielectrophoretic Cell Separation Systems, Thesis for Doctor of Philosophy in the departement of Electronics and Electrical Engineering, University of Glasgow, 2003.

[29]F.J. Blanco, M. Agirregabiria, J. Garcia, J. Berganzo, M. Tijero, M.T. Arroyo, J.M. Ruano, I. Aramburu, and K. Mayora, Novel three-dimensional embedded SU-8 microchannels fabricated using a low temperature full wafer adhesive bonding. Journal of Micromechanics and Microengineering 14 (2004) 1047-1056.

Chapter 4

Experimental methods

4.1 Introduction

This chapter describes the preparation methods for the various samples and solutions, and details the apparatus used for these experiments.

4.2 Materials and methods

4.2.1 Optical characterisation

In the literature, power loss measurements of optical structures are measured by fabricating isolated structures and measuring the optical losses when they are coupled to a light source, e.g. a laser [1; 2; 3]. Alternatively, power losses can be quantified by measuring the optical signal generated in the channel [4]. In evaluating the losses generated by planar waveguide, the fabrication of isolated structures is more accurate because this allows measurements of the losses from waveguides of different length and direct measurement of excitation and emission power. However, the use of independent structure is expensive and labour intensive because it requires an additional stage of design and fabrication. In this work clean room facilities where unavailable, therefore a method that measured the emission power of a fluorescence emitting dye (Rhodamine 6G) was chosen.

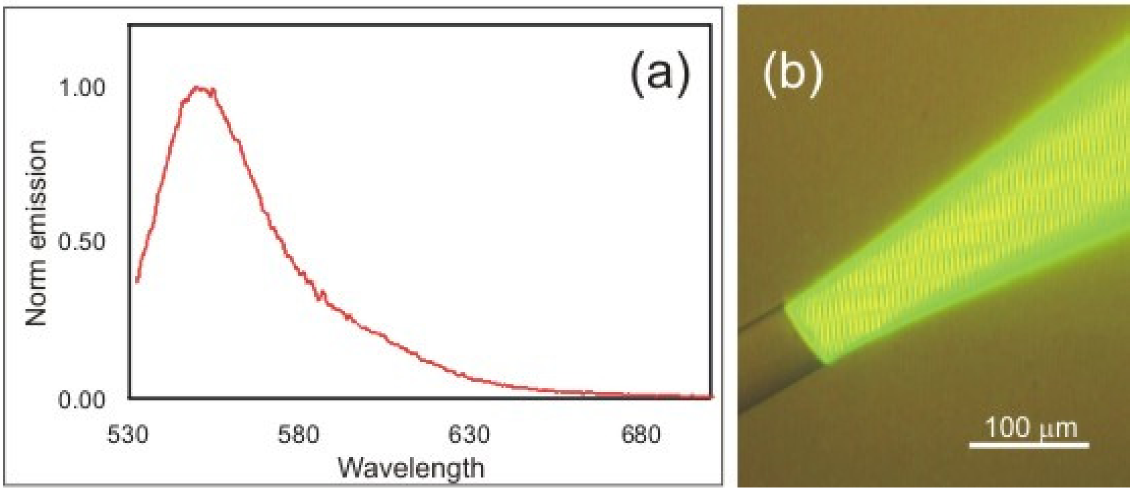

Figure 4.1 – (a) Fluorescence spectra of Rhodamine 6G in water obtained using an excitation wavelength of 532 nm. (b) Microscope picture of a 65 µm optical fibre immersed in Rhodamine 6G solution, coupled to a 532 nm laser.

4.2.1.1 Optical power losses

An optical fibre was coupled to a 532 nm laser (see section 4.8.3), and the excitable medium chosen for power loss measurement was a 0.18 mM solution of Rhodamine 6G dye (Sigma-Aldrich). The emission spectra of Rhodamine 6G was measured using a luminescence spectrometer (Perkin Elmer LS50B) with 532nm excitation light. When dissolved in water, Rhodamine 6G emits fluorescence with a peak at 550 nm (Figure 4.1(a)). The fluorescence power generated by Rhodamine 6G was measured using the set-up described in section 4.8.3.2 with a power meter positioned at the end of the microscope. The results were used for the determination of power losses of the various optical components (section 5.2).

4.2.1.2 Focussing light

Focusing power is usually evaluated with fluorescent solutions that are able to highlight the path of the light launched inside the microfluidic channel [5; 6; 7] as shown in Figure 4.1(b). Focussing was measured by photographing the light for channels filled with Rhodamine 6G solution. The intensity profiles were extracted from the pictures using MatLab and fitted to Gaussian curves using Origin® software. The spot widths generated by the various optical structures were finally evaluated by measuring the distance between the $1/e^2$ spots in each curve (see section 5.3).

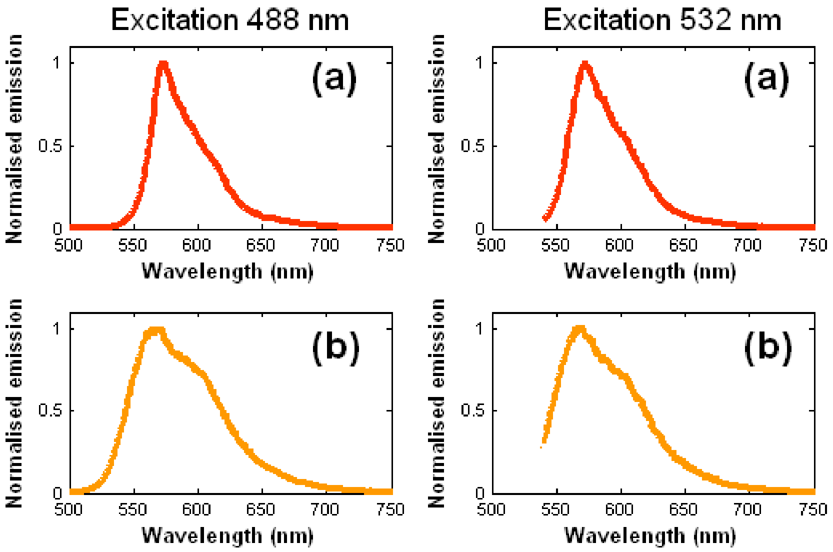

Figure 4.2 – Normalised fluorescence emission spectra for 15 and 31 µm microspheres. The spectra are for particles suspended in PBS medium and irradiated with 488 and 532 nm excitation wavelengths corresponding to the sources used on chip and in the commercial flow cytometer. (a) Emissions from 15 µm particles. (b) Emissions from 31 µm particles.

4.2.2 Polymer micro-spheres

The performance of chip B detection system was tested by flowing beads of different material, size and fluorescence properties through the detection region. The results obtained from the microfabricated cytometer were then compared with the particle properties (eg. size, CV, fluorescence). The following types of micro-spheres were used:

1. TransFluoSpheres®: 2.0 ± 0.51 µm diameter (CV of forward scattering of the lot ≤ 8%), fluorescent (633/760 nm) polystyrene micro-spheres for tracer studies. The micro-spheres were obtained from MOLECULAR PROBES as suspension in 0.5 ml of deionised water with 0.02% Tween® 20 and 0.02% thimerosal at a concentration of 10^9 beads/ml.
2. FluoSpheres®: 15.02 ± 0.98 µm diameter orange fluorescent (540/560 nm, Figure 4.2(a)) polystyrene micro-spheres for blood flow determination. The micro-spheres were obtained from MOLECULAR PROBES as suspension in 10 ml of 0.15M NaCl with 0.05% Tween® 20 and 0.02% thimerosal at a concentration of 10^6 beads/ml.
3. 25.0 µm and 45.0 µm mean diameter polystyrene micro-spheres crosslinked with divinylbenzene (DVB). The micro-spheres were obtained from

Polysciences as 2.5% solids (w/v) aqueous suspension and had a Coefficient of Variance (CV) of 20%.

4. 31.0 µm diameter, polystyrene divinylbenzene (PS-DVB) microsphere for flow tracing were acquired from Duke as a dry powder. The micro-spheres contained Firefli™ Red fluorescent dye (542/612 nm, Figure 4.2(b)) and had a CV of 11%. The manufacturer also specified a density of 1.05 g/cm^3 and a refractive index of 1.59 at 589 nm for the PS-DVB.

Micro-spheres suspensions were stored in a fridge at 4° C; dry micro-spheres were stored at room temperature. Experiments with the microfabricated cytometers were performed by suspending micro-spheres in a medium (sample medium) and using a buffer for the sheath flow. The base for both solutions was a phosphate buffered saline (PBS) solution obtained by dissolving a Dulbecco 'A' *PBS tablet* (*Oxoid,* Unipath Ltd, Basingstoke, U.K.) into 100 ml of DI water. The buffer medium was prepared by adding 11 g of sucrose to 89 g of PBS solution. The sample medium contained 0.1% (v/v) red food dye (RFD) (Super Cook, Leeds, UK) and 0.02% (v/v) Tween® 20 (Sigma-Aldrich). Solutions were prepared fresh before every experiment to reduce the formation of bacteria or aggregates generated by the high concentration of sucrose used.

Sucrose was added to increase solution density and avoid sedimentation of micro-spheres. Tween® 20 was added to keep micro-spheres from forming aggregates and to stop the growth of bacteria in solution. RFD was added to distinguish the sample stream from the sheath stream; since the dye fluoresced when excited with 532 nm wavelength, it was visible in both dark and bright fields (Figure 4.3).

Tween® was not added to the buffer to avoid bubble formation and malfunction in the hydrodynamic focussing system; sucrose was added to maintain the same electrical properties of sample medium. The difference in conductivity between buffer and sample medium was measured to be 0.8% (sample medium = 1.174 S/m; buffer medium = 1.165 S/m).

When a mixture of algae and microspheres was prepared, the latter were suspended in f2 medium (algae culturing medium, see section 4.3.1) and the suspension obtained was added to a culture already containing algae.

Micro-spheres were suspended in sample solution or culture medium (f2) using the following protocol:

1. Collect beads from the storage matrix, add to a 1.5 ml test tube and bring to 1.5 ml with sample medium.
2. Centrifuge for 2 min at 13000 rpm.
3. Remove supernatant and add 1.5ml of sample medium.
4. Repeat step 2, 3 (x2).
5. Resuspend particles in 10ml of sample medium.
6.

When particles were analysed using a commercial flow cytometer (see section 4.7) microspheres were resuspended in PBS. The sample solution used for the microfabricated cytometer was not used because the high concentration of sucrose had a refractive index that was different from PBS. Therefore, scatter signals were not detectable when using this medium with the commercial flow cytometer. The suspension protocol for microsphere in PBS was:

1. Collect beads from the storage matrix, add to a 1.5 ml test tube and bring to 1.5 ml with PBS buffer medium.
2. Centrifuge for 2 min at 13000 rpm.
3. Remove supernatant and add 1.5ml of PBS buffer medium.
4. Repeat 2, 3 (x2).

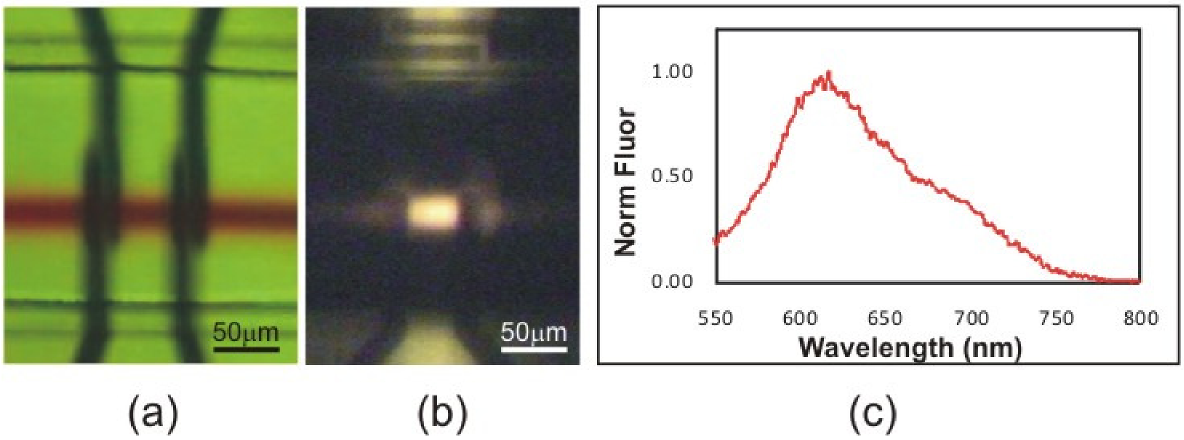

Figure 4.3 – Pictures showing food dye highlighting the central stream. (a) Microscope picture of hydrodynamic focussing irradiated by halogen lamp. (b) Microscope picture of hydrodynamic focussing irradiated by 532nm wavelength. The light is coming from an optical fibre integrated in the microfluidic chip. (c) Fluorescence spectra of red food dye diluted in water. The spectrum was taken using an excitation wavelength of 532nm.

4.3 Algae

4.3.1 Algae cultures

The phytoplanktonic species used were: *Lingulodinium polyedrum* (*L. polyedrum*), *Isochrysis galbana* (*I. galbana*), *Synechococcus sp.* and *Rhodosorus marinus* (*Rhodosorus m.*). Cultures of *L. polyedrum* were obtained from Dr. Debora Iglesias-Rodriguez (NOC, University of Southampton) and the rest of the algae were purchased from the Plymouth Algal Culture Collection (Marine Biological Association, UK). Algae cultures were grown by Dr John Gittins in the microbiology laboratory at the National Oceanographic Centre of Southampton. Batch cultures were grown in 250 ml conical flasks in a standard f/2 growth medium [8; 9], illuminated on a 12/12 hour light/dark cycle at a light intensity of 30-50 µmol photons sec^{-1} m^{-2} (fluorescent tubes: Philips Master TLD58W/840 REFLEX) at a temperature of 19°C. Sub-culturing was carried out every 2 weeks and the cultures were grown for 2 weeks before analysis. The cell diameters were measured using bright field microscopy and found to be in the range 3 to 4.5 µm for *I. galbana*; 4.5 to 7.0 µm for *Rhodosorus m.*, 0.5 to 2.0 µm for *Synechococcus sp.* and 37 to 52 µm for *L. polyedrum*. Photographs of each organism, are shown in Figure 4.1.

4.3.2 Gross anatomy of Algae

4.3.2.1 Isochrysis galbana

These organisms were first studied and described by Parke [10]. Cells have an ellipsoidal shape and a high tendency to change shape with age. In the central part of their life cycle they have a length of 5-6 µm, a breadth of 2-4 µm and develop flagella for swimming.

Motile cells are covered by organic scales enclosed in a mucilaginous matrix [11]. Some strains of *Isochrysis* have also been reported to form calcareous scales, still surrounded by a mucilaginous matrix [11]. The cytoplasm contains two large, elongate, parietal chromatophores, usually positioned laterally in the body. Small oil drops are randomly distributed in the body. As the cultures get older (more than 4 weeks), cells lose the flagella, and their mucilaginous matrix, a cellulose membrane develops and the average size of the cells increases to 7–8µm.

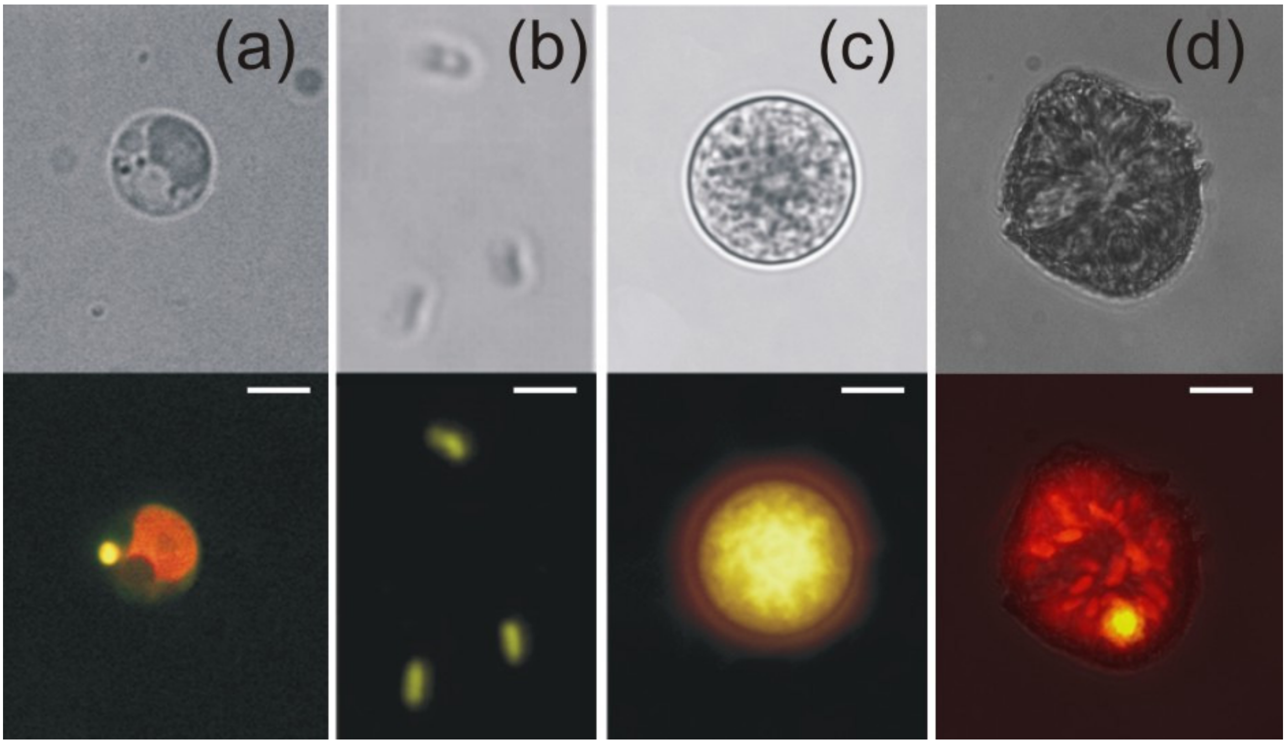

Figure 4.4 - Microscopic photograph taken in bright field with a halogen lamp (top) and with UV light at 488nm (bottom) to induce fluorescence. Scale bar = 2 µm unless otherwise indicated. (a) *Isochrysis Galbana*, (b) *Synechococcus sp*. (c) *Rhodosorus marinus*. (d) *Lingolodinium polyedrum;* scale bar is 15 µm.

Note that cells from two week old cultures grown in the laboratory were not motile although cells with flagella were found. This was probably due to the growth conditions used (medium, temperature and light intensity) that were different from that used for the organisms described in the literature. Furthermore, the growing conditions described in 4.3.1 were different from those used by the Plymouth Algal Culture Collection. Apart from the lack of movement, the dimensions and general structure of the cells grown in our laboratory matched the description provided by the literature [10; 11; 12].

4.3.2.2 Rhodosorus marinus

Rhodosorus m. were first studied by Geitler in 1930 [13]. The cells were approximately 7 µm in diameter and the most notable characteristic was a four-lobed bowl-shaped chloroplast with a large pyrenoid in the centre. The cells were further characterized as lacking a cell wall, but embedded within an irregular gelatinous matrix that makes them impermeable to many chemical treatments [14].

Further study on the ultrastructure of the algae [15] showed that the cells are spherical, ranging from 4 to 11 μm in diameter with a conspicuous, round, pyrenoid located in the middle of the cell. The single chloroplast was lobed (two to nine lobes) and the number of lobes is variable among the different cells isolated. The cells are larger when grown in bright light, but the number of chloroplast lobes does not seem to vary greatly between the two conditions. The nucleus is eccentrically located and the number of mitochondria in each cell is unknown.

4.3.2.3 Synechococcus sp.

These organisms belong to the class of unicellular cyanobacteria, a class of organism recognized as a major group of bacteria [16]. Cyanobacteria can be distinguished from bacteria by the nature of their pigment system and by their performance of aerobic photosynthesis.

Synechococcus sp. cells have a short elongated shape with a width of about 1 μm. These organisms are unicellular but they can form short filaments composed of two cells. The cell structure of *Synechococcus sp.* is comparable to the typical prokaryotic algae structure, with a cell wall and without internal organelles. As these organisms do not cluster in colonies they do not have a sheath layer covering the cell wall.

4.3.2.4 Lingulodinium polyedrum

L. polyedrum is a single celled marine organism belonging to the group of dinoflagellates. The group is widely studied for a number of reasons including the generation of red tide phenomena, the production of toxins, the production of luminescence (bioluminescence) and the adaptation to a variety of habitats ranging from arctic to tropical seas and estuaries as well as fresh to hyper-saline waters [17; 18].

L. polyedrum was described for the first time by Stain in 1883 (original name *Gonyaulax Polyedra*) [19]. Since then the organism has been widely studied and a recent review by Lewis *et al.* [20] summarizes all investigations performed on the organism. In this thesis *L. polyedrum* was analysed in their motile stage which is characterised by dimensions of 42-54 μm, angular or polyhedral shape in ventral view and a circular shape in apical[7] view (Figure 4.5). However, cell size can change according to temperature, irradiance and turbulence conditions. The cell wall consists of an outer

---

[7] Apex = the anterior-most part of the cell.

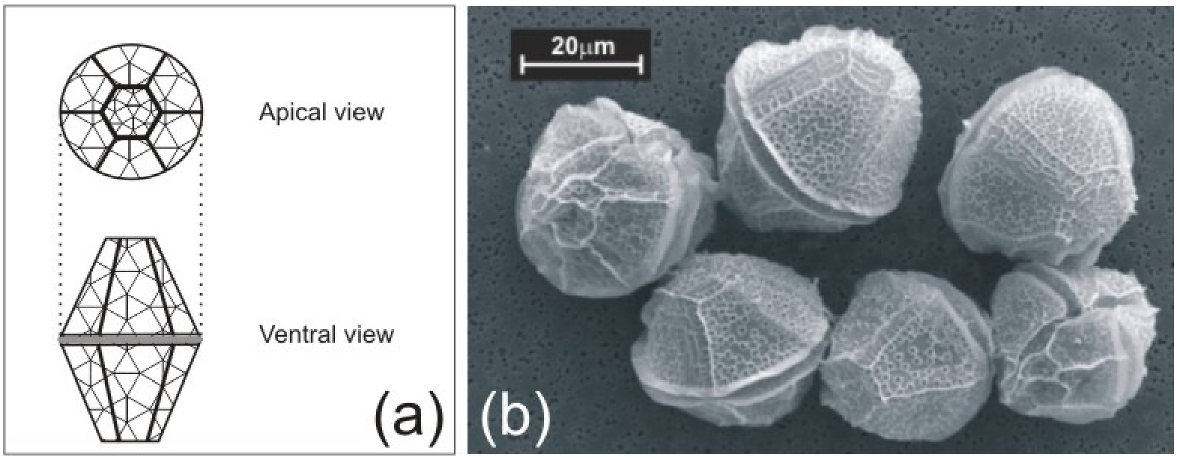

Figure 4.5 – SEM picture of *l. polyedrum* organisms. The ventral view shows the polyhedral shape and the apical view a circular shape. Courtesy of Dr Debora I. Rodriguez (NOC, Southampton).

plasma membrane within which lie membrane bound cellulose plates (theca). The inner layer of the wall (inside the plates) is termed pellicle and it is a continuous fibrous layer in which lies the cytoplasmic membrane. The most noticeable internal organelles are nucleus and chloroplasts. The nucleus occupies 9% of the cell volume and is a u-shaped envelope with annular pores and permanently condensed chromosomes. The chloroplasts are present in high number (about 34 per cell), are peripherally located and occupy 11% of the cell volume. The chloroplast envelope consists of three closely associated layers. Food reserves (starch) accumulate on the external part of the chloroplasts.

4.3.3 Emission spectra

Each species of algae contains different photo-pigments which produce different fluorescent emission spectra. The emission spectra of the four organisms were measured using a luminescence spectrometer (Perkin Elmer LS50B) with 488, 532 and 633 nm excitation light (Figure 4.6). When excited with 488 or 532 nm lasers, the data show that *I. galbana* and *L. polyedrum* emit only in the red region ($\lambda >$ 650 nm); *Rhodosorus m.* and *Synechococcus sp.* both emit in the orange (λ 550-620 nm) and in the red region but with different spectral intensities. Similar characteristics are seen when the excitation wavelength is 633nm.

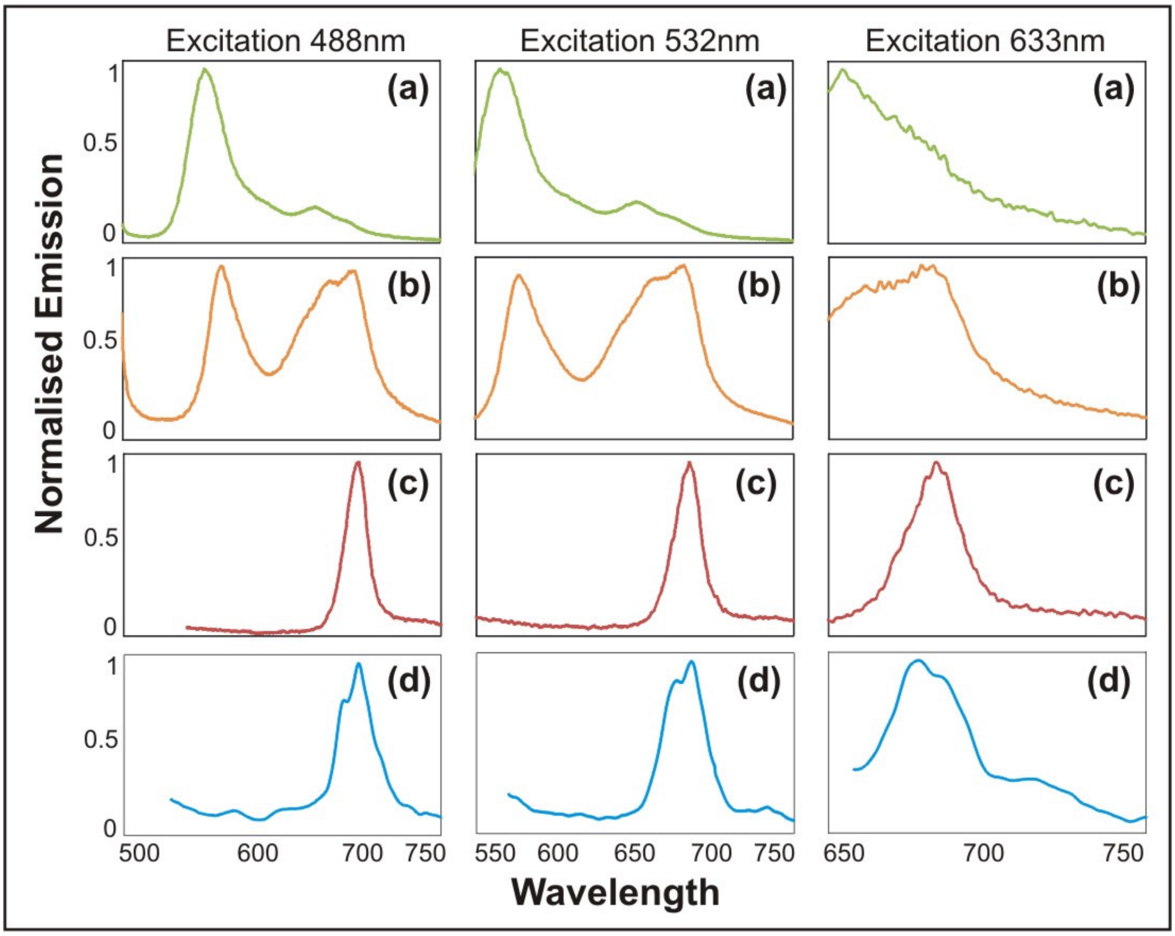

Figure 4.6 – Normalised emission spectra of the four algae species used in this work when illuminated with laser light at the three different excitation wavelengths corresponding to the sources used on chip and in the commercial flow cytometer. (a) Emissions from *Rhodosorus m*. (b) Emissions from *Synechococcus sp.* (c) Emissions from *I. galbana.* (d) Emission from *L. polyedrum.*

4.4 Algae preparation for AC electrokinetics experiments

Measurement of the electrical properties of cells with AC electrokinetic techniques (chapter 7) requires that the relative polarisabilities of the particle and the suspending medium are carefully chosen. Generally, this requires that the properties of the suspending media are controlled, rather than trying to alter the dielectric properties of the particle. Therefore, different buffers are prepared with different conductivities. The various buffers have different conductivities but the same osmolality as the culturing medium (enriched seawater) to circumvent possible cell stress due to decrease of osmotic pressure. KCl was used to adjust the conductivity of the solutions. Sucrose was used as a non-conductive replacement for the ions present in seawater allowing adjustment of the osmolality. The osmolality of the growing medium was measured using a Roebling Osmometer (Camlab) whilst the osmolality for sucrose and KCl were obtained from the CRC Chemistry Handbook [21]. The conductivity of the different solutions was measured using a conductivity meter (EC 215, HANNA instruments).

A solution of 25% (w/w) sucrose in DI water and a solution of 4.5% (w/w) KCl in DI water were prepared. The two solutions had the same osmolality as the algae growth medium (1.1 Os/kg). The solution of KCl and sucrose were mixed in different ratios to obtain a set of suspending media with the same osmolality but different conductivities. The solution of KCl was added drop by drop to the solution of sucrose and the conductivity was monitored with a conductivity meter.

Since no standard protocol exists for the resuspension of algae for AC electrokinetic measurements, the following protocol was set up:

1. Distribute 8.5 ml of algae culture into 6 1.5 ml test tubes.
2. Centrifuge for 3' at 4000 rpm, rotate 180° the test tubes and centrifuge for 6' at 4000 rpm.
3. Discard supernatant and add 0.1 ml of suspending medium of the desired conductivity.
4. Transfer the cells into 2 test tubes and bring each test tube to 1.5 ml volume every test tube with the chosen suspending medium.
5. Centrifuge 3' at 11000 rpm, rotate 180° the test tubes and centrifuge 6' at 11000 rpm.
6. Discard supernatant and add 1.5 ml of the selected suspending medium to every tube.
7. Centrifuge 3' at 13000 rpm, rotate 180° the test tubes and centrifuge 6' at 13000 rpm.
8. Discard supernatant and add 1.5ml of the selected suspending medium.
9. Centrifuge 3' at 13000 rpm, rotate 180° the test tubes and centrifuge 6' at 13000 rpm.
10. Discard supernatant, add 0.1ml of the selected suspending medium to each sample tube and transfer everything into a single sample tube.

Since it has been shown that the presence of chlorophyll autofluorescence is an effective method for assessment of the viability of algae cells [22], the presence of chlorophyll was verified using a microscope (Axiovert 200, Zeiss) to confirm that resuspended cells were still viable. The autofluorescence was observed by exciting the cells at 488nm and observing the emission at 516-556 nm using a FITC filter set (Semrock).

4.5 Algae preparation for Transmission Electron Microscopy (TEM)

The fine internal structure of the algae was investigated with TEM microscopy (section 7.3). Algae preparation and microscopy were performed by Anton Page (Biomedical Imaging Unit, University of Southampton).

Cells were centrifuged and resuspended in primary fixative comprising 3% glutaraldehyde, 4% formaldehyde in 0.1 M PIPES buffer, pH 7.2. They were then processed according to method 4 of Page *et al.* [23]. The alginate embedded cells were processed as normal for TEM. Briefly, the specimens were rinsed in 0.1 M PIPES buffer, postfixed in 1% buffered osmium tetroxide (1 hour), rinsed in buffer, block stained in 2% aqueous uranyl acetate (20 mins), dehydrated in an ethanol series and embedded in Spurr resin (TAAB Laboratories, Aldermaston, UK). All buffer and fixative solutions contained 1% sodium chloride to raise the osmotic pressure to reflect the marine environment of the organisms.

Silver sections were cut on a Leica OMU 3 ultramicrotome, stained with Reynolds lead stain and viewed on a Hitachi H7000 transmission electron microscope equipped with a SIS megaview III digital camera.

4.6 E. coli

The limit of detection of the chip A cytometer was tested with bacteria. The organisms used were *E. coli* bacteria (pLLC152/BL21(DE3)) prepared by L. Chan (Department of Chemistry, University of Southampton$^{)}$. *E. coli* are gram-negative bacteria with a rod-like shape and average dimensions of 1x3 µm. The strain of *E. coli* used expressed DS red protein, which emits light in the orange region when irradiated by blue/green light. The strain was also resistant to ampicillin, so that the antibiotic could be added to the culture medium to avoid the growth of other bacteria.

To prepare the culture of *E. coli,* a loop of cells was collected from a glycerol freeze and used to inoculate 10 ml of 2YT medium [24] containing 100 μg ml^{-1} of ampicillin (Invitrogen). The culture-medium was incubated overnight (>16 h) at 37^{o} C. The overnight culture of pLLC152/BL21(DE3) was used for a 1% inoculum of 2YT medium (10 ml) [24] containing ampicillin (100 μg ml^{-1}). The culture-medium was incubated at 37^{o} C and monitored measuring the optical density at 600 nm (OD600) using a spectrometer (Cary 100, Varian); when OD600 reached 0.6 the expression of DS red protein was induced by adding IPTG (Isopropyl β-D-1-thiogalactopyranoside, Melford) to give a final concentration of 100 mM. Cell growth was continued at 37^{o} C and after a further 3 h the culture was removed from the incubator and chilled on ice. 100 μl of this *E. coli* suspension (concentration = 10^{8} cell ml^{-1}) was then added to a 100 μl suspension of polystyrene micro-spheres (2.0 μm TransFluoSpheres® from MOLECULAR PROBES, see details in section 4.2.2) in a 15ml test tube. The mixture was then diluted with 4.8 ml of PBS (conductivity = 1.6 S/m at 20^{o}).

4.7 Commercial Flow Cytometer

Results from the microfabricated cytometers were compared with results obtained from a FACSAria flow cytometer (Becton Dickson) equipped with two lasers: a 488-nm (13mW-20mW) Coherent® SapphireTM solid state laser and a 633-nm (10mW-20mW) JDS UniphaseTM HeNe air-cooled laser.

FACSFlow sheath fluid (Becton Dickson) was forced at a pressures of 70 and 20 psi through 70 and 100 μm nozzles respectively. The instrument was controlled by a personal computer with FACSDiVa software. Measurements of Forward Scatter light (FSC), Side Scatter light (SSC), orange fluorescence (575/26nm) and red fluorescence (645/40nm) were made using laser excitation at 488nm.

4.8 Microfabricated flow cytometer

Cytometry experiments performed with chip A and chip B (chapter 6) were performed by coupling the chips with fluidic, optical and electronic equipment for flow generation and measurement of LIF, scatter light and IS. The layout of the IS detection apparatus was the same in all the experiments performed, while different fluidic connections and optical layout were used depending on the chip used.

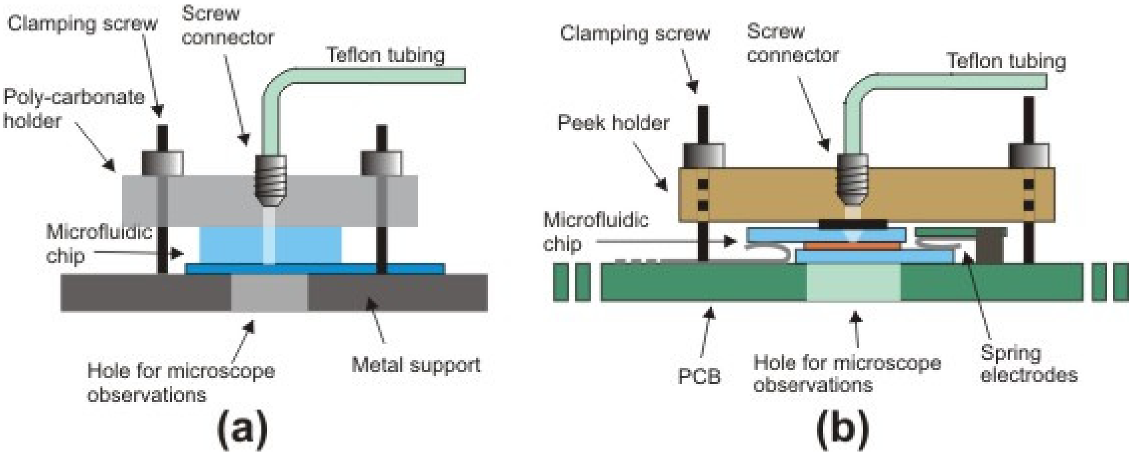

Figure 4.7 – Schematic layouts depicting fluidic interfaces used for chip A (a) and chip B (b).

4.8.1 Fluidic connections

The channels were connected to reservoirs containing the buffer and sample solutions, using Teflon tubing (Omnifit) and fluidic interfaces (chip holders) to connect tubing to the channels.

4.8.1.1 Chip A

The layout of fluidic connection for chip A is depicted in Figure 4.7(a). The PDMS layer was first punched with a PDMS punching kit (Technical Innovations Inc.) in order to create channel input and outlet. The microfluidic chip was then accommodated on top of a metal support and secured by a polycarbonate fluidic interface (chip holder) with clamping screws. No gasket was required between polycarbonate and PDMS as the latter has good sealing properties. Screw connectors (062 MINSTAC fitting system, The Lee Co.) applied to the extremity of the tubes allowed connection with the carbonate interface.

4.8.1.2 Chip B

Figure 4.7(b) depicts the schematic layout of the interface used for the fluidic connection of chip B. Holes were first drilled at inlet and outlet reservoirs of the chip using carbide spade drills (SPADEG-12M1, Drill Service Limited). The chip was then placed on a PCB for electric connections and secured by a Peek fluidic interface (chip holder) with clamping screws. A silicone gasket was placed between the peek holder and the chip. As for chip A, fluidic connection was completed using tubing terminating with screw connectors.

4.8.2 *IS detection system*

The layout of the impedance measurement system is shown in Figure 4.8. Cells pass between two pairs of electrodes which are configured to form two arms of an AC bridge. The bridge is driven by discrete sinusoidal excitation signals. As cells flow through the channel they pass over first one, then the other pair of electrodes, enabling a differential measurement to be made. The signal from the electrodes is measured using home made instrumentation amplifiers (for details see [25] for chip A amplifier and [26] for chip B amplifier) together with an RF lock-in amplifier (SR844, Stanford Research Instruments). The output is a complex signal, consisting of the real component (in phase) and imaginary component (90º out of phase). The output from the lock-in amplifier is sampled at frequencies ranging from 10 kHz to 190 kHz using a 16-bit A-D card (NI6034E, National Instruments) and the data captured and analysed with software written in LabVIEW^{TM}. The impedance data for the cells is measured simultaneously at two frequencies.

4.8.3 *Optical set-ups*

Since chip A used conventional optics and chip B used integrated optics, different optical set-ups were used for the experiments. Both set-ups used a diode pumped laser emitting at 532 nm (LCM-T-111, Power Technology Inc.) with a nominal power

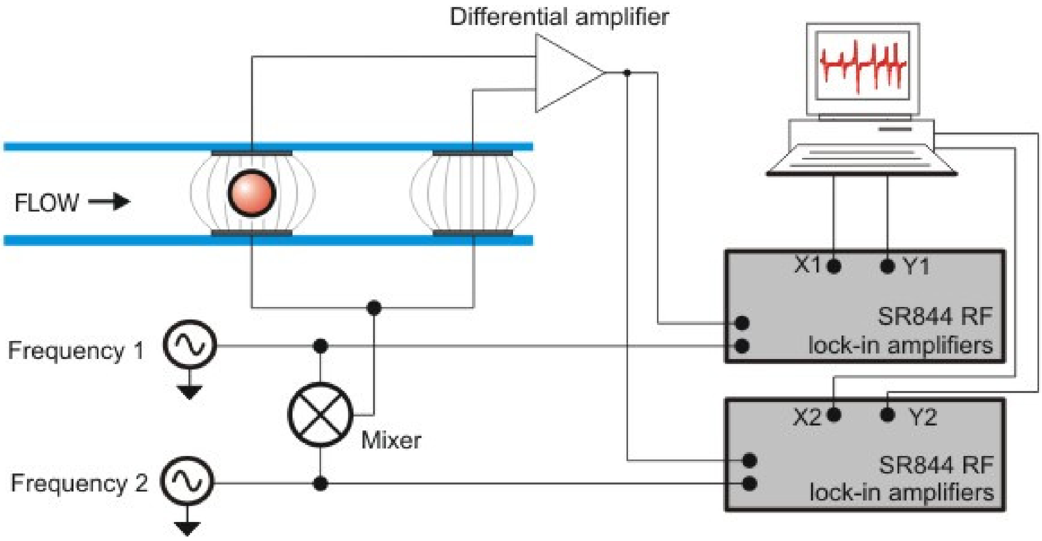

Figure 4.8 – Schematic layout of IS detection system featuring a microfabricated chip with facing electrodes and associated detection electronics.

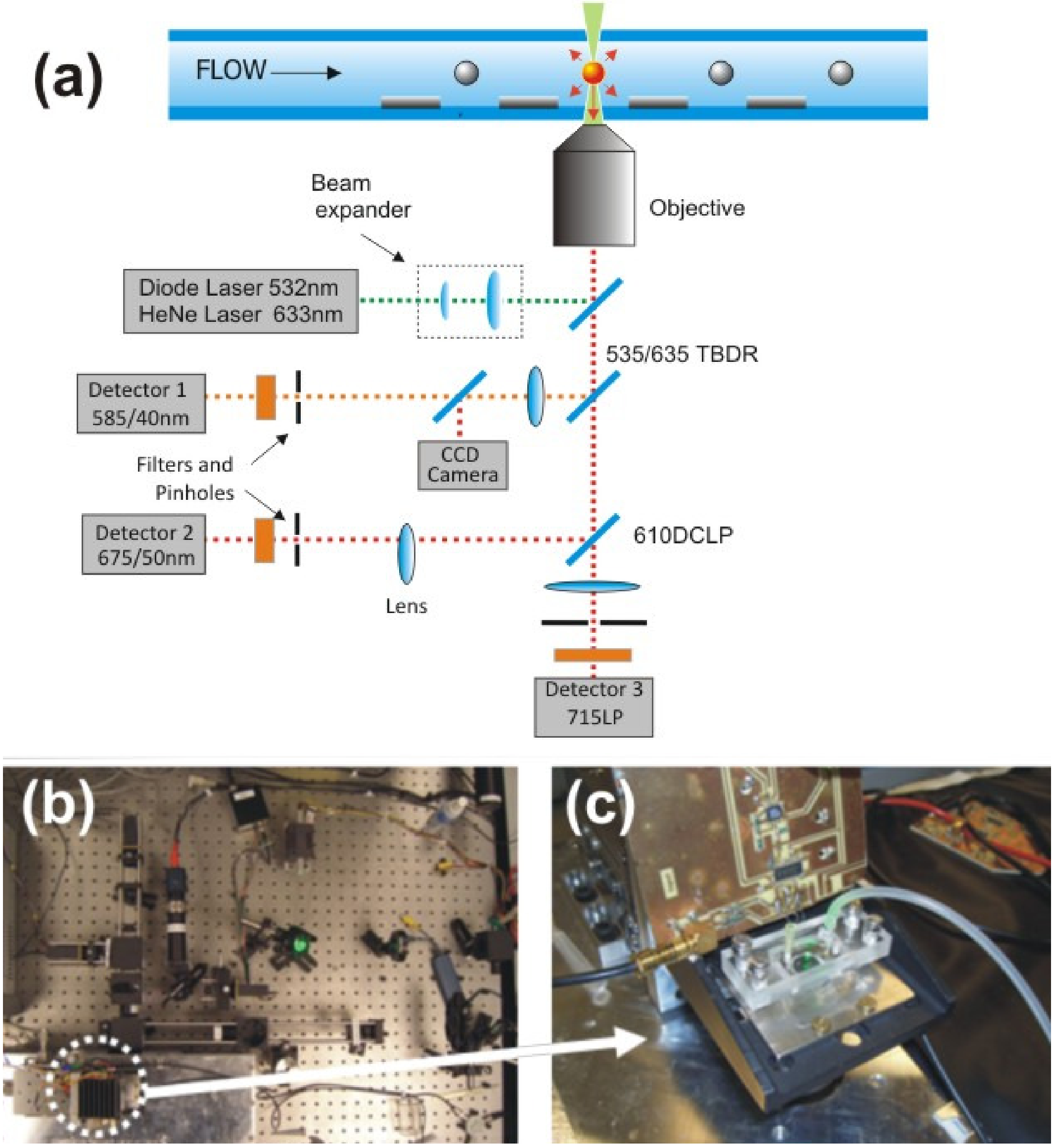

Figure 4.9 - (a) Optical system layout used with chip A; (b) photograph of the optical system; the circle shows where the chip is positioned; (c) detail of the PDMS chip.

of 50mW. In addition, the optical set-up coupled with chip A used a He-Ne laser emitting at 633 nm with a nominal power of 50mW.

The lens used to focus the light into and from the channel was a x20 planar objective with a Numerical Aperture of 0.50 (Nikon). All filters were from Chroma and Omega Opticals. Images were recorded with a Watec AC254-100-A1 CCD camera and a PC using a digital acquisition card.

Photomultiplier tubes (PMT) where used for measurement of fluorescence and scattered light (Hamamatsu). Model H9305-03 was used for fluorescence and model H6780-02 was used for scattered light. Each PMT was connected to an amplifier (C7319) and with a power supply (C7149) for photosensor modules.

4.8.3.1 *Chip A*

A detailed schematic view of the optical set-up used for chip A is shown in Figure 4.9(a). The system used two lasers whose beams were diverted to the chip using mirrors and focused into the microfluidic channel with the x20 objective lens. The fluorescent light emitted from the sample was collected by the same lens and passed through dichroidic mirrors into a CCD camera and through filters (585/40 nm, 675/50 n, 715LP) positioned in front of the PMTs.

4.8.3.2 *Chip B*

The schematic layout of the optical set-up for chip B is shown in Figure 4.10. A laser beam is focussed into an optical fibre through a system of mirrors and lenses. The second end of the optical fibre is inserted into an alignment groove and launches light into the detection region. Light from excited particles is collected by other optical fibres integrated within the chip and delivered into lenses and filters positioned in front of PMTs. An infinity objective is placed underneath the chip. The light collected by the objective passes through mirrors and lenses and is focussed on a CCD camera and a power meter.

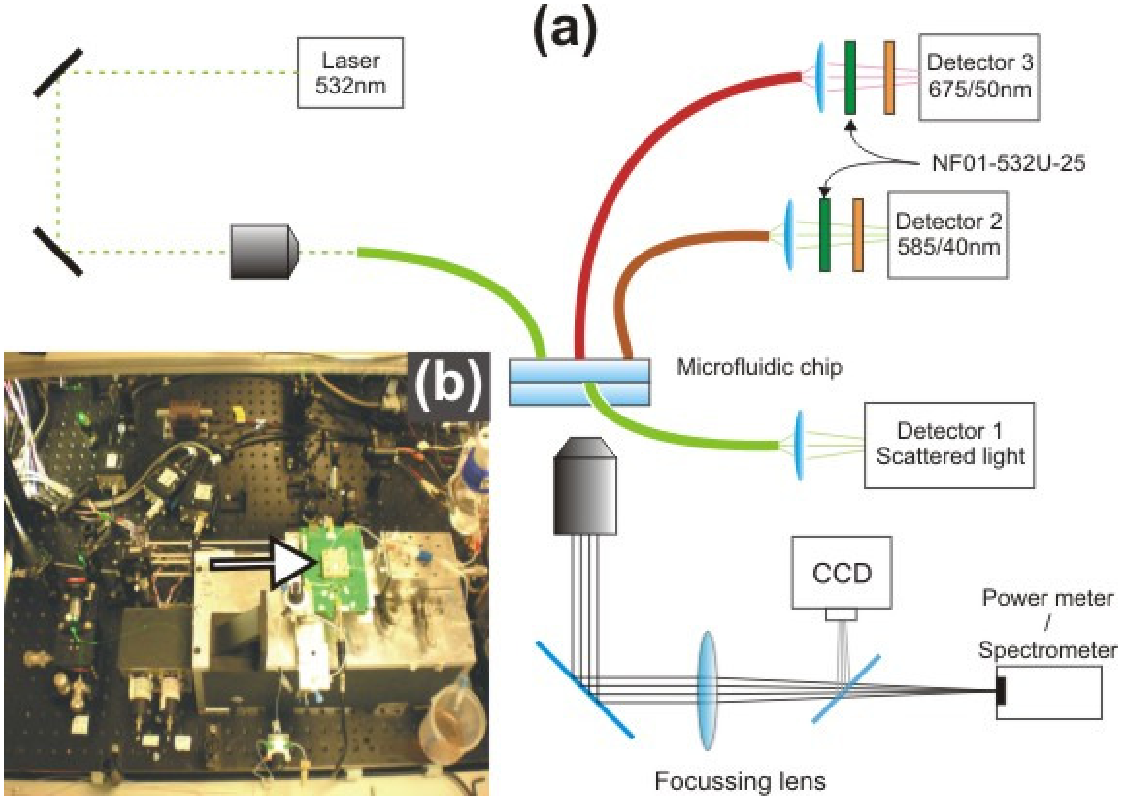

Figure 4.10 – (a) Schematic layout of the optical system used with chip B. (b) photograph of the optical system; the position of the chip is indicated be the arrow.

The optical fibre (FVP050055065, Polymicro Technologies, AZ, USA) had an external diameter of 65±2 μm and a core diameter of 50 μm. The lens used to focus the light into the fibre was a x100 objective (Plan 100, Olympus) with a Numerical Aperture of 0.90. The filters were 585/40 nm and 675/50 nm and 532 nm notch (one for every PMT detecting fluorescence). The alignment grooves were filled by capillarity with Norland 73 UV curable glue and exposed for 5 minutes to a 100 Watt, 365 nm light using an UV LAMP (Black-Ray® B-100AP High Intensity UV lamp). The glue was used as index matching material and reduced the light scattering at the fibre/wall interface. For optical power losses measurements, the grooves were filled with index matching oil (Immersion oil, Olimpus, n=1.516) so that the same fibre could be used for several chips.

A design-WL chip (see section 3.5) was used for all the experiments with chip B performed in this work. Excitation light exited from the normal groove, scatter light was detected from the 22° groove and fluorescence light was detected from the two 45° grooves on the same side of the normal groove to reduce the amount of incident excitation light entering the fluorescence detector. A fibre was coupled with the 532 nm laser, inserted in the normal groove and coupled with the integrated waveguide and lens to launch focussed excitation light into the channel. Two fibres ends were inserted in the 45° grooves on the same side of the complex waveguide/microlens for fluorescence collection, the other ends of the fibres were than connected to PMTs. Finally one fibre tip was inserted into the 22° groove for SSC collection.

4.8.4 Data acquisition

For both microfluidic designs the optical detection region was located between the pairs of electrodes (see Figure 4.9 and 3.14), allowing correlation between optical and impedance measurements. The output from the lock-in amplifier and the PMT are sampled at frequencies ranging from 10 kHz to 190 kHz using a 16-bit A-D card (NI6034E, National Instruments) and the data captured and analysed with software written in LabVIEW™. Software used with chip A experiments was written by Raphael Tornay (EPFL Lausanne, CH); software for chip B experiments was written by Christian Reccius (Philips Research Laboratories – Redhill - UK). Both data collection program automatically registered an event when the voltage in one channel exceeded a pre-set threshold level.

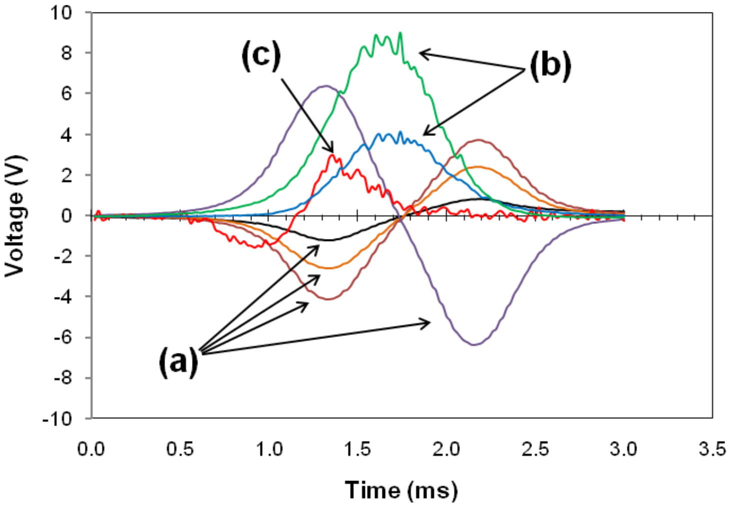

Figure 4.11 - A typical data set for a 31 µm orange fluorescent bead flowing into chip B. The four sinusoidal signals are: (a) the impedance signals, (b) the fluorescence signals and (c) the sinusoidal scatter light signal.

A typical data set for a single cell is shown in Figure 4.11. The four sinusoidal signals (a) are the impedance signals measured when particles flow across the two pairs of electrodes. The first set of peaks is the signal measured by the upstream pair of electrodes and the second peak by the downstream pair. The two data spikes labelled (b) are the fluorescence signals measured at wavelengths of 675/50 nm and 585/40 nm and the signal labelled (c) is generated by scattered light. The sinusoidal shape is due to the incident light entering the collection fibre that is first blocked as a particle enters the detection region (negative peak), and then generates a scatter signal as the particle enters the detection region completely (positive peak).

4.9 Particle tracking set-up

In order to track particles flowing in chip B, particle tracking experiments were performed (section 6.5.2). These experiments were performed by flowing fluorescent particles into the sample channel and recording positions with a digital camera. For particle-tracking, a microfluidic chip was positioned on top of a microscope (Zeiss Axiovert200). The microscope was coupled to a digital camera (Hamamatsu ORCA-ER) connected to a PC equipped with frame grabbing software (Simple PCI). A TRITC filter-set (Zeiss) was used for fluorescence observation of particles. Flow rates above 40 µl min^{-1} were created with a syringe pump (WW-74900-25, Cole-Parmer) set on withdraw mode and connected to the output reservoir. Flow rates below 40 µl min^{-1} were activated using gravity (see “differential pressure” at section 2.5).

4.10 AC electrokinetics measurements set-ups

In this thesis, two devices able to perform single cell impedance spectroscopy have been tested on algae. However, the correct interpretation of the data generated by impedance spectroscopy requires a good knowledge of the electrical properties of the particles analysed. Since little studies have been performed on the electrical properties of algae, in this work AC elektrokinetic experiments (DEP and ROT, see explanation in chapter 7) aimed to measure the electrical properties of algae. These were performed and the set-up used is presented in this section.

For the DEP and ROT measurements performed in this work, the core of the measurement device was an array of micro-electrodes fabricated on a glass slide (see Figure 4.12). The device was mounted on a PCB to allow connection between the slide and a Function Generator *(TTi TG2000)*. The slide was placed on a microscope (Zeiss Axiovert200) coupled to a digital camera and a PC equipped with frame grabbing software written in LabVIEW® by Diego Morganti (University of Southampton). The PC was also connected to the signal generator through a GPIB-US-HS interface (model 187965B-01, National Instruments).

For measurement of the cross-over frequency of *I. galbana* (section 7.4.1) an array of interdigitated-castellated electrodes with a characteristic size of 20 μm (Figure 4.12(a)) was used. A droplet containing cells was pipetted onto the electrodes and

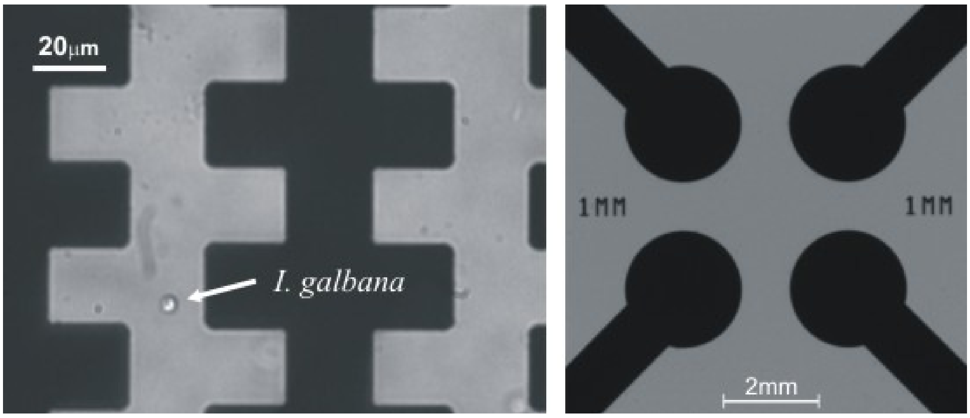

Figure 4.12 – Microscope pictures of microelectrodes (dark regions) patterned on glass slides and used for AC electrokinetics measurements. (a) Castellated electrodes for dielectrophoresis (DEP) measurements. Typical featured size of the electrodes is 20 μm. The picture was taken with sample on top of the microscope slide. One cell of *I. galbana* is indicated. (b) Lobed electrodes for electro-rotation (ROT) measurements. Adjacent lobes are spaced 1mm.

covered with a microscope coverslip. The electrodes were connected to the signal generator and voltages of 6 V_{pp} with frequencies ranging from 10 kHz to 40 MHz were applied. Cell behaviour was monitored through the microscope.

For electro-rotation experiments (section 7.4.2) an array of four lobed electrodes mounted at right angles to each other was used (Figure 4.12). The diameter of the lobes was 2.5 mm and the spacing of the electrodes was 1 mm. A droplet containing cells at low density was placed between the electrodes and four 90° phase-shifted 17 V_{pp} sine waves were applied to produce a rotating electric field. Electro rotation spectra were recorded from 100 kHz to 25 MHz. The frequency energizing the electrodes was controlled by the LabVIEW® software that also started the recording of a video every time the frequency was changed. The rotation speed was extrapolated from the videos and plotted as function of the frequency to generate electro-rotation spectra. Finally, the electro rotation spectra obtained where fitted to an electric model using Wolfram Mathematica®.

REFERENCES

[1]K.B. Mogensen, J. El-Ali, A. Wolff, and J.P. Kutter, Integration of polymer waveguides for optical detection in microfabricated chemical analysis systems. Applied Optics 42 (2003) 4072-4079.

[2]B. Bilenberg, T. Nielsen, B. Clausen, and A. Kristensen, PMMA to SU-8 bonding for polymer based lab-on-a-chip systems with integrated optics. Journal of Micromechanics and Microengineering 14 (2004) 814-818.

[3]G.B. Lee, C.H. Lin, and G.L. Chang, Micro flow cytometers with buried SU-8/SOG optical waveguides. Sensors and Actuators a-Physical 103 (2003) 165-170.

[4]C. Bliss, J. McMullin, and B. CJ, Rapid fabrication of a microfluidic device with integrated opitcal waveguides for DNA fragment analysis. Lab on a Chip 7 (2007) 1280-1287.

[5]J. Seo, and L.P. Lee, Disposable integrated microfluidics with self-aligned planar microlenses. Sensors and Actuators B-Chemical 99 (2004) 615-622.

[6]S.K.Y. Tang, C.A. Stan, and G.M. Whitesides, Dynamically reconfigurable liquid-core liquid-cladding lens in a microfluidic channel. Lab on a Chip 8 (2008) 395-401.

[7]Z. Wang, J. El-Ali, M. Engelund, T. Gotsaed, I.R. Perch-Nielsen, K.B. Mogensen, D. Snakenborg, J.P. Kutter, and A. Wolff, Measurements of scattered light on a microchip flow cytometer with integrated polymer based optical elements. Lab on a Chip 4 (2004) 372-377.

[8]R.R.L. Guillard, Culture of phytoplankton for feeding marine invertebrates. in: W.L.S.a.M.H. Chanley, (Ed.), Culture of Marine Invertebrate Animals. , Plenum Publishing Corp., New York, NY. , 1975, pp. 29-60.

[9]R.R.L. Guillard, and J.H. Ryther, Studies of marine planktonic diatoms. I. Cyclotella nana Hustedt, and Detonula confervacea (cleve) Gran. Can J Microbiol. 8 (1962) 229-39.

[10]M. Parke, Studies on Marine Flagellates. Journal of the marine biological association of the uk 28 (1949) 255-286.

[11]M. Parke, The production of calcareous elements by the algae belonging to the class haptophyceae (chrysophyta), II Planktonic Conference, Rome, 1970, pp. 929-937.

[12]T. Hori, and J.C. Green, The Ultrastructure of Mitosis in Isochrysis-Galbana Parke (Prymnesiophyceae). Protoplasma 125 (1985) 140-151.

[13]L. Geitler, Ein grunes Filarplasmodium und andere neue Protisten. Arch. Protistenk 69 (1930) 615-36.

[14]S. Broadwater, and J. Scott, Ultrastructure of unicellular red algae. , Seckbach, J. (Ed.) Evolutionary Pathways and Enigmatic Algae: Cyanidium Caldarium (Rhodophyta) and Related Cells., Kluwer Academic Publishers, 1994, pp. Netherlands, pp. 215–30.

[15]S. Wilson, J. West, J. Pickett-Heaps, A. Yokoyama, and Y. Hara, Chloroplast rotation and morphological plasticity of the unicellular alga Rhodosorus (Rhodophyta, Stylonematales). Phycological Research 50 (2002) 183-191.

[16]R.Y. Stanier, R. Kunisawa, M. Mandel, and Cohenbaz.G, Purification and Properties of Unicellular Blue-Green Algae (Order Cchroococcales). Bacteriological Reviews 35 (1971) 171.

[17]F.J.R. Taylor, The Biology of Dinoflagellates, Blackwell Scientific, Oxford, 1987.

[18]L.E. Graham, and L.W. Wilcox, Algae, Prentice-Hall 2000, Upper Saddle River, NJ 07458, 2000.

[19]F. Stein, Der Organismus der Infusionstiere. III. Abt. Der Organismus der Arthrodelen Flagellaten. Verlag von Wilhelm Engelmann, Leipzig (1883) 30., 25 pl.

[20]J. Lewis, and R. Hallett, Lingulodinium polyedrum (Gonyaulax polyedra) a blooming dinoflagellate. Oceanogr. Mar. Biol. 35 (1997) 97-161.

[21]CRC handbook of chemistry and physics : a ready-reference book of chemical and physical data, Boca Raton, Fla. : CRC Press, c1984. .

[22]I. Pouneva, Evaluation of algal culture viability and physiological state by fluorescent microscopic methods. Bulgarian Journal of Plant Physiology 23 (1997) 67-76.

[23]A.M. Page, J.R. Lagnado, T.W. Ford, and G. Place, Calcium alginate encapsulation of small specimens for transmission electron-microscopy. Journal of Microscopy-Oxford 175 (1994) 166-170.

[24]J. Sambrook, and D.W. Russell, Molecular cloning : a laboratory manual, Cold Spring Harbor Laboratory Press New York, NY, 2001.

[25]H. Morgan, D. Holmes, and N.G. Green, High speed simultaneous single particle impedance and fluorescence analysis on a chip. Current Applied Physics 6 (2006) 367-370.

[26]S. Gawad, K. Cheung, U. Seger, A. Bertsch, and P. Renaud, Dielectric spectroscopy in a micromachined flow cytometer: theoretical and practical considerations. Lab on a Chip 4 (2004) 241-251.

Chapter 5

Integrated optics characterisation

5.1 Introduction

This chapter presents measurements for characterising the integrated optical LOC based sensor (chip B). In particular, the chapter presents measurements and experiments to evaluate the optical power losses and the light profiles generated inside the microfluidic channel by the integrated optical system. These tests were used to enable selection of the best design for flow cytometry experiments and to facilitate interpretation of cytometric data.

Measurements on the integrated optical system showed significant differences in losses and focussing ability for different design of chip B. Furthermore, the optical losses measured for chip B were higher than the losses reported in the literature.

5.2 Optical power losses

A very important parameter in evaluating integrated optical elements is the amount of optical power lost when light travels through the integrated optical elements, especially when the driving idea is to build a portable device that requires low energy consumption.

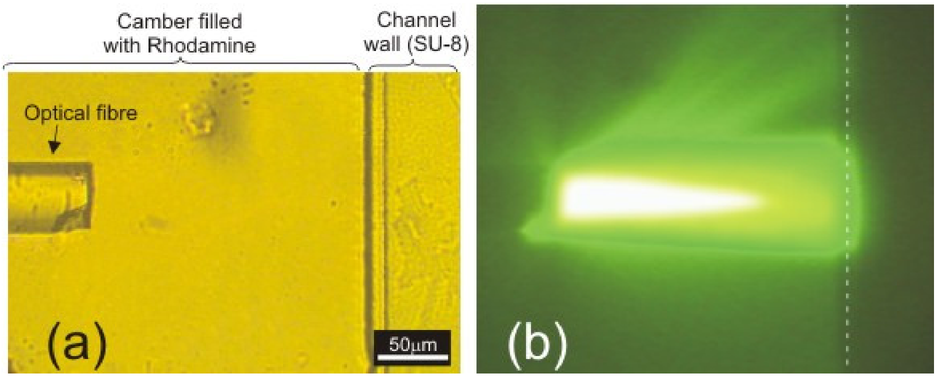

Figure 5.1 – (a) Microscope picture in bright field of fibre inserted into a micro-chamber 80 μm high. The fibre is placed 200 μm from the chamber wall. (b) Microscope picture obtained by filling the chamber in (a) with Rhodamine 6G and coupling the fibre with a 532 nm laser light. The edge of the wall is highlighted by the white dashed line.

The optical losses generated by the integrated optical systems implemented in chip B where measured by filling the microfluidic channel with a solution containing Rhodamine 6G (section 4.2.1) and measuring the fluorescence power emitted when the solution was excited with a 532 nm wavelength. Measurements were taken using the optical set up presented in section 4.8.3.2. For every chip design, the fluorescence emitted only by SU-8 was measured before filling with Rhodamine 6G. This value included fluorescence from the SU-8 and environmental noise and was subtracted from the emission power measured with Rhodamine 6G. Optical losses were expressed in decibels (dB) using the following equation [1]:

$$\mathrm{dB} = 10 \cdot \log_{10}\left(\frac{I_1}{I_0}\right) \tag{5-1}$$

where I_0 is the radiation measured in the channel and I_1 is the radiation measured at the tip of the optical fibre expressed in equivalent Rhodamine 6G radiation at 550 nm (obtained with the calibration curve described in the next section).

The power emitted by the optical fibre was correlated with the power emitted by Rhodamine 6G with a calibration curve. The data for the calibration curve was obtained by inserting the termination of one optical fibre into a chamber 1x1 mm wide and 80 μm high (see Figure 5.1). The chamber consisted of an SU-8 layer sandwiched between two Pyrex glass slides and was made using the same fabrication process used for chip B (section 3.6.2). The camber was filled with Rhodamine 6G and the fibre was positioned 200 μm from the wall so that the volume of Rhodamine 6G excited was the same as in the microfluidic channel. The second end of the fibre was coupled to the 532 nm

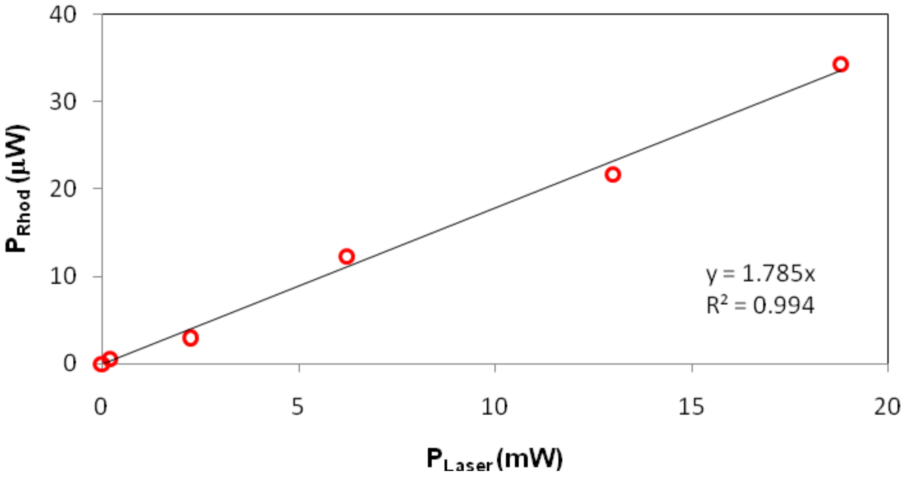

Figure 5.2 – Graph correlating the emission power at 532 nm measured at the laser output (P_{Laser}) and the fluorescence emission power of Rhodamine 6G at 550 nm (P_{Rhod}). The equation obtained for the trend line is inserted in the graph.

laser and the emission of the excited solution was measured, giving the emission power of the solution of Rhodamine when no light was lost between the fibre and the channel (full emission of Rhodamine 6G). The excitation radiation entering the fibre was modulated with a set of absorptive optical filters (FW1AND, Thorlabs) placed just after the laser output; the calibration curve obtained is showed in Figure 5.2.

The same fibre was used for all the measurement presented in this section to avoid variation due to fibre cleaving and laser/fibre coupling. For the fibre/lens and fibre/waveguide coupling it is assumed that the coupling efficiency was at maximum because the fibres were carefully positioned in the middle of the SAGs (see Figure 5.3). The losses obtained are reported in Table 5.1. As expected, design W and WL have higher losses than design G and L, due to the presence of waveguides. Furthermore, losses for W are higher than losses for WL probably because the latter has

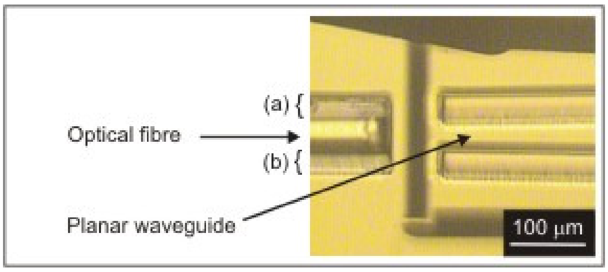

Figure 5.3 – Fibre/waveguide coupling in design WL for optical power losses measurements. Spaces (a) and (b) are the spacing between the fibre and the SAG walls.

Design	Losses (dB)	Input power at 532 nm (mW)		Rhodamine Emission Power at 550 nm (μW)		waveguide length (μm)	Relative losses (dB cm^{-1})
		Average	STD	Average	STD		
G	**0.6**	20.4	0.2	31.9	1.5	--	29.2
W	**6.6**	20.8	0.3	8.1	2.8	950	--
L	**1.3**	20.0	0.8	26.8	8.4	--	--
WL	**4.2**	19.6	0.3	13.7	2.8	600	--

Table 5.1 – Losses measured for the different designs implemented for the integrated optical system.

a shorter waveguide. Relative losses[8] were calculated only for light passing through plain SU-8 structure from design G. It was not possible to calculate relative losses for the waveguides in design W and WL as the input width of the waveguides was smaller than the core diameter of the optical fibre, therefore in design W and WL part of the light coming from the fibre is lost simply because it falls out of the waveguide input. In design L, relative losses due to the SU-8 structure were assumed to be the same as in design G, as the distance from the SAG end to the channel wall is the same; following this assumption it was then possible to calculate the absolute losses[9] of the compound microlens to be 0.5 dB. No measurements were performed for planar bent waveguides as relative losses reported for SU-8 already implied a reduction in power that could not be measured.

Relative losses for design G are one order of magnitude higher than losses reported in the literature for planar waveguides (from1 to 6 dB/cm [2; 3; 4; 5; 6; 7]). This is probably due to the polymeric structure that consisted of two layers of SU-8 thermally bonded together; it is possible that the bonding process creates a middle-layer with non-uniform refractive index and unbounded regions (see Figure 5.4) that are known to increase scattering losses [8]. The excitation wavelength used (532 nm) may also account for the high losses measured because it generates auto-florescence (see Figure 2.21) absorbing part of the radiation.

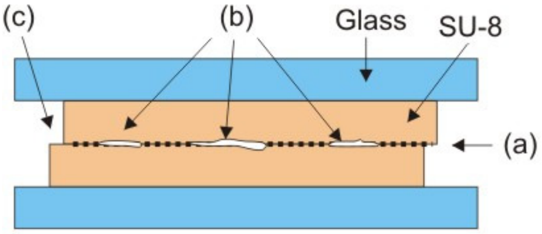

Figure 5.4 – Schematic depicting a cross-section of a generic SU-8 structure where (a) indicates the bonding region that causes irregular refractive index and (b) unbounded regions.

---

[8] Relative losses: optical power lost per unit of length (dB cm^{-1}).

[9] Absolute losses: total optical power lost in the layout considered.

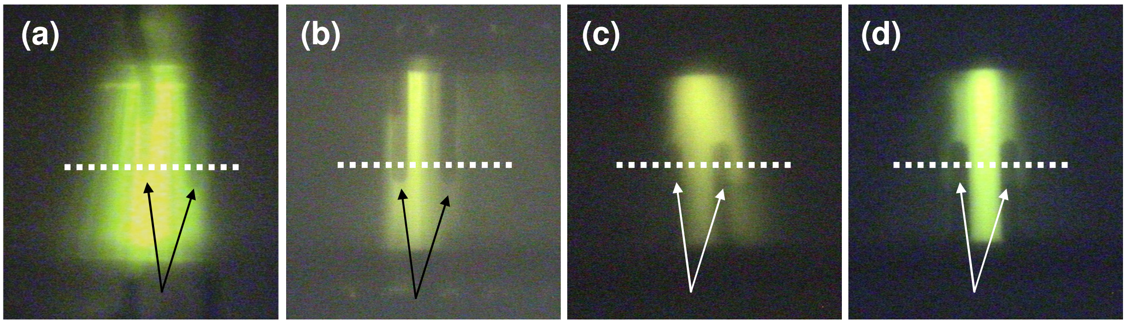

Figure 5.5 – Light profiles in the channels obtained from the different designs. Light is launched by optical fibres inserted into the normal grooves of: (a) design G; (b) design W; (c) design L; (d) design (WL). Dotted lines represent the line used for the measurement of the intensity profiles (see Figure 5.6). Arrows indicate positions where electrodes shadow or reflect fluorescent light.

5.3 Focusing light

Microscope photographs of the light profile generated by the various designs are shown in Figure 5.5. The linear intensity profiles along the dashed lines shown in Figure 5.5(a-d) were extracted and extrapolated using MatLab software (The MathWorks, Inc.). The profiles obtained are all approximately Gaussian although sometimes disturbed by the shadowing or reflecting effect of electrodes (see arrows in Figure 5.5). The data extrapolated from Figure 5.5(a-d) were fitted with Origin® software using the following equation for a Gaussian [1]:

$$y = y_0 + \frac{A}{w\sqrt{\pi/2}} e^{-2\frac{(x-x_c)^2}{w^2}} \qquad \textbf{5-2}$$

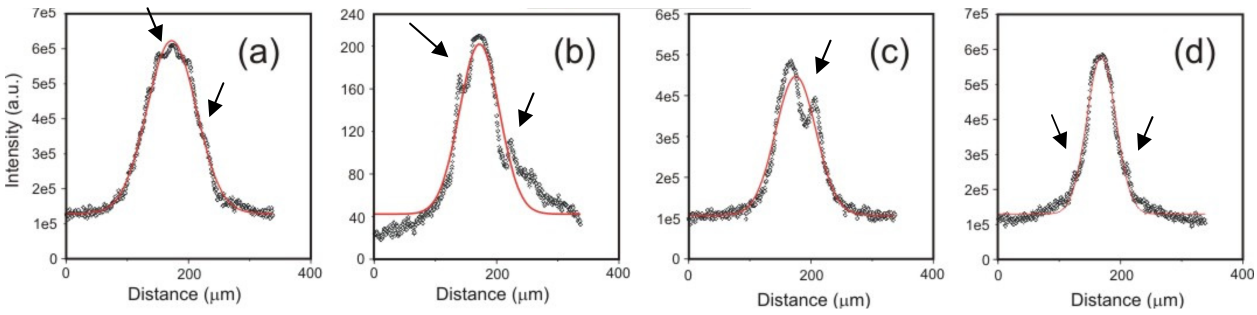

Figure 5.6 – Gaussian curves (lines) of the light intensity profile obtained from pictures in Figure 5.5. Circles represent experimental data used to fit the curve and arrows indicated regions that have been affected by the presence of electrodes. The profiles plotted are generated by the following configurations: (a) Design G. (b) Design W. (c) Design L. (d) Design WL.

where y_0 is the baseline offset, x is the horizontal axes, x_c is the horizontal coordinate of the centre of the peak, A is the total area under the curve from the baseline of the integral and $w = w_1 / \sqrt{\ln(4)}$ with w_1 being the full-width at half maximum (FWHM) of the Gaussian.

The results from the fitting and the width of the distribution fitted with the Gaussian curve (measured at the 1/e^2 points, see section 3.4.3.4) are presented in Figure 5.6 and Table 5.2. The design with the smallest width (i.e. the best focussing) is design WL, while the lowest level of focussing is with design G. Design L and W have similar performance although the fitting may be inaccurate, as also shown by the lower coefficient of determination (R^2) obtained compared to design G and WL, because the profiles are strongly affected by the shadow generated by the electrodes.

5.4 Summary

In this chapter measurements performed to characterise the performance of the optical systems of chip B showed that design WL presented the best focusing performances but higher losses than G and L. However, design G presented the lowest losses but also the least effective focusing. The design with the highest losses was W which had similar focusing to design L. It was also observed that power reduction generated by SU-8 structures were one order of magnitude higher than the structures reported in the literature, probably because of the chip structure (two layers of SU-8 bonded together) and maybe also because of the wavelength used (we used 532nm, whereas the results in the literature used 633 which would have avoided SU-8 fluorescence excitation).

Design	Width (µm)	y_0	x_c	w	A	STD	FWHM	Height	R^2
G	**161**	12962	172	80.6	5.0x10^6	40.3	94.9	4.9E+04	0.9917
W	**131**	42.4	172	65.3	1.3x10^4	32.7	76.9	1.6E+02	0.9225
L	**132**	10714	175	66.2	2.8x10^6	33.1	77.9	3.4E+04	0.9488
WL	**95**	12963	169	47.5	2.7x10^6	23.8	56.0	4.5E+04	0.9806

Table 5.2 – Values obtained from fitting the beam profiles with Gaussian curves. Width is calculated measuring the distance between the two points with intensity 1/e^2 (0.135) times the maximum intensity (see section 3.4.3.4). In addition to the parameter already explained, the table report the standard deviation of the Gaussian (STD) and the coefficient of determination (R^2).

REFERENCES

[1]D.A. Skoog, and J.J. Leary, Principles of Instrumental Analysis, Saunders College Publishing, Orlando, 1992.

[2]K.B. Mogensen, J. El-Ali, A. Wolff, and J.P. Kutter, Integration of polymer waveguides for optical detection in microfabricated chemical analysis systems. Applied Optics 42 (2003) 4072-4079.

[3]B. Bilenberg, T. Nielsen, B. Clausen, and A. Kristensen, PMMA to SU-8 bonding for polymer based lab-on-a-chip systems with integrated optics. Journal of Micromechanics and Microengineering 14 (2004) 814-818.

[4]M. Fleger, and A. Neyer, PDMS microfluidic chip with integrated waveguides for optical detection. Microelectronic Engineering 83 (2006) 1291-1293.

[5]D. Snakenborg, G. Perozziello, H. Klank, O. Geschke, and J.P. Kutter, Direct milling and casting of polymer-based optical waveguides for improved transparency in the visible range. Journal of Micromechanics and Microengineering 16 (2006) 375-381.

[6]J.M. Ruano-Lopez, M. Aguirregabiria, M. Tijero, M.T. Arroyo, J. Elizalde, J. Berganzo, I. Aranburu, F.J. Blanco, and K. Mayora, A new SU-8 process to integrate buried waveguides and sealed microchannels for a Lab-on-a-Chip. Sensors and Actuators B: Chemical 114 (2006) 542-551.

[7]C. Bliss, J. McMullin, and B. CJ, Rapid fabrication of a microfluidic device with integrated opitcal waveguides for DNA fragment analysis. Lab on a Chip 7 (2007) 1280-1287.

[8]W.T. Boyd, Fiber optics: communications, experiments and projects, Indianapolis 1982.

Chapter 6

Flow cytometry

6.1 Introduction

This chapter presents the results obtained by performing cytometric measurements with the sensors presented in chapter 3 (chip A and chip B). The response of the chip A cytometer has been previously characterised [1; 2], therefore it was used directly to analyse mixtures of different algae or bacteria and micro-spheres. The response of the chip B cytometer first needed to be characterised with single populations of micro-particles with different size and optical properties. The chip B cytometer was then used to characterise mixtures polymer microspheres and algae showing that detection and characterisation of biological particles is possible.

Results from flow cytometry experiments showed that the chip A cytometer was able to characterise algae according to size and fluorescence properties; the sensor was also proven to be capable of label free detection of bacteria although it needed improvement to perform detailed characterisations. However, despite the good results obtained, chip A was not suitable for phytoplankton analysis because of the small size range of cells that it could analyse (see section 3.4) and therefore chip B was designed and fabricated specifically for phytoplankton analysis. Characterisation experiments showed that the chip B cytometer was able to characterise different populations of microspheres and algae according to their optical and electrical properties. However, chip B showed an anomalous response probably due to inertial focussing phenomena taking place in the microfluidic channel at high flow rates.

6.2 Chip A - cytometry of a mixture of algae

The ability of chip A cytometer to characterise biological samples in seawater was tested by flowing a mixture of three algae (*Rhodosorus m., I. galbana, Synechococcus sp.*) through chip A. The mixture containing all three organisms was prepared by suspending the organisms in f/2 medium at a concentration of 3 x 10^5 cells ml^{-1}. The mixture was then filtered with an 11 µm nylon net filter (NY11 Millipore) and a sample of approximately 10 µl was passed through a chip A sensor with a channel 10 µm wide and 20 µm high and electrodes 20 µm wide with a gap of 20 µm.

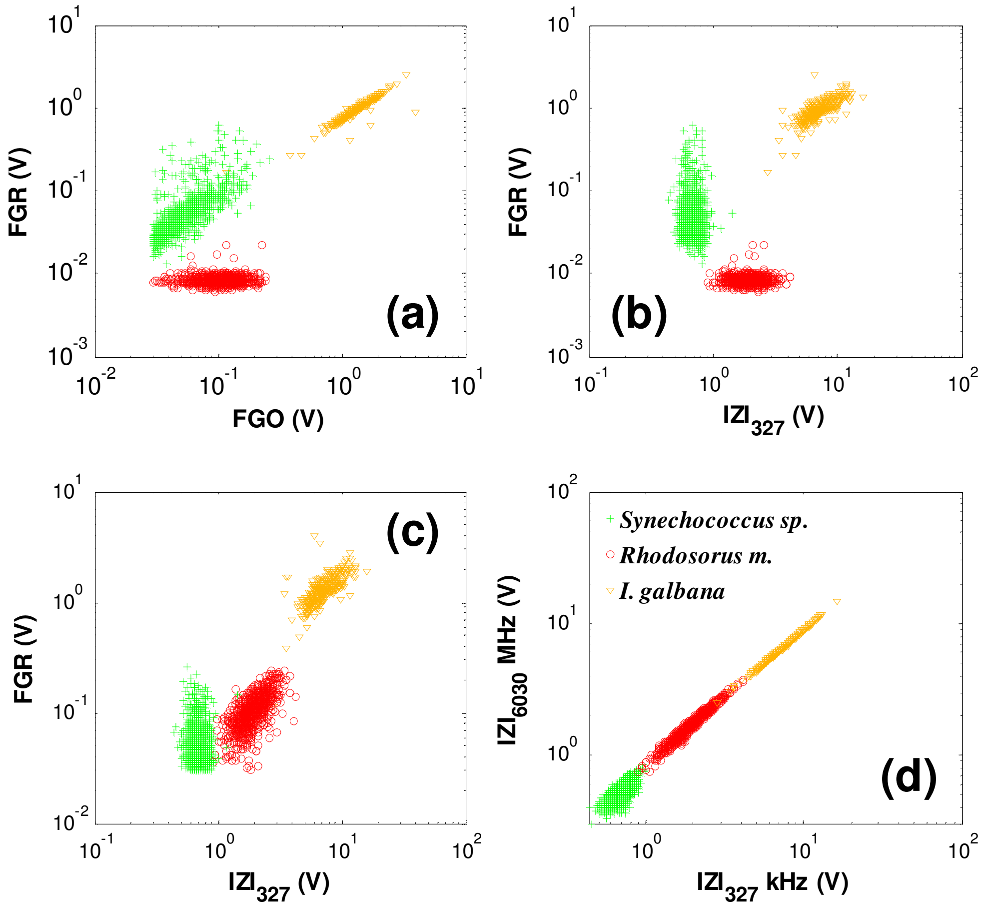

Figure 6-1 - Scatter plots (logarithmic scale) for a typical chip A cytometry experiment. FGO and FGR indicate green-orange and green-red fluorescence (see Table 1.1) measured at 585/45 and 675/50 nm respectively; $|Z|_{327}$ and $|Z|_{6030}$ indicate the magnitude of the impedance signal measured at 327 kHz and 6.03 MHz respectively. Legend for all plots is in the top left corner of graph (d).

The fluorescence from the particles was detected simultaneously through the two emission filters to measure orange and red fluorescence. At the same time, the electrical impedance was measured at two frequencies (327 kHz and 6.030 MHz). Impedance signals are here presented as magnitude that is given by $|Z| = \sqrt{X^2 + Y^2}$, where X and Y are the real and the imaginary part of the electrical signal. For these experiments, the red fluorescent light was used as the trigger because all three species fluoresce at these wavelengths. The flow rate for each species was determined by time of flight measurement over the known distance between the upstream and downstream electrode pairs (39 mm sec^{-1} for *I. galbana and* 30 mm sec^{-1} for *Rhodosorus m.*). No data is available for *Synechococcus sp.* as this species was too small to generate a detectable impedance signal.

Figure 6-1(a-d) are scatter plots for a typical experiment consisting of a sample of approximately 2500 cells. For this data set, the three populations of cells were mixed in a ratio of 50% *Synechococcus sp.*, 15% *Rhodosorus m.* and 35% *I. galbana* and re-suspended in f/2 medium, which has an electrical conductivity of 6.2 S/m.

Figure 6-1(a) shows the magnitude of the orange fluorescence plotted against the red fluorescence (log scale) for 2500 events. The data show that the three different populations can be easily resolved on the basis of their fluorescence emission spectra. *I. galbana* does not emit in the orange region (585/40nm), while *Rhodosorus m.* emits strongly in both the orange and the red spectra. *Synechococcus sp.* can be identified because it emits both in the red and orange spectra with a very low intensity.

The impedance properties of the cells measured at two discreet frequencies are plotted in Figure 6-1(d). In this figure, the magnitude of the impedance signal (measured at a 327 kHz) is plotted against the magnitude of the impedance measured at 6.030 MHz on a log scale. The magnitude of the electrical impedance signal scales with size, decreasing from *Rhodosorus m.* to *I. galbana* then *Synechococcus sp*. The figure shows how the impedance signal provides accurate information on the size of particles and can be used in an integrated device as an alternative to the standard method of measuring scattered light for size analysis.

Figure 6-1 (b) and (c) show fluorescence (orange and red) plotted against the magnitude of the impedance measured at a frequency of 327 kHz. The data shows that the three populations of algae can be distinguished according to the level of fluorescence light emitted. Figure 6-1(c) shows that the intensity of the red fluorescence differs according to the population, as indicated in Figure 6-1(a). In particular, the red fluorescence signal from *Rhodosorus m.* is at least one order of magnitude greater that that from *I. galbana* and *Synechococcus sp.*

This same mixture of cells was also analysed with the commercial Flow Cytometer (BD FACSAria). The data was generated by triggering on the red fluorescence signal (695/40nm), with a flow pressure of 70psi. The data from an analysis of 15000 events are shown in Figure 6-2(a–c). Figure 6-2(a) is directly comparable with Figure 6-1(a), except that the BD FACSAria excites the cells with a 488nm laser. The fluorescence emission patterns for each subpopulation are similar, and show that the cells can be differentiated. The correlation between the two data sets

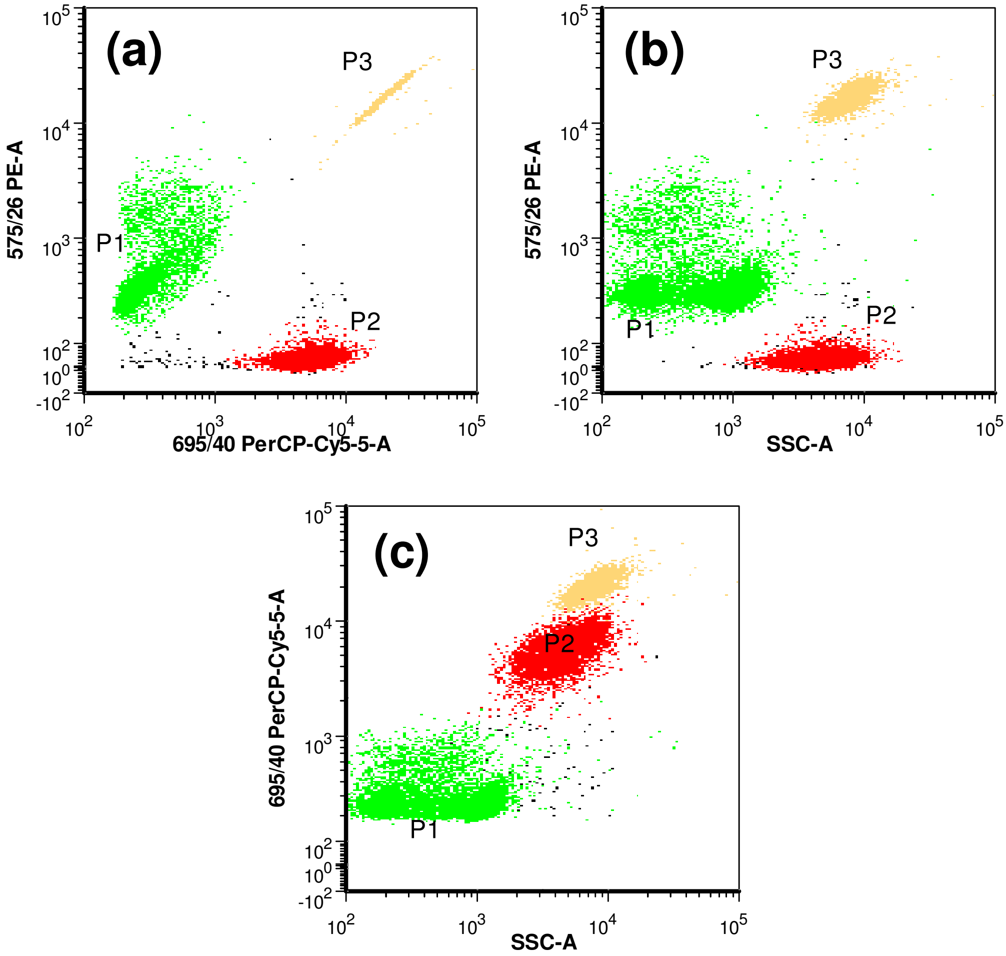

Figure 6-2 - Data from analysis with a commercial Flow Cytometer (BD FACSAria). (a) Orange fluorescence (575/26 nm) plotted against red fluorescence (645/40 nm); this plot is directly comparable with Figure 6-1(a), except that the BD FACSAria excites the cells with a 488nm laser. (b) Orange fluorescence (575/26nm) plotted against side scatter light. (c) Red fluorescence (695/40nm) plotted against side scatter light. P1, P2 and P3 are the signals generated by *Synechococcus sp.*, *I. galbana* and *Rhodosorus m.* respectively.

is excellent. For the data set analysed with the microflow cytometer, the relative percentage of cells was determined to be 51.9% *Synechococcus sp.*, 15.5% *Rhodosorus m.* and 32.6% *I. galbana*. The same population of cells analysed using the BD FACSAria, gave percentages of 51.1% of *Synechococcus sp.*, 13.4% of *Rhodosorus m.* and 34.3% of *I. galbana*.

The data shown in these figures was replicated for several different experimental runs at various ratios of the three algae. In each case the ratios of algae were different and the three populations could be clearly distinguished on the basis of either fluorescence or fluorescence and impedance. As an example, Figure 6-3(a-d) shows the results obtained with 892 events indicating a measured relative percentage of cells as

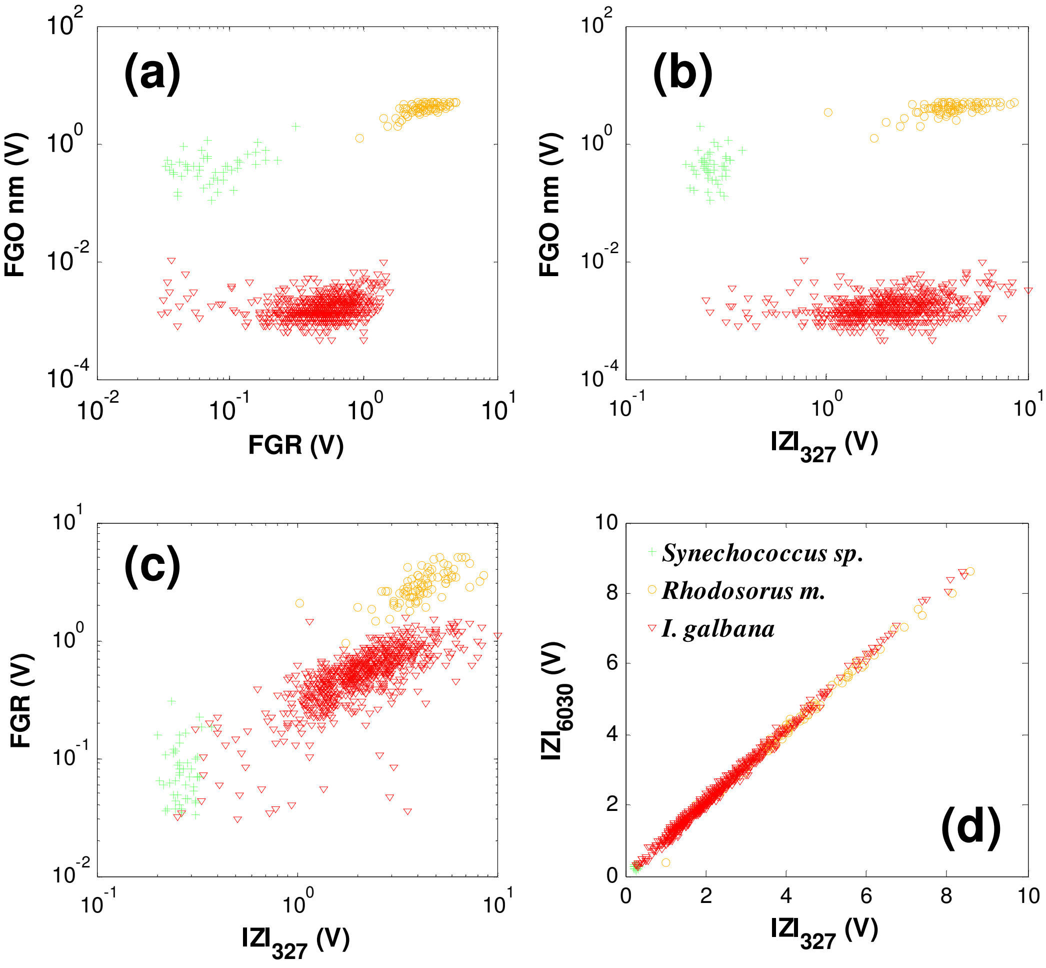

Figure 6-3 - Scatter plots in logarithmic scale for a typical experiment consisting of a sample of 892 events. FGO and FGR indicate green-orange and green-red fluorescence (see Table 1.1) measured at 585/45 and 675/50 nm respectively; $|Z|_{327}$ and $|Z|_{6030}$ indicate the magnitude of the impedance signal measured at 327 kHz and 6.03 MHz respectively. Legend for all plots is in the top left corner of graph (d).

CV	***I. galbana***	***Rhodosorus m.***	***Synechococcus sp.***
Micro flow cytometer **(Figure 6-1)**			
$\lvert Z \rvert_{327}$	25.6%	27.5%	--
$\lvert Z \rvert_{6030}$	31.0%	32.1%	--
FGO	14.6%	28.4%	90.5%
FGR	35.7%	31.0%	48.4%
BD FACSAria **(Figure 6-2)**			
SSC (%)	41.1%	105.7%	403.4%
Orange Fluorescence	63.7%	22.0%	105.6%
Red Fluorescence	30.4%	22.5%	50.8%

Table 6.1 – Statistical data from the microfluidic flow cytometer compared with that obtained from a BD FACSAria. The impedance signal from *Synechococcus* was too small to be detected reliably using the present channel dimension and is not shown. $|Z|_{327}$ and $|Z|_{6030}$ indicate the magnitude of the impedance signal measured at 327 kHz and 6.03 MHz respectively. FGO and FGR represent the orange and red fluorescence detected at 585/40 nm and 675/50 nm from the microfabricated cytometer. Orange and red fluorescence where detected by the BD FACS at 575/26 nm and 695/40 nm respectively.

follows: *I. galbana* 85.1% (759 cells), *Rhodosorus m.* 9.5% (85 cells), *Synechococcus sp.* 5.4% (48 cells). This data shows that a small number of events (5%) can be clearly distinguished using one or both wavelengths, but that impedance discrimination alone is not sensitive enough to discriminate the size differences between *Synechococcus sp.* and the other cells. This may reflect changes in the sizes of the sub-populations of cells during growth over extended periods of time.

Table 6.1 compares the coefficient of variation (CV) [3] for each method of analysis for all populations in both the microflow cytometer and BD FACSAria. These results show that similar variance is seen for fluorescence analysis in both systems. There is less variance in the IS data than SSC, though IS is unable to detect the smaller *Synechococcus sp.* The apparent difference in variance between Figure 6-1 and Figure 6-2 is probably due to the size of the channel in the microfluidic device that allows a better confinement of the cells within the detection region.

In the literature, microfabricated cytometers have shown CVs ranging from 2.5% to 30% [4; 5; 6; 7; 8]. However, the higher CV obtained by chip A is probably due to the use of irregular biological organisms, as also demonstrated by the high CV obtained for the same organisms by the commercial instrument.

6.3 Chip A label free detection of *E. coli* bacteria

Chip A was also used to investigate the possibility of detection of bacteria using impedance spectroscopy. The bacteria were a particular strain of *E. coli* (see section 4.6) expressing DS Red protein, which emits orange fluorescence when irradiated with green light. The bacteria were prepared following the procedure described in section 4.6. The microfluidic set-up described in section 4.8.3.1 was used for flow cytometry experiments. The chip used featured a 5 μm high and 10 μm wide microfluidic channel and electrodes 10 μm wide with a 10 μm gap. Channel and electrode dimensions were the smallest available for chip A because the detection volume must have similar dimension to the particles analysed in order to detect the electrical properties of particles [1; 9].

For standard saline solutions, the response of the impedance detection system is affected by the polarisation of membrane capacitance when the frequencies applied are in the range of MHz. When the frequency applied is in the range of kHz, the flowing cell is essentially non-conducting and the measured magnitude is proportional to volume or size [10]. In particular, frequencies of 327 kHz and 5 MHz were chosen for the experiments because preliminary tests showed no increase in the background noise due to the presence of external sources (i.e. radio-frequencies). The voltage applied to the electrodes was 1 V_{pp}, the sampling rate was 60 kHz and the particle flow speed was determined to be 39.8 mm sec^{-1} for *E. coli* and 49.8 mm sec^{-1} for red fluorescent microspheres. The particle speed was determined by measuring the transit time between the two pairs of electrodes. As for fluorescence light, although the DS protein excitation peak is at 553 nm [11] and the 2 μm bead excitation peak is 633 nm, it was observed that a 532 nm wavelength was adequate for the excitation of both specimens. Emitted light was detected with two filters: one at 585/40 nm and one at 715LP nm.

The first experiment (**experiment 1**) was performed using the X component of the impedance signal at 327 kHz as a trigger because preliminary tests showed that on average it gave a higher intensity than the other impedance signals (Y component of the 327 kHz signal; X and Y component of the 5 MHz signal). The scatter plots obtained from experiment 1 are shown in Figure 6-4. Signals generated from microspheres, bacteria and noise were first identified by plotting red fluorescence (715LP) against orange fluorescence (585/40 nm) (Figure 6-4(b)). Identification of microspheres was

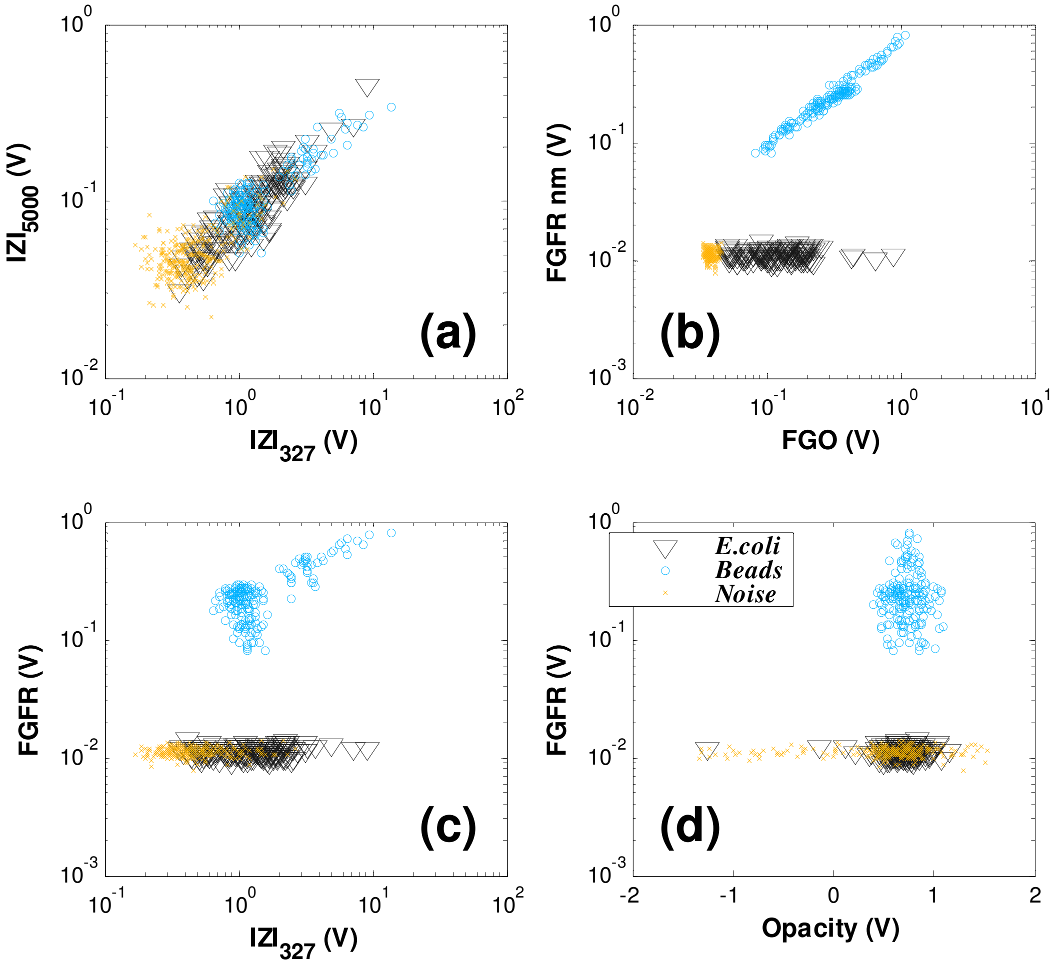

Figure 6-4 - Scatter plots obtained from experiment 1 (662 particles). FGO and FGFR indicate green-orange and green-far red fluorescence (see Table 1.1) measured at 585/45 and above 715 nm respectively; $|Z|_{327}$ and $|Z|_{5000}$ indicate the magnitude of the impedance signal measured at 327 kHz and 5 MHz respectively. Legend for all plots is in the top left corner of graph (d).

also possible by plotting impedance against fluorescence (Figure 6-4(c)) but bacteria could not be distinguished from noise signals without the use of orange fluorescence. Figure 6-4(a) shows the scatter plot for impedance magnitude at 5 MHz against magnitude at 327 kHz. Although some difference in distribution can be noted, impedance spectroscopy alone is not enough to clearly characterise the different events. Therefore, another parameter known as opacity was calculated and plotted. Opacity measures the difference in particles resistivity at high and low frequencies [12] and was used to normalise the data for cell size and cell position in the detection region, between the measurement electrodes in the microfluidic channel [13]. The results for opacity plotted against far red fluorescence are showed in Figure 6-4(d). This graph shows that microspheres and bacteria have similar opacity and that the latter is not suitable to characterise the different populations, probably because the membrane of the bacteria acts as a perfect insulator at both frequencies and signals are proportional only to the volume of the particle.

In order to obtain a clear characterisation of the populations present in the sample and fully characterise the ability of the microfabricated sensor for label-free detection of bacteria, a second experiment was performed (**experiment 2**) using the same mixture of experiment 1 and setting the trigger on the orange fluorescence channel. As for experiment 1, the two different populations can be identified from the red fluorescence against orange fluorescence (Figure 6-5(b)); note that due to the high sensitivity of the fluorescence induced detection system (FID) no noise signals where detected.

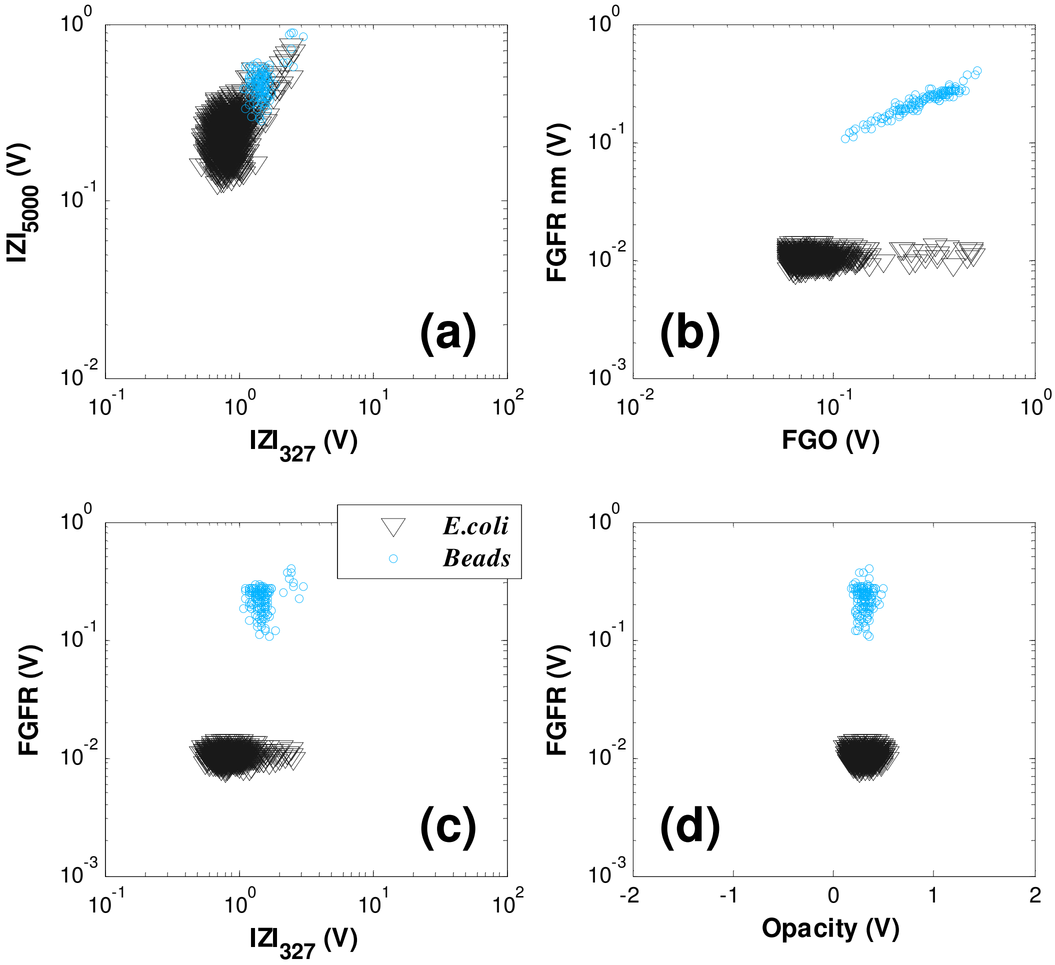

Figure 6-5 – Results obtained from experiment 2 (1837 particles). FGO and FGFR indicate green-orange and green-far red fluorescence (see Table 1.1) measured at 585/45 and above 715 nm respectively; $|Z|_{327}$ and $|Z|_{5000}$ indicate the magnitude of the impedance signal measured at 327 kHz and 5 MHz respectively. Legend for all plots is in the top right corner of graph (c).

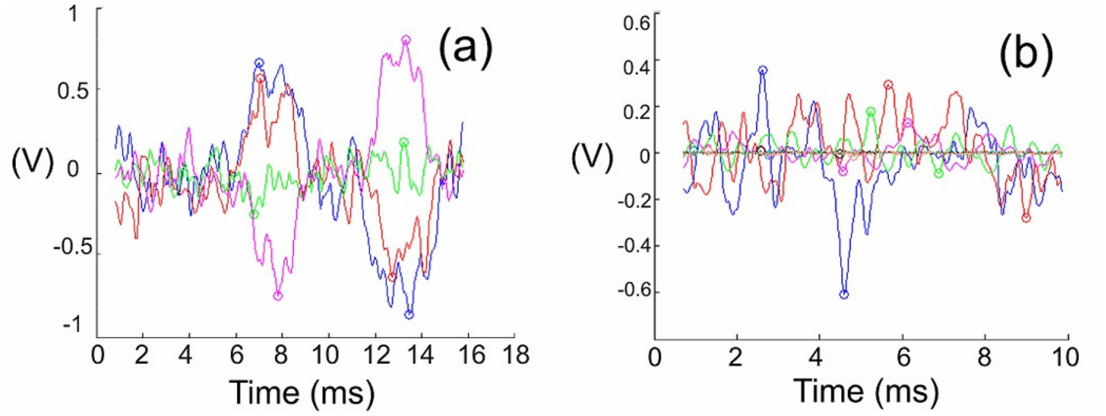

Figure 6-6 – Signal detected from the μflow cytometer. (a) signal from e. coli; (b) noise signal.

For the data set obtained from experiment 1, the relative percentage of particles was determined to be 46% bacteria and 54% microspheres. The same population of particles analysed using orange fluorescence as trigger, gave a relative percentage of 7.5% beads and 92.5% of *E. coli*. Therefore, impedance detection alone is not sensitive enough to detect approximately 90% of the bacteria. The low sensitivity of IS is confirmed by careful study of the signals obtained for experiment 1. For example, Figure 6-6 shows a generic *E. coli* signal (a) and a generic noise signal (b). The signal in (a) was clearly generated by a particle because 3 channels out of 4 show identical sinusoidal patterns. On the other hand, the signal in (b) was clearly generated by a high fluctuation in the baseline of the trigger channel (peak at -0.6 V) as the same pattern is not visible in the other channels.

The reason for the low sensitivity of IS is probably the small volume fraction occupied by the bacteria in the detection region. Therefore only the biggest bacteria are able to generate an impedance signal. On the other hand FID has higher sensitivity than IS and when the trigger is set to fluorescence the percentage of *E. coli* detected increase drastically. The sensitivity of the IS detection system can be increased by fabricating a chip with smaller channel and smaller electrodes. However, the development of a microfluidic device for label free bacteria detection was not the main objective of this thesis and therefore the project was not further investigated.

6.4 Chip B flow cytometry - Experimental conditions

As already explained (section 3.4) limits in channels size and optical system used induced to abandon chip A and to design and fabricate chip B specifically for the study of phytoplankton. However, the new device needed to be characterised first. Various types of microspheres were flowed through chip B for characterisation. Chip B cytometry experiments presented in this thesis were performed with design WL; this design was chosen because the characterisation measurements (Chapter 5) showed that although other designs generated lower power losses, the WL design generated the smallest beam width in the middle of the detection region. Focussing was chosen over power losses because poor focussing increases the amount of excitation radiation collected by optical fibres inserted in grooves designed to collect scatter light (see section 3.4.3.1), therefore increasing the signal to noise ratio (S/N) of the scatter signals.

All chip B experiments were performed with excitation light coming from the normal groove, scatter light detected from the 22° groove and fluorescence light detected by the two 45° grooves on the side of the normal groove to reduce the amount of incident excitation light entering the fluorescence detector. Electrical impedance was measured at 480 kHz and 6 MHz. Sampling rates ranged from 20 to 120 kHz and the voltage applied to the electrodes ranged from 0.35 to 3 V_{pp}. The sampling rate and the voltage were varied depending on flow speed, medium conductivity and particles dimensions. The threshold was chosen among the signals generated by all particles and was set on the signal with the highest S/N. Note that data for red fluorescence (675/50 nm) and impedance magnitude at 6 MHz are usually not shown because they have a similar pattern to orange fluorescence (585/40 nm) and impedance magnitude at 480 kHz respectively.

Polymer microspheres analysed with chip B were suspended in PBS, sucrose, Tween® and RFD as described in section 4.2.2 at concentrations of approximately 1×10^5 particles ml^{-1}. Samples of approximately 50 µl were run through the micro-chip and focussed in the middle of the channel using hydrodynamic focussing and a buffer of PBS and sucrose (section 4.2.2). The central stream was maintained at a width of 25 µm for all experiments. The particle flow speed was determined by time of flight measurement over the known distance between the upstream and downstream electrode pairs. Polymer particles analysed with the microfabricated cytometer were also suspended in PBS and analysed with the BD FACSAria. Since the dimension of the particles ranged from 15 to 45 µm, the BD FACSAria was equipped with a 100 µm nozzle and the flow rate pressure was set on 20 psi. During analysis, 300 rpm sample

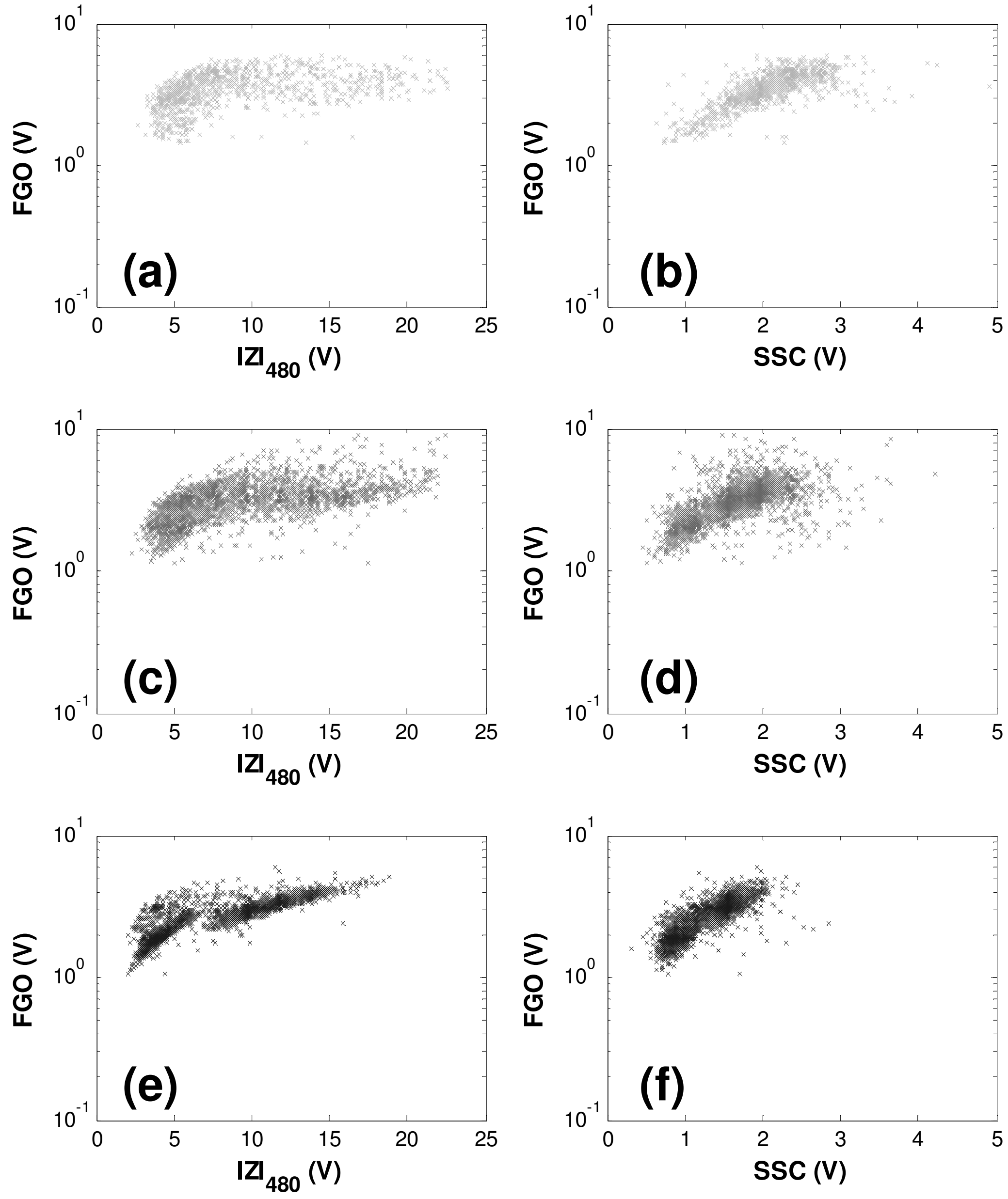

Figure 6-7 – Scatter plots for a sample of 31 μm fluorescent microspheres with chip B at three different flow rates. The voltage applied to the electrodes was 1 V_{pp} , the trigger was set on the X component of impedance at 480 kHz. The sampling rate was set to 20, 50 and 120 kHz for particles flow speeds of 19 mm sec^{-1}, 85 mm sec^{-1} and 359 mm sec^{-1} respectively. (a, b) Scatter plots obtained for an experiment of approximately 2000 particles at average flow velocity of 19mm sec^{-1}; (b, c) scatter plots obtained for an experiment of approximately 2400 particles at average flow velocity of 85 mm sec^{-1} and (e, f) scatter plots obtained from an experiments of approximately 2600 particles at average flow velocities of 359 mm sec^{-1}. In the plots, FGO and FGR indicate green-orange and green-red fluorescence measured at 585/45 and 675/50 nm respectively; $|Z|_{480}$ indicate the magnitude of the impedance signal measured at 480 kHz and SSC indicate side scatter light measured at 22°.

agitation was activated to prevent particles precipitation. The microsphere sample was first prepared in DI water and split in two fractions so that two samples with same composition where obtained; the two samples were resuspended in different media (section 4.2.2) so that they could be analysed with both the BD FACS and microfabricated cytometers.

6.5 Chip B - Cytometry of 31 μm particles

Characterisation experiments were performed with 31 μm orange microspheres (see section 4.2.2) at average particle flow speeds ranging from 15 to 360 mm sec^{-1} and the data obtained are shown in Figure 6-7 and Figure 6-8. Figure 6-7(a, c, e) are scatter plots of orange fluorescence against magnitude of impedance at 480 kHz for different particle flow speeds. A single distribution is generated at a particle flow speed of 19 mm sec^{-1} (Figure 6-7(a)), however, as the flow speed increases the distribution changes (Figure 6-7(b)) and eventually splits into two distinct regions at a particle flow speed of 359 mm sec^{-1} (Figure 6-7(c)). A similar behaviour is also observed for fluorescence against SSC Figure 6-7(b, d, f) although the distributions generated in this case are not clearly separated. The behaviour of the signal distribution can be better interpreted

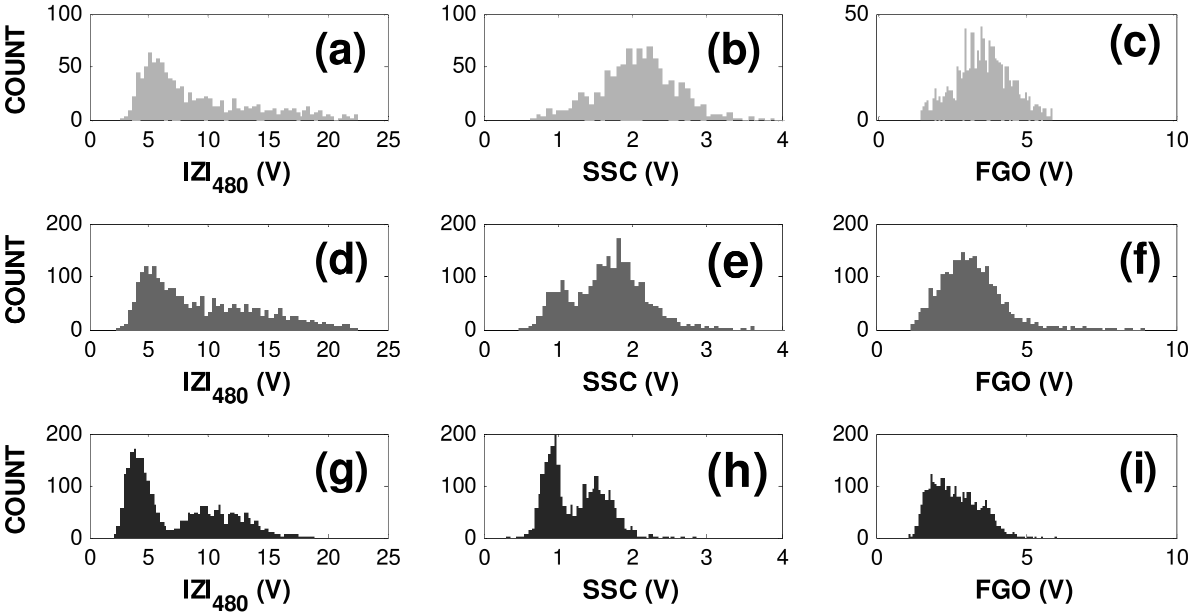

Figure 6-8 – Histograms of the experiment presented at Figure 6-7. (a, b, c) particle flow speed = 19 mm sec^{-1}; (d, e, f) particle flow speed = 85 mm sec^{-1}; (g, h, i) particle flow speed = 359 mm sec^{-1}. FGO and FGR indicate green-orange and green-red fluorescence measured at 585/45 and 675/50 nm respectively; $|Z|_{480}$ indicates the magnitude of the impedance signal measured at 480 kHz and SSC indicate side scatter light measured at 22°.

using the histograms presented in Figure 6-8. The histograms show that all signals generate single distributions at low flow rates (19 mm sec^{-1}). As the flow rate increases, the signals generated by impedance and light scatter gradually move to two distributions while the orange fluorescence signal starts as single distribution and forms two unresolved peaks at high flow speed.

31 μm particles were also analysed with the commercial cytometer using FSC as triggering signal. The data obtained for an experiment of approximately 900 particles are presented in Figure 6-9. No anomalous distribution was obtained by the commercial instrument, showing that 31 μm particles are uniformly distributed in terms of size and optical properties. Therefore, the particles used are not the cause of the two distributions seen in Figure 6-7 and Figure 6-8. Furthermore, the split distribution appear simultaneously in all three parameters suggesting the presence of a physical phenomena that affects all the output parameters and that is not directly related to the electric field generated by the electrodes or by the excitation light. This theory was also enforced by similar results obtained in various experiments with different particles.

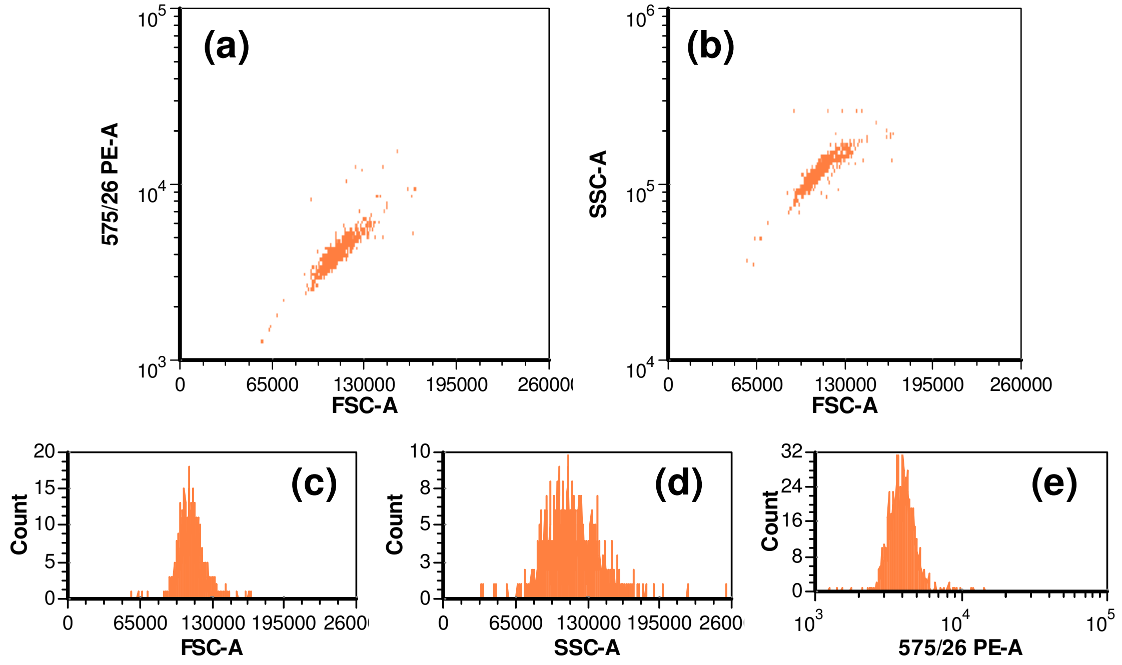

Figure 6-9 – Scatter plot and histograms obtained from BD FACS analysis of 31 μm microspheres. (a) Orange fluorescence (575/26-PE) against forward scatter light; (b) side scatter light against forward scatter light; (c) histogram of forward scatter light; (d) histogram of side scatter light; (e) histogram of orange fluorescence.

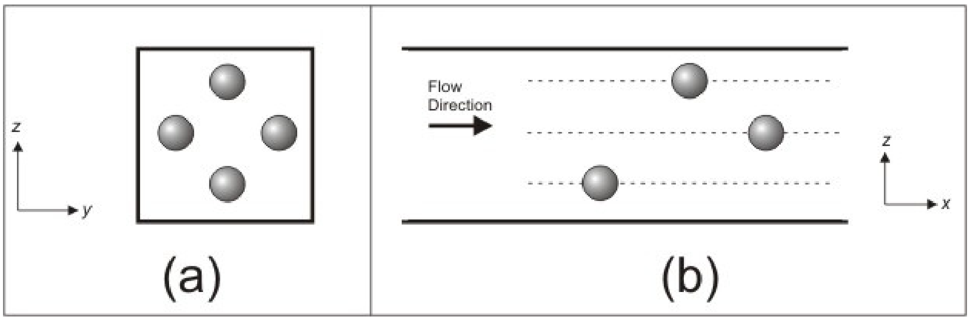

Figure 6-10 – Inertial focussing phenomenon described in [14] for a square section channel (50x50 μm^2). (a) Channel cross section: the circles represent particles positioned in the four symmetric equilibrium positions generated by the inertial focussing phenomena. (b) Channel side view: the circles represent particles flowing in the channel along the paths indicated by the dashed lines. The coordinates of the section are showed in each figure. Adapted from [14].

6.5.1 Inertial focussing

A recent study by Di Carlo *et al.* [14] described an inertial focussing phenomenon in a square section channel that focus particles into 4 symmetric equilibrium positions close to the faces of the channel (see Figure 6-10). The phenomenon happened at a channel Reynold's number ($R_c = 90$) and a particle Reynold's number ($R_p = 2.9$) similar to the ones obtained for chip B (Table 6.2), it is therefore possible that a similar inertial focussing phenomenon is taking place into chip B. Moreover, since the detection system integrated in chip B are not symmetrical in every direction, the focussing positions generated by inertial phenomena may be asymmetrical in respect to the detection systems. Since two identical particles flowing in two different position can give two different signals [15], inertial focussing phenomena may be the cause of the distribution split observed in section 6.5 and therefore needed to be investigated.

In Di Carlo *et al.* [14], the following equation for the calculation of the channel Reynolds number, the particle Reynolds number and particle migration velocity from the centre to the edge of the channel (v_p) are given:

$$R_c = \frac{v_{max} D_h}{\nu} \qquad \textbf{6.1}$$

$$R_p = R_c \frac{a^2}{D_h^2} \qquad \textbf{6.2}$$

$$v_p = \frac{v_{max}^2 a^3}{3\pi \nu D_h^2} f_c(R_c, x_c) \qquad \textbf{6.3}$$

|V| **mm sec^{-1}**	**V_{max}** **mm sec^{-1}**	**R_c**	**R_p**	**V_p** **m sec^{-1}**	**Migration** **(m)**
19	**25**	2.15	0.04	$7.2 \cdot 10^{-06}$	$1.2 \cdot 10^{-6}$
85	**103**	8.90	0.16	$1.2 \cdot 10^{-04}$	$4.8 \cdot 10^{-6}$
359	**513**	44.1	0.82	$3.0 \cdot 10^{-03}$	$2.4 \cdot 10^{-5}$

Table 6.2 – The values of R_p, R_c and v_p obtained from equations 6.1, 6.2 and 6.3 for the microfluidic channel of chip B at different average particle flow velocities (|v|).

where v_{max} is the maximum channel velocity, ν is the kinematic viscosity, a is the particle radius, D_h is the hydraulic diameter defined as $2w_{ch}l_{ch}/(w_{ch}+l_{ch})$ (w_{ch} and l_{ch} being width and height of the channel) and f_c (R_c , x_c) is a lift coefficient that depends on the position of the particle in the cross section of the channel. f_c is considered equal to zero when the particle reaches the equilibrium position. An average value of 0.5 for f_c was considered when calculating v_p of particles [14].

The values of R_p, R_c, v_p for 31 μm particles flowing into chip B were calculated using equations 6.1, 6.2 and 6.3, while migration was calculated by multiplying v_p for the travel time required by a particle to go from the inlet to the detection region. The results obtained are presented in Table 6.2. A migration of 24 μm was obtained for a particle flowing at a speed of 513 mm sec^{-1}. Since the radius of the particles is 15.5 μm, the displacement calculated would place a particle on the edge of the channel (a distance of 1 μm). Therefore, the calculations support the possibility of inertial focussing taking place in the microfluidic channel at high particle flow velocities and suggest performing experiments and simulations to verify the presence of the phenomena in chip B.

6.5.2 Particle tracking

Particle tracking experiments were performed to verify if particles flowing in the microfluidic channel show the presence of preferential positions. Particle tracking experiments were performed using the set up described in section 4.9. 31 μm orange fluorescent microspheres (see section 4.2.2) were positioned within the channel using hydrodynamic focussing; the width of the central stream was set to 25 μm to match experiments (section 6.4). Videos of particles flowing into the channel were recorded (Figure 6-11(1, 2)) so that automated counting and positioning of the particles could be performed with a software written in LabVIEW^{TM} by Diego Morganti (University of

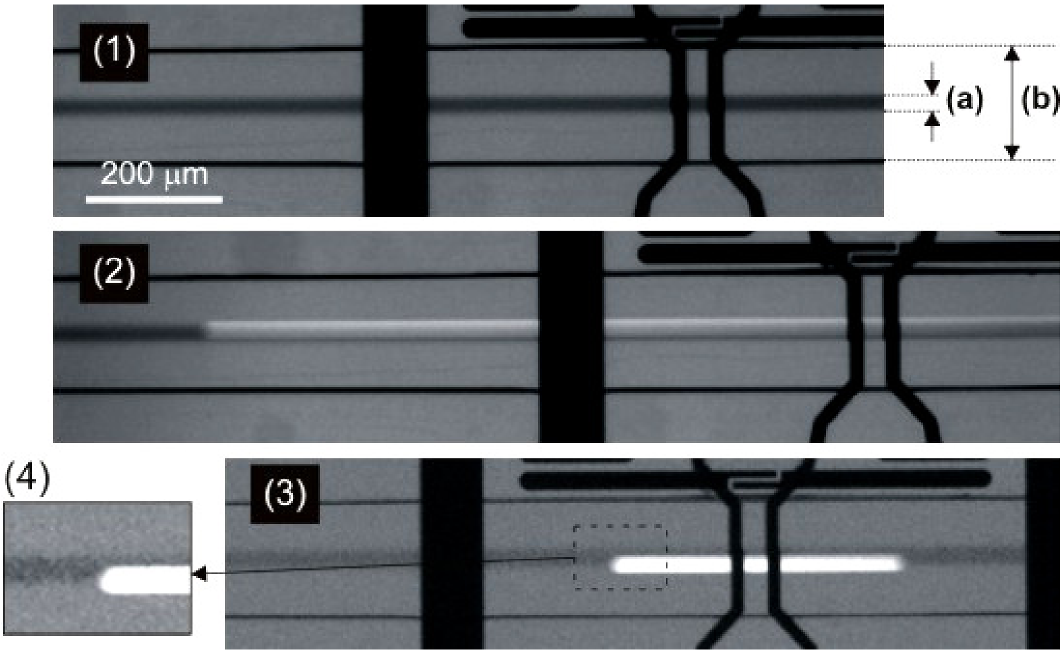

Figure 6-11 – Microscope pictures extracted from videos of particle tracking experiments. The detection region of the chip is illuminated with a halogen lamp and 488 nm radiation simultaneously so that is possible to see particle fluorescence and channel outlines simultaneously. (1) Picture of the detection region with no particle flowing; (a) indicates the central stream that is coloured with red food dye (RFD) and (b) indicates the channel. (2) Picture taken with high exposure time (0.07 sec) to obtain long tracks for automated positioning analysis. (3) Picture taken with low exposure time (0.01 sec) to obtain short tracks for particles speed measurements. (4) detail of (3) showing that the particle is suspended between buffer and sample medium.

Southampton); as the software recorded particles only from a section of the channel, the camera exposure time was set to generate long particle tracks. Particle flow speed was obtained by recording an additional video with a reduced camera exposure time so that short tracks (Figure 6-11(3)) were generated and particle speed could be measured from track length. Note that Figure 6-11(3,4) shows that sometimes particles were suspended exactly in the middle between sample and buffer medium.

Experiments were performed at average speeds of 36 mm sec^{-1} (R_p = 0.07) and 393 mm sec^{-1} (R_p = 0.89). Histograms plotting the position along the width of the channel (*y* dimension) for approximately 300 particles are shown in Figure 6-12. The data produce Gaussian distributions centred in the middle of the channel confined by the limits of the hydrodynamic focussing (the distributions were fitted with Origin software (OriginLab) using equation 5.2). The Gaussian fitting of the particle tracking data have correlation of 0.9604 for 36 mm sec^{-1} and 0.9892 for 200 mm min^{-1}. It is therefore possible to assume that the inertial focussing phenomenon described by Di Carlo *et. al.* [14] is not taking place along the *y* axis for chip B.

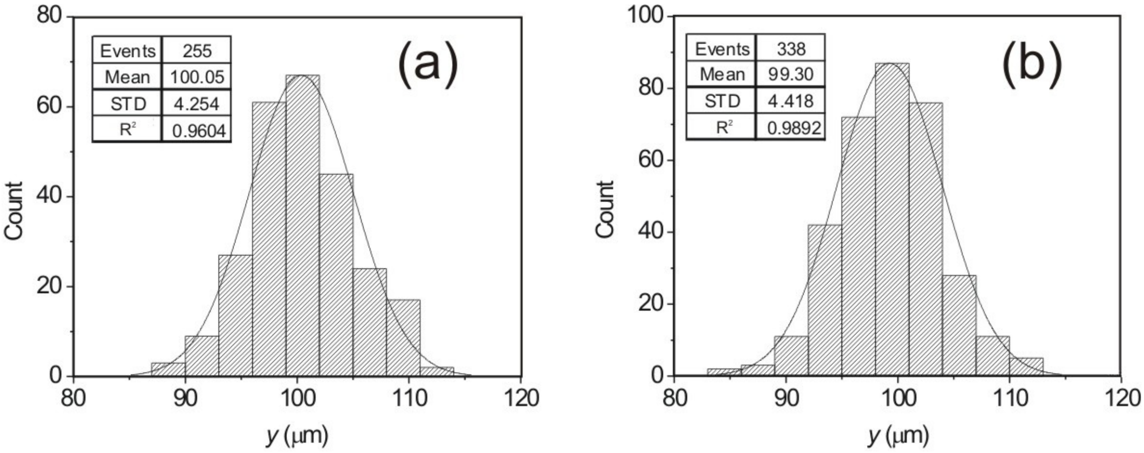

Figure 6-12 – Histograms for 31 μm microspheres flowing through microfluidic channel at different particle flow speeds (FS) and sample stream widths (SSW): (a) FS = 36 μm sec^{-1}, SSW=25 μm; (b) FS = 393 μm sec^{-1}, SSW = 25 μm. The horizontal axis is the position of particles along the width of the channel (*y* coordinate*)* with zero and 200 μm being the channel walls. The Gaussian fitting curves are also shown on the graphs together with the fitting results.

6.5.1 Hydrodynamic simulations

Particle tracking experiments showed no sign of inertial focussing along channel width. Since it was not possible to optically image particles flowing behaviour along the depth of the channel, the position of particles along *z* was extrapolated from particle speed. Hydrodynamic simulations were undertaken to better understand how flow

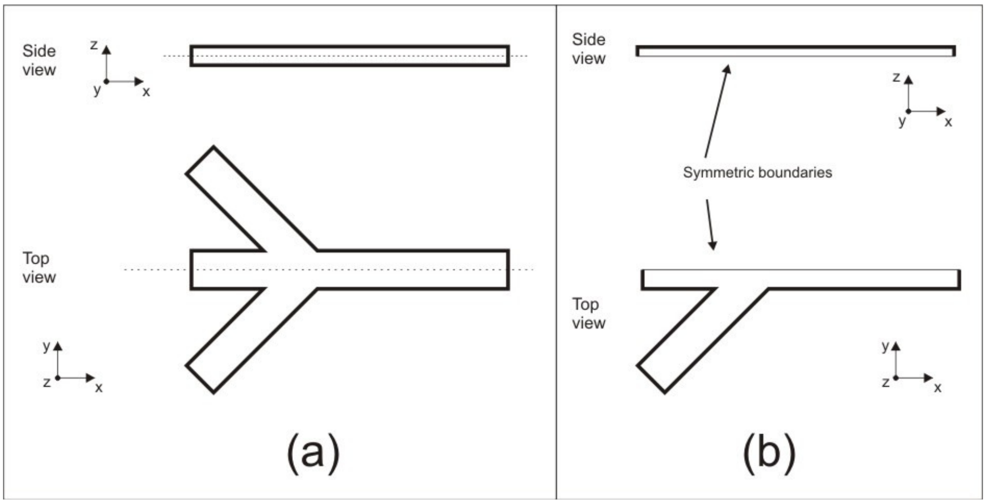

Figure 6-13 – Layouts used for the simulations of hydrodynamic behaviour. (a) Complete layout considered. Planes of symmetry are represented by the dashed lines running along the middle of top and side view. Channels dimensions are all 200 μm wide and 80 μm high. (b) Effective layout used for simulations. Boundaries subjected to symmetric conditions are indicated.

speed correlates to particles position. Simulations were performed using COMSOL Multiphiscs® software (COMSOL, Inc.) that uses the finite-element method (FEM). The software was set to use the incompressible Navier-Stokes equation that describes the motion of fluids expressed as [16]:

$$-\nabla p + \eta \nabla^2 \mathbf{v} = \rho\left(\frac{\partial \mathbf{v}}{\partial t} + (\mathbf{v}\cdot\nabla)\mathbf{v}\right) \qquad \textbf{6.4}$$

where p is the applied pressure, $\mathbf{v}$ is the velocity vector, ρ is the fluid density and η is the viscosity of the fluid. Simulations where performed using a 3D layout depicted in Figure 6-13(a). The channels were all 200 μm wide and 80 μm high to emulate the dimensions of chip B microfluidic channels (see section 3.4). The array included three inlet channels on the left hand-side of the layout, the channel in the middle is the sample channel and the channels on top and bottom are the sheath channels. The fluid had a density of a 11% solution of sucrose in water (ρ = 1.0423 kg/m^3 and η = 1.378 mPa·s [17]). Since the microfluidic chip had two planes of symmetry (*xy* and *xz*), only one quarter of the array was simulated (see Figure 6-14(b)). The boundary conditions were:

- Zero flow at every wall boundary.
- Symmetry for boundaries generated by dividing the channel in four identical regions (see Figure 6-13).
- Pressure ratio between sample and sheath flow inlet surfaces = 0.92.

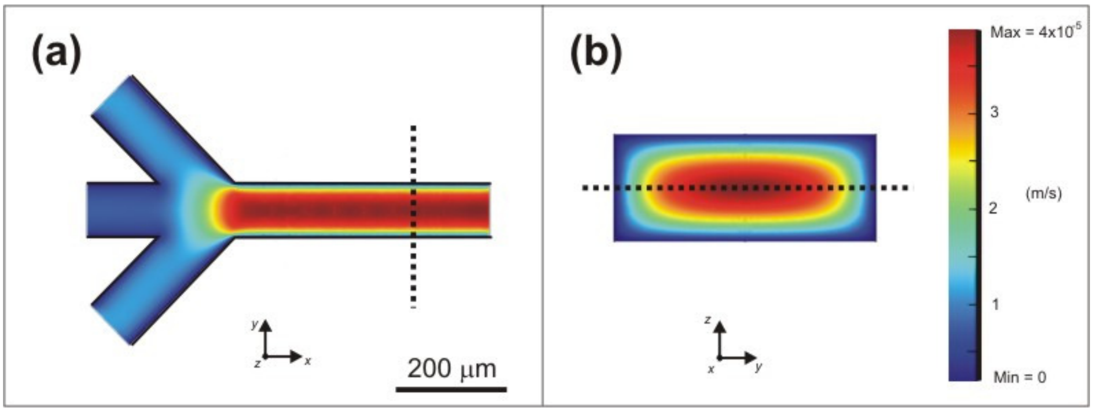

Figure 6-14- Boundary plot of velocity profile for a chip B with channels 200 μm wide and 80 μm high. The values of pressure applied are 92 Pa in the inlet and 100 Pa in each of the sheath flow channels. (a) Velocity profile along the *xy* plane for *z* = 40 μm (dashed line in (b)). (b) Velocity profile along the *yz* plane for *x* = 2.6 mm (dashed line in (a)), that correspond to the position of the detection region.

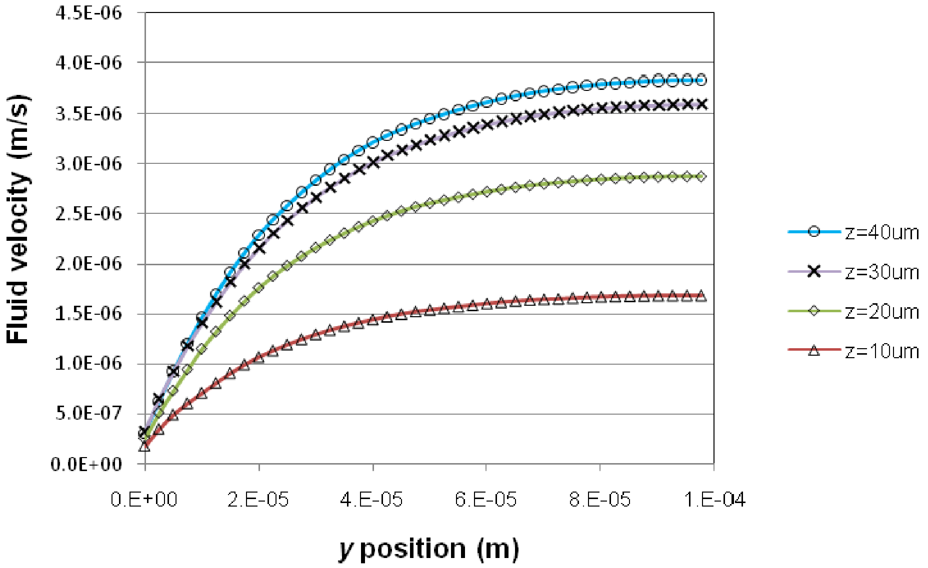

Figure 6-15 – Graph showing fluid velocity along the dashed line of Figure 6-14(a). Since the microfluidic channel has two planes of symmetry, only values within half width (0 < *y* < 100 μm) and half height (0 < *z* < 40 μm) are reported. Note that *y, z* = 0 correspond to channel edges.

Simulations were performed for sample inlet pressure ranging between 0.92 and 92,000 Pa and an example of velocity profile obtained is presented in Figure 6-14, Figure 6-15 and Figure 6-16. The results show that a parabolic profile of velocity is formed in the detection region. The width of the sample stream (defined by the outermost streamlines of the sample stream within the main channel in Figure 6-16) was predicted to be 25 μm. The velocity profiles obtained were parabolic and in the interval included by the central stream (between y = 87.5 μm and y = 112.5 μm) the flow velocity was approximately constant along the y dimension (channel width) and changed only along the z dimension (channel depth), therefore indicating that speed can be used as indicator of particles position along channel height.

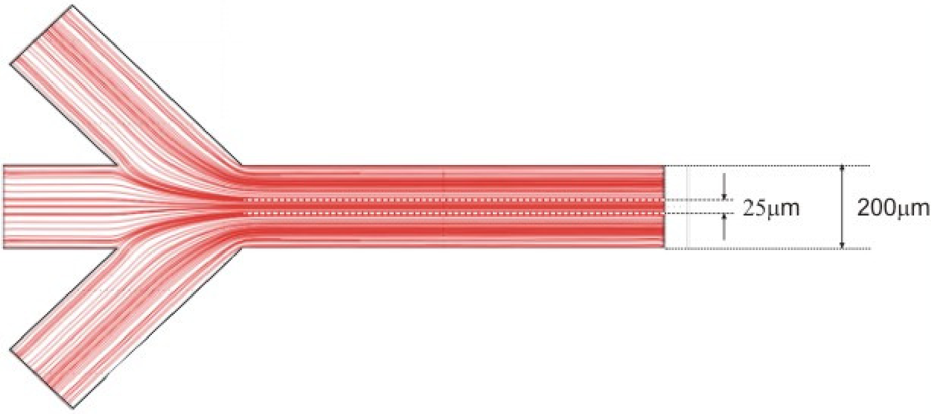

Figure 6-16 – Streamlines diagram of velocity profile for the same conditions as Figure 6-14. The width of the central stream is identified by following the streamlines coming from the corner at the channel junctions.

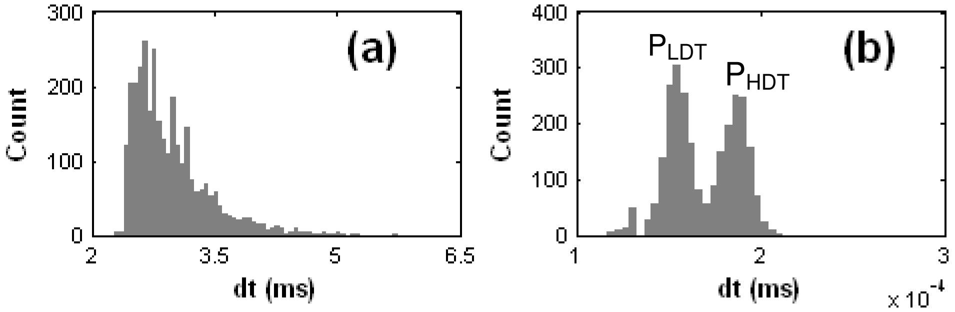

Figure 6-17 – Histograms of the transit time (dt) for the experiment presented at Figure 6-7. (a) Particles average flow speed = 19 mm sec^{-1}; (b) particles average flow speed = 359 mm sec^{-1}. P_{LDT} and P_{HDT} indicate the distribution at low and high dt respectively.

6.5.2 Velocity related phenomena

Since hydrodynamic simulations showed that particle velocity is directly related to particle position along channel depth, this section presents and discusses results for particles transit times (dt, inversely related to particles velocity) for the experiments presented in section 6.4. Figure 6-17 are histograms of dt while Figure 6-18 shows intensity plots correlating dt with the intensity of the signals detected by the microfabricated cytometer. Since average velocities of 85 mm sec^{-1} are an intermediate stage, only data for the experiment at 19 and 359 mm sec^{-1} are presented.

The transit times for particles with average velocities of 19 mm sec^{-1} appear as half-Gaussian distributions (Figure 6-17(a)), suggesting that no inertial focussing is achieved. The peak is at the lowest dt because it is related to particles flowing in the middle of the channel. Because of the symmetrical distribution of flow velocities along the *z* direction, particles flowing below and above the centre of the channel have the same flow velocities and higher transit times than the peak. T

he transit time histogram for average particle flow velocities of 359 mm sec^{-1} (Figure 6-17(b)) show two well resolved distributions (P_{HDT} and P_{LDT}). Since there are no evident anomalies in the signals presented in P_{HDT} and P_{LDT} (see Figure 6-19), and considering the results obtained for the particle migration velocity (Table 6.2) the two distributions are probably caused by inertial focussing. The two distributions were fitted to Gaussian curves (see Figure 6-22) and gave coefficients of determination (R^2) of 0.991 and 0.978 for P_{LDT} and P_{HDT} respectively. Since both distributions can be fitted with Gaussian curves they are probably related to particles that are not flowing in the middle of the channel (z = 40 μm), otherwise they would give half-Gaussian symmetry similar to the one in Figure 6-17(a). However, inertial focussing is expected to give particles in symmetrical positions [14] but the parabolic profile of velocities showed in section 6.5.1 indicates that symmetrical positions would have the same velocity pattern. Therefore the two distributions in Figure 6-17(b) indicate the presence of asymmetrical focussing positions. The impression that the two inertial focussing positions are not symmetrical is also confirmed by the response of the various output signals in correlation with the transit time, Figure 6-18(d, e, f). The scatter plots show that particles with the lowest transit time (and therefore highest speed) have the highest signal. In terms of fluorescence, the effect is explained by the ray trace simulations presented in section3.4.3.4. The simulations show that the excitation intensity is

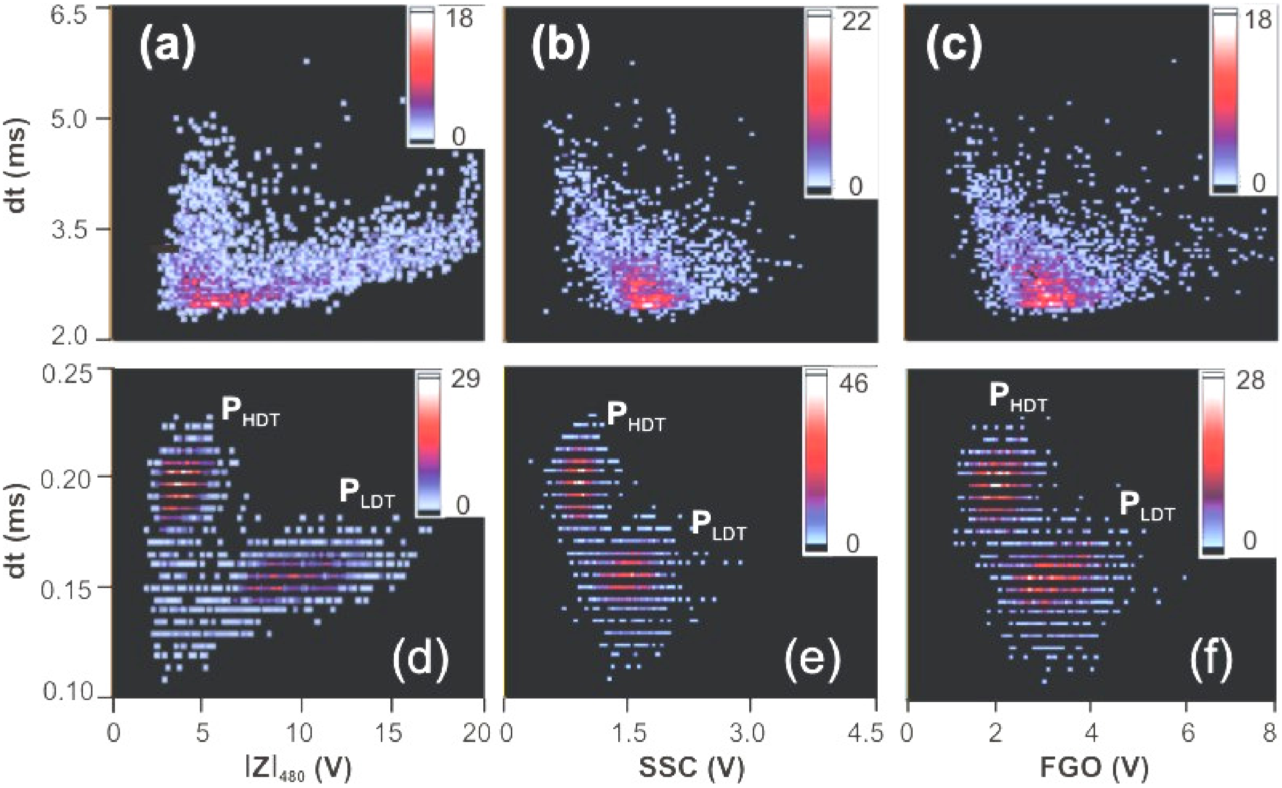

Figure 6-18 – Intensity scatter plots of the experiment presented at Figure 6-7. The plots correlate particle speed with the magnitude of the impedance signal at 480 kHz (a, d), the magnitude of the scatter signal (b, e) and the magnitude of fluorescence at 585/40 nm (c, f). The plots are relative to experiment with average particle velocity of 19 (a, b, c) and 359 mm sec^{-1} (d, e, f). P_{HDT} and P_{LDT} indicate the distribution at high and low dt respectively, obtained at particle velocities of 359 mm sec^{-1}. Note that in figures (d, e, f) the distributions are formed by lines separated of approximately 1x10^{-2} ms; this is due to the sampling frequency that was set on 120 kHz, giving a minimum resolution of dt of 8x10^{-3} ms.

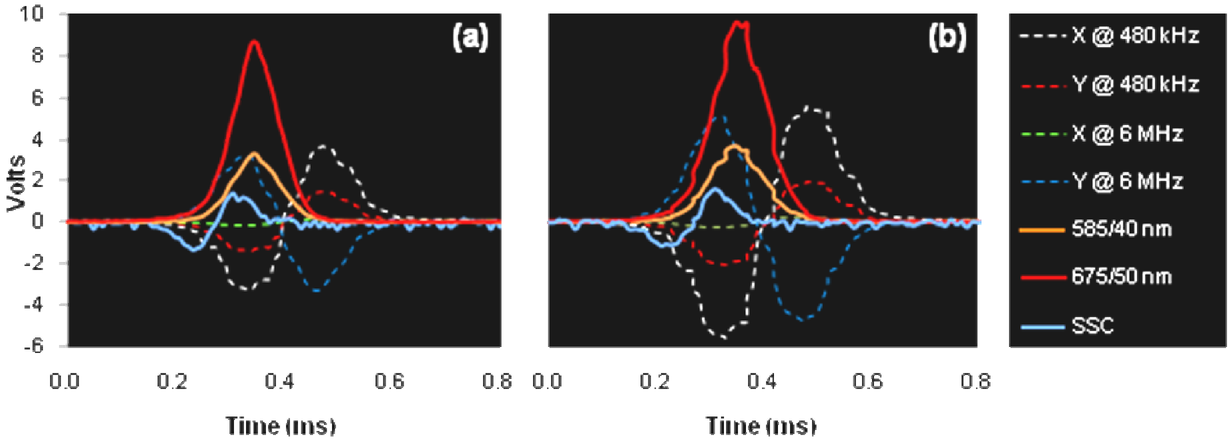

Figure 6-19 – Examples of signal sets from the two distributions shown in Figure 6-33. (a) Signal set from P_{HDT}; (b) signal set from P_{LDT}. Dashed lines are impedance signals and continuous lines are optical signals.

maximum in the centre of the channel (z = 40 µm) and decreases towards the edges (z = 0, 80 µm). Therefore two identical particles flowing at different distances from the centre of the channel give optical signals of different intensity; in particular, the particle flowing closer to the centre of the channel (hence with the lowest dt) will give the highest optical signal.

For the impedance signals, COMSOL simulations (Figure 6-20) showed that the distribution of the electric field is not uniform. Particles in different positions will therefore experience different field intensities and will give impedance signals of different intensity.

The considerations of transit time and the intensity of the output signals imply the presence of phenomena that generate asymmetry in the position of the particles along channel depth and width. The displacement is probably generated by bonding together four different layers.

Figure 6-20 – Schematic diagrams depicting the distribution of the electric field in the detection region as obtained by COMSOL simulations. The position of the electrodes is indicated by the thick lines on top and bottom of the channel cross-sections.

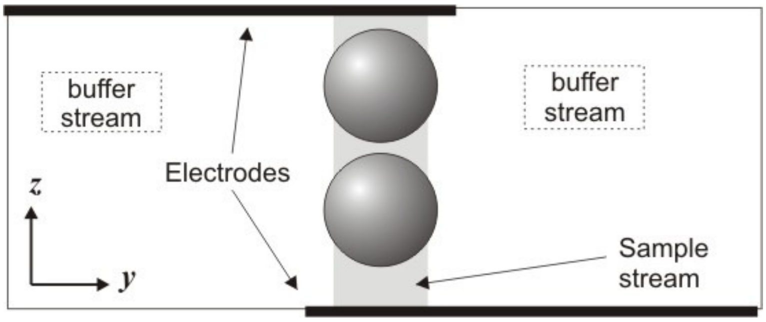

Figure 6-21 – Schematic diagrams depicting the cross section of the microfluidic channel with two particles centred 20 and 27 µm away from the edges (top and bottom) of the channel. The position of the particles in the schematic was estimated matching data for the flow rate, for the average flow velocity and for the velocity profile calculated from COMSOL simulations. The coordinates of the channel are indicated at the bottom right of the graph.

The *z* coordinates of the focussing positions for particles flowing at an average speed of 359 mm sec^{-1} were estimated considering the following equation for the average flow velocity of the fluid in a microfluidic channel [18]:

$$\left|\mathbf{v}_{mean}\right| = \mathrm{Q} / \mathrm{A} \tag{6.5}$$

where Q is the channel flow rate and A is the cross-section area of the channel. Since the flow in the channel was generated using a syringe pump, it is known that the total flow rate in the channel was 200 µl min^{-1} and therefore the average velocity was calculated to be 208 mm sec^{-1}. A simulation was then performed with the same conditions of section 6.5.1 that gave the same average flow velocity and the profile of velocity for $z = 0 \div 40$ µm in the middle of the detection region ($x = 2.6$ mm, $y = 100$

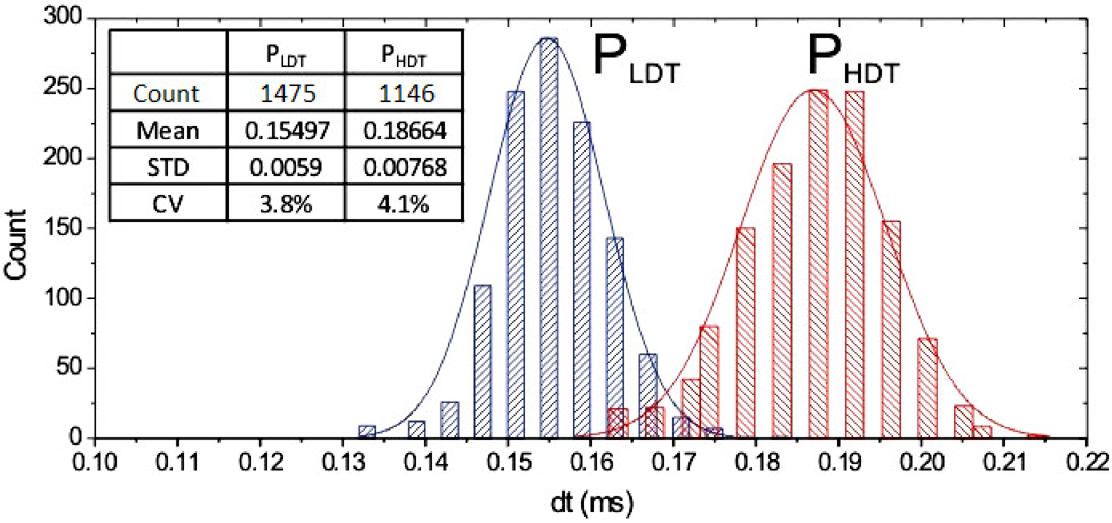

	P_{LDT}	P_{HDT}
Count	1475	1146
Mean	0.15497	0.18664
STD	0.0059	0.00768
CV	3.8%	4.1%

Figure 6-22 – Overlapping histograms obtained by the two speed distribution generated in chip B at particles average flow speeds of 359 mm sec^{-1}. Number of events and statistical data obtained are reported on the top left of the graph.

	IS		SSC		FGO	
	P_{HDT}	P_{LDT}	P_{HDT}	P_{LDT}	P_{HDT}	P_{LDT}
Mean (V)	4.23	11.10	0.98	1.55	2.14	3.28
STD (V)	0.95	2.27	0.24	0.23	0.52	0.58
CV	22.6%	20.5%	24.0%	15.1%	24.1%	17.6%
Relative peaks separation	62%		37%		35%	

Table 6.3 – Statistical data obtained by the two distributions generated by inertial focussing effects at average particles speed of 359 mm sec^{-1}. P_{LDT} and P_{HDT} are related to the distributions indicated in Figure 6-17. The relative peak separation was obtained by calculating the difference between the signal intensities obtained for the two distributions and dividing it by the average signal intensity obtained for P_{LDT}. In the table FGO indicates green-orange fluorescence measured at 585/45 nm, $|Z|_{480}$ indicates the magnitude of the impedance signal measured at 480 kHz and SSC indicate side scatter light measured at 22°.

μm) was extrapolated. Finally the average speeds obtained for P_{LDT} and P_{HDT} (387 and 321 mm sec^{-1} respectively) where matched with the profile obtained from the simulations and P_{LDT} and P_{HDT} were estimated to be cantered 27 and 20 μm away from the edges (top and bottom) of the channel. Following these results a possible layout for the expected position of the particles in the channel was designed and presented in Figure 6-21.

As already mentioned, the two distributions obtained at average particle velocities of 359 mm sec^{-1} were fitted to Gaussian curves and the results are presented in Figure 6-22. The statistic data for the two distributions are presented in Table 6.3 and indicate that the inertial focussing obtained at high particle flow speed gives a lower CV than the values found at low particle velocities, probably because of better particles confinement, as indicated by the standard deviation of the transit times (Figure 6-22).

An approximate estimate of the standard deviation for the data at Figure 6-17 can be performed considering the theory of a Gaussian curve: since the interval between ±2.5 times the standard deviation contains 99% of the events [3], and because the distribution in Figure 6-17(a) is half-Gaussian, the interval between the peak and the highest value obtained for dt is equal to 2.5 times the standard deviation. A standard deviation of approximately 1 ms is found that compared with a peak velocity of 2.5 ms, gives a CV of 40% for particle flow velocities. This CV is approximately 34% higher than the CVs obtained for P_{LDT} and P_{HDT}, suggesting that the particles confinement along the *z*-axes obtained for P_{LDT} or P_{HDT} is better than the confined obtained for average particle flow velocities of 19 mm sec^{-1}.

The intensity plots presented in Figure 6-18 and the statistical data presented in

Table 6.3 can be used for qualitative evaluation of the detection systems. For example, the statistical data for SSC and orange fluorescence show a smaller CV for particles with lower dt (P_{LDT}). Since the CV of the dt was the same for P_{LDT} and P_{HDT}, the better results obtained by P_{LDT} for the CV of optical measurements indicate that the excitation light has lower variation close to the centre of the detection region.

The data of the relative peak separation (see Table 6.3, legend) and the distributions obtained for the scatter plot of dt against magnitude of the output signals at 19 mm sec^{-1} (Figure 6-18(a, b, c)) indicates that the IS response is sensitive to particle position. In particular, the plot shows an anomalous V-shaped distribution despite particle tracking and transit times indicating Gaussian distributions along both *y* and *z* dimensions. The V-shaped distribution is probably due to the non uniform distribution of the electric field (Figure 6-20) that causes a position-dependent response for IS. It is possible that the influence of particle position on the impedance signals is also the reason for the anomalous distribution noticed in Figure 6-23(a), Figure 6-26(d) and Figure 6-28(c).

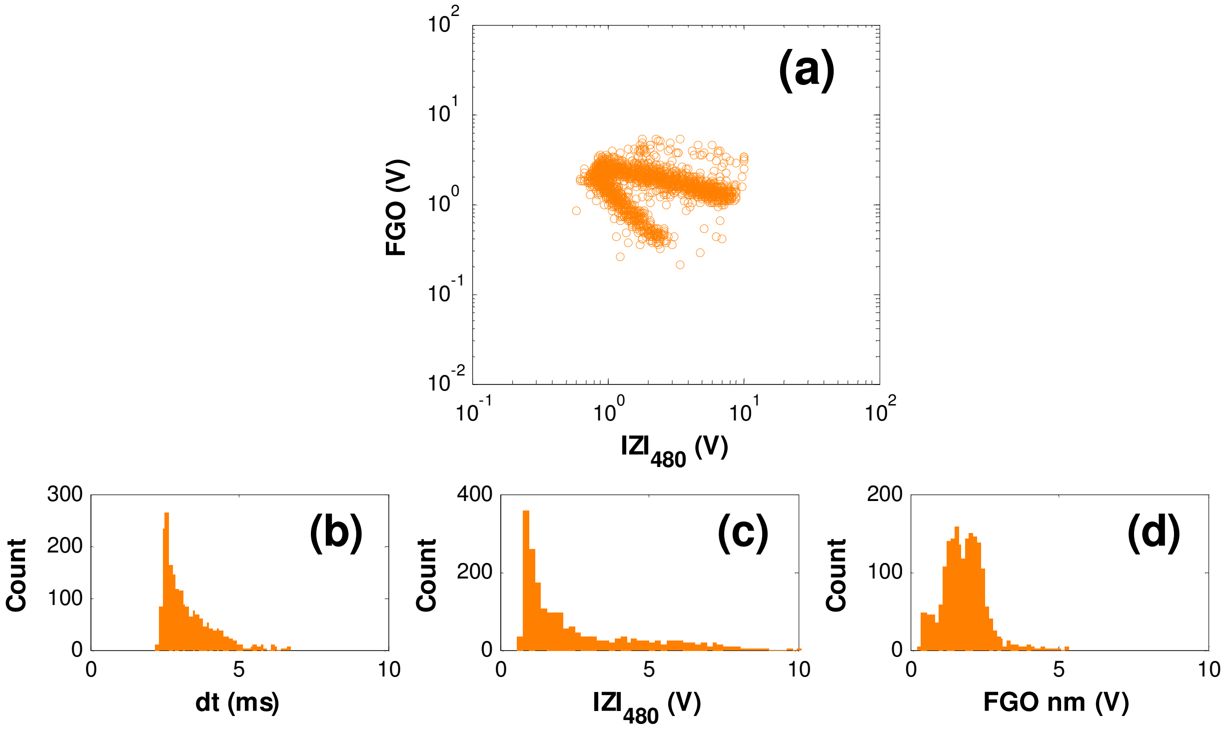

Figure 6-23 – Scatter plot and histograms of 15 µm florescent micro particles with chip B. Particles were flowed through the chip at an average speed of 18.6 mm sec^{-1}, the sample rate was 30 kHz, the voltage applied to the electrodes was 3 V_{pp} and the triggering was set to the orange fluorescence channel. (a) Scatter plot of orange fluorescence (measured at 585/40 nm) against the magnitude of the impedance signal at 480 kHz. (b) Histogram of the transit time (dt). (c) Histogram of the magnitude of the impedance signal at 480 kHz. (d) Histogram of the orange fluorescence signal. Number of events = 1970.

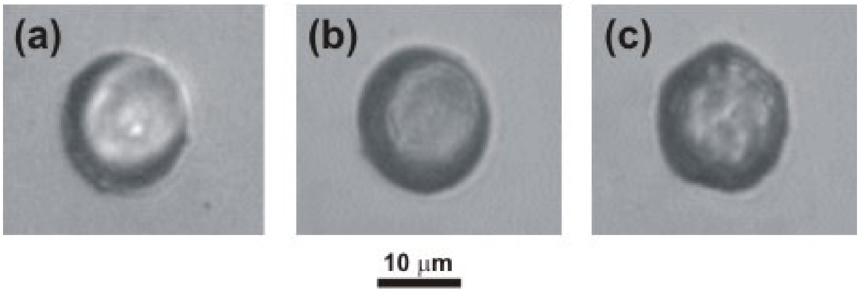

Figure 6-24 – Microscope pictures of 15 µm microspheres. The images show the presence of three types of particles in the sample: (a) perfectly spherical with a smooth surface; (b) perfectly spherical with rough surface; (c) spherical with uneven surface.

6.6 Chip B – cytometry of 15 µm polymer microspheres

Chip B was also characterised with 15 µm orange fluorescence microspheres (section 4.2.2) to test the lower limit of detection of the system. All detection systems but SSC were able to detect the particles and the results obtained are shown in Figure 6-23. An anomalous distribution is evident in the scatter plot of fluorescence against impedance magnitude (Figure 6-23(a)). As discussed in section 6.5.2 and 0 and confirmed by the histogram in Figure 6-23(b), at average particles flow speed of ~20 mm sec^{-1} no inertial focussing phenomena take place and particle distribution is Gaussian along channel height and width, suggesting that the anomalous distribution is not due to inertial phenomena. The reason of the anomalous may be the signal-dependent response of IS as discussed in section 0. However, microscope analysis

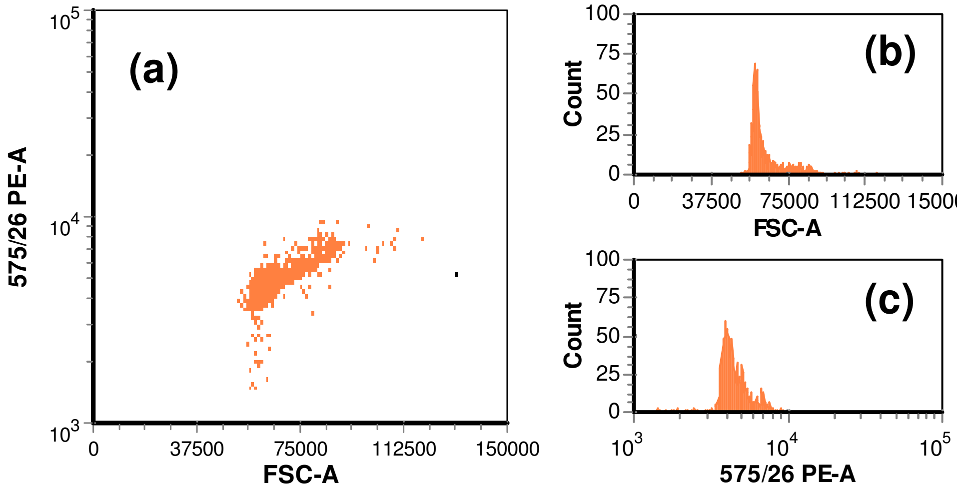

Figure 6-25 – Scatter plots obtained analysing 15 µm micro-spheres with the BD FACSAria cytometer. (a) Forward scatter light against orange fluorescence emitted by particles excited with 488nm light. (b) Histograms of forward scatter light distribution. (c) Histogram of orange fluorescence distribution.

of 15 μm beads suggested that the reason may be the presence of particles with different surface characteristics (Figure 6-24) that may generate different optical and electrical signals.

A sample of 15 μm orange fluorescent microspheres was also suspended in PBS buffer and analysed with the BD FACS using FSC as trigger. The data from an analysis of 1400 events are shown in Figure 6-25. The scatter plot of orange fluorescence versus FSC (Figure 6-25(c)) shows an anomalous distribution. In particoular, the FACS data show an non-Gaussian distribution for FSC signals (Figure 6-25(a, b)) that is probably due to the presence of particles with different surface characteristics (Figure 6-24) that give different scatter signals. Confirming that the sample contains particles with different optical properties.

6.7 Chip B – analysis of mixed populations

The characterisation power of the system was assessed flowing different mixtures of microspheres in chip B and comparing the data with the results from the BD FACS; the experiments are summarised in Table 6.4.

6.7.1 Mixture 25+31

A mixture of 25 μm non-fluorescent and 31 μm fluorescent micro-spheres (mixture 25+31) was flowed through the system at average particle speed of 20.1 mm sec^{-1} for 25 μm particles and 20.7 mm sec^{-1} for 31 μm particles. The results obtained for an experiment of 4756 particles are presented in Figure 6-26(a-d). Figure 6-26 (a) is

Sample		**chip B**		**BD FACSAria**	
Mixture	**Particle**	**Events**	**%**	**Events**	**%**
25+31	25	1700	35.7	991	37.1
	31	3056	64.3	1679	62.9
	Total	4756		2670	
31+45	31	1927	60.3	1992	60.9
	45	1270	39.7	1278	39.1
	Total	3197		3270	
15+31	15	1487	62.8	963	58.9
	31	882	37.2	672	41.1
	Total	2369		1635	

Table 6.4 – Summary of the experiments performed with mixtures of microspheres.

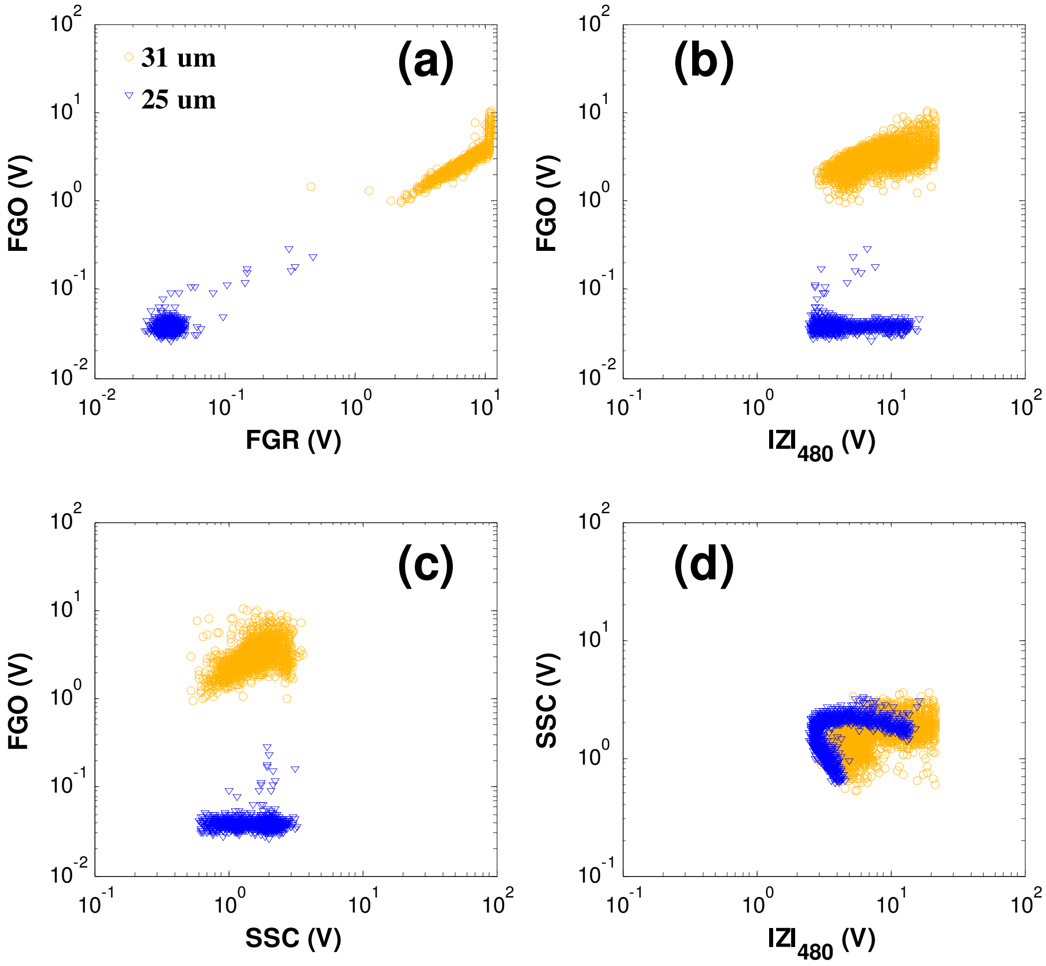

Figure 6-26 – Scatter plots obtained analysing mixture 25+31 with chip B. The sampling was set on 30 kHz, the voltage applied to the electrodes was 1 V_{pp} and the triggering was set on the X component of impedance at 480 kHz. In the plots, FGO and FGR indicate green-orange and green-red fluorescence measured at 585/45 nm and 675/50 nm respectively, $|Z|_{480}$ indicates the magnitude of the impedance signal measured at 480 kHz and SSC indicates side scatter light measured at 22°. Legend for all plots is in the top left corner of graph (a).

a plot of orange fluorescence (585/40 nm) against red fluorescence (675/50 nm). The data show that the two different populations can be easily resolved on the basis of their fluorescence properties (section 4.2.2). The plots of orange fluorescence plotted against side scatter and impedance (Figure 6-26(b, c)) together with the plot of the electrical properties measured at two discrete frequencies (Figure 6-26(e)) show that SSC and impedance signals generate intersecting and almost overlapping distributions. The overlap is probably due to the CVs of the microspheres (11% for 31 µm beads and 20% for 25 µm) that generate particles with overlapping sizes. In particular, the CVs indicate size ranges of 12.5-37.5 µm and 22.5-39.5 µm for non-fluorescent and fluorescent particles respectively. On the other hand, the anomalous distribution obtained for the plot of side scatter light against the magnitude of the impedance signal at 480 kHz in Figure 6-26(d) is probably the position-dependence of impedance signals as discussed in section 0.

The mixture 25+31 was also analysed by FACS. The data from 2670 particles (Figure 6-27(a–d)) shows a good correlation with the microfabricated cytometer (Figure 6-26(a-d)). In particular, the fluorescence patterns are similar, proving that particles can be distinguished on the basis of their fluorescence properties. Furthermore, Figure 6-27(d) shows overlapping populations generated for the FSC signal, demonstrating that the two types of particles have overlapping size.

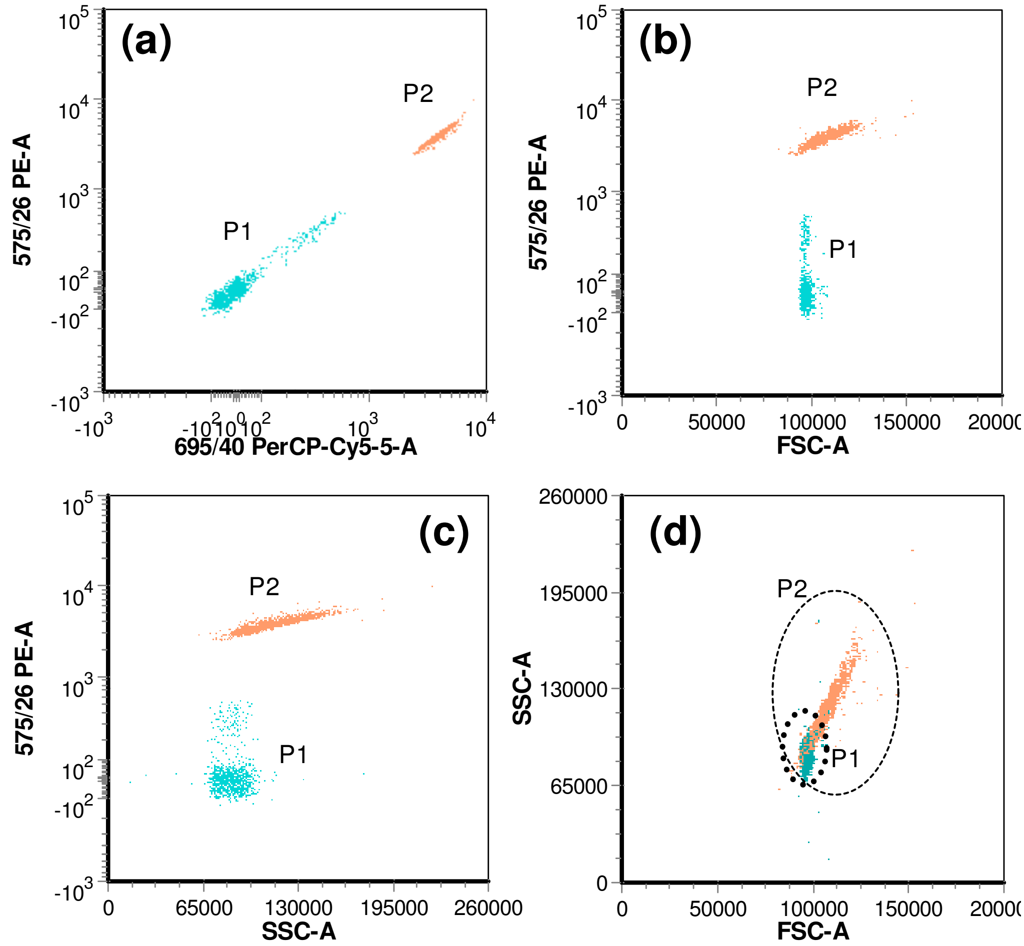

Figure 6-27 – Scatter plots from analysis of 2670 particles with the BD FACSAria. (a) Orange fluorescence (575/26 nm) plotted against red fluorescence (695/40 nm). (b) Orange fluorescence plotted against forward scatter light (FSC); (c) Orange fluorescence plotted against side scatter light (SSC). (d) Scatter light plotted against forward scatter light. In the graphs, P1 and P2 indicates events generated by 25 and 31 μm particles respectively.

Once again there is an excellent correlation between the data obtained from the two cytometers. The relative percentages obtained were 35.7% for 25 µm particles and 64.3% for 31 µm particles for the microfabricated cytometer, and 37.1% of 25 µm particles and 62.9% of 31 µm particles for the BD FACSAria.

6.7.2 Mixture 31+45

Since mixture 25+31 proved inadequate to characterise the ability of the system to distinguish particles of different size, experiments were performed with a mixture of

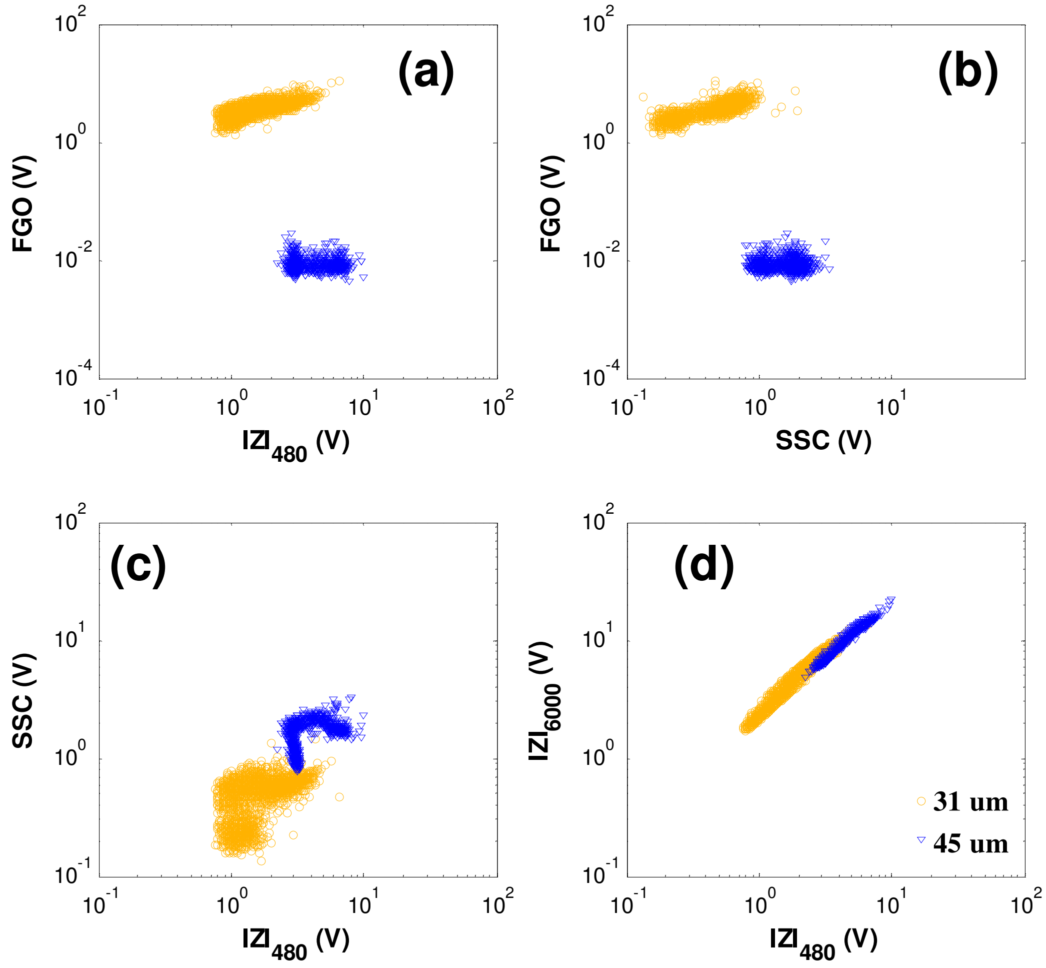

Figure 6-28 – Scatter plot for a cytometry experiment of 3197 particles performed on mixture 31+45 with chip B. The sampling rate was 50 kHz, the voltage applied to the electrodes was 1 V_{pp} and the triggering was set on the X component of impedance at 480 kHz. In the plots, FGO indicates green-orange measured at 585/45 nm, $|Z|_{480}$ indicates the magnitude of the impedance signal measured at 480 kHz and SSC indicates side scatter light measured at 22°. The legend for all plots is in the bottom right corner of graph (d).

31 μm orange fluorescent and 45 μm non-fluorescent microspheres (mixture 31+45) at flow speeds of 79.8 mm sec^{-1} for 31 μm particles and 73.6 mm sec^{-1} for 45 μm particles. Such speeds were chosen because with slower flow rates the sample blocked the system, probably because non-fluorescent particles had a CV of 20% (section 4.2.2) and therefore included particles bigger than 65 μm. The results for chip B cytometry are presented in Figure 6-28.

Figure 6-28(a, b) is a plot of orange fluorescence against side scatter light and impedance at 480 kHz. The particles are identified on the basis of fluorescence properties because 45 μm microspheres are not fluorescent while 31 μm microspheres emits orange fluorescence when irradiated with a 532 nm wavelength (section 4.2.2). Figure 6-28(a, b) also shows that, although SSC and the impedance signals taken alone

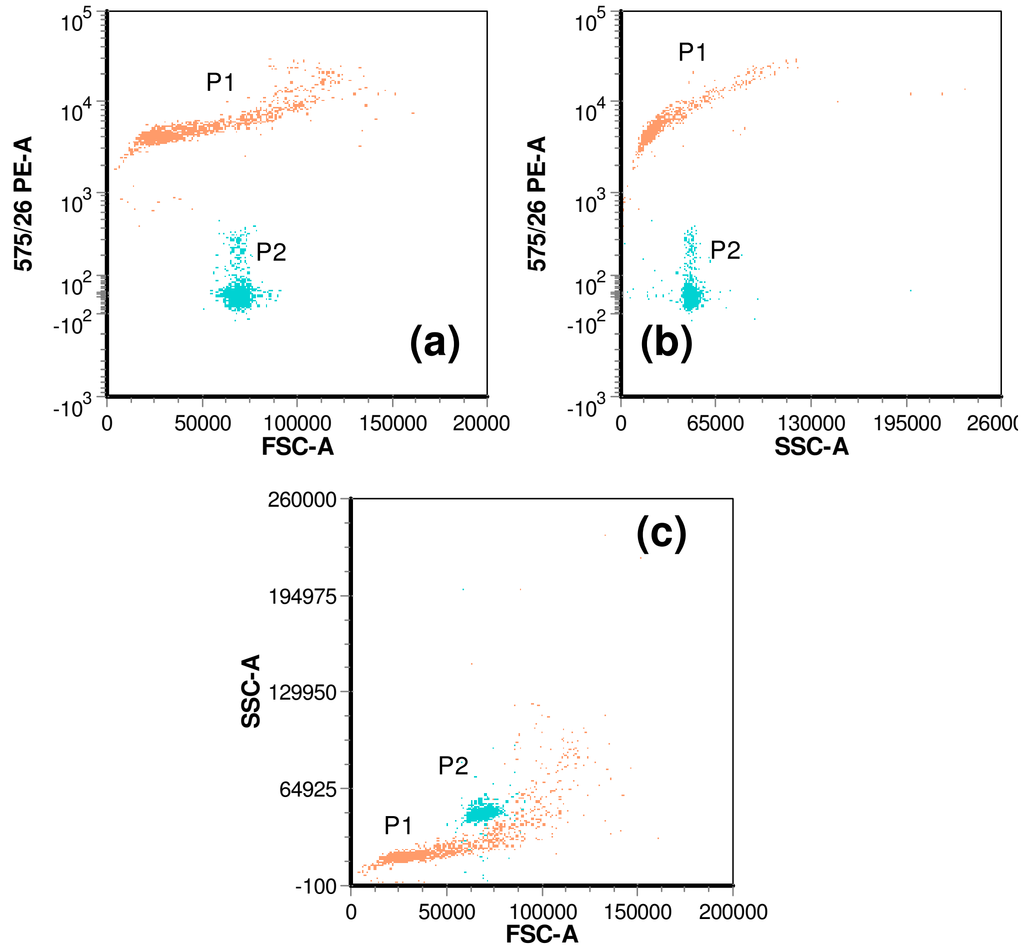

Figure 6-29 – Scatter plots obtained analysing the 31+45 mixture with BD FACSAria. (a) Orange fluorescence (575/26 nm) plotted against forward scatter light (FSC). (b) Orange fluorescence plotted against side scatter light (SSC). (c) Side scatter light plotted against forward scatter light. P1 and P2 indicates events from 31 and 45 μm particles respectively. Number of events 3270.

have overlapping distribution, when they are plot against each other give 2 resolved distributions. Therefore, impedance and side scatter can be used instead of fluorescence for particles characterisation.

Mixture 31+45 was also analysed with the BD FACSAria (Figure 6-29). The subpopulations of the two cytometers are similar and the data in Figure 6-28(a-c) are directly comparable with the data in Figure 6-29(a-c). Moreover, there is an excellent correlation between the two data sets as the relative percentages obtained were 60.3% for 31 µm orange particles and 39.7% for 45 µm non-fluorescent particles with the microfabricated cytometer and 60.9% for 31 µm orange particles and 39.1% for 45 µm non-fluorescent particles with the BD FACSAria.

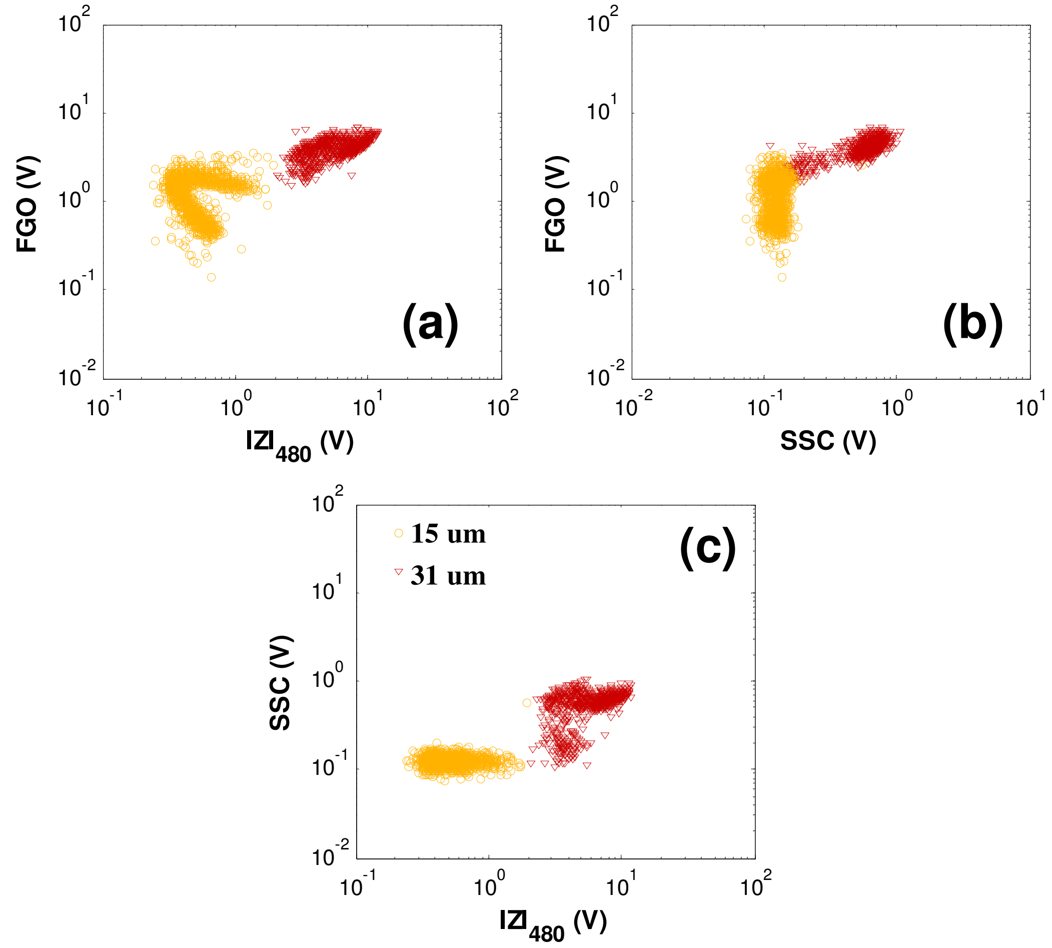

Figure 6-30 – Scatter plots of a cytometry experiment of 2369 particles performed with the chip B cytometer. Particles were passed into the chip at average speeds of 68.6 mm sec^{-1} for 15 µm particles and 69.6 sec^{-1} for 31 µm particles. The voltage applied to the electrodes was 1 V_{pp}, the sampling rate was set on 20 kHz and the threshold was set on the orange fluorescent channel. In the plots, FGO indicates green-orange and measured at 585/45 nm, $|Z|_{480}$ indicates the magnitude of the impedance signal measured at 480 kHz and SSC indicates side scatter light measured at 22°. The legend for all graph in the bottom right corner of graph (d).

6.7.3 *Mixture 15+31*

An additional experiment was performed to test the ability of the system to differentiate a mixture of 15 and 31 μm microspheres (mixture 15+31) with similar fluorescence properties (Figure 6-30). 31 μm particles were expected to generate higher impedance and fluorescence signals than 15 μm particles and were therefore with the distribution at the top right of the graph in Figure 6-30(a). Furthermore, the population on the bottom left has a pattern identical to the one in Figure 6-23(a), confirming that it is generated by 15 μm particles.

A second mixture of 15+31 was analysed with the BD FACSAria (Figure 6-31). The data shows a difference in the orange fluorescence signals, in particular Figure 6-31(a) orange fluorescence (575/26 nm) against forward scatter light, which shows

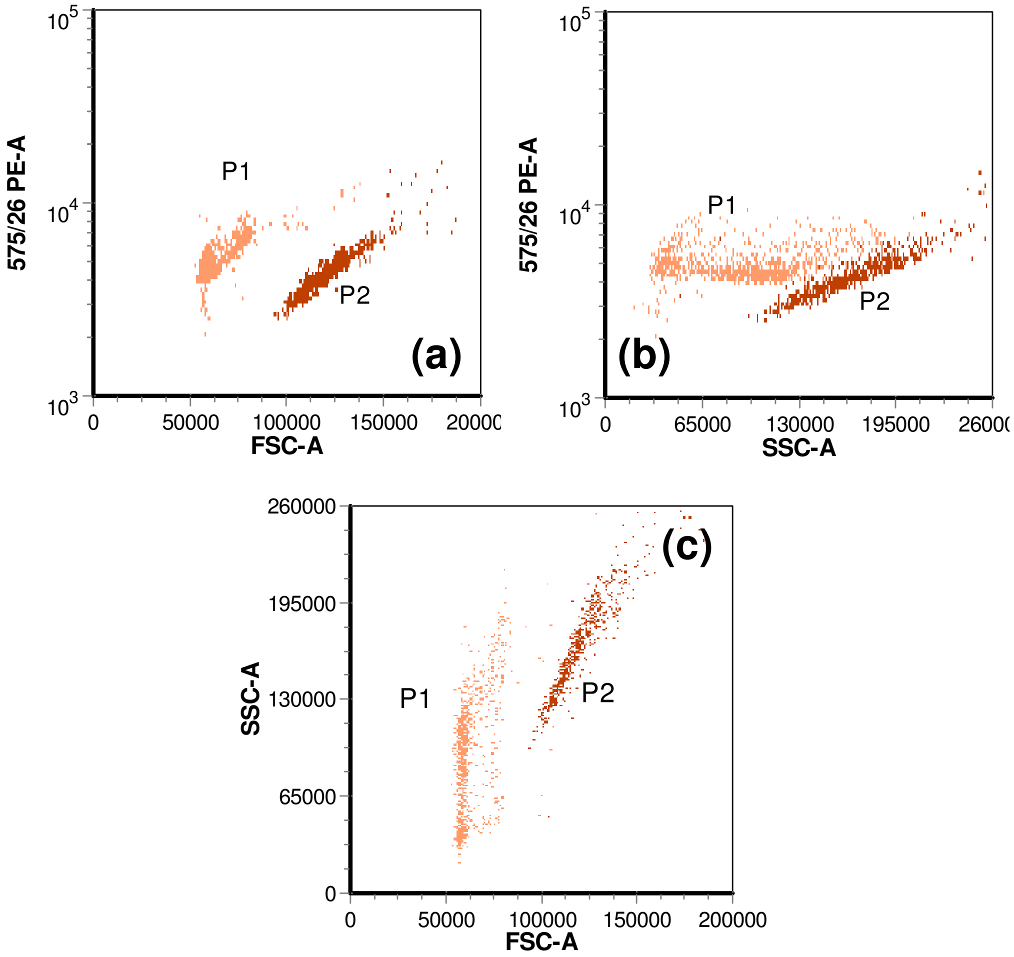

Figure 6-31 – Scatter plot of a cytometry experiment of approximately 1635 particles performed with the BD FACSAria. (a) Orange fluorescence (575/26 nm) plotted against forward scatter light. (b) Orange fluorescence plotted against side scatter light. (c) Side scatter light plotted against forward scatter light. In the plots P1, P2 indicates 15 μm microspheres and 31 μm microspheres respectively.

that 31 μm particles (highest FSC signal) have lower fluorescence than 15 μm particles. This is because the excitation spectra of the two particles are different and the two instruments use different excitation wavelength and detection filters (see section 4.7 and 4.8.3.2).

6.8 Algae mixture

The ability of chip B to detect multiple colour fluorescence and biological particles was assessed passing a mixture of *Lingulodinium polyedrum* (section 4.3),

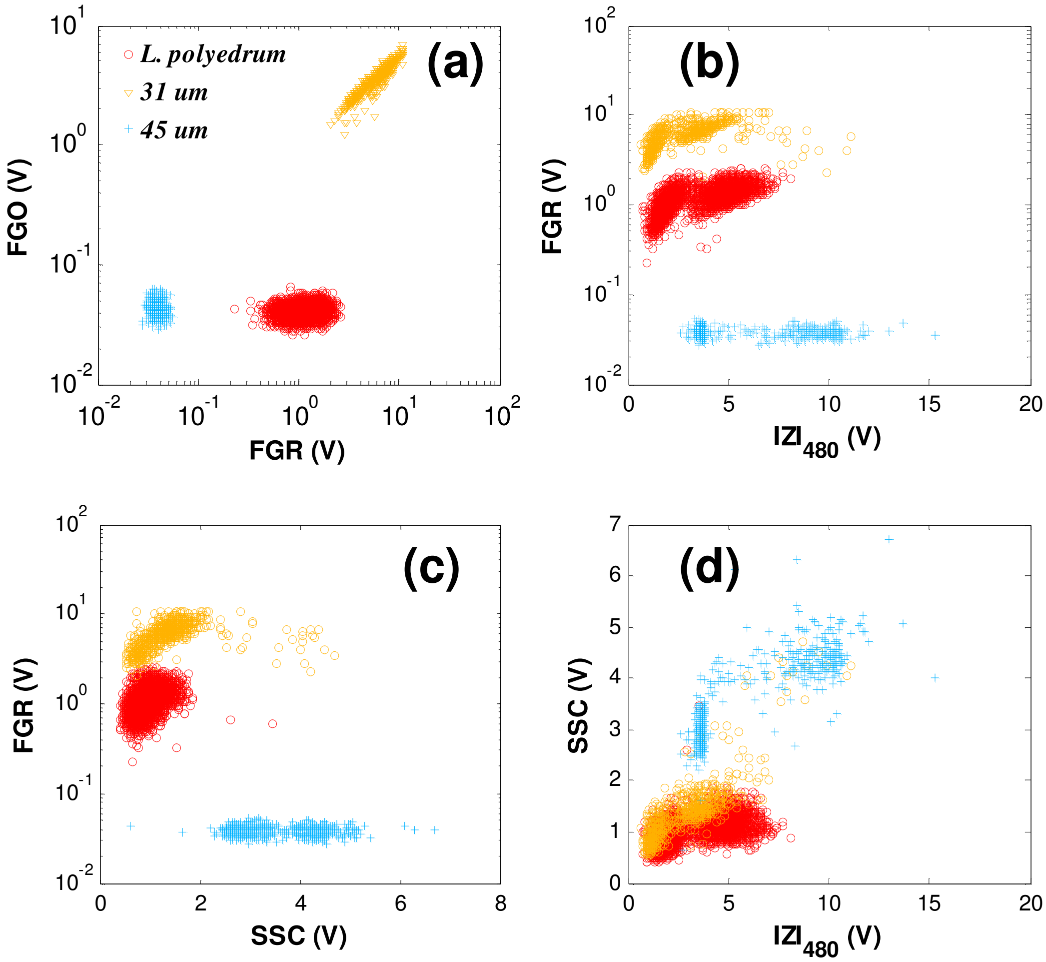

Figure 6-32 – Scatter plots for a typical chip B cytometry experiment of a mixture of L. polyedrum, 31 and 45 μm microspheres. The sample rate was 120 kHz, the voltage applied to the electrodes was 350 mV$_{pp}$ and the triggering was set on the Y component of the impedance at 480 kHz. In the plots, FGO and FGR indicate green-orange and green-red fluorescence measured at 585/45 nm and 675/50 nm respectively, $|Z|_{480}$ indicates the magnitude of the impedance signal measured at 480 kHz and SSC indicates side scatter light measured at 22°. The legend for all plots is inserted on the top left corner of graph (a).

31 μm fluorescence microspheres and 45 μm non-fluorescent microspheres (algae mixture) through the system. Algae and microspheres were suspended in f2 medium that was also used as sheath fluid. Average particle speeds of 333, 342 and 312 mm sec^{-1} were measured for *L. polyedrum*, 31 μm and 45 μm microspheres respectively. And the results are shown in Figure 6-32. The three populations were easily resolved on the basis of their fluorescence emission spectra (Figure 6-32(a)) as 45 μm microspheres are non-fluorescent, *L. polyedrum* emits only red fluorescence (section 4.3.3) and 31 μm microspheres emits both red and orange fluorescence (section 4.2.2).

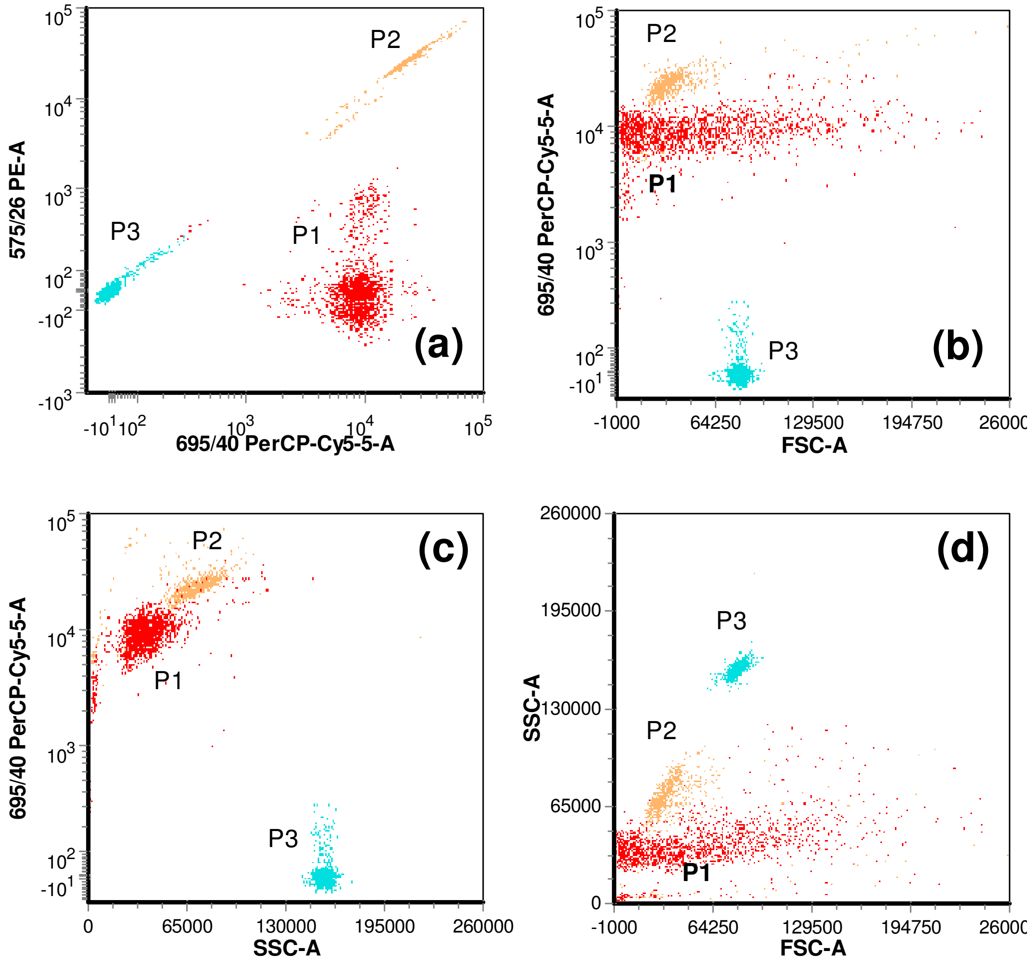

Figure 6-33 – Data from analysis of a mixture composed of *L.* polyedrum, 31 fluorescent and 45 non fluorescent particles. The particles were suspend in f2 medium and analysed with the commercial flow cytometer (BD FACSAria). (a) Orange fluorescence (575/26 nm) plotted against red fluorescence (695/40 nm). (b) Red fluorescence (695/40 nm) plotted against forward scatter light. (c) Red fluorescence (695/40 nm) plotted against side scatter light. (d) Side scatter light plotted against forward scatter light. Note that red and orange fluorescence are reported on linear/logarithmic scales. In the plots P1, P2 and P3 indicates *L. polyedrum*, 31 μm microspheres and 45 μm microspheres respectively.

		L. polyedrum	31	45	Total
Chip B	**Count**	3157	764	1220	5141
	%	61.4%	14.9%	23.7%	100%
Hematocytometer	**Count**	93	34	67	194
	%	47.9%	17.5%	34.5%	100%
BD FACS	**Count**	1625	705	1071	3401
	%	47.8%	20.7%	31.5%	100%

Table 6.5 – Number of events and relative percentage of cells obtained analysing with different techniques the mixture of *L. polyedrum*, 31 and 45 μm polymer microspheres.

The algae mixture was counted before the experiment with a hematocytometer (Bright-Line™, Sigma-Aldrich). The mixture of microspheres and algae was also analysed with the BD FACSAria, (Figure 6-33). Although chip B experiments were performed at high flow rate, the subpopulations patterns of the two flow cytometers have excellent correspondence, and the data in Figure 6-33(a-d) are directly comparable with the data in Figure 6-32(a-d).

The results obtained by the various cytometers are showed in Table 6.5. Despite the excellent results obtained in terms of distributions patterns, there is a low correlation between the data sets obtained by chip B, the BD FACS and the hematocytometer (Table 6.5). In particular, the data from chip B is dominated (61.4%) by *L. polyedrum* with a reduced percentage (38.6%) of signals from the microspheres. The data set from the BD FACSAria has a good correlation with the data obtained by the hematocytometer; both data sets have high levels of *L. polyedrum* but higher percentage of microspheres than in the data set of the microfabricated cytometer. The difference in populations is probably due to the different sampling system used. In particular, the BD FACSAria is equipped with an agitation system that spins the sample tube at 300 rpm during the analysis while an automated agitation system was not implemented for the microfabricated cytometer and particles were maintained in suspension by manually tapping the tube every 30 seconds. Furthermore, the sampling probe was collecting from the bottom of the test tube in the BD FACS and from the middle of the sample tube in the chip B cytometer.

6.9 Influence of the central stream width

In order to asses whether the central stream width was affecting precision, experiments were performed with central stream widths ranging from 5 to 40 μm and the data are presented in Table 6.6. Widths were measured up to 40 μm because that

Average part. speed (mm sec^{-1})		19	18	432		470		460	
Particles used		30 µm		15 µm					
Central stream width (µm)		25	40	5		20		40	
Distribution		--	--	P_{LDT}	P_{HDT}	P_{LDT}	P_{HDT}	P_{LDT}	P_{HDT}
Average particles speed (mm sec-1)		19	18	389	439	382	430	387	434
CV (%)	$\lvert Z\rvert_{480}$	51.0	54.0	14.8	20.3	14.5	21.9	18.5	23.0
	$\lvert Z\rvert_{6000}$	50.0	50.0	14.6	19.3	14.1	21.2	17.7	22.4
	SSC	26.0	25.0	--	--	--	--	--	--
	FGO	32.0	38.0	12.9	13.2	13.7	14.0	12.2	11.9

Table 6.6 – Statistical data obtained for cytometric analysis with changeable stream widths. Note that for particles velocities of 20 mm sec^{-1} a width narrower than 25 µm was not achievable because it made the flow instable. FGO indicates green-orange fluorescence measured at 585/45 nm and 675/50 nm respectively; $|Z|_{480}$ and $|Z|_{6000}$ indicate the magnitude of the impedance signals measured at 480 kHz and 6 MHz respectively; SSC indicates side scatter light measured at 22°.

was the overlapping of the electrodes. No scatter plots or histograms are showed as they had the same pattern of the experiments already presented for the same type of particles. On average the increase of CV was 8.8% for particle velocities of ~20 mm sec^{-1} and 15.2% for particle velocities of ~450 mm sec^{-1}, confirming that a narrower confinement of the sample increases the precision of the analysis.

6.10 Discussion

6.10.1 System precision

Precision and sensitivity of the systems were investigated by calculating the coefficient of variation (CV) and the signal to noise ratio (S/N) respectively for experiments with 15 and 31 µm particles, and comparing them with the values from the BD FACSAria and the literature.

The signal to noise ratio for the various parameters are presented in Table 6.6. S/N was calculated by dividing the average value of the signals by the standard deviation for 50000 pulses without particles in the detection region. All parameters but the X component of the impedance at 6 MHz and the SSC signals presented S/Ns that were at least 12 times the limit of detection. The X component of the impedance signal at 6 MHz has a low S/N because of the low signal generated by the particles in this channel (see Figure 6-19). In SSC the low S/N is due to a considerable amount of

Sample	Particle flow velocity		(X) 480 kHz	(Y) 480 kHz	(X) 6 MHz	(Y) 6 MHz	$\lvert Z \rvert_{480}$	$\lvert Z \rvert_{6000}$	SSC	FGO	FGR
15 µm microspheres	19 mm sec^{-1}		110	21	3.9	115	133	122		292	
31 µm microspheres	19 mm sec^{-1}		73	221	29	555	603	555	11	164	364
	359 mm sec^{-1}	**P_{HDT}**	227	86	13	241	384	279	3.6	89	224
		P_{LDT}	613	189	25	600	1009	693	5.7	137	355

Table 6.7 – Values of S/N obtained for the experiments performed with the chip B cytometer on 15 and 31 µm particles. In the table (X) and (Y) indicate the two components of the impedance signals at two discrete frequencies, $\lvert Z \rvert$ indicates the magnitude of the impedance signals, SSC indicates side scattered light at 22° while FGO and FGR indicate green-orange (532 nm excitation and 585/40 nm emission) and green-red (532 nm excitation and 675/50 nm emission) fluorescence respectively. Note that only the X and Y component of the impedance signals were detected during the experiments while the magnitude at the different frequencies was calculated afterwards.

incident radiation collected by the fibre at 22°, which increases the level of noise of the SSC channel.

The S/N obtained for chip B is one order of magnitude higher than the value (9.7) reported for Tung *et al.* device [19] that featured a similar integrated optics layout. The comparison of the data indicate that, overall, chip B has better performances than Tung system, however, the latter implemented PIN photodiodes coupled with lock-in amplifiers as detectors, hindering a direct comparison with the optical detection systems implemented in chip B.

In the CV obtained for 15 µm particles (Table 6.8), there is a difference between the values obtained from the micro-fabricated and the commercial cytometer with the most noticeable differentiation between impedance and FSC signals. A big difference in the value of CVs is also noticed between the value obtained for impedance and FSC signals of 31 µm particles. However, the CVs obtained by the integrated optical system

CV	Chip B cytometer	BD FACSAria
Events	1970	908
$\lvert Z \rvert_{480}$	79.3%	--
$\lvert Z \rvert_{6000}$	74.1%	--
FSC	--	15.5%
Orange Fluorescence	39.5%	22.3%

Table 6.8 – Statistical data obtained from the chip B and the FACS. Magnitude at 480 kHz ($\lvert Z \rvert_{480}$)can be directly compared with forward scatter light (FSC). Note that the two cytometer use different excitation and detection wavelength for orange fluorescence (sections 4.7 and 4.8.3.2).

for 31 μm (Table 6.9) particles flowing at 19 mm sec^{-1} are comparable to the corresponding values obtained from the commercial instrument.

The main reason for higher CV obtained by chip B is probably the hydrodynamic focusing system implemented that is not able to confine particles along channel depth. This hypothesis is supported by the following: (1) for 31 μm particles, all parameters give a lower CV than for 15 μm particles. (2) The CVs given by chip A are similar and sometimes better than the CVs of the commercial flow cytometer (Table 6.1). The result is important because chip A implemented a microfluidic channel with size similar to the particles analysed and therefore obtained a good confinement without the need of a focussing system. (3) The high S/N obtained for all the signals but SSC indicate that the CV is not affected by the sensitivity of the system. (4) Simonnet et Groisman [5] show that an increase in the width of the central stream gives an increase in CV of fluorescence signals.

For high particle velocities (Table 6.9), the two distributions obtained gave two different levels of precision. In particular, very interesting is the data obtained for P_{LDT} that are on the same level or even better than the CVs obtained by the BD FACSAria. This result suggests not only the good quality of the integrated detection system but that the implementation of a 2D focussing system in chip B would increase the performance of the microfabricated cytometer.

Parameter	**Microfabricated cytometer**			**BD FACSAria**
	19 mm sec^{-1}	**359 mm sec^{-1}**		
		P_{HDT}	**P_{LDT}**	
Events	1018	1476	1147	965
$\lvert Z \rvert_{480}$	51%	22.6%	20.5%	--
$\lvert Z \rvert_{6000}$	48%	21.7%	19.5%	--
FSC	--	--	--	9.8%
SSC	25%	24.0%	15.1%	20.5%
Orange Fluorescence	26%	24.1%	17.6%	25.6%
Red Fluorescence	26%	26.7%	16.4%	22.8%

Table 6.9 – Coefficients of variation for 31 μm microspheres analysed with the microfabricated and commercial cytometers. In the table, $|Z|_{480}$ and $|Z|_{6000}$ indicate the magnitude of the impedance signal measured at 480 kHz and 6 MHz respectively, FSC is the forward scatter signal and SSC indicates side scatter light (measured at 22° in the microfabricated cytometer). Orange and red fluorescences are measured at 585/40 nm and 675/50 nm in the microfabricated cytometer and at 575/26 nm and 695/40 nm in the BD FACS.

Overall, the data for both 15 and 31 μm microspheres show that the integrated optical system has a better performance than the impedance detection system; as already discussed in section 0 this is probably because of the more uniform distribution of the excitation power along the depth of the channel.

The precision and particle flow velocity obtained with chip B are comparable with microfabricated cytometers presented in the literature that use 1D particle focussing (CVs between 15 and 35%; particles flow speed between 0.1 and 20 mm sec^{-1} [20; 21; 22; 23; 24]). Better performances were shown by systems implementing 2D particles focussing systems (CV ranging from 2.5% to 15% and particles flow speeds up to 3 m sec^{-1} [4; 5; 6; 7; 8]). However, the integrated detection system in chip B demonstrated high precision for flow rates up to 360 mm sec^{-1} but is hindered by structural problems and inertial phenomena that affect particles focussing. It follows that the implementation of a 2D particle focussing system is critical to improve the performances of the system and should be investigated in future work.

6.10.2 SSC and Impedance correlation with particles dimensions

In order to investigate the correlation between the intensity of the impedance signals and the size of the beads, the (average) values obtained from the impedance detection system for a mixture at 15+31 and 31+43 were plotted in the graph of intensity against particle size and fitted to trend lines (Figure 6-34(a)). Furthermore, the correlation between SSC signals and particles size was assessed by running individual samples in chip B and plotting the results for the average intensities against particles size (Figure 6-34(b)).

Interestingly, a size calibration plot for SSC shows that 25 and 31 μm micro-particles have the same SSC intensity. Similar results were also obtained for mixture 25+31, giving consistent results. Since 25 and 45 μm microspheres were made by a different manufacturer than 31 μm particles they were probably fabricated with a different procedure that may have generated particles with a different refractive index. It is therefore possible that SSC reflects differences in the refractive index of the particles and, ultimately, in their internal properties.

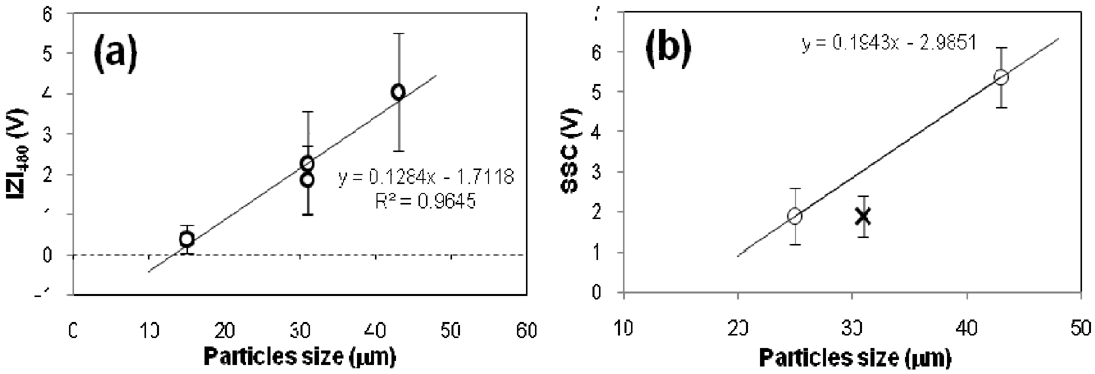

Figure 6-34 – (a) Average intensity of impedance signals plotted against particle size. The data are obtained from the experiments presented sections 6.7.2 and 6.7.3. (b) Average intensity of SSC signals obtained for analysis of 25, 31, and 45 µm microspheres. The particles were suspended in F2 medium and flown individually into chip. The circles indicate 25 and 45 µm particles and the cross indicates 31 µm particles. Trend line of 25 and 45 µm points is also displayed on the graph together with equation.

In conclusion, impedance and SSC signals can be correlated to particles size. However, the data suggested that SSC intensity is also correlated to the refractive index of the particle while the impedance magnitude is dominated by the size.

6.10.3 Particle characterization

Cytometry experiments on mixtures of particles demonstrated the ability of the detection system to characterise particles according to their size, fluorescence and, potentially, optical properties. Furthermore, the system was able to detect and characterise particles ranging from 15 to 45 µm with flow velocities up to 500 mm sec^{-1}. Unfortunately, inertial and structural problems limited the system at high flow velocities. The system however demonstrated characterisation performances comparable to the commercial cytometer at velocities of about 20 mm sec^{-1}.

A number of microfabricated cytometers have been published, but they are not comparable with chip B. In fact, most of the devices that were capable of multi parameters detection used conventional optics [20; 22; 24; 25]. Devices that used integrated optics or electrodes could detect only a limited number of parameters [7; 8; 21; 26; 27; 28; 29; 30; 31], or the integrated detection system was coupled with conventional optics to increase the characterisation power [4; 21; 32]. Tung *et al.* [19] presented a device that was able to detect multiple fluorescence of particles using only integrated optics. However, the device had a relatively low S/N and was not able to detect either scatter light or electrical impedance. Therefore chip B represents the first fully integrated device able of optical and electrical multi-parameter detection cytometry.

6.11 Summary

In this chapter, the results of cytometry experiments using chip A and chip B have been presented. Experiments performed with chip A demonstrate the ability of the sensor to detect and characterise biological samples on the basis of their electrical and optical properties. Despite excellent results obtained for analysis of a mixture of algae, chip A cytometry showed major limitations in the size range of particles that could be analysed. In fact, a channel width of 11 μm limited the maximum size of particles while experiments showed that particles smaller than 2 μm could be detected only with fluorescence.

Chip B was able to detect and characterise particles with different size and optical properties with excellent sensitivity and characterisation performances comparable with a commercial cytometer. In fact, the system was able to perform multiple fluorescence, scatter light and impedance detection. Impedance signals were dominated by particle size while SSC signals showed to be also affected by particle's internal properties.

Analysis of the precision (CV) and sensitivity (S/N) of the results obtained indicated that chip B was limited by the use of a mono-dimensional particle focussing system. In fact, similar precision (15-35%) was reported in the literature for system that implemented mono-dimensional particle focussing but better performances (2.5-15%) was obtained by system implementing 2D focussing.

Test performed on chip B showed that the system is affected by inertial phenomena that affect the performance of the system at particle flow velocities of about 10^{-1} m sec^{-1}. However, the detection system was capable of excellent performances at flow rates up to 0.5 m sec^{-1}. The implementation of a bi-dimensional particle focussing system could drastically increase precision and velocity of the microfabricated cytometer.

In conclusion, chip B represents a considerable step forward in the LOC panorama being the first fully integrated microfabricated cytometer able to simultaneously detect and characterise polymer and biological particles on the basis of multiple colour fluorescence, scattered light and impedance at multiple frequencies.

The performance of the system is good even though limited by the use of a mono-dimensional particles focussing system.

REFERENCES

[1]D. Holmes, B. Neal, N. Green, and H. Morgan, Microfabricated Device for Rapid Impedance Measurements on Single Biological Cells, Proceedings of 15th MicroMechanics Europe Workshop, Leuven Belgium, 2004, pp. pp. 195-198.

[2]H. Morgan, D. Holmes, and N.G. Green, High speed simultaneous single particle impedance and fluorescence analysis on a chip. Current Applied Physics 6 (2006) 367-370.

[3]D.A. Skoog, and J.J. Leary, Principles of Instrumental Analysis Saunders Cllege Publishing, Orlando, 1992.

[4]A. Kummrow, J. Theisen, M. Frankowski, A. Tuchscheerer, H. Yildirim, K. Brattke, M. Schmidt, and J. Neukammer, Microfluidic structures for flow cytometric analysis of hydrodynamically focussed blood cells fabricated by ultraprecision micromachining. Lab on a Chip 9 (2009) 972–981.

[5]C. Simonnet, and A. Groisman, High-throughput and high-resolution flow cytometry in molded microfluidic devices. Analytical Chemistry 78 (2006) 5653-5663.

[6]X. Mao, J.R. Waldeisen, and T.J. Huang, "Mircrofluidic drifting" - implememnting three-dimensionla hydrodynamic focusing with a single-layer planar microfluidic device. Lab on a Chip 7 (2007) 1260-1262.

[7]D. Holmes, H. Morgan, and N.G. Green, High throughput particle analysis: Combining dielectrophoretic particle focussing with confocal optical detection. Biosensors & Bioelectronics 21 (2006) 1621-1630.

[8]A. Wolff, I.R. Perch-Nielsen, U.D. Larsen, P. Friis, G. Goranovic, C.R. Poulsen, J.P. Kutter, and P. Telleman, Integrating advanced functionality in a microfabricated high-throughput fluorescent-activated cell sorter. Lab on a Chip 3 (2003) 22-27.

[9]H. Morgan, and N.G. Green, AC Electrokinetics: colloids and nanoparticles, Research Studies Press, Ltd, Baldock, Hertfordshire, England, 2003.

[10]R.A. Hoffman, and W.B. Britt, Flow-System Measurement of Cell Impedance Properties. Journal of Histochemistry & Cytochemistry 27 (1979) 234-240.

[11]http://www.bdbiosciences.com.

[12]R.A. Hoffman, T.S. Johnson, and W.B. Britt, Flow cytometric electronic direct-current volume and radiofrequency impedance measurements of single cells and particles. Cytometry 1 (1981) 377-384.

[13]S. Gawad, K. Cheung, U. Seger, A. Bertsch, and P. Renaud, Dielectric spectroscopy in a micromachined flow cytometer: theoretical and practical considerations. Lab on a Chip 4 (2004) 241-251.

[14]D. Di Carlo, D. Irimia, R.G. Tompkins, and M. Toner, Continuous inertial focusing, ordering, and separation of particles in microchannels. Proceedings of the National Academy of Sciences of the United States of America 104 (2007) 18892-18897.

[15]M.S. Howard, (Ed.), Practical Flow Cytometry, John Wiley & Sons, 2003.

[16]R.P. Feynman, The feynman lectures on physics, 1965.

[17]CRC handbook of chemistry and physics : a ready-reference book of chemical and physical data, Boca Raton, Fla. : CRC Press, c1984. .

[18]N.-T. Nguyen, and S.T. Wereley, Fundamentals and applications of microfluidics, Boston, London, Artech House, 2006.

[19]Y.C. Tung, M. Zhang, C.T. Lin, K. Kurabayashi, and S.J. Skerlos, PDMS-based opto-fluidic micro flow cytometer with two-color, multi-angle fluorescence detection capability using PIN photodiodes. Sensors and Actuators B-Chemical 98 (2004) 356-367.

[20]D.P. Schrum, C.T. Culbertson, S.C. Jacobson, and J.M. Ramsey, Microchip flow cytometry using electrokinetic focusing. Analytical Chemistry 71 (1999) 4173-4177.

[21]Z. Wang, J. El-Ali, M. Engelund, T. Gotsaed, I.R. Perch-Nielsen, K.B. Mogensen, D. Snakenborg, J.P. Kutter, and A. Wolff, Measurements of scattered light on a microchip flow cytometer with integrated polymer based optical elements. Lab on a Chip 4 (2004) 372-377.

[22]N. Pamme, R. Koyama, and A. Manz, Counting and sizing of particles and particle agglomerates in a microfluidic device using laser light scattering: application to a particle-enhanced immunoassay. Lab on a Chip 3 (2003) 187-192.

[23]M.A. McClain, C.T. Culbertson, S.C. Jacobson, and J.M. Ramsey, Flow cytometry of Escherichia coli on nucrifluidic devices. Analytical Chemistry 73 (2001) 5334-5338.

[24]L.-M. Fu, R.-J. Yang, C.-H. Lin, Y.-J. Pan, and G.-B. Lee, Electrokinetically driven micro flow cytometers with integrated fiber optics for on-line cell/particle detection. Analytica Chimica Acta 507 (2004) 163-169.

[25]A.Y. Fu, H.P. Chou, C. Spence, F.H. Arnold, and S.R. Quake, An Integrated Microfabricated Cell Sorter, 2002, pp. 2451-2457.

[26]R. Bernini, E. De Nuccio, F. Brescia, A. Minardo, L. Zeni, P.M. Sarro, R. Palumbo, and M.R. Scarfi, Development and characterization of an integrated silicon micro flow cytometer (vol 386, pg 2257, 2006). Analytical and Bioanalytical Chemistry 386 (2006) 2257-2257.

[27]Q. Xiang, X.C. Xuan, B. Xu, and D.Q. Li, Multi-functional particle detection with embedded optical fibers in a poly(dimethylsiloxane) chip. Instrumentation Science & Technology 33 (2005) 597-607.

[28]J. Kruger, K. Singh, A. O'Neill, C. Jackson, A. Morrison, and P. O'Brien, Development of a microfluidic device for fluorescence activated cell sorting. Journal of Micromechanics and Microengineering 12 (2002) 486-494.

[29]K. Cheung, S. Gawad, and P. Renaud, Impedance spectroscopy flow cytometry: On-chip label-free cell differentiation. Cytometry Part A 65A (2005) 124-132.

[30]S. Gawad, L. Schild, and P. Renaud, Micromachined impedance spectroscopy flow cytometer for cell analysis and particle sizing. Lab on a Chip 1 (2001) 76-82.

[31]L. Cui, T. Zhang, and H. Morgan, Optical particle detection integrated in a dielectrophoretic lab-on-a-chip. Journal of Micromechanics and Microengineering 12 (2002) 7-12.

[32]Y.-N. Wang, Y. Kang, D. Xu, C.H. Chon, L. Barnett, S.A. Kalams, D. Li, and D. Li, On-chip counting the number and the percentage of CD4+ T lymphocytes. Lab on a Chip 8 (2008) 309-315.

Chapter 7

Dielectric measurements of *I. galbana*

7.1 Introduction

In chapter 2 impedance spectroscopy was introduced as an alternative detection system to fluorescence for microfluidic devices. In that chapter it was also illustrated that the output signal is proportional to the volume of the particle and of the distinctive electrical properties of the organism analysed (e.g. membrane capacitance and cytoplasm resistance). In addition, calculations presented in section 3.2.1 showed that the output of the impedance signal is proportional to the specific membrane capacitance of the cell considered. Therefore, a better knowledge of the electrical properties is essential for the correct interpretation of the data obtained from the impedance spectroscopy detection system. This is particularly important for microscopic algae because of the little knowledge of their electrical properties due to the small number of studies performed on this type of organisms.

Therefore, in the optics to improve the performance and interpretation of the integrated detection systems and start the creation of a database useful for the future interpretation of data from algae, a study to measure the electrical properties of *I. galbana* was carried out in this work. These measurements were performed with techniques developed specifically for the measurement of the dielectric properties of biological samples at the single cell level. These techniques are called AC electrokinetic methods and measure the movement of polarisable particles in non-uniform AC electric fields [1]. These techniques were chosen because they are based on models that have been studied over the last twenty years and are now widely accepted.

In the first part of this chapter the theoretical principles of the two AC electrokinetic techniques used in this work are presented. The techniques are dielectrophoresis (DEP) and electro-rotation (ROT). This chapter contains only a simplified explanation of the phenomena involved in the measurement of the dielectric properties of particles. A detailed explanation can be found in a number of publications [1; 2; 3; 4; 5; 6]. In the second part of this chapter measurement of the cross-over frequency and the electro rotation (ROT) of *I. galbana* organisms are presented.

AC electrokinetic measurements were performed with different cells at different suspending medium conductivities. The data obtained were used to calculate dielectric properties such as the specific membrane capacitance (C_{smem}), the specific membrane conductance (G_{smem}), the cytoplasm permittivity (ε_{cyt}) and conductivity (σ_{cyt}).

7.2 Theory

7.2.1 Dielectrophoresis (DEP)

If a non uniform external electric field is applied to a particle in suspension, a dielectrophoretic force acts on the particle and causes it to move. The force is generated by the interaction of the electric field with an induced dipole moment generate by the electric field itself. The DEP force acting on the particle is [2]:

$$\langle \mathbf{F} \rangle = \pi \varepsilon_m a^3 \operatorname{Re}\{f_{CM}\} \nabla |\mathbf{E}|^2 \qquad \textbf{7-1}$$

Where ε_m is the permittivity of the medium, a is the radius of the particle, $\mathbf{E}$ the electric field and $\operatorname{Re}\{f_{CM}\}$ is the real part of the Clausius-Mossotti factor that is given by [1]:

$$f_{CM} = \left(\frac{\varepsilon_p^* - \varepsilon_m^*}{\varepsilon_p^* + 2\varepsilon_m^*} \right) \qquad \textbf{7-2}$$

where ε_p^* and ε_m^* are the complex permittivities of the particle and medium respectively. In general the complex permittivity of a material is given by [1]:

$$\varepsilon^* = \varepsilon - i\frac{\sigma}{\omega} \qquad \textbf{7-3}$$

where ε is the permittivity, σ the conductivity, ω is the angular frequency and $i = \sqrt{-1}$.

The frequency dependence of the DEP force is given by the Clausius-Mossotti factor [1]. If the medium complex permittivity (ε_m^*) is lower than the particle permittivity (ε_p^*), then $\mathrm{Re}\{f_{CM}\} > 0$ and the particle will be attracted to the region of high intensity electric field. This phenomenon is called *positive dielectrophoresis* (pDEP) while the opposite case is called *negative dielectrophoresis* (nDEP). Note that when the electric field is uniform (i.e. $\nabla|\mathbf{E}| = 0$) Equation 7-1 indicates that the DEP force is zero.

Figure 7.1 shows the DEP force for a latex particle suspended in a conductive medium. The graph shows that a particle suspended in a conductive medium can experience positive or negative DEP according to the frequency applied. Furthermore, there is a specific frequency at which the particle experiences no movement as the DEP force is zero. This frequency is called *cross-over frequency* (f_0) and it can be easily measured experimentally (see section 7.4.1).

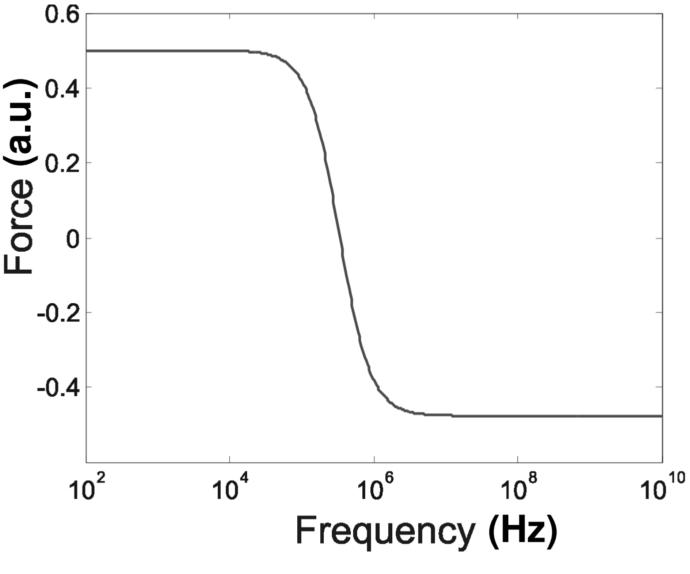

Figure 7.1 – Normalized DEP force experienced by a 10 μm latex particle suspended in water. $\varepsilon_{latex} = 2.5\ \varepsilon_0$, σ_{latex}=0.4 mS m^{-1}, $\varepsilon_m = 80\ \varepsilon_0$, σ_m = 500 mS m^{-1} where $\varepsilon_0 = 8.85\times10^{-12}$ F m^{-1}.

7.2.2 Electrorotation (ROT)

If a rotating electric field is applied to a particle in suspension, the induced dipole moment created on the particle by the action of the electric field produces a torque on the particle. This happens because the polarization process is not immediate and the dipole needs a finite time to align with the field. As a result, the dipole lags or leads the external field, generating a frequency dependent external torque. The final result of this interaction is particle rotation due to the action of the torque (ROT). The rotation speed $\Omega(f)$ is given by [7]:

$$\Omega(f) = -\frac{\varepsilon_m |\mathbf{E}|^2}{2\eta} \operatorname{Im}\left[\frac{\varepsilon_p^* - \varepsilon_m^*}{\varepsilon_p^* + 2\varepsilon_m^*}\right] \qquad \textbf{7-4}$$

where $|\mathbf{E}|^2$ is the applied field strength and η is the dynamic viscosity of the external medium. The rotation speed is a function of the imaginary rather than the real part of the Clausius-Mossotti factor: the particle rotates with the field if $\operatorname{Im}\{f_{CM}\}$ is negative while it rotates against the field if the $\operatorname{Im}\{f_{CM}\}$ is positive.

7.2.3 Dielectric models of real particles.

In general, it is possible to experimentally measure the cross-over frequency and rotation rate and use them to determine characteristic properties of the particle considered. Various models have been studied and presented in order to correlate the cross-over frequency or the frequency dependent rotation with internal properties.

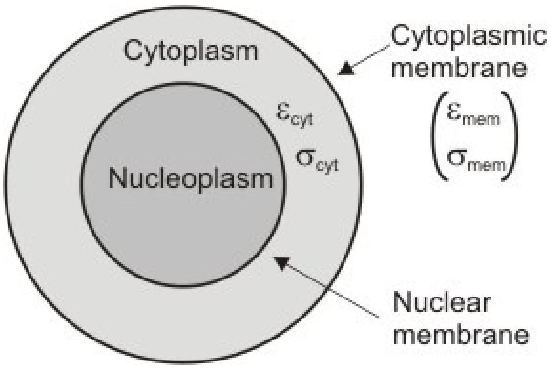

Figure 7.2 - Simplified model of a cell.

For a cell, the membrane permittivity can be calculated using a simplified model where the cell is considered as a particle composed of an insulating outer membrane that encloses an aqueous suspension (cytoplasm). The membrane actively transports ions across itself maintaining the differences in the properties outside and inside the membrane compartments; the cytoplasm is a suspension rich in ions. Within the cytoplasm lies the cell nucleus, formed again by an external membrane that encloses an aqueous suspension called nucleoplasm. A schematic representation of this model is showed in Figure 7.2.

The model of the cell can be used for the calculation of the complex permittivity that can then be inserted into the Clausius-Mossotti factor to predict the frequency dependent behaviour in non-uniform and rotating electric fields. Since a cell can have more structures than the ones mentioned (e.g. wall or other internal organelles) the solution is to assume the cell geometry spherical and the different part concentric in their orientation (Figure 7.3). The multishell model can be used to describe the dielectric properties of biological particles and, for a spherical cell, is expressed by [1]:

$$\varepsilon^*_{peff} = \varepsilon^*_{Neff} = \varepsilon^*_{N+1}\left[\frac{\left(\frac{a_{N+1}}{a_N}\right)^3 + 2\left(\frac{\varepsilon^*_{N-1eff} - \varepsilon^*_{N+1}}{\varepsilon^*_{N-1eff} + 2\varepsilon^*_{N+1}}\right)}{\left(\frac{a_{N+1}}{a_N}\right)^3 - \left(\frac{\varepsilon^*_{N-1eff} - \varepsilon^*_{N+1}}{\varepsilon^*_{N-1eff} + 2\varepsilon^*_{N+1}}\right)}\right] \qquad \textbf{7-5}$$

where ε^*_{Neff} is the effective complex permittivity of the N-shelled sphere model. a_N and a_{N+1} is the radius of the Nth-shell and the N+1th shell respectively. ε^*_{N-1eff} is the effective complex permittivity of the N-1th shell working from the innermost shell. ε^*_{N+1eff} is the effective complex permittivity of the N+1th shell.

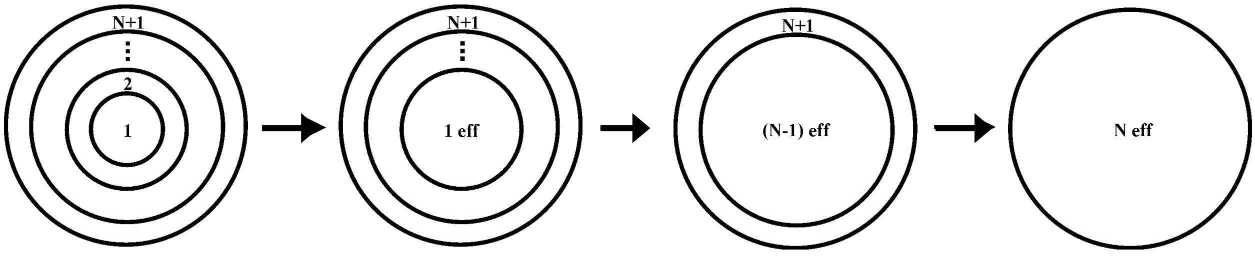

Figure 7.3 - Multi-shell model of a spherical dielectric particle.

7.2.4 Cross-over frequency and membrane capacitance

It has been demonstrated that the cross over frequency is proportional to the specific membrane capacitance (C_{smem} [10]) [8; 9]. Assuming that the radius of the cell (*a*) is substantially larger than the thickness of the cytoplasmic membrane (*d*) and the specific membrane conductance (G_{smem} [11]) is equal to zero, the C_{smem} can be calculated using the following equation [10; 11]:

$$C_{smem} = \frac{\sigma_m}{\pi\sqrt{2} f_0 a} \qquad \textbf{7-6}$$

Equations 7-2 and 7-4 show that different medium conductivities affect the frequency dependent behaviour of the particle. Therefore, the f_0 of a particle will depend on the medium conductivity. In a typical experiment, the measurement of the cross-over frequency is done by suspending particles of the same type in different medium conductivities. The cross-over frequency of a number of particles at each medium conductivity is recorded and the values are plotted on a graph of σ_m against (f_0*a). From the graph it is possible to obtain the value $\sigma_m/(f_0*a)$ (Figure 7.7), allowing the experimental determination of C_{smem} [11].

7.2.1 ROT and model fitting

In this work a single shell model was used to numerically fit the rotation spectra obtained from *I. galbana* cells. Multi shell models were also used in other works [12; 13] because they take into account the complexity of the cells, that have wall and internal organelles (e.g. nucleus or chloroplasts). However, the solutions of multi shell models have a higher number of parameters and the results are less reliable compared to results from single shell models [7].

The solution for the Clausius-Mossotti factor for a single shelled spherical particle where the membrane thickness is negligible compared to the cell radius (*d* >> *a)* can be defined as follows [7]:

---

[10] $C_{smem} = \varepsilon_0 \varepsilon_{mem}/d$ $\quad$ ε_{mem} = the membrane permittivity; d = membrane thickness.

[11] $G_{smem} = \sigma_{mem}/d$ $\quad$ σ_{mem} = the membrane conductivity; d = membrane thickness.

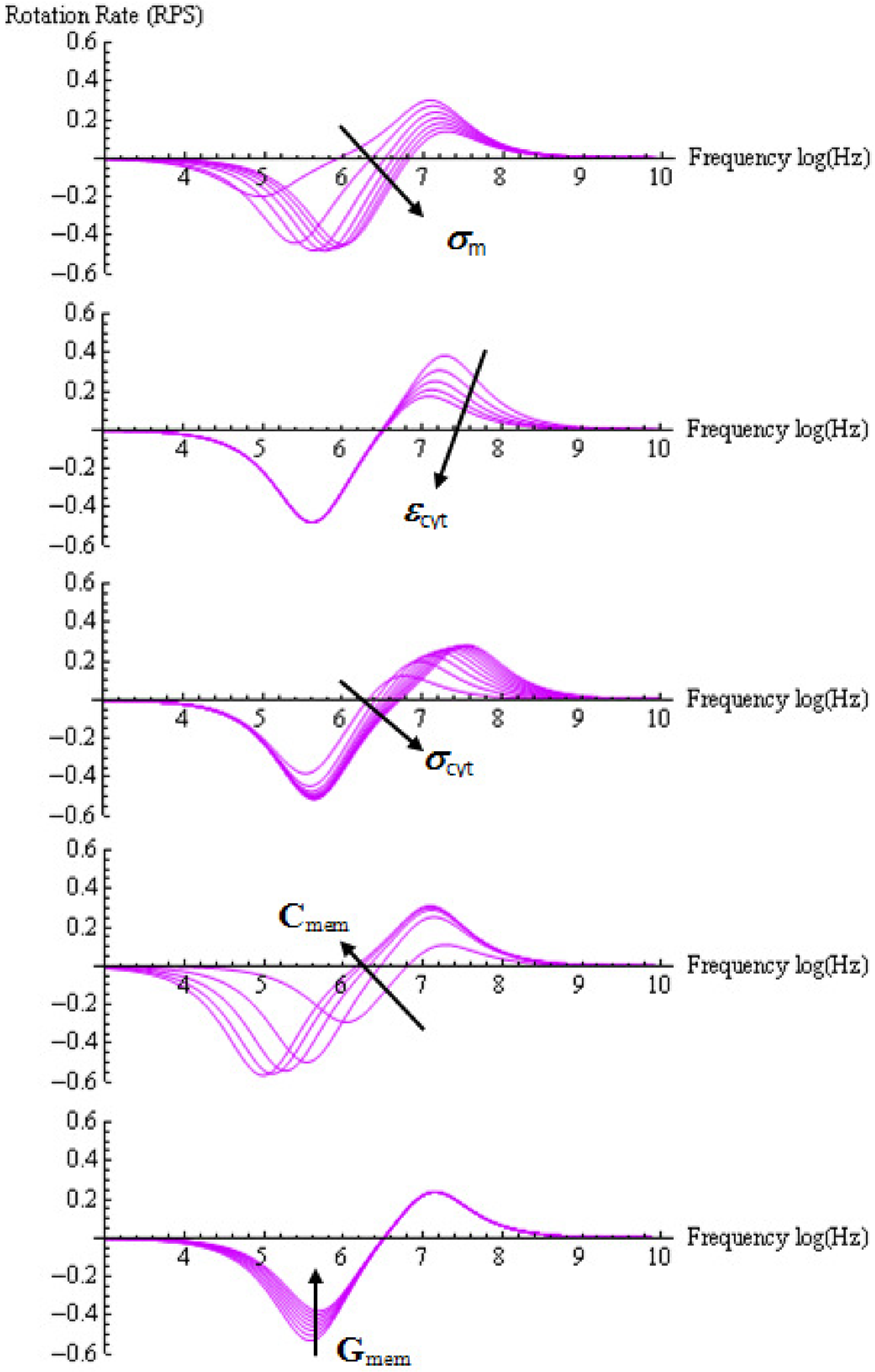

Figure 7.4 – Results of modelling *I. galbana* cells as a single-shelled object (see section 7.2.3). Each parameter influences the rotation spectrum in a characteristic manner. The basic parameters used are: σ_m = 10 mS m^{-1}, ε_{cyt} = 130 ε_0, σ_{cyt} = 170 mS m^{-1}, C_{smem} = 4 mF m^2, G_{smem} = 1500mS m^2. Parameter were varied as follow: σ_m → 5 equal steps in the range 1-30 mS m^{-1}; ε_{cyt} → 5 equal steps in the range 50-190 ε_0; σ_{cyt} → 10 equal steps in the range 50-500 mS m^{-1}, C_{smem} → 6 equal steps in the range 1-25 mF m^2, G_{smem} → 7 equal steps in the range 500-4000 S m^{-2}.

$$f_{CM} = \frac{aC_{smem}\left(\varepsilon_{cyt}^* - \varepsilon_m^*\right) - \varepsilon_{cyt}^* \varepsilon_m^*}{aC_{smem}\left(\varepsilon_{cyt}^* + 2\varepsilon_m^*\right) + 2\varepsilon_{cyt}^* \varepsilon_m^*} \qquad \textbf{7-7}$$

This solution is used in section 7.4.2 for fitting the rotational spectra obtained from *I. galbana* and to obtain the values for the specific membrane capacitance (C_{smem}), the specific membrane conductance (G_{smem}), the cytoplasm permittivity (ε_{cyt}) and conductivity (σ_{cyt}).

Figure 7.4 shows spectra calculated by substituting equation 7-7 into equation 7-4. The conductivity of the medium, the conductivity of the cytoplasm and the specific membrane capacitance are affecting both the anti-field peak in the kHz range and the co-field peak in the MHz range; the permittivity of the cytoplasm mainly affects the co-field peak and the specific membrane capacitance mainly affects the anti-field peak.

7.3 TEM of I. galbana

Detailed information of cell structure is necessary for the correct interpretation of AC electrokinetic data. Transmission electron microscopy (TEM) pictures of *I. galbana* were taken by Dr Anton Page (see section 4.5) and the results are presented in Figure 7.5 and Figure 7.6. The first is a small magnification image of *I. galbana* cells, most of which appear damaged. This phenomenon has two possible explanations: (1) the

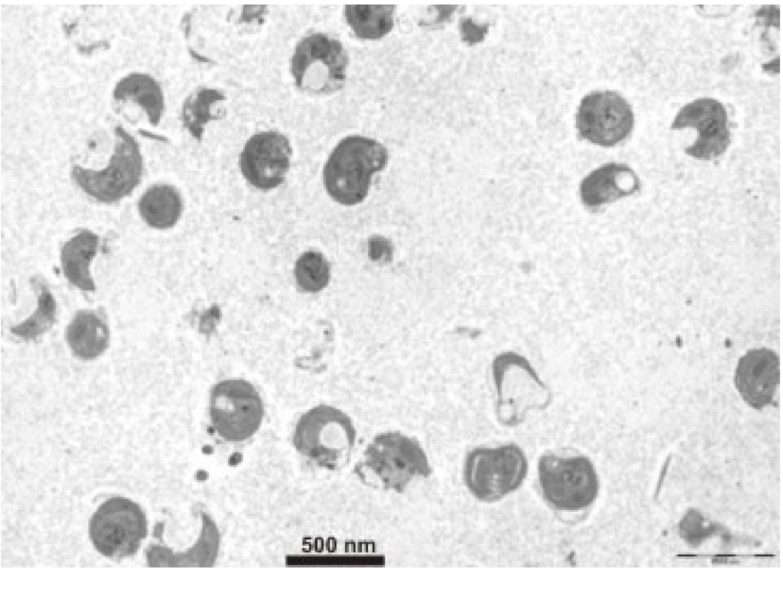

Figure 7.5 – Low magnification TEM picture of *I. galbana* cells. In the picture, most of the cells appears damaged because they do not have circular shape and in many cases the immobilising resin penetrated within the cell.

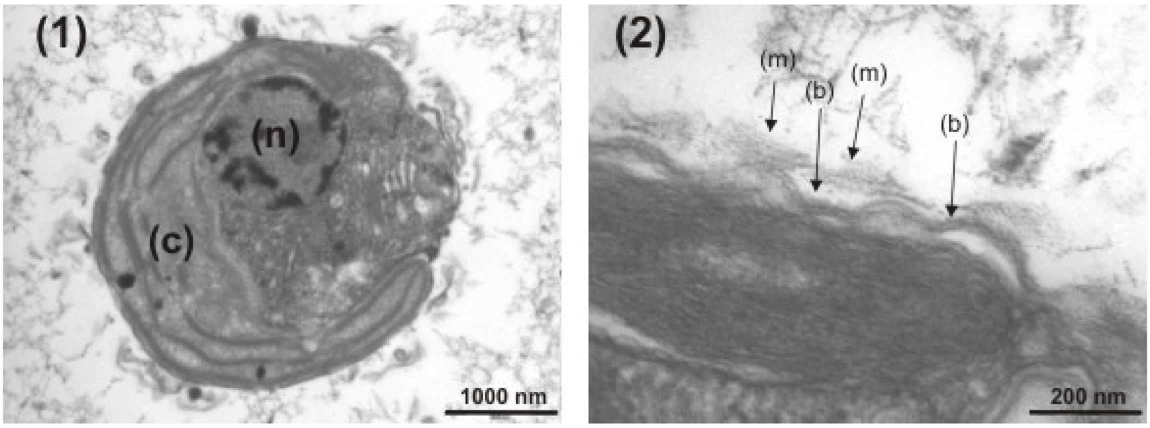

Figure 7.6 – TEM pictures of *I. galbana*. (1) Cross section of an *I. galbana* cell where (c) is the chloroplast and (n) the nucleus. (2) Detail of cell wall and membrane where (m) indicates the mucilaginous matrix and (b) the cytoplasmic membrane.

osmotic pressure of the fixative was 1200 mOsmol whilst the osmotic pressure of the growth medium was about 1000 mOsmol. Algae have mechanisms to self adjust to changes in osmolality [14], but since the fixative kills them immediately they did not have the time to react to the osmolality change. (2) Since the preparation procedure included a centrifugation immediately before a fixation (see section 4.5), it is possible that cells were damaged during centrifugation and did not have time to heal before fixation.

Figure 7.6(1) shows the section of a *I. galbana* cell: the large chloroplast and nucleus occupy a large portion of the cell. Figure 7.6(2) shows detail of membrane and cell wall, the picture was used to measure the membrane thickness, which was found to be 12±2 nm.

7.4 Results

I. galbana organisms were grown and suspended in media of different conductivities following the procedure described in section 4.3.1 and 4.4. Only non-damaged cells were selected for the measurements.

The viability of the cells after re-suspension in the conductive medium (see section 4.4) was assessed by verifying chlorophyll content (see section 4.4) and by re-culturing the cells in f2 medium. Cells analysed immediately after centrifugation still contained chlorophyll and when re-cultured they were able to grow again. In reference to damaged cells found for TEM microscopy (section 7.3) note that the shape of cells analysed for cross-over and ROT measurement appeared not damaged. It is therefore possible that cells were damaged during the centrifugation process but recovered the shape due to self-healing properties (already proven for algae [12] and other cells [15]).

7.4.1 Measurement of the cross-over frequency

Measurements of the cross-over frequency were performed on *I. galbana* cells in media with conductivities ranging from 21 to 87 mS m^{-1}. The cross-over frequency and the cell radius were measured for each cell and the average value of (f_o*a) was calculated for the different medium conductivities. The results were plotted on a graph with (f_o*a) vs σ_m (Figure 7.7). As the gradient of the slope is equal to (f_0*a)/σ_m, this value was inserted in equation 7-6 for the computation of C_{smem}. The value obtained for the specific membrane capacitance was 4.08 mF m^{-2}.

7.4.2 Electro-rotation of I. galbana

The rotation data of cells were recorded using the set-up described in section 4.10 for frequencies ranging from 10 kHz to 25 MHz. The rotation rate was obtained by analysing a minimum of four complete cycles or 2 minutes of rotation with VirtualDub video software.

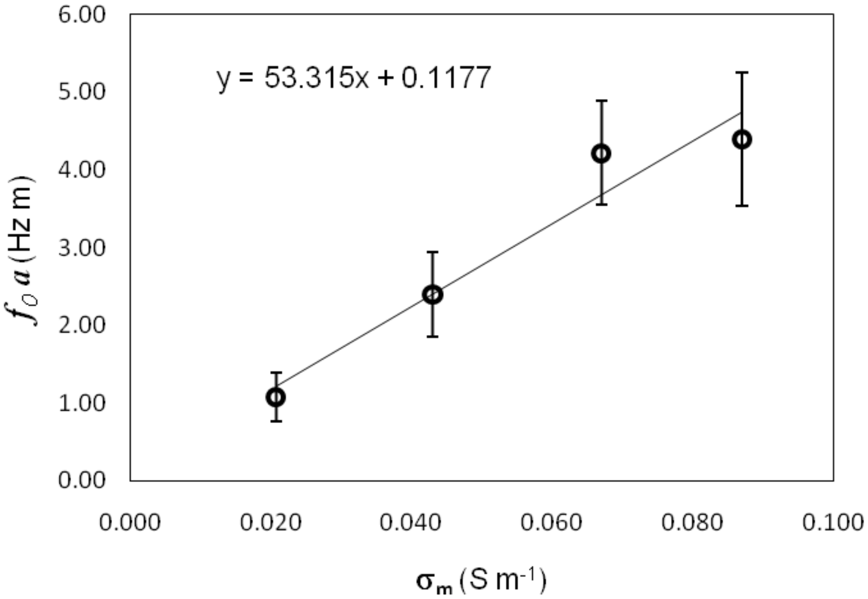

Figure 7.7 – Variation of the product of the cross-over frequency (f_0) and cell radius (a) versus the medium conductivity (σ_m). Trend line of the points is also displayed on the graph together with equation.

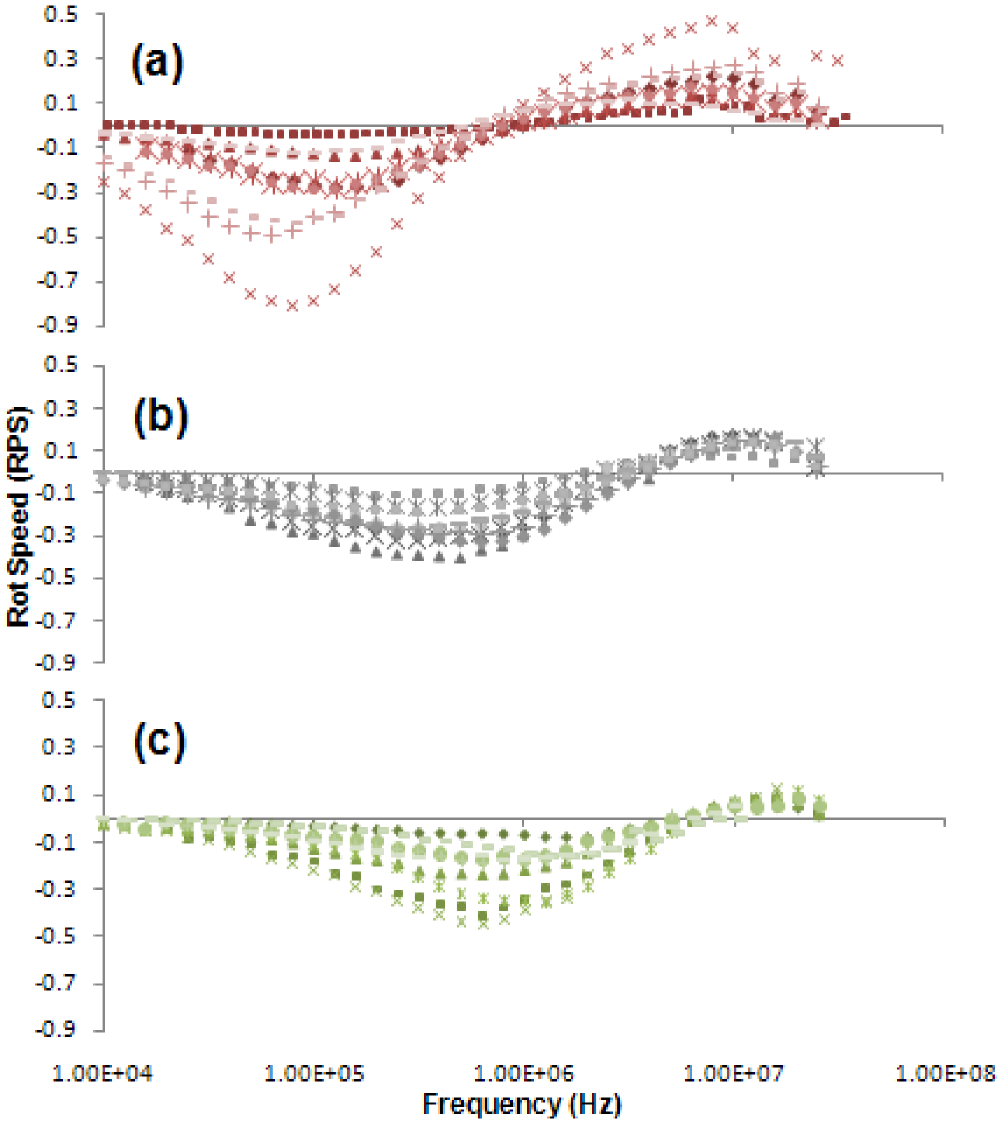

Figure 7.8 – Rotation spectra of *I. galbana* obtained at frequency intervals of the electric field between 10 kHz and 25 MHz. The rotation spectra were obtained by suspending the cells in media of different conductivities: (a) 1 mS m^{-1}, (b) 10 mS m^{-1}, (c) 20 mS m^{-1}.

Example rotation spectra are shown in Figure 7.8 (a-c). The spectra show anti-field rotation peaks in the lowest frequency regions and co-field rotation in the highest frequency regions. The anti-field peaks typically occurred at frequencies of approximately 200, 500 and 700 kHz for conductivities of 1, 10 and 20 mS m^{-1} respectively, whereas co-field peaks occurred at a frequency of approximately 1, 1.2 and 1.6 MHz for conductivities of 1, 10 and 20 mS m^{-1} respectively. In agreement with the simulations presented in Figure 7.4, the anti-field and co-field peaks are shifted to higher frequencies when the conductivity of the medium is increased.

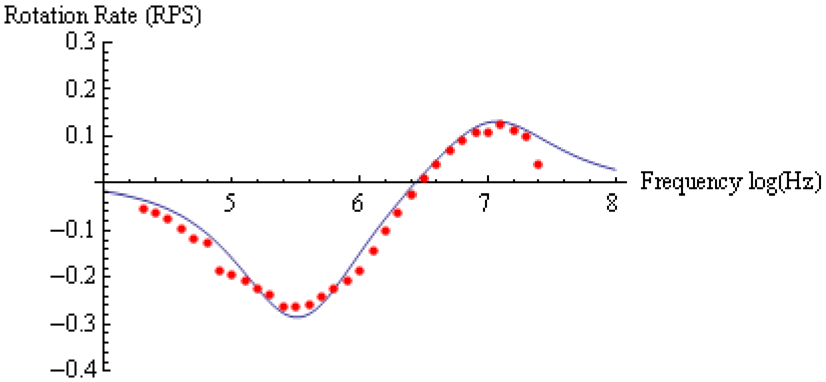

Figure 7.9 – ROT spectra for a *I. galbana* cell suspended in a medium with conductivity of 10 mS m^{-1}. The dots indicate the experimental data while the best fit for the spectrum is represented by the solid line and gave the following parameters: C_{smem} = 5.35 mF m^{-2}, ε_{cyt} = 130, σ_{cyt} = 178 mS m^{-1} and G_{smem} = 486 S m^{-2}.

Rotation spectra were fitted by substituting equation 7-7 into equation 7-4. The best fit for a single ROT spectrum for a cell of *I. galbana* suspended in a 10 mS m^{-1} conductive medium is represented by the solid line in Figure 7.9 along with the rotation data measured (dots). It is evident that the spectrum could be fitted satisfactorily. The averages of the data obtained from the numerical fit of the different spectra were ε_{cyt} = 140±20 ε_0, σ_{cyt}=200±150 mS m^{-1}, C_{smem} =3.6±2 mF m^{-2}, G_{smem} =1400±1600 S m^{-2} while the average radius measured for the cell measured was 1.9±0.3 µm.

7.5 Discussion

The value found for the specific membrane capacitance (approximately 4 mF m^{-2}) differs from the majority of the values found in the literature (i.e. higher than 10 mF m^{-2} [11; 13; 16; 17; 18]) however, values between 1 and 6 mF m^{-2} have also been reported for cells and lipid bilayer membranes [12; 15; 19; 20; 21; 22; 23]. The low value of C_{smem} found for *I. galbana* cells can be explained by the thick membrane found from TEM microscopy which was 12 nm. This value is critical because the capacitance is proportional to the area and inversely proportional to the thickness of the dielectric material ($C = \varepsilon_0\, \varepsilon_r\, (A/d)$ [1]). Average thicknesses found for cell membranes are of the order of 5 nm [24] whilst the value found for *I. galbana* was more than twice this average. The membrane thickness was used to calculate the permittivity of the membrane from C_{smem}, giving a value of $6\varepsilon_0$ which is in close agreement with the value of $8\varepsilon_0$ found for snow algae (*Chloromonas nivalis* and *Chlamydomonas nivalis*) by Muller *et al.* [13].

ROT measurement gave a specific membrane conductance of 1400 S m^{-2}, a cytosol permittivity of $140\varepsilon_0$ and a conductivity of the cytoplasm of 200 mS m^{-2}. The first two values are within the range found in the literature (between 50 and 3500 S m^{-2} for G_{mem} and between 80 and $150\varepsilon_0$ for ε_{cyt} [7; 11; 12; 13; 15]) while the conductivity of the cytoplasm shows a lower ion concentration than in the literature (600 mS m^{-1} [12; 13; 18]) which may be due to the presence of large chloroplast and nucleus that occupy a large section of the cell (see Figure 7.6(1)).

The results for C_{smem}, G_{smem} and ε_{mem} of *I. galbana* (~4 mF m^{-2}, 1400 S m^{-2} and $6\varepsilon_0$ respectively) are comparable with results obtained for other marine organisms (C_{smem} between 1 and 12 mF m^{-2}, G_{smem} approximately 200 and $\varepsilon_{mem} = 8\varepsilon_0$) [12; 13]. There are noticeable differences between the values of cytoplasmic conductivity and permittivity for *I. galbana* (200 mS m^{-1} and $140\varepsilon_0$ respectively) and the values obtained for snow algae and protoplasts (500 mS m^{-1} and 50÷70 ε_0). This outcome is difficult to explain because they have similar internal structures with a large chloroplast and an elevated number of organelles. It is therefore possible that *I galbana* cells analysed suffered minor membrane damages. In fact, damaged cell membranes were noticed from TEM pictures (Figure 7.6). Furthermore, Kriegmaier *et al.* [15] showed that permeabilised cell membranes gave an increased cytosol permittivity. In addition to increase cytosol permittivity, the permeabilisation of cell membranes can generate an efflux of ions from the highly conductive cytoplasm to the low conductive suspending medium, explaining the lower value obtained for σ_{cyt} of *I. galbana* compared to snow algae. In *I. galbana* cells, the damage to the membrane may have been generated by the mechanical stress applied during the re-suspension process (section 4.4) as the procedure involves acceleration during centrifugation, shear forces during sample withdrawal (operated with a pipette) and mixing.

Only cells with intact membranes were selected for analysis. However it is possible that small damage were not visible with the microscope used. Alternatively, since self healing processes have been documented for marine organisms and other cells [12; 15], it is possible that the cells analysed had internal properties changed by temporary permeabilisation induced by mechanical stress. Cells may have healed before DEP and ROT experiments so that the values obtained for specific membrane capacitance and conductance reflected the value of undamaged cells.

Membrane integrity can be investigated in future work using techniques initially developed to test the viability of cells [24]. Some of these tests (dye exclusion methods) are based on acid or basic dyes (trypan blue, eosin, erythrosine, nigrosin, primulin and propidium) which are not able to penetrate the cell membrane. Since these dyes are not normally able to penetrate a membrane, only cells with damaged membranes will appear coloured when observed under the microscope. Alternatively, tests based on esters of fluorescein (e.g. fluorescein diacetate or FDA) or related other fluorescing compounds can also be used to verify membrane integrity. These compounds are non-fluorescent and can easily cross cell membranes because they are uncharged and lipofilic. Once inside the cell they are hydrolyzed by nonspecific esterases to produce fluorescent compounds that are retained by cells with intact membranes and lost by cells with damaged membranes.

As an example of future work, dye exclusion methods can be added to the suspension solution before the preparation process so that they can enter the cells if the membrane is damaged. After the preparation, FDA can also be added to the suspending medium to verify if the membrane is repaired or damaged.

7.6 Summary

Measurements of cross-over frequency and electro-rotation spectrum were performed on *I. galbana* cells to determine their dielectric properties. In particular, the dielectric models of real particles developed for the interpretation of electrokinetic response of biological particles (section 7.2.3) enabled a detailed analysis of the electrical properties of plasma membrane and cytosol of living *I. galbana* cells.

The result for C_{smem} obtained by the measurement of the cross-over frequency (4.08 mF m^{-2}) is consistent with the data obtained by the measurement of the electro rotation (3.6 mF m^{-2}), confirming the reliability of the experiments. The value obtained is low compared to the literature but is probably due to the thick cell membrane measured with TEM microscopy.

The values found for the permittivity and conductivity of the cytoplasm differed from those found in the literature. TEM analysis and literature suggest that the difference might have originated from the mechanical stress applied during the preparation process. However, ε_{cyt} and σ_{cyt}, together with *Gsmem*, are within the range found in the literature. Therefore, future work should verify whether the cell analysed have a damaged membrane, for example by treating part of a sample with methanol and comparing the results with untreated cells [13].

In addition to further research on marine organisms, the values of the dielectric parameters obtained from DEP cross-over and ROT measurements can be used for modelling of cells behaviour in a range of electric field geometries such as those used in microfluidic devices. For example, the data obtained can be inserted in a model for the IS detection system implemented in chip A to perform simulations able to predict the output impedance signal [25]. These simulations also inspires further research on the development of experimental methods with the optimum analytical conditions (e.g. frequency to apply to integrated electrodes) and for the fabrication of an innovative cell detection device.

REFERENCES

[1]H. Morgan, and N.G. Green, AC Electrokinetics: colloids and nanoparticles, Research Studies Press, Ltd, Baldock, Hertfordshire, England, 2003.

[2]T.B. Jones, (Ed.), Electromechanics of Particles, Cambridge University Press, Cambridge, 1995.

[3]S. Grimnes, and Ø.G. Martinsen., Bioimpedance and bioelectricity basics, Academic, London, 2000.

[4]P.R.C. Gascoyne, and J. Vykoukal, Particle separation by dielectrophoresis. Electrophoresis 23 (2002) 1973-1983.

[5]J. Israelachvili, Intermolecular and Surface Forces, 1992.

[6]J. Lyklema, Fundamentals of Interface and Colloid Science Vol II, London, 1995.

[7]M. Kiesel, R. Reuss, J. Endter, D. Zimmermann, H. Zimmermann, R. Shirakashi, E. Bamberg, U. Zimmermann, and V.L. Sukhorukov, Swelling-activated pathways in human T-lymphocytes studied by cell volumetry and electrorotation. Biophysical Journal 90 (2006) 4720-4729.

[8]J. Gimsa, P. Marszalek, U. Loewe, and T.Y. Tsong, Dielectrcophoresis and electrorotation of neurospora slime and murine myeloma cells. Biophysical Journal 60 (1991) 749-760.

[9]P.R.C. Gascoyne, J. Noshari, F.F. Becker, and R. Pethig, Use of dielectrophoretic collection spectra for characterizing differences between normal and cancerous cells. Ieee Transactions on Industry Applications 30 (1994) 829-834.

[10]K. Asami, Characterization of biological cells by dielectric spectroscopy. Journal of Non-Crystalline Solids 305 (2002) 268-277.

[11]K.L. Chan, H. Morgan, E. Morgan, I.T. Cameron, and M.R. Thomas, Measurements of the dielectric properties of peripheral blood mononuclear cells and trophoblast cells using AC electrokinetic techniques. Biochimica Et Biophysica Acta-Molecular Basis of Disease 1500 (2000) 313-322.

[12]J. Wang, V.L. Sukhorukov, C.S. Djuzenova, U. Zimmermann, T. Muller, and G. Fuhr, Electrorotational spectra of protoplasts generated from the giant marine alga Valonia utricularis. Protoplasma 196 (1997) 123-134.

[13]T. Muller, T. Schnelle, and C. Fuhr, Dielectric single cell spectra in snow algae. Polar Biology 20 (1998) 303-310.

[14]R.E. Lee, Phycology, Cambridge University Press, Cambridge, 1989.

[15]M. Kriegmaier, M. Zimmermann, K. Wolf, U. Zimmermann, and V.L. Sukhorukov, Dielectric spectroscopy of Schizosaccharomyces pombe using electrorotation and electroorientation. Biochimica Et Biophysica Acta-General Subjects 1568 (2001) 135-146.

[16]A. Surowiec, S.S. Stuchly, and C. Izaguirre, Dielectric-Properties of Human-B and Lymphocytes-T at Frequencies from 20-Khz to 100-Mhz. Physics in Medicine and Biology 31 (1986) 43-53.

[17]Y. Polevaya, I. Ermolina, M. Schlesinger, B.Z. Ginzburg, and Y. Feldman, Time domain dielectric spectroscopy study of human cells - II. Normal and malignant white blood cells. Biochimica Et Biophysica Acta-Biomembranes 1419 (1999) 257-271.

[18]J. Yang, Y. Huang, X. Wang, X.-B. Wang, F.F. Becker, and P.R.C. Gascoyne, Dielectric Properties of Human Leukocyte Subpopulations Determined by Electrorotation as a Cell Separation Criterion. Biophysical Journal 76 (1999) 3307–3314.

[19]G. Fuhr, and P.I. Kuzmin, Behavior of Cells in Rotating Electric-Fields with Account to Surface-Charges and Cell Structures. Biophysical Journal 50 (1986) 789-795.

[20]G. Fuhr, R. Glaser, and R. Hagedorn, Rotation of dielectrics in a rotating electric high-frequency field - model experiments and theoretical explanation of the rotation effect of living cells. Biophysical Journal 49 (1986) 395-402.

[21]W.M. Arnold, and U. Zimmermann, Rotating-field-induced rotation and measurement of the membrane capacitance of single mesophyll-cells of avena-sativa. Zeitschrift Fur Naturforschung C-a Journal of Biosciences 37 (1982) 908-915.

[22]R. Glaser, G. Fuhr, and J. Gimsa, Rotation of erythrocytes, plant-cells, and protoplast in an outside rotating electric-field. Studia Biophysica 96 (1983) 11-20.

[23]R.V.E. Lovelace, D.G. Stout, and P.L. Steponkus, Protoplast rotation in a rotating electric-field - The influence of cold-acclimation. Journal of Membrane Biology 82 (1984) 157-166.

[24]B. Alberts, A. Johnson, J. Lewis, M. Raff, K. Roberts, and P. Walter, Biologia molecolare della cellula, 2004.

[25]S. Gawad, K. Cheung, U. Seger, A. Bertsch, and P. Renaud, Dielectric spectroscopy in a micromachined flow cytometer: theoretical and practical considerations. Lab on a Chip 4 (2004) 241-251.

Chapter 8

Conclusions

8.1 Introduction

This thesis describes the design and testing of a novel lab-on-a-chip flow cytometric system for phytoplankton analysis. The system represents the first step towards creating a portable device to be used for *in-situ* analysis in place of traditional flow cytometers. In particular, the work is aimed at realising and testing a sensor with fully integrated functionalities, proving the ability of the device to detect and characterise particles with different optical and electrical properties. AC electrokinetics measurements of the dielectric properties of algae were also performed.

In this section a short summary of the work is given and the results are presented together with suggested improvements and topics for future research.

8.2 Background

The literature shows that flow cytometry is already widely used to study marine organisms, but suffers major problems that prevent it reaching its full potential. In particular, the technique is not always able to characterise single taxa and it is only occasionally deployed *in-situ* due to the size, complexity and cost of the instruments. Improvements are therefore needed to create affordable systems able to perform rapid and accurate *in-situ* characterisation of marine organisms.

The design of a new cytometric system is based on lab-on-a-chip techniques. In addition to reduced size, cost and complexity, the device features flexible layouts and integrates innovative detection and characterisation methods, therefore increasing the characterisation power of the system.

8.3 Design

Two designs of microfabricated flow cytometer were presented (chip A and B). Both devices featured simultaneous detection of optical and electrical properties that made them powerful analytical tools compared to commercial cytometers that are limited to only optical or electrical detection. Furthermore, flow cytometers based on electrical measurements (Coulter counters) can only measure particle sizes, while the IS system implemented on chips A and B is potentially able to give information on the internal properties of particles [1].

Chip A featured a simple channel layout, conventional optics and co-planar electrodes; Chip B was entirely developed in this work and had several improvements compared with chip A such as a wider sample channel coupled with hydrodynamic focussing that allowed a wider size range to be analysed; monolithically integrated optical elements that, in addition to creating a more robust and compact system, could detect scattered light and multiple fluorescence; opposing electrodes that were demonstrated to have a higher sensitivity than coplanar electrodes [2].

8.4 Results

Analysis of samples with the microfabricated and commercial cytometers were undertaken and the performances of the systems were compared. Chip A and B were able to detect and characterise mixtures composed of polymer microspheres and algae with results comparable to the FACS. Chip A was also able to detect *E. coli* bacteria using impedance spectroscopy, demonstrating that label free detection of bacteria is possible. However, complete detection and characterisation of bacteria was possible only using the optical detection system because the dimensions of the impedance detection region were inadequate to size the bacteria. Chip B is the first integrated device capable of multi-parameter optical and electrical cytometry. The device demonstrated characterisation abilities comparable to a commercial instruments and precision similar to other microfabricated cytometers presented in literature that implement 1D particle focussing (CVs between 15 and 35% [3; 4; 5; 6; 7; 8]).

Although good results were obtained, precision and particle flow velocities in chip B were limited by the implementation of a 1D focussing system, the position dependence of the IS system, the low sensitivity of the side scatter detection system and inertial phenomena that limited the use of the device at high particle velocities (0.5 m sec^{-1}). Nevertheless, tests performed at high particle velocities demonstrated excellent performances for all the integrated detection systems. Since most of the problems are related to particles position the implementation of a bi-dimensional focussing system can drastically improve the performances of the microfabricated cytometer.

Another drawback of chip B was in the integrated optical detection system that had losses one order of magnitude higher than similar systems published in the literature, probably because of inadequate resolution of the optical structures and the autofluorescence generated by SU-8 when irradiated with a 532 nm wavelength. Furthermore, the scatter detection system was unable to detect signals at 7° because of the excessive excitation light entering the collection fibre. The inadequate focussing was also the cause of the low sensitivity of scattered light at 22°.

AC electrokinetic measurements were performed to obtain the dielectric properties of *I. galbana.* Two different types of experiments were used to measure C_{smem}, which was found to be 4.08 mF m^{-2} from cross-over frequency data and 3.6 mF m^{-2} from measurements of the electro rotation. The values of C_{smem} were significantly lower to values found in the literature (higher than 10 mF m^{-2} reported in the literature) and were probably due to the high thickness of the cell membrane (12 nm).

Electro-rotation experiments gave also the value for specific membrane conductance of 1400 S m^{-2}, a cytosol permittivity of $140\varepsilon_0$ and a conductivity of the cytoplasm of 200 mS m^{-1}. Despite the first two being in the ranges indicated by literature (between 50 and 3500 S m^{-2} for G_{mem} and between 80 and $150\varepsilon_0$ for ε_{cyt} [9; 10; 11; 12; 13]), the conductivity of the cytoplasm showed a lower ion concentration than in literature (600 mS m^{-1} [11; 12; 14]). However, cytoplasmic conductivity and permittivity obtained for *I. galbana* were different with values found for other algae organism and at the present stage it is not clear whether this difference reflects different internal properties or is due to damages of the cell membrane generated by mechanical stress induced during the preparation of the sample.

8.5 Future work

This work demonstrated that a portable low cost and powerful flow cytometric device can be used to measure phytoplankton. However, the device had a number of problems that need to be addressed in future projects.

Since the performance of the impedance detection system was limited to a one-dimensional focussing system, future work should aim towards the implementation of a 2D focussing system. In fact, a series of solutions were presented in the last years that featured relatively simple fabrication and flow control: Kummrow *et al.* [15] suggested an easy to fabricate, three dimensional structure with characteristics similar to mono-dimensional hydrodynamic focussing; Golden *et al.* [16] suggested a conventional mono-dimensional hydrodynamic focussing system with chevrons after the sheath junction that were supposed to focus the particles in the vertical direction; Shi *et al.* [17] proposed a system that used standard surface acoustic waves. However, considering the *in-situ* intention of the system considered, the most interesting solution was presented by Di Carlo and co-worker [18] as they took advantage of hydrodynamic effects to obtain 2D focussing of particles in a curved channel. The design is the best solution for a low cost and portable device because it is simple to fabricate and features a single channel, therefore reducing the control complexity and energy and buffer consumption.

Alternatively, instead of a focussing system, an array of single channels could be implemented with sizes fitted to specific cell ranges. The single channel solution was effective for chip A whose CVs were comparable to, and sometimes better than, the results from the BD FACSAria. Furthermore, the implementation of a single channel would simplify the flow control as a pressure balance control is not required.

Future development of an integrated optical system with reduced power losses and a narrower light spot in the detection region are also needed: (1) reduced power losses are critical for the long-life of a portable device but the values reported for chip B are one order of magnitude higher than the values reported in literature. Power losses could be reduced by the use of high resolution fabrication process and the use of polymers that do not generate fluorescence when irradiated with the excitation wavelength (e.g. PDMS [19]). (2) The width of the light-spot generated in the detection region affected scattered light detection, as it lead to low values of S/N for SSC and made impossible the detection of FSC.

Improvement of the design of the impedance detection system is also advisable to reduce the dependence of the system on particle position. However, the implementation of a bi-dimensional focussing system for particles should solve most of the problems affecting the impedance detection system.

Chip A could be modified for efficient label free detection of bacteria. Improvements require the fabrication of a channel with a detection region with dimensions similar to the organism investigated, because the sensitivity of the impedance detection system is directly related to the volume fraction of the particle in the detection region [20; 21; 22]. Furthermore, the new design should implement facing electrodes which have been shown to have a higher sensitivity than coplanar electrodes [1].

Additional future work may include the expansion of the work presented in chapter 7 for the determination of the dielectric properties of algae. In addition to a better knowledge of marine organisms, the values of the dielectric parameters obtained from DEP cross-over and ROT measurements can be used to model cell behaviour in a range of electric field geometries such as those used in microfluidic devices. For example, the data obtained can be inserted in a model for the impedance detection system implemented in chip B to perform simulations to predict the output impedance signal [2]. These simulations can be used to find the best analytical conditions for the design of a better detection cell.

8.6 Final conclusions

In conclusion, the first steps toward the creation of a small, inexpensive and powerful analytical tool for the detection and characterisation of phytoplankton were successfully achieved: high precision detection and characterisation of phytoplankton with a microfabricated cytometer was demonstrated; a fully integrated biosensor able of multi-parameter detection (optical and electrical) was successfully fabricated and tested; increase knowledge of marine organisms was obtained with AC electrokinetics measurements.

The next step will be the design of an improved design for the fully integrated microfluidic device using the feedback obtained by testing chip B and the information collected by AC electrokinetic measurements of marine algae.

REFERENCES

[1]K. Cheung, S. Gawad, and P. Renaud, Impedance spectroscopy flow cytometry: On-chip label-free cell differentiation. Cytometry Part A 65A (2005) 124-132.

[2]S. Gawad, K. Cheung, U. Seger, A. Bertsch, and P. Renaud, Dielectric spectroscopy in a micromachined flow cytometer: theoretical and practical considerations. Lab on a Chip 4 (2004) 241-251.

[3]D.P. Schrum, C.T. Culbertson, S.C. Jacobson, and J.M. Ramsey, Microchip flow cytometry using electrokinetic focusing. Analytical Chemistry 71 (1999) 4173-4177.

[4]Z. Wang, J. El-Ali, M. Engelund, T. Gotsaed, I.R. Perch-Nielsen, K.B. Mogensen, D. Snakenborg, J.P. Kutter, and A. Wolff, Measurements of scattered light on a microchip flow cytometer with integrated polymer based optical elements. Lab on a Chip 4 (2004) 372-377.

[5]N. Pamme, R. Koyama, and A. Manz, Counting and sizing of particles and particle agglomerates in a microfluidic device using laser light scattering: application to a particle-enhanced immunoassay. Lab on a Chip 3 (2003) 187-192.

[6]M.A. McClain, C.T. Culbertson, S.C. Jacobson, and J.M. Ramsey, Flow cytometry of Escherichia coli on nucrifluidic devices. Analytical Chemistry 73 (2001) 5334-5338.

[7]L.-M. Fu, R.-J. Yang, C.-H. Lin, Y.-J. Pan, and G.-B. Lee, Electrokinetically driven micro flow cytometers with integrated fiber optics for on-line cell/particle detection. Analytica Chimica Acta 507 (2004) 163-169.

[8]Y.-N. Wang, Y. Kang, D. Xu, C.H. Chon, L. Barnett, S.A. Kalams, D. Li, and D. Li, On-chip counting the number and the percentage of CD4+ T lymphocytes. Lab on a Chip 8 (2008) 309-315.

[9]K.L. Chan, H. Morgan, E. Morgan, I.T. Cameron, and M.R. Thomas, Measurements of the dielectric properties of peripheral blood mononuclear cells and trophoblast cells using AC electrokinetic techniques. Biochimica Et Biophysica Acta-Molecular Basis of Disease 1500 (2000) 313-322.

[10]M. Kiesel, R. Reuss, J. Endter, D. Zimmermann, H. Zimmermann, R. Shirakashi, E. Bamberg, U. Zimmermann, and V.L. Sukhorukov, Swelling-activated pathways in human T-lymphocytes studied by cell volumetry and electrorotation. Biophysical Journal 90 (2006) 4720-4729.

[11]T. Muller, T. Schnelle, and C. Fuhr, Dielectric single cell spectra in snow algae. Polar Biology 20 (1998) 303-310.

[12]J. Wang, V.L. Sukhorukov, C.S. Djuzenova, U. Zimmermann, T. Muller, and G. Fuhr, Electrorotational spectra of protoplasts generated from the giant marine alga Valonia utricularis. Protoplasma 196 (1997) 123-134.

[13]M. Kriegmaier, M. Zimmermann, K. Wolf, U. Zimmermann, and V.L. Sukhorukov, Dielectric spectroscopy of Schizosaccharomyces pombe using electrorotation and electroorientation. Biochimica Et Biophysica Acta-General Subjects 1568 (2001) 135-146.

[14]J. Yang, Y. Huang, X. Wang, X.-B. Wang, F.F. Becker, and P.R.C. Gascoyne, Dielectric Properties of Human Leukocyte Subpopulations Determined by

Electrorotation as a Cell Separation Criterion. Biophysical Journal 76 (1999) 3307–3314.

[15]A. Kummrow, J. Theisen, M. Frankowski, A. Tuchscheerer, H. Yildirim, K. Brattke, M. Schmidt, and J. Neukammer, Microfluidic structures for flow cytometric analysis of hydrodynamically focussed blood cells fabricated by ultraprecision micromachining. Lab on a Chip 9 (2009) 972–981.

[16]J.P. Golden, J.S. Kim, J.S. Erickson, L.R. Hilliard, P.B. Howell, G.P. Anderson, M. Nasir, and F.S. Ligler, Multi-wavelength microflow cytometer using groove-generated sheath flow. Lab on a Chip 9 (2009) 1942-1950.

[17]J. Shi, X. Mao, D. Ahmed, A. Colletti, and T.J. Huang, Focusing microparticles in a microfluidic channel with standing surface acoustic waves (SSAW). Lab on a Chip 8 (2007) 221-223.

[18]D. Di Carlo, D. Irimia, R.G. Tompkins, and M. Toner, Continuous inertial focusing, ordering, and separation of particles in microchannels. Proceedings of the National Academy of Sciences of the United States of America 104 (2007) 18892-18897.

[19]C. Bliss, J. McMullin, and B. CJ, Rapid fabrication of a microfluidic device with integrated opitcal waveguides for DNA fragment analysis. Lab on a Chip 7 (2007) 1280-1287.

[20]D. Holmes, B. Neal, N. Green, and H. Morgan, Microfabricated Device for Rapid Impedance Measurements on Single Biological Cells, Proceedings of 15th MicroMechanics Europe Workshop, Leuven Belgium, 2004, pp. pp. 195-198.

[21]H. Morgan, T. Sun, D. Holmes, S. Gawad, and N.G. Green, Single cell dielectric spectroscopy. J. Phys. D: Appl. Phys. 40 (2007) 61-70.

[22]H. Morgan, and N.G. Green, AC Electrokinetics: colloids and nanoparticles, Research Studies Press, Ltd, Baldock, Hertfordshire, England, 2003.

List of Publications

Journal articles

Barat D., Benazzi G., Mowlem M.C, Ruano J. M. and Morgan H. *Design, Simulation and Characterisation of Integrated optics for a microfabricated flow cytometer.* Optics Communications (in press, available on-line at www.sciencedirect.com).

Benazzi G., Holmes D., Sun T., Mowlem M.C and Morgan H. *Discrimination and analysis of phytoplankton using a microfluidic cytometer.* IET Nanobiotechnology, 2007. **1**(6): p. 94-101.

Book

Gawad, S., Holmes, D., Benazzi, G., Renaud Ph. and Morgan H. *Impedance spectroscopy and optical analysis of single biological cells and organisms in microsystems.* in Microengineering in Biotechnology: methods and protocols. Eds Hughes, M.P. and Hoettges, K.F. The Humana Press Inc. USA. 2009.

Conference proceedings

Holmes D., Benazzi G., Mowlem M.C and Morgan H. *A microfluidic device for the rapid measurement of the inherent fluorescence and impedance properties of individual marine algae*, Micro Total Analysis System Kluwer Academic Publ., Boston, Massachussets, 2005, pp. 892-894.

Conferences

Benazzi, G., Holmes, D., Mowlem, M., Ruano-Lopez, J.M. and Morgan, H. *Microfabricated flow cytometer for simultaneous optical and impedance measurements of phytoplankton.* FlowcytometryUK. 19th -20th July 2007. King's College, Cambridge, UK.

Benazzi, G., Holmes, D., Mowlem, M., Ruano-Lopez, H. and Morgan, H. *Analysis of fluorescence spectra from individual marine phytoplankton in a microfluidic device.* in NanoTech2006: The 10th Annual European Conference on Micro & Nanoscale Technologies for the Biosciences. Montreux, Switzerland, 2006.

Morgan, H., Benazzi, G., Tao, S., Green, N., Holmes, D. and Gawad, S. *Single cell impedance spectroscopy.* IoP Dielectrics Group, Annual Conference 2006. Bio-dielectrics: theories, mechanisms and applications. 10-12 April 2006. Stamford Hall, Leicester, UK.

Holmes, D., Benazzi, G., Mowlem, M. and Morgan, H. *Microdevices for optical and impedance based detection of marine organisms*. IoP Dielectrics Group, Annual Conference 2006. Bio-dielectrics: theories, mechanisms and applications. 10-12 April 2006. Stamford Hall, Leicester, UK.

Benazzi, G., Holmes, D., Mowlem, M.M. and Morgan H. *Detection and Discrimination of Marine Algae with Micro-Flow Cytometry.* NanoTech2005: The 9th Annual European Conference on Micro & Nanoscale Technolgies for the Biosciences Montreux, Switzerland, 2005.

Benazzi, G., Holmes, D., Mowlem, M.M. and Morgan H. *Lab-on-a-chip- for rapid measurement of the inherent fluorescence and impedance properties of individual marine algae*. BioNano3: 19th -21st Sept, 2005. Brighton, UK.

Benazzi, G., Holmes, D., Mowlem, M. and Morgan, H. *Micro-flowcytometry for marine analysis*. Optics and Microfluidics Meeting, Centre for Science at Extreme Conditions, University of Edinburgh, Edinburgh. 13th May 2005.

Benazzi, G., D. Holmes, M.M. Mowlem, and H. Morgan, *Developing of a micro-flow cytometer for phytoplankton in-situ monitoring* Science & Management Audit, Oceanography Centre, Southampton, UK, 2005.